UNIVERSITY *of the*
WESTERN CAPE

Development of Palladium Nickel/Tin Metal Oxide Catalysts on Carbon Nanotube Supports for Direct Alcohol Fuel Cells

---

by

Thando Juqu

Student Number: 3341994

Dissertation in fulfilment of the requirement for the degree

MASTERS

in

CHEMISTRY

in the

FACULTY OF SCIENCE

of the

UNIVERSITY OF THE WESTERN CAPE

Supervisor : Prof Lindiwe Khotseng

Co-supervisors : Dr Mmalewane Modibedi

DECLARATION

I, hereby declare that "*Development of Palladium Nickel/Tin Metal Oxide Catalysts on Carbon Nanotube Supports for Direct Alcohol Fuel Cells*" is the result of my own work that was done by me under the supervision of Prof. Lindiwe Khotseng and co-supervision of Dr. Mmalewane Modibedi, and that it has not been previously submitted for any degree or examination in any other university or higher education; and that all the sources and quotations have been indicated and acknowledged by complete references.

MASTERS DEGREE IN CHEMISTRY

to the University of the Western Cape, Department of Chemistry, is, apart from the recognised assistance of my supervisors, my own work and has not previously been submitted by me to another institution to obtain a research diploma or degree.

_____ on this ____ day of _____

(Candidate)

_____ on this ____ day of _____

(Supervisor)

_____ on this ____ day of _____

(Co-supervisor)

DEDICATION

This work is dedicated to my family; Mrs. Ntsebeng Anatoha Juqu (Mother), Mr. Thanduxolo Abraham Juqu (late father), Miss. Busiswa Juqu (sister), Mr. Nkosinathi Juqu (brother), Mr. Yanga Juqu (brother) and Mr. Tshitso Juqu (nephew) for their moral support, prayers and love throughout this process.

ACKNOWLEDGEMENTS

Firstly, I would like to thank God for the strength and wisdom to carry me this far, I could not have made it on my own.

Secondly, I would like to express my appreciation to my supervisor Prof. Lindiwe Khotseng for giving me this opportunity to further my studies and career. This opportunity has given me great and better understanding about life and education. Thank you very much.

To my family, my mother I truly thank you for emotional support and pushing me to achieve my goals in life. To my sister and two brother's thanks for constantly asking how my school work is going and keeping me on track with my goals. To my wonderful and naughty nephew thank you for keeping me smiling and even when I'm stressed, your constantly happy personality is much appreciated.

I would like to thank my friends especially Adam Daniel Reynard and Kelechi Chiemezie Nwambaekwe for his constant checking on me, I have found two new brothers in you guys. Thank you for being reliable, jovial and kind friends and for being my brothers. To Mr Andrew Reynard and Mrs Adele Reynard thank you for your support and wisdom. To Penny Mathumba, Masande Yalo, Victor Manele and Matthew Reynard thanks for the kind friendship.

I would also love to acknowledge and thank my school sisters and brothers Nzaliseko, Zandile, Nelia, Rabelani, Sazi, Kevin for their support, encouragement and grace.

I am very grateful for all the support, understanding, patience, prayers, encouragement, and care when I needed them most. Thank you very much and may the Almighty God continue to bless you abundantly in every aspect of your lives and keep you safe at all times.

ABSTRACT

Palladium can be used as an anodic catalyst for the alkaline direct alcohol fuel cells (ADAFCs). Palladium has displayed high tolerance towards carbon monoxide (CO) poisoning and high catalytic activity for alcohol oxidation reaction in alkaline medium. Palladium-based catalysts have arisen as an alternative to performing alcohol oxidation reaction, especially when combined with other transition metals and multi walled carbon nanotubes (MWCNT) as a support, which induces changes in the palladium electronic structure, and thus, increasing its activity. This research is focused on the development of palladium catalysts incorporated with nickel and tin (transitional metals) on multi walled carbon nanotubes for alkaline direct glycerol fuel cells. To improve the efficiency of the fuel cell, catalyst activity, selectivity ability and good thermal stability need to be increased.

The palladium-based catalysts were synthesized by modified polyol method using functionalized multi walled carbon nanotubes as supports. The ethylene glycol was used for the synthesis which allowed controlling the particle size and to minimize particle agglomeration and also act as a reducing agent for Pd^{2+} to Pd synthesized catalyst were palladium on multi walled carbon nanotubes (Pd/MWCNT), palladium nickel on multi walled carbon nanotubes (PdNi/MWCNT), palladium tin on multi walled carbon nanotubes (PdSn/MWCNT), palladium nickel and cobalt oxide on multi walled carbon nanotubes ($PdNiCo_3O_4$/MWCNT), palladium tin and cobalt oxide on multi walled carbon nanotubes ($PdSnCo_3O_4$/MWCNT), palladium nickel and cerium oxide on multi walled carbon nanotubes ($PdNiCeO_2$/MWCNT), palladium tin and cerium oxide on multi walled carbon nanotubes ($PdSnCeO_2$/MWCNT), palladium cobalt oxide on multi walled carbon nanotubes ($PdCo_3O_4$/MWCNT) and palladium cerium oxide on multi walled carbon

nanotubes ($PdCeO_2$/MWCNT). The functionalization of MWCNT was validated using FTIR and the spectrum obtained reveals the presence of some functional group such as O-H stretching, C=O stretching, C-C stretching, C-O stretching and C-H stretching.

The electrochemical active surface area (ECSA) of the synthesized catalysts was obtained from cyclic voltammetry plot. The calculated ECSA were 0.72 m^2/g for commercial Pd/C, 0.75 m^2/g for Pd/MWCNT, 4.8 m^2/g for PdNi/MWCNT, 0.85 m^2/g for PdSn/MWCNT, 0.74 m^2/g for $PdNiCo_3O_4$/MWCNT, 1.3 m^2/g for $PdSnCo_3O_4$/MWCNT, 5.02 m^2/g for $PdNiCeO_2$/MWCNT, 1.14 m^2/g for $PdSnCeO_2$/MWCNT, for 0.99 m^2/g $PdCeO_2$/MWCNT and 1.89 m^2/g for $PdCo_3O_4$/MWCNT. The ECSA obtained for the alloyed palladium catalysts shows a successful outcome of the introduction of the secondary metal and oxide into the palladium. The morphology of the synthesized catalysts from TEM gave the expected dot-like appearance mostly reported for palladium catalysts, with the structure of the MWCNT support showing a rod-like appearance. The TEM micrographs as well as the SAXS plot of shape revealed that the nanoparticles were polydispersed due to slight agglomeration of catalyst particles. The particle size of the nanoparticles was obtained through SAXS plot of size distribution which confirm that the synthesized particle was of small size radius in nanoscale. The particle size obtained were 20 nm for Pd/C, 15 nm for Pd/MWCNT, 15 nm for PdNi/MWCNT, 15 nm for PdSn/MWCNT, 18 nm for $PdNiCo_3O_4$/MWCNT, 20 nm for $PdSnCo_3O_4$/MWCNT, 20 nm for $PdCo_3O_4$/MWCNT, 15 nm for $PdNiCeO_2$/MWCNT, 19 nm for $PdSnCeO_2$/MWCNT and 16 nm for $PdCeO_2$/MWCNT. The crystallite size of the nanoparticles was obtained using Debye-Scherrer equation from XRD data of the nanoparticles and were 8.4 nm for Pd/C, 11 nm for Pd/MWCNT, 11.4 nm for PdNi/MWCNT, 9.5 nm for PdSn/MWCNT, 9.7 nm for $PdNiCo_3O_4$/MWCNT, 10 nm for $PdSnCo_3O_4$/MWCNT, 12 nm for $PdCo_3O_4$/MWCNT, 8.5 nm for $PdNiCeO_2$/MWCNT, 14 nm for $PdSnCeO_2$/MWCNT and 15 nm for

$PdCeO_2$/MWCNT. The TEM micro graphs were used to obtain the particle size of the synthesized catalysts, the obtained particle sizes were 3.4 nm for Pd/C, 13.7 nm for Pd/MWCNT, 11.5 nm for PdNi/MWCNT, 8.2 nm for PdSn/MWCNT, 11 nm for $PdNiCo_3O_4$/MWCNT, 11.1 nm for $PdSnCo_3O_4$/MWCNT, 16.83 nm for $PdCo_3O_4$/MWCNT, 12.3 nm for $PdNiCeO_2$/MWCNT, 18 nm for $PdSnCeO_2$/MWCNT and 15.33 nm for $PdCeO_2$/MWCNT. The crystallinity of the nanoparticles was examined through XRD and SAED. The plot of the XRD data revealed the presence of the palladium phase (fcc for Pd) in all the synthesized catalysts. The peaks obtained in the XRD were further confirmed by the SAED micrograph.

The electroactivity of the catalysts was evaluated through CV, EIS and CA. The CV results of Pd/C and Pd/MWCNT were compared to the bimetallic catalysts PdNi/MWCNT and PdSn/MWCNT. PdNi/MWCNT showed highest peak current density in glycerol oxidation with 6.657 mA/cm^2 followed by 1.277 mA/cm^2 for PdSn/MWCNT, 0.842 mA/cm^2 for Pd/C and 0.449 mA/cm^2 for Pd/MWCNT respectively. PdSn/MWCNT had the highest ECSA and was expected to have the highest oxidation peak, however, it had poor particles distribution on the surface of the MWCNT which resulted into agglomeration and can be seen on the SAXS plot. The addition of the secondary metal to palladium did improve the glycerol oxidation current density. The catalyst poisoning by the carbonaceous species is traced from the forward scan to backward (I_f/I_r) scan peak current density ratio, with PdNi/MWCNT having the highest ratio at 10.91 meaning low catalyst poisoning followed by 2.13 for Pd/C, 0.92 for PdSn/MWCNT and 0.31 for Pd/MWCNT. This trend is confirmed by EIS with PdNi/MWCNT being the best overall performing catalyst followed by Pd/C, Pd/MWCNT and PdSn/MWCNT. However Pd/MWCNT is performing better than PdSn/MWCNT while PdSn/MWCNT has a higher (I_f/I_r) ratio, this is due to the agglomeration of which affects it kinetically PdSn/MWCNT. Plus Pd/C, Pd/MWCNT and

PdSn/MWCNT display a capacitive feature expected for hydrogen adsorption/desorption and double layer charging/ discharging phenomena. PdNi/MWCNT there is a changeover from capacitive behaviour to resistive behaviour as indicated by a semicircle, which can be assigned to the kinetically controlled reaction. The stability of the catalysts was evaluated through Chronoamperometry. The addition of the secondary metal to palladium did improve the catalyst stability with PdNi/MWCNT having the best catalyst stability, followed by PdSn/MWCNT, Pd/C and Pd/MWCNT respectively. Ni has similar electronic properties to Pd compared to Sn, as it is a group above Pd in the periodic table this contributes to Pd catalyst stability and electroactivity. The electroactivity results of $PdNiCo_3O_4$/MWCNT, $PdSnCo_3O_4$/MWCNT, $PdNiCeO_2$/MWCNT and $PdSnCeO_2$/MWCNT were compared. The peak current density (If) for $PdNiCo_3O_4$/MWCNT is 14.46 mA/cm^{-2} which is highest compare to $PdNiCeO_2$/MWCNT 6.137 mA/cm^{-2}, $PdSnCo_3O_4$/MWCNT is 1.412 mA/cm^{-2} and $PdSnCeO_2$/MWCNT is 1.358 mA/cm^{-2} respectively. The forward scan results show that the addition of a secondary metal Ni in Pd to form catalysts with an oxide can significantly improve the catalytic activity of Pd for glycerol oxidation in alkaline media. The catalyst poisoning against the carbonaceous species is traced from the forward scan to backward (I_f/I_r) scan peak current density ratio. The ratio for $PdNiCeO_2$/MWCNT was 22.59 and showed a higher value compared to 9.81 for $PdSnCeO_2$/MWCNT, 5.23 for $PdNiCo_3O_4$/MWCNT and 2.68 for $PdSnCo_3O_4$/MWCNT respectively. The CeO_2 oxide promotes the adsorption of oxygen species such as OH on bimetallic PdNi and PdSn surface to oxidize CO or adsorbed CO-like carbonaceous species on Pd sites. Plus the fewer amount of oxygen on the oxides helps reduce amount of CO carbonaceous species produced. Therefore $PdNiCeO_2$/MWCNT showed better oxidation of glycerol to carbon dioxide during anodic scan and less accumulation of carbonaceous species on the catalyst surface compared to

$PdSnCeO_2$/MWCNT, $PdNiCo_3O_4$/MWCNT and $PdSnCo_3O_4$/MWCNT. EIS results of $PdNiCeO_2$/MWCNT and $PdSnCeO_2$/MWCNT catalyst display an ionic resistance that may be due to a less homogenous catalyst layer on the ink prepared for electrode coating and the addition of CeO_2 oxide may have contributed to the behavior. $PdSnCo_3O_4$/MWCNT shows better performance with a semi-circle capacitive behavior at -30mv only and mostly displaying a capacitive behavior with $PdNiCo_3O_4$/MWCNT. The stability of $PdNiCeO_2$/MWCNT was better than that of $PdSnCeO_2$/MWCNT. $PdSnCo_3O_4$/MWCNT was most stable compared to $PdNiCo_3O_4$/MWCNT. The overall stability trend from the best stable catalyst to the least stable catalyst is as follows $PdNiCeO_2$/MWCNT, $PdSnCo_3O_4$/MWCNT, $PdSnCeO_2$/MWCNT and $PdNiCo_3O_4$/MWCNT. On the CeO_2 oxide the PdNi alloy has better stability compared to PdSn alloy and on the Co_3O_4 oxide, PdSn alloy has better stability than PdNi alloy.

$PdCeO_2$/MWCNT showed highest (I_f) peak current density in glycerol oxidation of 3.899 mA/cm^2 followed by 0.8295 mA/cm^2 for $PdCo_3O_4$/MWCNT. The catalyst poisoning against the carbonaceous species is traced (I_f/I_r) current density ratio. The ratio for $PdCeO_2$/MWCNT was 4.53 and showed a higher value compared to 2.05 for $PdCo_3O_4$/MWCNT. The CeO_2 oxide promotes the adsorption of oxygen species such as OH on Pd surface to oxidize CO or adsorbed CO-like carbonaceous species on Pd sites. In EIS at -30mv and -10mv $PdCeO_2$/MWCNT shows better performance with a semi-circle capacitive behaviour to compared to $PdCo_3O_4$/MWCNT that displayed an ionic resistance. At 30mv and 10mv $PdCo_3O_4$/MWCNT display better ionic resistance compared to $PdCeO_2$/MWCNT catalyst. The overall best catalysts performance for the binary catalysts is PdNi/MWCNT, for the oxides is $PdCeO_2$/MWCNT and for the ternary catalysts is $PdNiCeO_2$/MWCNT.

TABLE OF CONTENTS

Section ***Page***

LIST OF FIGURES

LIST OF TABLES

LIST OF ABBREVIATIONS

AORs:	Alcohol Oxidation Reactions
CV:	Cyclic Voltammetry
DAFCs:	Direct Alcohol Fuel Cells
DEFC:	Direct Ethanol Fuel Cells
DMFC:	Direct Methanol Fuel Cells
DGFC:	Direct Glycerol Fuel Cells
EG:	Ethylene glycol
EIS:	Electrochemical Impedance Spectroscopy
EDX:	Energy Dispersive Spectroscopy
FTIR:	Fourier Transform Infra-Red Spectroscopy
Gly:	Glycerol
HRTEM:	High Resolution Transmission Electron Microscopy
ICP:	Inductively Coupled Plasma
MWCNTs:	Multi Walled Carbon nanotubes
Pd/MWCNT:	Palladium on multi walled carbon nanotubes
PdNi/MWCNT:	Palladium nickel on multi walled carbon nanotubes
PdSn/MWCNT:	Palladium tin on multi walled carbon nanotubes

$PdNiCo_3O_4$/MWCNT: Palladium nickel and cobalt oxide on multi walled carbon nanotubes

$PdSnCo_3O_4$/MWCNT: Palladium tin and cobalt oxide on multi walled carbon nanotubes

$PdCo_3O_4$/MWCNT: Palladium cobalt oxide on multi walled carbon nanotubes

$PdNiCeO_2$/MWCNT: Palladium nickel and cerium oxide on multi walled carbon nanotubes

$PdSnCeO_2$/MWCNT: Palladium tin and cerium oxide on multi walled carbon nanotubes

$PdCeO_2$/MWCNT: Palladium cerium oxide on multi walled carbon nanotubes

SAXS: Small-Angle X-ray Scattering

XRD: X-ray Diffraction Spectroscopy

CHAPTER 1

INTRODUCTION

1.1 BACKGROUND

Over the past few decades energy demand has drastically increased due to the growth in human population, urbanization and modernization. This rise in energy demand is expected to increase as the number of years go by. Energy is extremely crucial for human life and it drives the continued human development. Energy is the power derived from the utilization of physical or chemical resources, especially to provide light and heat or to work machines. The world is largely dependent on fossil fuels energy such as oil, gas and coal providing 80 % of energy produced, with renewable energy 13.5 % and nuclear energy suppling 6.5 % of the remaining energy [1]. This large amount of energy consumed has major environmental impact with the fossil fuels contributing to about 70-75 % of greenhouse gases that has an effect to global warming [2]. The current energy supplies are unable to cope with the rapidly increasing energy demand and the emission regulations are changing and will create constrains on energy production. An alternative method of energy production has to be considered that will be able to provide for the increase in energy demand while decreasing the environmental impact (pollution).

For some time nuclear energy was found to be the most suitable energy to meet the energy demand. Nuclear energy is based on the use of radioactive materials, such as uranium, plutonium and tritium to produce electricity. It does not fall under renewable energy, however it was accepted due to low cost of energy production, low ozone layer depletion compared to fossil fuel life cycle and good quality of energy produced [3]. However, it has

suffered a major setback due to the Hiroshima incident on 11 March 2011- one the largest earthquakes to ever hit east Japan [4]. Another major concern associated with nuclear energy is nuclear waste, if not handled properly it is highly hazardous to the environment. It is difficult to eliminate, it requires special containment based on the physical and chemical characteristic and reactivity. This has pushed the world away from nuclear energy and it has left one option which is renewable energy.

Renewable energies are solar, geothermal heat, wind, hydrogen, tides, water, fuel cells, and various forms of energies produced from biomass. These energies cannot be exhausted and they are constantly renewed and they produce little to nothing greenhouse gases that contribute to global warming emissions [5]. Hydrogen has attracted a wide spread of research as source of energy that is renewable for fuel cells. Hydrogen has a high power density and produces water as the only emission when used as a fuel [6]. There are various fuels that fall under hydrogen research as alternative fuels for fuel cells, namely alcohols, and dilute light hydrocarbons, like methane.

A fuel cell is an energy device that directly converts chemical energy into electricity by oxidizing the fuel. However, it is not a renewable energy device, it is only renewable if the source of the fuel used is renewable [7]. Direct alcohol fuel cells (DAFC) are devices that uses liquid fuel like methanol, ethanol, glycerol and ethylene glycol as the fuel, with platinum as the main catalyst for many commercial fuel cells and they have several advantages over proton-exchange membrane fuel cells (PEMFCs) and alkaline fuel cells (AFCs) that uses hydrogen as the fuel. Some of the challenges associated with hydrogen are; firstly hydrogen is primary not a fuel, it is obtained from other sources such as reforming of natural gas and coal-to-gas processes just to name a few. Storage and large scale production of hydrogen have proven problematic and this has led up to the search of alternative potential liquid fuels [8]. Alcohol fuel cells have attracted a lot of attention as a

low temperature cell for portable and stationary devices. They have high energy density (5–8 kWh kg^{-1}) that is close to that of gasoline (12 kWh kg^{-1}), and they can be easily obtained from renewable sources such as biomass. The most commercially used fuel cells are hydrogen fuel cells and Direct Methanol Fuel Cells (DMFC).

This study will focus on palladium (Pd) catalysts incorporated with nickel (Ni) and tin (Sn) (transitional metals) on multi walled carbon nanotube (MWCNT) support for direct alcohol fuel cells in alkaline medium, and the alcohol used is glycerol.

With respect to anode kinetics, there are unique characteristics provided by alkaline environments for the efficient operation of alkaline-based fuel cells (alcohol cells): (i) faster kinetics of the alcohol oxidation reactions (AOR) allow the use of low-cost, non-noble-metal electrocatalysts; (ii) facile AORs at low anodic overpotential; (iii) reduced alcohol cross-over; (iv) enhanced water management, since the electro-osmotic drag will remove water formed at the anode through the cathode side, avoiding the possibility of water-flooding; (v) reduced risks of the electrode materials being subjected to corrosion, thus ensuring longevity; and (vi) reduced risk of the spectator ions adsorbing onto the Membrane Electrode Assembly (MEA), which might hamper the electrocatalytic process [9].

Palladium catalyst is the best candidate for use in alkaline environments compared to platinum (Pt). Palladium is three times less expensive and is more than fifty times abundant on the earth than platinum. It has similar properties to platinum since they are in the same group in the periodic table, same face center cubic (fcc) crystal structure, and similar atomic size [10]. Palladium when combined with other transitional metals such as nickel, cobalt or iron has the ability to produce the same or better catalytic activity than platinum at low cost [11].

1.2 RATIONALE, AIM AND OBJECTIVES

1.2.1 RATIONALE

The demand for clean and sustainable energy is on the rise as environmental regulation gets tighter and crude oil reserve is depleting over the century. Fuel cell technology has great potential to power everyday devices, through converting chemical energy into electrical energy. Fuel cell cost is one constrains that is not allowing commercialization in different applications of fuel cell technology. Reactant storage is another technically challenging problem, including durability and reliability of fuel cell system. The use of glycerol as a fuel will allow better fuel storage. The development of Palladium nickel/tin on cobalt oxide/cerium oxide and carbon nanotubes support will allow increase in catalytic activity and reliability of the fuel cell system

1.2.2 AIM

The study is aimed at studying and improving the electro-catalytic behavior of palladium based anodic catalyst on glycerol oxidation reaction for direct glycerol fuel cells. The aim of the study will be achieved by synthesizing the following catalysts and studying them: Pd/MWCNT, PdNi/MWCNT, PdSn/MWCNT, $PdNiCo_3O_4$/MWCNT, $PdSnCo_3O_4$/MWCNT, $PdCo_3O_4$/MWCNT, $PdNiCeO_2$/MWCNT, $PdSnCeO_2$/MWCNT and $PdCeO_2$/MWCNT. All of the catalysts synthesized in this study were supported on MWCNT due to its physicochemical properties including ability to adsorb metal ions on its surface, porosity and high surface area, good electrical conductivity and high chemical stability.

1.2.3 OBJECTIVES

- Synthesize Palladium nickel/tin on cobalt oxide and multi walled carbon nanotubes as support using modified polyol method.
- Determine the electrochemical behavior of all synthesized Palladium catalysts by Cyclic Voltammetry (CV), Electrochemical Impedance Spectroscopy (EIS) and Chronoamperometry to determine the electrochemical catalytic active surface area (ECSA), electron kinetics and stability, respectively.
- Determine the palladium based catalysts structure and crystallite size using X-ray diffraction spectroscopy (XRD)
- Determine particle size distribution using small-angle X-ray scattering (SAXS)
- Obtain the shape of the surface and internal structure of the catalyst using High-resolution transmission electron microscopy (HRTEM).
- Determine metal loading concentrations using Inductively Coupled Plasma (ICP) and validate the elemental composition by Energy Dispersive X-ray Spectroscopy (EDS).

1.3 THESIS ORGANIZATION

This Thesis is constructed as follows

Chapter 1: Provides an overview of current issues with polymer electrolyte membrane fuel cells, together with a summary of the experimental objectives and methodology used in this work

Chapter 2: Consists of a literature review including low and high temperature fuel cells, direct alcohol fuel cells, Alcohol oxidation reaction and Pd based alloys.

Chapter 3: Describes experimental methods and techniques used in this study and details of the experimental procedures used in catalysts synthesis, electrodes preparation and characterization of the catalysts.

Chapter 4: Describes the results of Pd/C, Pd/MWCNT, PdNi/MWCNT and PdSn/MWCNT on physiochemical characterization including X-Ray Diffraction (XRD), Small-Angle X-ray Scattering (SAXS) and Transmission Electron Microscopy (TEM). Followed by electrochemical characterization using a three-electrode cell to determine the activity towards the glycerol oxidation reaction of carbon-supported Pd nanoparticles.

Chapter 5: Describes the results of $PdNiCo_3O_4$/MWCNT, $PdSnCo_3O_4$/MWCNT, $PdNiCeO_2$/MWCNT and $PdSnCeO_2$/MWCNT on physiochemical characterization including X-Ray Diffraction (XRD), Small-Angle X-ray Scattering (SAXS) and Transmission Electron Microscopy (TEM). Followed by electrochemical characterization using a three-electrode cell to determine the activity towards the glycerol oxidation reaction of carbon-supported Pd nanoparticles.

Chapter 6: Describes the results of $PdCo_3O_4$/MWCNT and $PdCeO_2$/MWCNT on physiochemical characterization including X-Ray Diffraction (XRD), Small-Angle X-ray Scattering (SAXS) and Transmission Electron Microscopy (TEM). Followed by

electrochemical characterization using a three-electrode cell to determine the activity towards the glycerol oxidation reaction of carbon-supported Pd nanoparticles.

Chapter 7: Provides conclusions drawn from this study and recommendations for future work.

References

[1]. Asif, M. and Muneer, T. Ã. (2007) 'Energy supply , its demand and security issues for developed and emerging economies', 11, pp. 1388–1413. doi: 10.1016/j.rser.2005.12.004.

[2]. Hoel, M. (1996) 'Depletion of fossil fuels and the impacts of global warming', *Science Direct.* Elsevier Ltd,18(0928), pp. 115–136.

[3]. *Nuclear Energy* ' Nuclear energy' . Available at: https://nuclear-energy.net/ (Accessed: 9 April 2019).

[4]. Matsuura, M. (2014) 'Efforts to Improve Safety of Nuclear Power Plants', Hitachi Review Vol. 63(4), pp. 191–198.

[5]. Herzog, A. V, Lipman, T. E. and Kammen, D. M. (2001) 'Renewable energy sources', *Environment, Vol. 43 No. 10.* pp. 1–63.

[6]. Of, N. T. and Of, A. T. E. S. (2001) 'Renewable Energy; An Overview ': *U.S. Department of Energy (DOE).* Energy Efficiency and Renewable Energy. pp.1-8.

[7]. Energy R. and Energy, A. (1950) 'Renewable energy and other alternative energy sources', *Energy*. Chapter 12. pp. 149–157.

[8]. Gosselink, J. W. (2002) 'Pathways to a more sustainable production of energy: sustainable hydrogen—a research objective for Shell', *International Journal of Hydrogen Energy*. Pergamon, 27(11–12), pp. 1125–1129. doi: 10.1016/S0360-3199(02)00092-7.

[9]. Ozoemena, K. I. (2016) 'Nanostructured platinum-free electrocatalysts in alkaline direct alcohol fuel cells: catalyst design, principles and applications', *RSC Adv.* Royal Society of Chemistry, 6(92), pp. 89523–89550. doi: 10.1039/C6RA15057H.

[10]. Antolini, E. *et al.* (2011) 'Palladium-based electrodes: A way to reduce platinum

content in polymer electrolyte membrane fuel cells', *Electrochimica Acta*. Elsevier Ltd, 56(5), pp. 2299–2305. doi: 10.1016/j.electacta.2010.11.101.

[11]. Shao, M. (2011) 'Palladium-based electrocatalysts for hydrogen oxidation and oxygen reduction reactions', *Journal of Power Sources*. Elsevier, 196(5), pp. 2433–2444. doi: 10.1016/J.JPOWSOUR.2010.10.093.

CHAPTER 2

LITERATURE REVIEW

2.1 BRIEF HISTORY OF FUELS

The first fuel cell concept was drawn in the year 1801 by Humphry Davy and this concept is what has become a fuel cell today. Then almost forty years later in 1839 William Grove created the gas battery the first fuel cell. Charles Langer and Ludwig Mond developed Grove idea in 1889 and named it fuel cell. They pursed scaling up the fuel cell to deliver power from converted fuel [1]. Mond had developed a process to convert coal and coke to gas comprised of large quantities of hydrogen, but impurities from the gas poisoned the platinum black catalyst. This became a cost constrain as the required catalyst loading is high cost. They managed to introduce powdered electro-catalyst platinum black and used a porous matrix to contain the electrolyte, this significantly increased the power density of the cell by improving the notable surface of action.

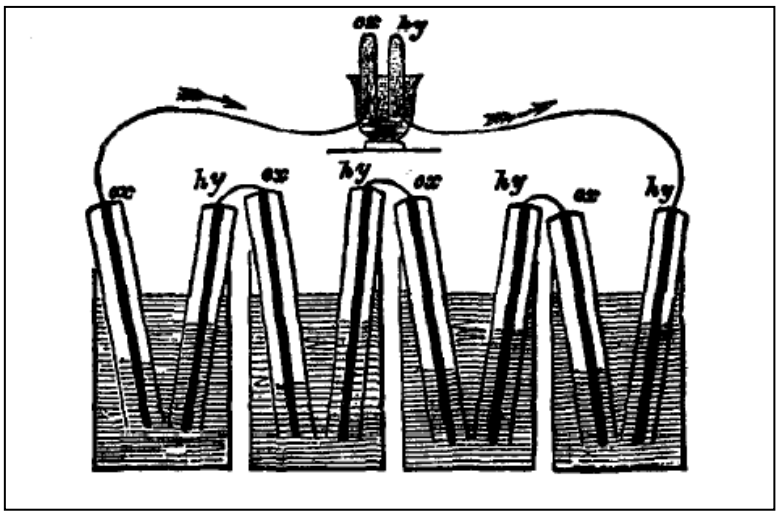

Figure 2. 1 Groves Gas Battery [4]

In 1955 William Grubb contrived the Proton Exchange Membrane Fuel Cell (PEMFC) at General Electric. At the time the PEMFC had a short lifetime in a fuel cell environment, polymer-electrolyte membranes were made from polystyrene-divinylbenzene sulfonic acid combined with an inert fluorocarbon film. The oxidative degradation of the C-H bonds in the membrane, which occurred at the alpha-H sites where the functional groups are bonded resulted in the short lifetime [2, 3]. In the beginning of 1962 General Electric made a power plant created from this technology and successfully implemented it in the U.S. Gemini program. Sir Francis Bacon started advancing the technology of hydrogen-oxygen cell that operated at medium temperatures using alkaline electrolytes and improved catalysts in 1933. He developed a high power density alkaline fuel cell (AFC) that operated at very high pressures and temperature with 1.11 A/cm^2 at 0.6 V at 240°C. Nickel electrodes cells were used with a double permeable structure along with different gas pressures throughout the cell gave a narrow electrolyte film in greater pores. However, the disintegration of porous nickel cathodes caused a quick deterioration of the cell performance. The problem was resolved with the employed of nickel-oxide electrode dope with lithium for improved electronic conductivity that was more reluctant to disintegration [4]. In 1960s this technology was used in fuel cell system developed for U.S Apollo space mission by Pratt and Whitney.

The 1970s are climax of the oil crisis and this saw a decrease in the amount of publication of fuel cells and increase in environmental awareness amongst governments, businesses and individuals. This resulted in the advancement of Phosphoric Acidic Fuel Cell (PAFC) as an alternative source of power supply, with enhanced stability and performance. International Fuel Cells (IFC) developed a 1MW that displayed potential for off- grid power. The fundamental technical and commercial evolution of fuel cells resumed in the

1980s, primarily in PAFC. The future forecast for stationary application was modelled during this period in time. Initially designs were laid up for municipal utility power plant applications of up to 100 MW output. However, small traces of the power plants materialized by that time. Then Substantial stationary PAFC constructed, but hints of them were commercialized during the 1980s. Nearly two decades later masses of PAFC integrated heat and power applications turned out with significant improvements in membrane durability and system performance. The projects that were started in the 1990s still resumed with different tactical focal point. Important improvements in DMFC technology materialized synchronic to adaptation of PEMFC for direct methanol portable devices.

Prior application incorporated soldier-borne power and power for devices such as laptops and mobile phones. The retailing of fuel cells in different types started in 2007, accompanied by written warranties and service capabilities. This resulted in a huge increase in demand, the commercialization expanded leisure applications, such as boats and campervans. The products being sold the most were PEMFC and DMFC as auxiliary power units (APU), while micro fuel cells were sold for portable application in toys and education units. Then in 2009 large a mounts of PEMFC were installed in Japan residential, with the fuel cell functioning as a combined heat and power units (CHP) [5]. This was accompanied by the introduction of the first commercial available fuel cell electric vehicle (FCEV) produced by Honda (FCX Clarity) [6].

Figure 2. 2: Honda FCX Clarity (FCEV) [6]

As such fuel cells are proving to be an interesting and very promising alternative, which can realize the promise of clean reliable electric power generation with high efficiency [5]. They are believed by many to be the ideal energy source for the future generations. Manufacturing reports in 2010 showed a 40 % retail increase for fuel cell, and 95% of fuel cells are portable cells, while 97% of fuel cell technology that is currently being consumed are PEMFC [1]. These figures arises from numerous application of fuels cells ranging supplying home heating to mobile phone chargers and electric cars, with the potential to replace a range of power supplies from batteries to internal combustion engines. Plus fuel cells can employ any fuel as source of hydrogen, this provides the chance to use renewable fuels that contribute to the growth of micro-portable fuels cells, which represents only the 2.6% of the global power supplied [7]. At this stage fuel cell are demonstrating prospective future of providing clean reliable electric power generation with high efficiency [5]. They provide a bright future for green energy and maintaining the essence of being the ideal energy source for the future generations.

2.2 FUEL CELLS

2.2.1 BASIC OPERATION OF FUEL CELLS

Fuel cell is an electrochemical device that converts chemical energy stored in a fuel to electricity. There many types of fuel used such as hydrogen, natural gas, methanol, gasoline, and formic acid. Different from battery, as a fuel cell will keep on producing electricity as long as fuel is available. The structure of a simplified fuel cell is shown below in Figure: 2.3

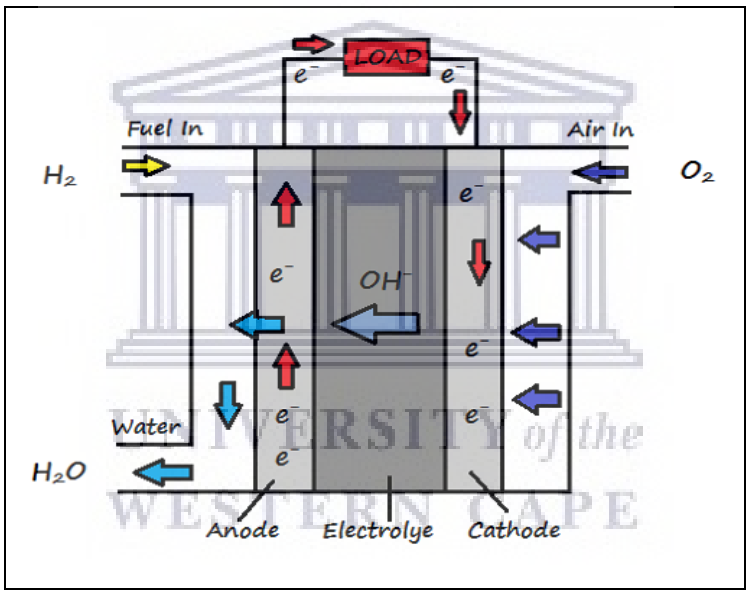

Figure 2. 3: Alkaline Fuel Cell diagram [8]

A fuel cell is comprised of main three components namely anode, cathode and electrolyte. The anode and cathode are enclosed around an electrolyte. An electrolyte is a substance, solid or liquid, capable of conducting moving ions from one electrode to other. The fuel is fed into side anode, where an electro-catalyst is used oxidize the hydrogen fuel into protons and electron meanwhile on the cathode side oxygen is fed in. The protons are transported from one electrode to the other through the electrolyte to combine with their counterparts on the cathode, while electrons travel through the external circuit producing

the electrical current. Then at the cathode reduction process occurs, where protons, electrons and the oxidant recombine to form water. The chemical reactions involved in the anode and cathode and the overall reactions in alkaline are given below as [8, 9]:

Anode: $H_2 + 2OH^- \rightarrow 2H_2O + 2e^-$ (2.1)

Cathode: $½O_2 + H_2O + 2e^- \rightarrow 2OH^-$ (2.2)

Overall reaction: $H_2 + ½O_2 \rightarrow H_2O$ (2.3)

2.2.2 BENEFITS OF FUEL CELLS

Fuel cells present a distinctive integration of advantages well equipped for a multitude of applications and provide an indispensable technology. There are a few advantages that make fuel cells appealing as an energy source. A fuel cell stack has no actively moving parts making them dependable and noiseless compared to modern electric generators which results in high reliability. Fuel cells will always run as long as the fuel is provided to the cell giving of high power quality all the time , however batteries are relinquished when the chemical reaction inside is depleted [10]. Fuel cells that run on refined hydrogen as a fuel source releases no greenhouse gases, while only producing electricity, water and heat. Even other fuels like natural gas and hydrocarbons when they are used emit less pollution compared to standard power plants. This capability of zero emission and near zero emissions is the incentive for the increased attraction in growth of fuel cell technology over the past decades and the continuous development of this technology today. Fuel cells generate energy by electro-chemical reaction and there is no combustion engine involved. This results in more efficiency for the cells compared to combustion engines. A fuel cells model produces about 40-50 % efficiency from converting fuel to electricity using natural gas or hydrocarbons as fuel [10, 11]

2.2.3 DRAWBACKS OF FUEL CELLS

Fuel cells are currently highly priced energy producing systems due to the materials used with certain properties, as such PEMFC and DMFC uses expensive nafion membranes and platinum catalyst due to required material properties. However, the challenge is to maintain the same standards of efficiency while reducing material production cost by creating low cost replacements [12]. Substantial amount of research has been put into altering and improving the nafion membrane, while the evolution of catalyst has been looking into decreasing the amount of catalyst used (catalyst loading) without jeopardizing the efficiency of the catalyst by creating binary and ternary platinum based electro-catalyst. Or the use of non-platinum catalyst by completely replacing the platinum catalyst with another catalyst (palladium) with similar properties and less expensive. Transportation and storage of pure hydrogen in enormous capacity for various applications comes with challenges that hydrogen has a low volumetric energy density. However the use of hydrocarbon as a fuel source resolves the complication that comes up with storage and transportation [10]. Reliability and robustness of fuel cells is a vital concern and disadvantage for the development of the technology. Currently the US Department of energy has fixed operation lifetimes that fuel cells need to meet to be competitive combustion engines, those lifetimes are: 5 000 hours; 20 000 hours for bus application and 40 000 hours of continuous operation for stationary applications [10, 11]. Substantial advancements have been made over the years, however the targets are yet to be accomplished.

2.2.4 TYPES OF FUEL CELLS

There are many types of fuel cells and they are differentiated by the electrolyte employed, which also entails the operation temperatures and the temperatures governs which catalyst is chosen [13]. There are currently five major types of fuel cells and are listed on the table below.

Table 2. 1: Types of fuel cells [14]

	PEMFC	AFC	PAFC	MCFC	SOFC	DAFC
Electrolyte	Polymer Membrane	Immobilized Liquid KOH	Immobilized H_3PO_4	Molten Carbonate	Perovskites (Ceramics)	Liquid KOH
Electrode	Carbon	Carbon	Transition Metals	Nickel Oxide	Perovskite	Carbon
Catalyst	Platinum	Platinum	Platinum	Platinum	None (electrode material)	Platinum
Temperature	40-80 °C	65 -100 °C	100 – 250 °C	600-700 °C	700–1000 °C	40–100 °C
Charge Carrier	H^+	OH^-	H^+	CO_3^{2-}	O^{2-}	OH^-
Fuel	H_2	H_2	H_2	H_2, CH_4	H_2, CH_4	CH_3OH, C_2H_5OH, $C_2H_4(OH)_2$, $C_3H_5(OH)_3$
Fuel cell efficiency	40 - 50%	40 – 65 %	40 – 55 %	50 – 60 %	50 – 60 %	50 – 75 %

2.2.4.1 PROTON EXCHANGE MEMBRANE FUEL CELL (PEMFC)

PEMFC utilizes a polymeric membrane as an electrolyte. Which carries protons created by the hydrogen oxidation reaction at the anode to the cathode, at which they take part in oxygen reduction reaction. Meanwhile producing water and heat as the only by products. One of the advantages of PEMFC is less wear on system components thus enhancing the cell robustness and this arises from the low operating temperature that allows for quick starts up (low warm-up time). This is accompanied by very high power density of the cell and make them ideal and competitive for commercial portable devices such as laptops, computers and mobile phones including transportation. However, the platinum catalyst employed in these cells is very expensive and it's sensitive to CO contamination due to their low operating temperature. [14]

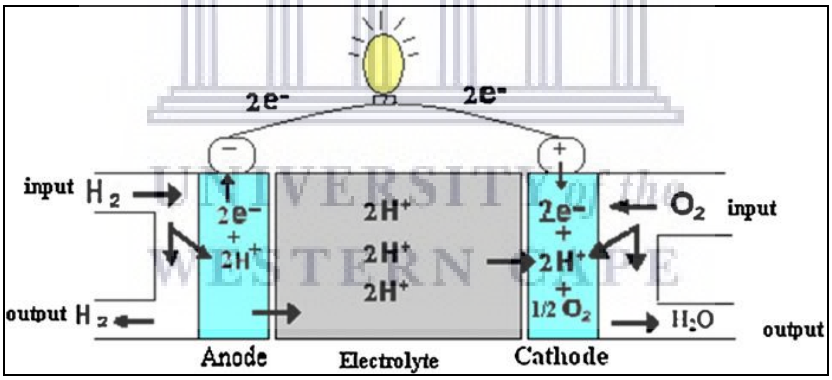

Figure 2. 4: Proton Exchange Membrane Fuel Cell [15]

2.2.4.2 ALKALINE FUEL CELL (AFC)

AFCS are low temperature cells that were the first develop for NASA's space mission. AFC uses an aqueous solution potassium hydroxides as an electrolyte, which carries protons through the solution from the anode to the cathode and produces water as a byproduct. Advantages of the cell include fast start up due to low temperatures and highly simple structures designed that promotes competitive costs for the cell production.

However, a huge disadvantage prevents the AFCs from being the dominant fuel cell technology on the market and that is the CO_2 poisoning of the electrolyte, including the expensive process of purifying oxygen as AFCs required pure oxygen to avoid CO_2 poisoning. [14]

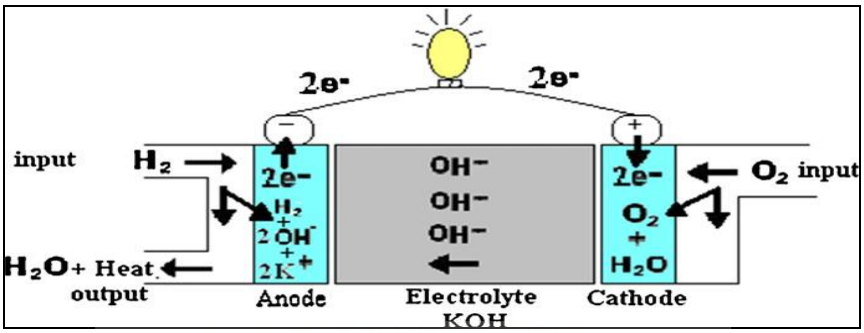

Figure 2. 5: Alkaline Fuel Cell (AFC) [15]

2.2.4.3 PHOSPHORIC ACID FUEL CELL (PAFC)

PAFC uses liquid phosphoric acid as an electrolyte. The cell operates at temperatures between 100 – 250 °C, which is due to the poor conductivity of the electrolyte. However this is also an advantage as PAFC uses hydrogen as a fuel and does not require the use of pure hydrogen due to high operating temperatures and the electrolyte does not react with CO_2 to form carbonate ions. PAFCs can withstand carbon monoxide poisoning if the concentration of the gas is below 1.5 % and the formation of carbonate are not an issue for PAFCs. The only major drawback is the use of expensive platinum catalyst [16].

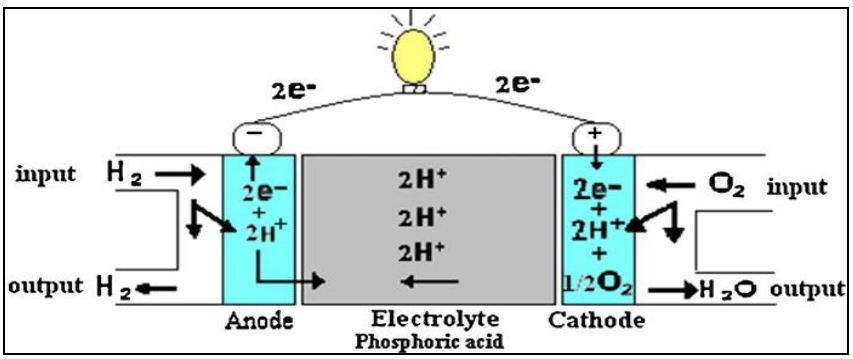

Figure 2. 6: Phosphoric Acid Fuel Cell (PAFC) [15]

2.2.4.4 MOLTEN CARBONATE FUEL CELL (MCFC)

MCFC uses a ceramic matrix electrolyte made up of two mixtures of lithium carbonate and potassium carbonate or lithium carbonate and sodium carbonate. The mixtures are melted and combined inside the cell by the use of high temperatures 650 °C - 700 °C, which also allows the use of cheap nickel catalyst instead of expensive platinum. However, MCFCs are prone to slow start up as the temperature requires time to reach 650 °C for the reaction to occur. The cell has a short life time as degradation of the cells is caused by the electrolyte and the electrolyte can be lost via evaporation due to high temperatures. [17, 18].

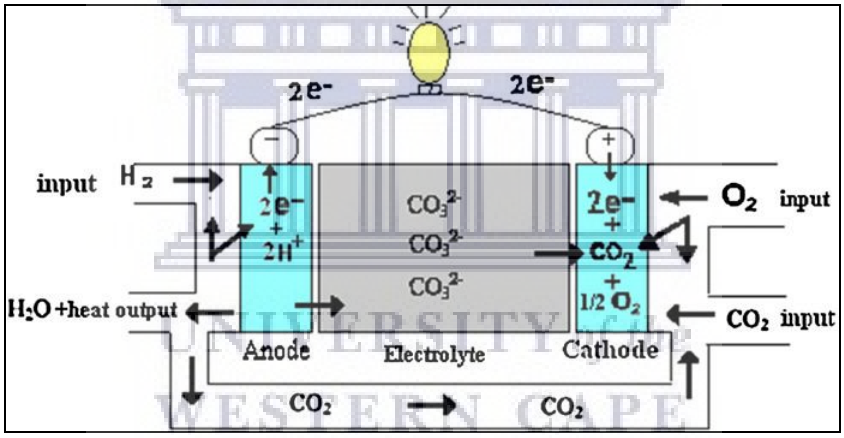

Figure 2. 7: Molten Carbonate Fuel Cell (MCFC) [15]

2.2.4.4 SOLID OXIDE FUEL CELL (SOFC)

SOFC utilize Yttrium doped zirconium oxide (YSZ) electrolytes made as a thin sold ceramic material. The electrolyte has good ionic conductivity, chemical stability and mechanical strength, however conductivity required high temperature in order for the cell to operate properly. The cell operates by feeding air into the cathode and the oxygen molecules are broken down into oxygen ions (O^{2-}) with the insertion of four electrons. The electrons travel through the external circuit to the anode and generate electricity, while the

ions are travel through the electrolyte. Upon reaching the anode where hydrogen is fed in they recombine releasing more electron producing heater water. The advantages of the cell include the use of different multiples low cost hydrocarbons fuels, non-use of expensive noble catalyst and long operating life cycle. Disadvantages are the required long start time in order to reach high temperatures and poor thermal cycling which makes them only applicable for stationary application. [19, 20]

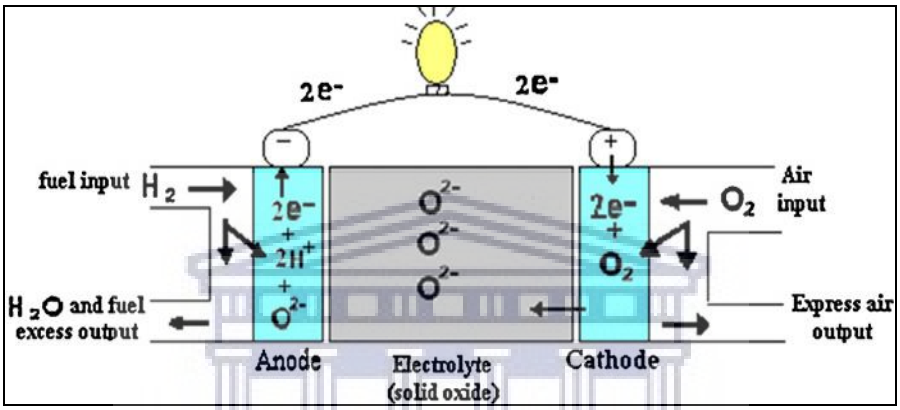

Figure 2. 8: Solid Oxide Fuel Cell (SOFC) [15]

2.2.4.5 DIRECT ALCOHOL FUEL CELLS

A direct alcohol fuel cell uses alcohol as a source of fuel. There are several types of fuels being used which are mainly methanol, ethanol, ethylene glycol and glycerol. Direct Methanol fuel cells (DMFC) have attracted a lot of research due to their advantages such as easy transport, storage and distribution of methanol. However it also has some drawbacks that hinder the widespread commercialization due to the fact that methanol is toxic and has high costs that arise from the use of precious materials such as catalyst (platinum) and membrane electrode assembly parts. Plus they have low power density when compared to PEMFC, poor kinetics on anodic methanol oxidation reaction, poor proton conductivity, and significant methanol cross over through the polymer electrolyte membrane [21, 23].

Direct Ethanol fuels cells (DEFC) use ethanol as a fuel. Ethanol is not as toxic as compared to methanol and has higher energy density of 8.0 $kWh.Kg^{-1}$ compared to 6.1 $kWh.Kg^{-1}$of methanol [24]. There are many difficulties associated with ethanol oxidation demanding high activation energies to be overcome for the scission of a C–C bond that involves 12 electrons to complete the oxidation of ethanol to CO_2. Catalytic efficiency is reduced by production of CO and -CHO during the oxidation reaction that poisons the anode catalyst [25]. Both DMFC and DEFC have challenges that associated with catalyst poisoning in acidic medium, however Pt catalyst poisoning is weak in alkaline environment. Pt is easily poisoned by CO during Alcohol Oxidation Reactions (AORs) in acidic media, which means that it is possible to employ low-cost electro-catalysts compared to platinum [26, 27].

Direct Ethylene Glycol fuels cells (DEGFC) uses ethylene glycol as a fuel with a 5.2 kWh/kg energy density. It is slightly less toxic compared to methanol and ethanol, and popular as an antifreeze in the automobile industry and as an ingredient for polyethylene terephthalate, which has a well-established supply chain, with more than 7 million tons produced annually. It has superior properties to a single hydroxyl group alcohol fuel, as its vapour pressure is much higher, which reduces fuel loss due to evaporation.

The electrochemical oxidation of ethylene glycol on Pt yields a mixture of products: glycolic acid and CO_2 in acidic media, and glycolate, oxalate and carbonate in alkaline media [28]. The catalyst is poisoned by intermediates that have been identified as CO-like species [29]. The performance of PEM-DEGFCs is usually rather low at room temperature because of the sluggish kinetics associated with acid membranes and the mixed potential caused by ethylene glycol crossover [30-31].

2.3 DIRECT GLYCEROL FUEL CELL (DGFC)

Direct Glycerol Fuel Cells has shown great promise to be a source of energy in the nearest future. DGFCs can be employed for portable devices such as laptops, cellphones and small toys. Plus it has distinctive properties that make it attractive over other types of fuel cells and those features include.

- High energy density of glycerol 5.0 $kWh.Kg^{-1}$
- High energy efficiency
- Low operating temperatures (0 -100 °C)
- Simple designed cell structures
- Vast availability of glycerol
- Produces highly valuable by-products

However, DGFC still has challenges that need to be rectified before it can be made commercially available and provide reliable quality to end users. The challenges are the sluggish electro-kinetics of glycerol oxidation reaction (GOR) at the anode and oxygen reduction reaction at the cathode (ORR), they both contribute to low DGFC performance. Additional losses are glycerol crossover and internal currents. Because electrolytes are not ideal, fuel can diffuse through it and pass to the other side without participating in reaction. Furthermore, since electrolytes are not ideal electrical insulators, small amount of electron conduction will happen. [32]

2.3.1 GLYCEROL AS FUEL

Glycerol ($C_3H_8O_3$) is non-toxic, non-volatile, and non-flammable viscous liquid that is colorless and also odorless with a theoretical energy density of 5.0 $kWh.Kg^{-1}$[33]. It is widely used in food additives and pharmaceutical formation. Most of it is synthesized commercially from petrochemical [34]. Even though it is used in food and personal care products, its supply is currently more than the demand. This supply-demand imbalance results in up to 350,000 tons of glycerol to be destroyed by burning in the U.S every year [35]. The life-cycle of biodiesel could be made more environmentally friendly if the extra glycerol were to be used. Also, the economic viability of the supply chain of biodiesel would be enhanced.

Glycerol can be converted into chemicals like aldehydes, acids, or alcohols. Since it can be converted into other useful chemicals, its production has increased which has caused it to become reasonably priced. Glyceraldehyde, which is a substance required for the manufacturing of a multitude of cosmetics, and dihydroxyacetone, which is employed in an artificial tanning agent, are produced when glycerol is oxidized. When it is reduced, it can form compounds like diols, which are required in products like antifreeze, detergent, or in the manufacturing of textile fibers [24, 35].

In 2018, Tseng et al reported the results that clearly indicated that glycerol can be used as a fuel in the simple, membrane-less fuel cell configurations. As the concentration of glycerol increases, there is an increase in power production. However there is a lack of linearity of power production above 2 M glycerol. There is a possibility that as the concentration of glycerol increases, the viscosity of the solution begins to alter the activity of the glycerol at the anode surface. It is also a possibility that the higher concentration of glycerol results in

the production of more carbonate product which would lower the concentration of the available activity of the electrolyte in solution [106].

2.3.2 WORKING PRINCIPLE OF THE DIRECT GLYCEROL FUEL CELL (DGFC)

The use of liquid alcohol over hydrogen provide easy storage and transportation of the fuel .The working principle of a direct glycerol fuel cell is shown below in figure 2.9, with a mixture of glycerol, water and hydroxide. The cell contains catalyst layers on both side were the electro-chemical reaction takes place, surrounding the electrolyte in a chamber. The catalyst layers accelerates the reaction taking place, assists electron and proton transportation. The electrolyte conducts protons from the anode to the cathode while operation as an electric insulator to avoid small amount of electron conductions from taking place. The electrolyte used is potassium hydroxide because its solution is conductive. [36]

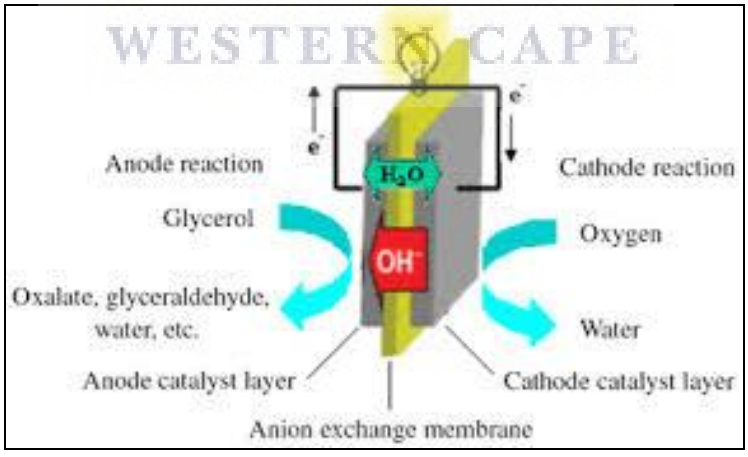

Figure 2. 9: Direct Glycerol Fuel Cell [36]

Glycerol is fed through the anode fuel channel to the anode diffusion layer then transported to the anode catalyst layer. An electro-chemical reaction takes place in the exchange membrane, were glycerol is oxidized by a binary catalyst e.g. (Pd-Ni, Pd-Ag and Pd-Ru) to

create proton, electron and carbon dioxide. The residual unreacted glycerol is transferred to the cathode catalyst layer through the electrolyte as shown in figure 2.9. The transfer of the unreacted glycerol across the electrolyte is called alcohol cross-over in this instance glycerol crossover, this results in fluctuations of potential and decreases the cathode potential. The formed by products (Oxalate, glyceraldehyde, etc) on the anode catalyst layer is then redirected to the flow channel and travels through the anode diffusion layer, to where it is released on the flow channel. The produced protons on the catalyst layer are transported to the cathode catalyst layer through the electrolyte. The electrolyte operates as an electric insulator to electrons and conducts protons, the electrons travel through the external circuit producing the electrical current to the cathode catalyst layer. On the cathode, oxygen is fed through the channel to the diffusion layer and then transferred to the catalyst layer. The oxygen is then reduced in the presence of electron, proton and the Pd catalyst to produce water. Based on the previous study the major electro-oxidation of glycerol by using catalyst in alkaline media can be described as equation (2.3.1 – 2.3.3) follow [37, 38]

Anode Reaction: $C_3H_8O_3 + 14OH^- \longrightarrow 3CO_2 + 11H_2O + 14e^-$ (2.3.1)

Cathode Reaction: $7H_2O + 14e^- + 7/2O_2 \longrightarrow 14OH^-$ (2.3.2)

Overall Reaction: $C_3H_8O_3 + (7/2)\ O_2 \longrightarrow 3CO_2 + 4H_2O$ (2.3.3)

Glycerol is a complex molecule, due to this the oxidation of glycerol in alkaline medium can form numbers of possible oxide/hydrous or oxide/hydroxyl surface molecules. Equation 2.3.3 is an overall reaction of the cell, where glycerol reacts with oxygen to produce electricity and water as by product. Figure 2.10. Below show the major parts of the unit cell of DGFC. The main parts of a direct glycerol fuel cell are: 1) the membrane electrode assembly (MEA) is composed of electrodes (anode and cathode) and an electrolyte in between the electrodes. The membrane assembly center off the cell as the

main reaction occurs within the MEA. 2) The catalyst is fabricated to be an uneven permeable powder this enables for the ultimate surface area exposure of the palladium catalyst to the glycerol or oxygen. The palladium catalyst glazed on the catalyst layer and faces the electrolyte [37].

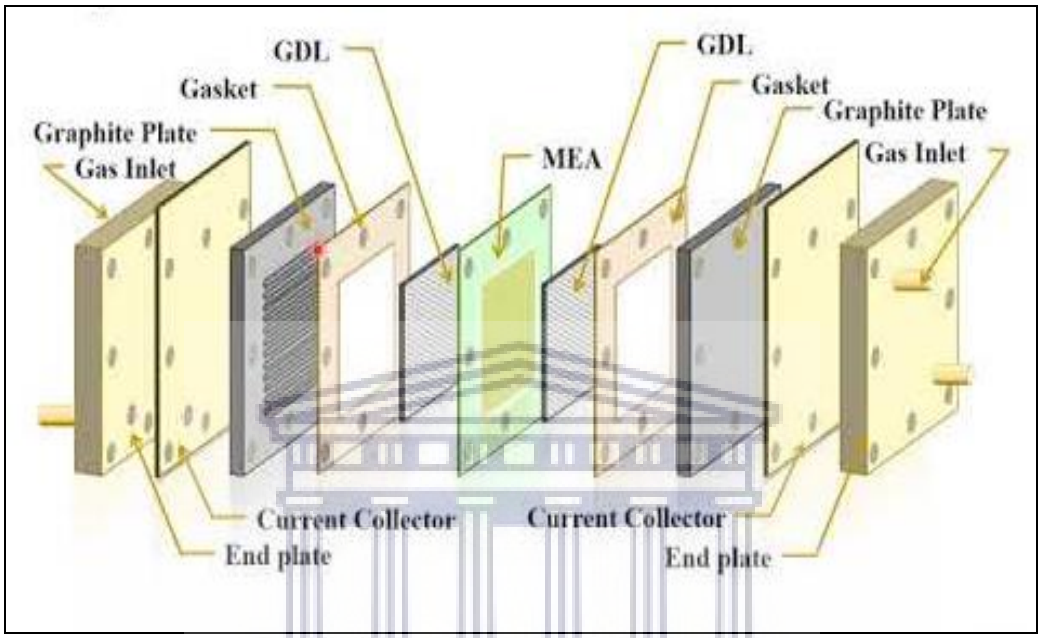

Figure 2. 10: Key Components of DGFC [41]

3) The gas diffusion layer (GDL) assures that reactants are successfully distributed to the catalyst layer and reduce mass transport overpotential. Plus supply an electrical link among the CL and the current collector, furthermore serve as a water control by enabling significant portion of water to extend to the membrane and be contained for hydration. GLDs are fabricated from permeable carbon paper or carbon cloth with 100- 300 μm range in opacity. 4) The overall equipment is manufactured out of backing up layers, flow controllers and current collectors are all mapped out to amplify current out of the MEA [38,39]. The gas inlet and outlet functions as reactants delivery and products extractor. [40]

2.3.3 CHALLENGES FACING THE COMMERCIALIZATION OF DGFC

The challenges that face the commercialization Direct Glycerol Fuel Cell are low stability, robustness, high cost and catalyst, with the catalyst being the focal point of the matter. Advancement have been made into creating low cost catalysts, however the major problem arise with the replication of the activity and stability of the expensive catalyst and no improvements have been reported in that regard. Vital improvements have to be made in enhancing catalyst activity, reliability, robustness and decreasing catalyst cost to introduce fuel cell into the commercial market [42]. The following are vital objections impeding the introduction of DGFC into the market and they have to be resolved before commercializing them.

2.3.3.1 SLOW ELECTRO-OXIDATION REACTION

Glycerol oxidation is a very significant complex reaction network as the oxidation of glycerol produces many by-products. Glycerol oxidation may proceed via various reaction pathways, however the reaction conditions and catalyst determine the reaction pathway [43]. Some parts of the reaction pathways are not easily oxidized as glycerol has high viscosity and the residual is attached to the catalyst sites, this halts additional oxidation of new glycerol molecules. Carbon monoxide is formed as an intermediate and poisons the catalyst generating sluggish electro-kinetics of glycerol electro-oxidation and enhances glycerol crossover from anode to cathode through the electrolyte. The CO poisoning is averted by alloying the palladium catalyst with transitional metals such as Sn, Ni, Mo and Cr, to enhance catalytic activity and oxidation of the chemisorbed CO. [44]

2.3.3.2 GLYCEROL CROSSOVER

Glycerol crossover is associated with KOH electrolyte used as electrolytes are not ideal, fuel can diffuse through it and pass to the other side without participating in reaction. Furthermore, this will result in decreased cell voltage with fluctuating potential on the cathode that are generated from glycerol being absorbed on the Pd sites of the cathode catalyst layer for the reaction taking place between glycerol and oxygen, accompanied by reduced fuel efficiency as the fuel is wasted by glycerol crossover. This pilot's reduced cell performance as the poisoning of the Pd sites by CO an intermediate of glycerol oxidation will result in affected cell stability. Various ways to reduce glycerol crossover have been explored, reducing glycerol concentration on the anode catalyst layer is one of them. Dilute concentrations of glycerol (0.5-2.0 M) are used to diminish glycerol crossover. A balance needs to be accomplished by reducing the fuel concentration as too low concentration of glycerol will result in too low rates of glycerol transfer causing low concentrations on the anode catalyst layer, resulting in a large mass-transport loss and thus lower cell voltage. [45, 46]

2.4 ELECTROCATALYSTS

2.4.1 OVERVIEW OF ELECTROCATALYSTS

An electro-catalyst is a catalyst that partakes in an electrochemical reaction. The catalyst material improves and enhances the rate of chemical reaction without being absorbed or consumed during the reaction, and after the reaction it is theoretically recuperated from the reaction mixture unaltered. An electro-catalyst comes in different forms, it can be heterogeneous like nanoparticles or platinum surface or be homogeneous, like an enzyme and can operates on the electrode surface or be the electrode surface itself. With the main

function of lowering the activation energy of the reaction for the reaction to occur quicker at lower temperature. It also aids with the transportations of electrons from reactants to electrodes or promote the transformation of chemical intermediates described by the overall half- reaction [48].

2.4.2 CATHODE ELECTROCATALYST FOR OXYGEN REDUCTION REACTION (ORR)

Essentially, it is possible to consider similar problems in the cathode in comparison with those observed for the anode, in terms of cost issues and activity/technical limitations. This reaction starts with the adsorption of oxygen on catalyst surface, but different pathways can be followed (see Figure 2.11), as the direct forming process of water, which implies the maximum production of electrons (four electrons). However, production of hydrogen peroxide is also possible, a fact that results in the increase of the corrosive operation conditions of the DMFCs and the decrease in their performance, considering the production of two electrons during the reduction from molecular oxygen to H_2O_2 [48].

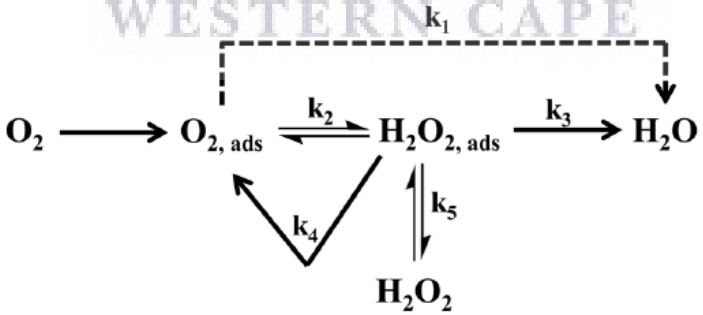

Figure 2. 11: Mechanism and pathways for the oxygen reduction reaction [48].

Other typical drawbacks in the cathodes of direct methanol fuel cells are related with the adsorption of oxygen on the catalytic nanoparticles, the kinetics associated with the cleavage, the crossover of methanol and the reduction of surface metal oxides once the oxygen has been transformed in water [48]. In this sense, significant progress has been

achieved by researchers studying the ORR reaction on palladium-based catalysts [49, 50 and 51]. Regarding the catalyst supported on carbon materials different than carbon blacks, Zheng et al. supported palladium nanoparticles on carbon nanofibers and activated carbons in order to determine the influence of the carbon support on the ORR [52]. They found that this reaction is controlled by surface phenomena if the catalyst is supported on activated carbons, whereas diffusion of electroactive species is the factor controlling this reaction if the catalyst is supported on carbon nanotubes. Furthermore, carbon supports played a crucial role in the onset potentials for the ORR, being the Pd nanoparticles supported on activated carbons which displayed the most negative onset potential (0.50 V vs. RHE in acid media), whereas the catalysts supported on carbon nanofibers displayed values close to 0.70 V for the fishbone carbon nanofibers and 0.72 V for the platelet carbon nanofibers. In other study, Chakraborty and co-workers synthesized spherical and rod-like shapes nanosized Pd particles supported on multiwall carbon nanotubes (MWCNTs) [52] employing an electro-less procedure.

The results of this study indicated that these MWCNT-supported nanoparticles have remarkable catalytic activity towards the oxygen reduction, controlled by the surface morphology and coverage of particles on the carbon nanotubes, with a reaction mechanism that promoted the formation of hydrogen peroxide. The most important facts related with the electro-catalytic activity of these materials were related with the positive onset potentials for the ORR, the high stability of the catalysts as well as the definition of several peaks, which indicated the production of H_2O_2 in the first step of the ORR mechanism. Subsequently, this hydrogen peroxide is reduced to H_2O (second stage of the mechanism). Regarding the Pd alloys, Pd-Ni supported on carbon blacks exhibited high activity, as shown by Li and co-workers, who found high ORR activities, even better than those produced for a Pd/C catalyst [53]. The number of transferred electrons was also calculated,

and it was demonstrated that a high content of surface Ni atoms promote the yielding of H_2O_2. This behavior was modified with a heat treatment at 800°C, which induced the segregation of Pd atoms to the nanoparticles surface, generating a major number of produced electrons and thus, promoting the formation of water and increasing the current densities.

2.4.3 ANODE ELECTROCATALYST

2.4.3.1 ANODE ELECTROCATALYST FOR GLYCEROL OXIDATION REACTION (GOR)

The problem of catalysis is decisive if considering platinum-free anodic catalysts for the partial oxidation of polyols. It has been shown that palladium is an active material for ethylene glycol electro-oxidation [54]. The aim is to study the activity and selectivity of nano-catalysts based on this metal and some of its alloys toward glycerol electro-oxidation. The catalyst composition and structure are indeed very important in electro-catalysis. The oxidation reaction of glycerol is a very complex, involving several elementary steps for all fuel cells: adsorption and alcohol dehydrogenation reaction, electron transfer, reaction with adsorbed OH and product desorption [55]. Each step can limit the anode performance. It is then necessary to develop multifunctional catalysts allowing the most advanced partial oxidation reaction of glycerol at lower over-potentials. The mechanism of electrochemical oxidation of glycerol on Pd in alkaline media is as follows; Glycerol was converted to a plethora of species such as glyceraldehyde, glycerate, tartonate, glycolate, oxalate and CO_3^{-2}[56, 57]. The oxidation processes of glycerol may undergo additional complicated reaction steps. This is because scission of more C–C and C–H bonds is necessary together with more efficient removals of intermediate species produced. Therefore, the oxidations not only depend on the activity of the respective catalyst for C–C and C–H bond breaking,

but also, in particular, on its ability for oxidative removal of poisoning intermediates adsorbed.

On the anode, glycerol oxidation on the Pd catalyst active sites and it's slow gradual response that calls for more than one active sites for the adsorption of glycerol and the active sites that can donate OH species for the desorption/oxidation of the adsorbed glycerol residue. As is well-known, natural platinum at moderate temperatures is effortlessly poisoned by using CO, an intermediate in the oxidation of glycerol to this point, the technique to overcome this hassle has been to alloy Pd with transition metals inclusive of, Ni, Sn, Ru and Ag, where the second one metal is reckon to aid with the advancement of CO to CO_2, and as a result enhance the catalytic pastime and CO tolerance of the alloyed electro-catalyst.

2.4.3.2 BINARY CATALYSTS

Alloying is known to improve the catalytic activity and stability of the based precious metals. The electro-catalytic activity of alloys is strongly dependent on the manner in which the atoms are organized on surface the catalysts [66, 67 and 68]. This arrangement of the atoms is governed by ability of the atoms to migrate from the center of the particle to the surface layer (i.e., 'floor segregation'). The phenomenon of surface segregation has been shown by means of each concept and experiment to be of vital significance in the layout and overall performance of new electro-catalysts. Some of the elements referred to in the literature that determine surface segregation consist of the segregation strength, cohesive strength, surface strength, atomic radii, and electronegativity [69, 70]. For instance, Wang and Johnson mentioned that the tendency for atoms in metallic nanoparticles to decide upon the 'center' or 'shell' role of the alloys may be commonly described by means of impartial elements; (i) cohesive power (associated with vapour

pressure) and (ii) atomic length (quantified by using the Wigner–Seitz (WS) radius), and the interaction among them [70]. Those impartial factors had been determined to determine the tendencies for surface segregation preference for atoms in nanoparticles and semi-infinite surfaces.

Table 2. 2: Typical calculated segregation energies (eV) for binary alloy nanoparticles [58]

	Shell					
Core	Ag	Pd	Ni	Ir	Co	Fe
Ag	0	-0.82	-2.29	-3.54	-2.15	-5.20
Pd	0.70	0	-1.09	-1.71	-1.29	-3.26
Ni	0.67	0.46	0	- 0.67	-0.20	-2.02
Ir	1.51	1.34	0.33	0	-0.04	-1.97
Co	0.36	0.75	0.15	0.04	0	-2.24
Fe	0.60	0.74	-0.10	0.00	0.07	0

Table 2.2: exemplifies the segregation energies (eV) of selected on binary alloy nano-catalysts. observe that a positive energy value, DE(X)Y, method that the core–shell shape favors X within the core and Y in the shell, and the larger the value, the more the tendency. As an evaluation, a negative DE(X) Y describes the opposite (i.e., X on the outer the shell and Y in the core). For example, for a Ni-core and Pd-shell configuration, the positive SE (+0.46 eV) specifies that the existing configuration is preferred, while a negative SE (-1.09 eV) for a Pd-core and Ni-shell configuration indicates that a Pd shell and Ni-core is favored. Yamauchi coined a rule of thumb that an element with a larger

Wigner–Seitz radius (lower average electron density) in a binary alloy segregates to the surface [71].

In other words, metallic elements with smaller atomic radii gravitate to occupy the core to ease compression strain. As a result, if one knows the WS radii or the electron densities of metals, one is then capable of predict, design and make the favored nano-catalysts. As an example, table 2.3 compares the Wigner–Seitz radii and electron densities of a few metal factors which are useful for making alloy catalysts for AFC systems.

Table 2. 3: Representative Wigner–Seitz radii of some relevant metallic elements for making alloy nano-catalysts for application in Pt-free alkaline fuel cell systems [58].

Element	Wigner-Seitz radius, r_{ws}/A
Sn	1.89
Ti	1.62
Ag	1.60
Pd	1.52
Ir	1.50
Mn	1.43
Fe	1.41
Co	1.39
Ni	1.38

Table 2.3 virtually shows that Pd, as an example, has a more potent tendency to surface-segregate in Ni, Fe, or Fe–Co alloys. this is in settlement with the latest finding through Ozoemena and co-people, [68,72,73 and 74] where Fe turned into observed to occupy the ‘shell’ function in a FeCo alloy, and Pd occupied the ‘shell’ position in a high-overall performance sub 10 nm FeCo@Fe@Pd catalyst for alkaline direct alcohol fuel cell

systems. Also, in an AgPd nanoalloy catalyst, [75] Ag is expected to floor-segregate on Pd. It is believed that the improved ORR activity at the AgPd alloy results from a mixture of factors; amendment of the electronic structure and ensemble results. Alloying become proved to regulate the electronic structures of the two metals (via shifts inside the binding power in XPS). The ensemble effect in reality describes the proper arrangement of the Ag next to the Pd floor atoms. In this work, we present the most recent advancements about Pd-based catalysts, considering Pd, Pd alloys with different transition metals and carbon supported nanoparticles in DGFCs**.**

2.5 CATALYST USED IN THIS STUDY

In this work, a review of the progress of Pd-based catalysts for the anodic reaction in DGFCs is presented, considering metal oxide-carbon supported catalysts.

2.5.1 Pd AS CATALYST

Platinum-primarily based substances are general as the correct electro-catalysts for anodes and cathodes in direct alcohol fuel cells (DAFCs). Although, the increased demand and scarce global reserves of Pt, in addition to some technical predicaments associated with its use, have stimulated a wide research concentrated to design Pd-based catalysts, considering the similar properties between Pd and Pt. Particularly, an alternative substitution of platinum and its alloys within the anode require more investigation, being the first-class solution the use of non-platinum catalysts in alkaline electrolytes. Palladium has been advised for replacing the platinum in anodes and cathodes of DAFCs because of the correlation among those metals, in addition to the fundamental abundance and low value of Pd [58].

Mining sources of palladium are greater abundant than the ones for Pt, a fact that makes Pd less expensive ($654.1 per oz.) than Pt ($1796 per oz.) [59]. Pd has an electronic configuration identical to Pt and forms a not very strong bond to most absorbates. The key differences are that the *d* bands of Pd are closer to the cores than that of Pt. There are less *d* electron densities available for bonding. This leads to weaker interactions with *d* bonds, which allows unique chemistry to occur. Pd has higher oxidation potential than Pt and the Pd oxides are more stable. Weak inter-atomic bonds between Pd atoms compared with Pt lead to easier formation of the subsurface species. Also, Pd has a very similar lattice constant to that of Pt. The electro-catalysis of formic acid on a Pd single crystal surface could be significantly enhanced as the *d*-band centre of Pd shifted down with an appropriate value due to the modest lattice compressive strain. All these electronic properties make Pd a promising alternative to Pt or even better than Pt in many situations. From the recent 5-year price change of the Pd, its price has changed from one forth to two fifth of the Pt [60].

However, Pd still has some advantages considering the reservation and price. As one of the most studied materials, Pd has attracted considerable interest for its applications in many fields. Similar to Pt, most of the Pd is used in the automotive industry for catalytic converters to reduce the toxicity of emissions from a combustion engine [61]. Pd also has vast applications in electronic, dental and jewellery. Only a small percentage of Pd is used in chemistry. In electrochemistry, Pd nanoparticles are very important catalyst, especially for the oxidation of formic acid, ethanol oxidation in alkaline solution, hydrogen oxidation and the ORR. Furthermore, within the case of the anode, palladium has displayed excessive tolerance toward CO poisoning and excessive catalytic activity for alcohols oxidation in alkaline medium [60, 62, 63 and 64]. Regarding the cathode, Pd-primarily based catalysts have also arisen as an alternative to perform the oxygen reduction response

(ORR), mainly if this metal is blended with different transition metals, which instigates modifications in the Pd electronic structure, and consequently, increasing its activity [65].

2.5.2 PdNi ELECTROCATALYSTS

Pd-Ni is one of many extensively suggested alloy for the use in methanol oxidation. Evidently nickel produces a similar effect to that of ruthenium in phrases of the ability to form OHads at lower potentials than Pd. Moreover, Ni can induce modifications inside the electronic structure of Pd, which is similar to the silver effect [76]. These facts are pondered within the increased currents related to the hydrogen adsorption/desorption process and the resistance towards the carbonaceous intermediates poisoning throughout the methanol oxidation [77]. In an effort to elucidate the origin of the enhanced activity in Pd-Ni catalysts supported on carbon blacks, Amin et al. decided the Ni surface coverage in these alloys, seeking to correlate the presence of Ni oxides and hydroxides with the methanol oxidation current densities [78, 79].

The authors discovered improved current densities at massive Ni coverages, because of the Ni oxophilic ability to generate adsorbed Ni hydroxides at low potentials. Another conclusion from these works changed into the capability of the NiOH and NiOOH for oxidizing the COads generated at some point of the methanol oxidation, which occupies active Pd sites. Besides the incorporation of oxygenated species by using Ni, it has additionally been cautioned the appearance of some defects on palladium crystalline lattice, with a major activity towards methanol oxidation [80]. Atomic ratio between Pd and Ni additionally played a key role within the activity of these carbon black-supported catalysts, as proven via Calderon et al. in a latest work [81]. They synthesized Pd-Ni catalysts supported on chemically treated with carbon blacks, which contained surface oxygen and nitrogen groups.

The metallic contents of these catalysts become close to 25 wt %, while the studied Pd:Ni atomic ratios had been near 1:1 and 1:2. Despite the fact that no evident consequences associated with the presence of O- and N-floor functional groups have been found, those catalysts exhibited a better CO poisoning tolerance than that discovered for a Pd/C catalyst, which was explained from the extended amount of OHads formed on floor Ni atoms, even as the methanol oxidation produced better current densities inside the catalysts with Pd:Ni = 1:2, in contrast with current densities generated with the catalysts with the atomic ratio near 1:1 and the catalysts with none content of Ni (catalyst Pd/C), being this fact of evidence of the useful effect of Ni in this reaction. regarding different novel carbon substances as support for Pd-Ni catalysts, Singh et al. [82] synthesized PdNi alloys supported on multi-walled carbon nanotubes (MWCNTs), finding notable activities towards the methanol oxidation, which had been explained from the increased electroactive area of these composites, promoted by using the use of MWCNTs and the electronic properties of the alloys, as defined above.

2.5.3 PdSn ELECTROCATALYST

Sn electro-catalysts have so far been less employed for the AOR in comparison with other metals such as Fe, Co, Cu, and Ni etc. It is observed that the addition of Sn to Pd promotes growth in the lattice parameter of the Pd (fcc) crystal. The PdSn/C catalysts have higher electro-catalytic activity for formic acid oxidation than a comparative Pd/C catalyst [83]. The addition of Sn as a small ratio into the carbon-supported Pd catalyst has largely increase the current density of the formic acid oxidation and shift the onset potential towards the negative in comparison with that of Pd/C [85]. The alloy catalysts exhibited extensively higher catalytic activity and stability for formic acid oxidation than that of Pd/C catalyst was altered by Sn via an electronic effect which can lower the adsorption

strength of the poisonous intermediates on Pd and thus promote the formic acid oxidation. The Pd_2Sn_1/C catalyst exhibited higher current density and better electro-catalytic stability in comparison with Pd/C, there was additionally a negative shift of the peak potential on Pd_2Sn_1/C than that of Pd/C. Zhang et al. [84] synthesized PdSn/C catalysts with distinct atomic ratios of Pd to Sn. The cause for the development of the catalyst changed into probable attributed to the excessive dispersion of the Pd and due to the exchange within the electronic properties of the Pd.

2.6 CATALYST SUPPORT FOR FUEL CELLS

A fuel cell is predicted to perform for heaps of hours or cycles throughout its existence time. Catalyst-support materials remain to be one of the most vital element of the fuel cell on the way to allow for such long operation. Certainly, it's far common place understanding that efficient interplay between the electro-catalyst and its supporting material is accountable for some of the essential parameters that manage the efficient performance of fuel cells: particle size, catalyst dispersion, and stability [87]. An ultimate support for the electro-catalyst should possess the following critical properties:[88,89] (i) first-class electric conductivity, (ii) sturdy catalyst support interplay to lessen the possible deactivation of the catalysts and permit for efficient charge transfer, (iii) large surface area, (iv) a suitable porous structure to allow precise reactant and product flux, (v) precise water-handling with capability to keep away from flooding, (vi) good resistance to corrosion to allow for excessive stability in fuel-cell running environments, and (vii) ease of catalyst recuperation.

2.6.1 CARBON SUPPORT MATERIALS

The function of carbon material as support for catalysts in all the groups of polymer electrolyte membrane fuel cells is well known, and is cognitive with different factors: (1) enhancement of high electroactive area, as a result of a higher dispersion of nanoparticles [90]; (2) enhance electroactive species diffusion via the porous structure of carbon support [91]; and (3) promotion of the electronic transfer, both for the presence of surface functional groups or the decrease in Fermi level of the catalysts [92]. Catalyst-supports for fuel cells can be easily divided into two classes: (i) carbon-based support and (ii) non-carbon support. Carbon materials are the most critical catalyst-support substances for fuel cell electro-catalysts, with the aid of adopting exclusive sorts of synthesis methods, different morphologies of carbons had been obtained, along with core–shells, spheres, hole spheres, nanotubes, and onion-like.

The significance of carbon as a catalyst support material stems from its specific advantages, which include vast availability, low-value, high stability in acidic and base media, and capability to be burnt off without difficulty, as a consequence making an allowance for easy recuperation of the valuable metal catalysts if needed. Regardless of those important advantages, carbons are plagued by the subsequent shortcomings, which have restricted their overall performance as catalyst-supports: (i) severe corrosion/oxidation beneath regular running conditions, resulting in poor stability of the electro-catalysts as they are electrically isolated or separated from the support, following aggregation of small particles of those catalyst particles (Ostwald ripening), which could cause the formation of an inhomogeneous structure over the years [93,94,95]. Indeed, the main cause for the loss of electrochemically-active surface area (ECSA) of the electrode and the resultant lack of electro-catalytic activity is associated to (i) the ability of the

small-sized particles to agglomerate into large-sized particles thru diffusion, followed by coalescence or the Ostwald ripening mechanism; (ii) the presence of a massive quantity of micropores (<1 nm), that may obstruct fuel supply to the surface, and present a low availability of surface area for the deposition of metal particles; (iii) low polarity and high hydrophobicity, which decreases the permeability of gases and liquids; and (iv) poor stability at temperatures higher than 373 k and shortage of proton conductivity [96,97].

2.6.1.1 CARBON NANOTUBES

Carbon nanotubes (CNTs) are cylindrical molecules that consist of rolled-up sheets of single-layer carbon atoms (graphene). They can be single-walled (SWCNT) with a diameter of much less than 1 nano-meter (nm) or multi-walled (MWCNT), including numerous concentrically interlinked nanotubes, with diameters attaining more than 100 nm. Carbon nanotubes are members of the fullerene family. Despite the fact that the primary fullerene molecules were found in 1985, it was not until Sumio Iijima stated his findings. Their length can attain several micro meters or even milli-meters.

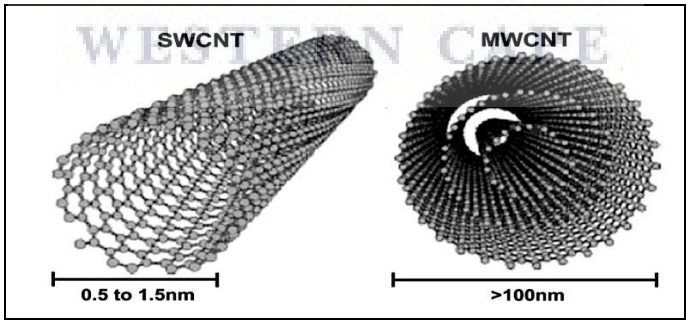

Figure 2. 12: Single Walled Carbon Nanotubes and Multi Walled Carbon Nanotubes [100]

Like their building block graphene, CNTs are chemically bonded with sp^2 bonds, an extremely robust form of molecular interaction. This selection mixed with carbon nanotubes natural inclination to rope together via van der Waals forces, offer the possibility to develop extremely-high energy, low-weight materials that possess highly

conductive electrical and thermal properties. The rolling-up route (rolling-up or chiral vector) of the graphene layers determines the electric properties of the nanotubes. Chirality describes the angle of the nanotube's hexagonal carbon-atom lattice. Even as MWCNTs are always accomplished and attain at least the identical degree of conductivity as metals, SWCNTs' conductivity relies upon on their chiral vector: they could behave like a metallic and be electrically conducting; show the properties of a semi-conductor; or be non-conducting. A slight change in the pitch of the helicity can remodel the tube from a metal into a huge-gap semiconductor [98]. MWCNTs are commonly synthesized by diverse techniques such as arc discharge, laser ablation, plasma enhanced chemical vapour deposition (PECVD), and catalytic chemical vapour deposition (CCVD). The synthesis of CNTs via CCVD has been extensively used, because it gives a promising path for bulk manufacturing of CNTs that could feasible result in commercialization [99].

MWCNTs are chemically inert as a consequence makes it difficult to connect metal nanoparticles on them. As a result of their inertness, surface change of MWCNTs earlier than steel deposition became discovered to be essential for reaching most effective interplay between the support and the catalyst precursor. Surface amendment introduces surface oxygen groups (using strong acid inclusive of HNO_3, H_2SO_4, etc.) to be able to make the surface highly hydrophilic and as a result improve the catalytic support interaction. The most normally used pre-treatment is that of refluxing CNTs in a nitric acid solution (chemical treatment) to create acid sites on the surface, that can act as nucleation centre for metal ions, making it viable to acquire better dispersion of metal nanoparticles, better length manage and distribution. MWCNTs had been used to support a wide type of mono, binary (e.g. PtRu and PtFe) in addition to ternary catalyst (e.g. PtRuPd, PtRuOs, and PtRuNi) systems the use of both noble and non-noble metals [101, 102]. The advantages of MWCNTs encompass, fewer impurities whilst in comparison to CBs, are more resistant to

corrosion than CBs while on the equal time they may be free from the deep cracks that exist in CBs in which the Pt nanoparticles deposited will lose catalytic activity due to the fact the electro-chemical triple phase boundary (TPB) does no longer form [103]. It's far due to these benefits already said above, that MWCNTs were chosen as support material for this study. They had been used in this take a look at to improve catalyst activity and stability of the binary electro-catalysts.

2.6.1.2 INORGANIC OXIDES AS SUPPORTS

This study investigated Pd binary catalyst and oxides (CeO_2 and Co_3O_4)-promoted on carbon nanotubes support for electro-oxidation reactions of glycerol.

The exact role of oxides in the promotion of activity and stability of Pd/C electro-catalysts, and the mechanism of alcohol oxidation reaction on Pd-based electro-catalysts are still unclear. Nevertheless, since Pd/C catalysts alone have only limited activity and stability toward alcohols investigated in the present study, it must be the interaction between the palladium and the oxides that provides the significantly enhanced activity and stability. Nevertheless, the stability of the Pd/C and Pt/C electro-catalysts for the alcohol oxidation reaction is very poor. Pd/C promoted with the oxides (CeO_2 and Co_3O_4) gives a much higher activity and significantly enhanced performance stability for the electro-oxidation reactions of methanol, ethanol, EG and glycerol than that on un-promoted Pd/C in alkaline media. This appears to explain the significant enhancing effect of the oxides in the Pd/C electro-catalysts for the electro-oxidation reaction of alcohols [104]. However, at low oxide content, there are not enough oxide sites to effectively assist the releasing of adsorbed CO-like poisoning specie and the promotion effect is not most effective. With the increasing of the oxide content, the sites for the formation of oxygen-containing species, OHad, increase, leading to the quick recovery of the active sites on the Pd and thus high

oxidation current density for the reaction. Decreasing in the oxidation current with further increasing in the oxide content can be rationalized in terms of an inhibition of alcohol adsorption probably due to the diminution of Pd sites. The decease of the electro-catalytic activity with further increase in the oxide content may also be due to the reduction in the electro-catalyst conductivity since CeO_2 and Co_3O_4 are semiconductors [105].

References

[1]. L, C., R, L. and Sec, R. S. (1889) 'new Form of Gas Battery." By', 8, pp. 296–304.

[2]. Cell, F. (1959) '/au/enfor Wan 7. Grubé, u/',.

[3]. Perry, M. L. and Fuller, T. F. (2002) 'A Historical Perspective of Fuel Cell Technology in the 20th Century', *Journal of The Electrochemical Society*, 149(7), p. S59. doi: 10.1149/1.1488651.

[4]. Bacon, F. T. (1969) 'FUEL CELLS , PRESENT AND FUTURE *', 14(April 1968).

[5]. *Fuel Cell History - Fuel Cell Today* (2017) *Johnson Matthey Plc*. Available at: http://www.fuelcelltoday.com/history (Accessed: 4 April 2019).

[7]. Lucia, U. (2014) 'Overview on fuel cells', *Renewable and Sustainable Energy Reviews*. Elsevier, 30, pp. 164–169. doi: 10.1016/j.rser.2013.09.025.

[9]. *Fuel cells, what is a fuel cell, disadvantages, benefits* (no date). Available at: http://www.altenergy.org/renewables/fuel_cells.html (Accessed: 4 April 2019).

[8]. Paul Breeze. (2017). Chapter 3 - The Alkaline Fuel Cell. *Academic Press.* p23-32.

[10]. Farooque, M. and Maru, H. C. (2001) 'Fuel cells-the clean and efficient power generators', *Proceedings of the IEEE*, 89(12), pp. 1819–1829. doi: 10.1109/5.975917.

[11]. *A Basic Overview of Fuel Cell Technology* (no date). Available at: https://americanhistory.si.edu/fuelcells/basics.htm (Accessed: 4 April 2019).

[12]. Kirubakaran, A., Jain, S. and Nema, R. K. (2009) 'A review on fuel cell technologies and power electronic interface', *Renewable and Sustainable Energy Reviews*, pp. 2430–2440. doi: 10.1016/j.rser.2009.04.004.

[13]. Vielstich, W. *et al.* (2003) *Handbook of fuel cells : fundamentals, technology, and applications*. Wiley. Available at: https://books.google.co.za/books?hl=en&lr=&id=qG7VeAB94u4C&oi=fnd&pg=PR9&dq=U.S.+Department+of+Energy.+Fuel+cell+hand+book,+7th+ed.,+West+Virginia:+Office+of+Fossil+fuel,+National+Energy+Technology+Laboratory%3B+October+2000.+&ots=U-ruFio_pq&sig=NI6jtqqUiGSisUoeyNL2AWztVew#v=onepage&q&f=false (Accessed: 4 April 2019)

[14]. Giorgi, L. (2013) 'Fuel Cells: Technologies and Applications', *The Open Fuel Cells Journal*, 6(1), pp. 0–0. doi: 10.2174/1875932720130719001.

[15]. Andújar, J. M. and Segura, F. (2009) 'Fuel cells: History and updating. A walk along two centuries', *Renewable and Sustainable Energy Reviews*. Pergamon, 13(9), pp. 2309–2322. doi: 10.1016/J.RSER.2009.03.015.

[16]. Laughton, M. A. (2002) 'Fuel cells', *Engineering Science & Education Journal*, 11(1), pp. 7–16. doi: 10.1049/esej:20020102.

[17]. Larminie, J. and Dicks, A. (no date) *Fuel Cell Systems Explained Second Edition*. Available at: www.wiley.co.uk/fuelcellsystems. (Accessed: 4 April 2019).

[18]. Fermeglia, M. *et al.* (2005) 'Process Simulation for Molten Carbonate Fuel Cells', *Fuel Cells*. John Wiley & Sons, Ltd, 5(1), pp. 66–79. doi: 10.1002/fuce.200400049.

[19]. Kawamoto, H. (2008) 'Research and Development Trends in Solid Oxide Fuel Cell Materials', *Science & Technology Trends*, pp. 52–70.

[20]. Stambouli, A. B. and Traversa, E. (2002) 'Solid oxide fuel cells (SOFCs): A review of an environmentally clean and efficient source of energy', *Renewable and Sustainable Energy Reviews*, 6(5), pp. 433–455. doi: 10.1016/S1364-0321(02)00014-X.

[21]. Tripković, A. . *et al.* (2002) 'Methanol electrooxidation on supported Pt and PtRu catalysts in acid and alkaline solutions', *Electrochimica Acta*. Pergamon, 47(22–23), pp. 3707–3714. doi: 10.1016/S0013-4686(02)00340-7.

[22]. Prabhuram, J. and Manoharan, R. (1998) 'Investigation of methanol oxidation on unsupported platinum electrodes in strong alkali and strong acid', *Journal of Power Sources*. Elsevier, 74(1), pp. 54–61. doi: 10.1016/S0378-7753(98)00012-3

[23]. Zhang, J. and Liu, H. (2009) *Electrocatalysis of direct methanol fuel cells : from fundamentals to applications*. Wiley-VCH. Available at: https://books.google.co.za/books?hl=en&lr=&id=xHsJJieZlHwC&oi=fnd&pg=PA1&dq=A.+Aric%60o,+V.+Baglio+and+V.+Antonucci,+Electrocatal.+Direct+Methanol+Fuel+Cells+From+Fundam.+to+Appl.,+2009,+pp.+1–78.&ots=iEZyEIcvl5&sig=1nftIRPgAaVKF24QX02-WAR7XZw#v=onepage&q=A.Aric%60o%2C V. Baglio and V. Antonucci%2C Electrocatal. Direct Methanol Fuel Cells From Fundam. to Appl.%2C 2009%2C pp. 1–78.&f=false (Accessed: 4 April 2019).

[24]. Padayachee, D. (2013) 'Development of electrocatalysts for glycerol oxidation'. University of Canterbury. Chemical and Process Engineering. Available at: https://ir.canterbury.ac.nz/handle/10092/8985 (Accessed: 4 April 2019)

[25]. Meng, H., Zeng, D. and Xie, F. (2015) 'Recent Development of Pd-Based Electrocatalysts for Proton Exchange Membrane Fuel Cells', *Catalysts*, 5(3), pp. 1221–1274. doi: 10.3390/catal5031221.

[26]. White, R. E., Bockris, J. O. and Conway, B. E. (eds) (1995) *Modern Aspects of Electrochemistry*. Boston, MA: Springer US (Modern Aspects of Electrochemistry). doi: 10.1007/978-1-4899-1724-9.

[27]. Lamy, C., Coutanceau, C. and Leger, J.-M. (no date) 'The Direct Ethanol Fuel Cell: a Challenge to Convert Bioethanol Cleanly into Electric Energy', in *Catalysis for Sustainable Energy Production*. Weinheim, Germany: Wiley-VCH Verlag GmbH & Co. KGaA, pp. 1–46. doi: 10.1002/9783527625413.ch1.

[28]. Christensen, P. A. and Hamnett, A. (1989) 'The oxidation of ethylene glycol at a platinum electrode in acid and base: An in situ FTIR study', *Journal of Electroanalytical Chemistry and Interfacial Electrochemistry*. Elsevier, 260(2), pp. 347–359. doi: 10.1016/0022-0728(89)87149-9.

[29]. Orts, J. M. *et al.* (1990) 'Electrochemical oxidation of ethylene glycol on Pt single crystal electrodes with basal orientations in acidic medium', *Journal of Electroanalytical Chemistry and Interfacial Electrochemistry*. Elsevier, 290(1–2), pp. 119–133. doi: 10.1016/0022-0728(90)87424-I.

[30]. Yang, C.-C. (2004) 'Preparation and characterization of electrochemical properties of air cathode electrode', *International Journal of Hydrogen Energy*. Pergamon, 29(2), pp. 135–143. doi: 10.1016/S0360-3199(03)00090-9.

[31]. Agel, E., Bouet, J. and Fauvarque, J. . (2001) 'Characterization and use of anionic membranes for alkaline fuel cells', *Journal of Power Sources*. Elsevier, 101(2), pp. 267–274. doi: 10.1016/S0378-7753(01)00759-5.

[32]. Martins, A. *et al.* (2018) 'Electrochimica Acta Towards a fuel- fl exible direct alcohol micro fl uidic fuel cell with fl ow-through porous electrodes : Assessment of methanol , ethylene glycol and glycerol fuels', 271, pp. 537–543. doi: 10.1016/j.electacta.2018.03.197.

[33]. Simões, M., Baranton, S. and Coutanceau, C. (2010) 'Electro-oxidation of glycerol at

Pd based nano-catalysts for an application in alkaline fuel cells for chemicals and energy cogeneration', *Applied Catalysis B: Environmental*, 93(3–4), pp. 354–362. doi: 10.1016/j.apcatb.2009.10.008.

[34]. F. Shahidi. (2005) 'Bailey's industrial oil and fat products', John Wiley & Sons 3, pp 555-565.

[35]. Zheng, Y., Chen, X. and Shen, Y. (2010) 'Commodity Chemicals Derived from Glycerol, an Important Biorefinery Feedstock', *Chemical Reviews*, 110(3), pp. 1807–1807. doi: 10.1021/cr100058u.

[36]. Geraldes AN, Silva DF, Silva JCM, Souza RFB, Spinacé EV, Neto AO, et al. (2014). *Glycerol Electrooxidation in Alkaline Medium Using Pd/C, Au/C and PdAu/C Electrocatalysts Prepared by Electron Beam Irradiation.* Available from: https://www.jbcs.sbq.org.br/default.asp?ed=202. [Accessed: 8/4/2019].

[37]. Su, L. *et al.* (2009) 'Palladium/titanium dioxide nanofibers for glycerol electrooxidation in alkaline medium', *Electrochemistry Communications*. Elsevier, 11(11), pp. 2199–2202. doi: 10.1016/J.ELECOM.2009.09.030.

[38]. Ong, B. C., Kamarudin, S. K. and Basri, S. (2017) 'Direct liquid fuel cells: A review', *International Journal of Hydrogen Energy*. Elsevier Ltd, 42(15), pp. 10142–10157. doi: 10.1016/j.ijhydene.2017.01.117.

[39]. Gasteiger, H. A. *et al.* (2005) 'Activity benchmarks and requirements for Pt, Pt-alloy, and non-Pt oxygen reduction catalysts for PEMFCs', *Applied Catalysis B: Environmental*, 56(1–2), pp. 9–35. doi: 10.1016/j.apcatb.2004.06.021.

[40]. Fal Desai, M. S., Kerkar, R. D. and Salker, A. V. (2019) 'Detoxification of NO and CO gases over effectively substituted Pd and Rh in cupric oxide catalysts', *International*

Journal of Environmental Science and Technology, 16(3), pp. 1541–1550. doi: 10.1007/s13762-018-1744-5.

[41]. Hsueh, K.-L. (2018) *fuel cell components - Google Search*. Available at: https://www.google.com/search?q=fuel+cell+components&tbm=isch&tbs=rimg:CRfEpDC3Gl9VIjhUERUc-Sczs1LG8mH3e_1kbgLukPyNHR7zAKWFe9YbDN58_1EuLocMkvRKDzXjqDjfzkbC2W-nLuGioSCVQRFRz5JzOzEVgPlSg_1SsGnKhIJUsbyYfd7-RsRxNw_10fuAQjYqEgmAu6Q_1I0dHvBH-EmdTmmtI1yoSCcApYV7 (Accessed: 8 April 2019).

[42]. Liu, H. *et al.* (2006) 'A review of anode catalysis in the direct methanol fuel cell', *Journal of Power Sources*. Elsevier, 155(2), pp. 95–110. doi: 10.1016/J.JPOWSOUR.2006.01.030.

[43]. Yu, X. and Manthiram, A. (2018) 'Scalable Membraneless Direct Liquid Fuel Cells Based on a Catalyst-Selective Strategy', *Energy & Environmental Materials*, 1(1), pp. 13–19. doi: 10.1002/eem2.12000.

[44]. Okada, K. (2013) 'Electrochemical Oxidation of Glycerol in a Proton-Exchange-Membrane Reactor', *Thesis*.

[45]. Benipal, N. *et al.* (2017) 'Direct glycerol fuel cell with polytetrafluoroethylene (PTFE) thin film separator', *Renewable Energy*, 105, pp. 647–655. doi: 10.1016/j.renene.2016.12.028.

[46]. Silva, J. C. M. *et al.* (2014) 'Glycerol Electrooxidation in Alkaline Medium Using Pd/C, Au/C and PdAu/C Electrocatalysts Prepared by Electron Beam Irradiation', *Journal of the Brazilian Chemical Society*. doi: 10.5935/0103-5053.20140044.

[47]. Nascimento, A. P. and Linares, J. J. (2014) 'Performance of a direct glycerol fuel cell using KOH doped polybenzimidazole as electrolyte', *Journal of the Brazilian Chemical Society*, 25(3), pp. 509–516. doi: 10.5935/0103-5053.20140018.

[48]. Toda, T. *et al.* (1999) 'Enhancement of the Electroreduction of Oxygen on Pt Alloys with Fe, Ni, and Co', *Journal of The Electrochemical Society*. The Electrochemical Society, 146(10), p. 3750. doi: 10.1149/1.1392544.

[49]. Calderón Gómez, J., Moliner, R. and Lázaro, M. (2016) 'Palladium-Based Catalysts as Electrodes for Direct Methanol Fuel Cells: A Last Ten Years Review', *Catalysts*, 6(9), p. 130. doi: 10.3390/catal6090130.

[50]. Mustain, W. E. and Prakash, J. (2007) 'Kinetics and mechanism for the oxygen reduction reaction on polycrystalline cobalt–palladium electrocatalysts in acid media', *Journal of Power Sources*. Elsevier, 170(1), pp. 28–37. doi: 10.1016/J.JPOWSOUR.2007.04.005.

[51]. José L. Fernández, Darren A. Walsh, and and Bard*, A. J. (2004) 'Thermodynamic Guidelines for the Design of Bimetallic Catalysts for Oxygen Electroreduction and Rapid Screening by Scanning Electrochemical Microscopy. M−Co (M: Pd, Ag, Au)'. American Chemical Society . doi: 10.1021/JA0449729.

[52]. Mustain, W. E., Kepler, K. and Prakash, J. (2006) 'Investigations of carbon-supported CoPd3 catalysts as oxygen cathodes in PEM fuel cells', *Electrochemistry Communications*. Elsevier, 8(3), pp. 406–410. doi: 10.1016/J.ELECOM.2005.12.015.

[53]. Serov, A. A. *et al.* (2007) 'Modification of palladium-based catalysts by chalcogenes for direct methanol fuel cells', *Electrochemistry Communications*. Elsevier, 9(8), pp. 2041–2044. doi: 10.1016/J.ELECOM.2007.06.005.

[54]. Zheng, J.-S. *et al.* (2007) 'Effect of carbon nanofiber microstructure on oxygen reduction activity of supported palladium electrocatalyst', *Electrochemistry Communications*. Elsevier, 9(5), pp. 895–900. doi: 10.1016/J.ELECOM.2006.12.006.

[55]. Chakraborty, S. and Retna Raj, C. (2010) 'Electrocatalytic performance of carbon nanotube-supported palladium particles in the oxidation of formic acid and the reduction of oxygen', *Carbon*. Pergamon, 48(11), pp. 3242–3249. doi: 10.1016/J.CARBON.2010.05.014.

[56]. Li, B. and Prakash, J. (2009) 'Oxygen reduction reaction on carbon supported Palladium–Nickel alloys in alkaline media', *Electrochemistry Communications*. Elsevier, 11(6), pp. 1162–1165. doi: 10.1016/J.ELECOM.2009.03.037.

[57]. Coutanceau, C. *et al.* (2006) 'Development of electrocatalysts for solid alkaline fuel cell (SAFC)', *Journal of Power Sources*. Elsevier, 156(1), pp. 14–19. doi: 10.1016/J.JPOWSOUR.2005.08.035.

[58]. Vigier, F. *et al.* (2006) 'Electrocatalysis for the direct alcohol fuel cell', *Topics in Catalysis*. Kluwer Academic Publishers-Plenum Publishers, 40(1–4), pp. 111–121. doi: 10.1007/s11244-006-0113-7.

[59]. Bambagioni, V. *et al.* (2009) 'Pd and Pt-Ru anode electrocatalysts supported on multi-walled carbon nanotubes and their use in passive and active direct alcohol fuel cells with an anion-exchange membrane (alcohol = methanol, ethanol, glycerol)', *Journal of Power Sources*, 190(2), pp. 241–251. doi: 10.1016/j.jpowsour.2009.01.044.

[60]. Kang, Y. *et al.* (2017) 'An effective Pd-NiOx-P composite catalyst for glycerol electrooxidation: Co-existed phosphorus and nickel oxide to enhance performance of Pd', *Chemical Engineering Journal*. Elsevier B.V., 308, pp. 419–427. doi:

10.1016/j.cej.2016.09.087.

[61]. Ozoemena, K. I. (2016) 'Nanostructured platinum-free electrocatalysts in alkaline direct alcohol fuel cells: catalyst design, principles and applications', *RSC Adv.* Royal Society of Chemistry, 6(92), pp. 89523–89550. doi: 10.1039/C6RA15057H.

[62]. Antolini, E. *et al.* (2011) 'Palladium-based electrodes: A way to reduce platinum content in polymer electrolyte membrane fuel cells', *Electrochimica Acta*. Elsevier Ltd, 56(5), pp. 2299–2305. doi: 10.1016/j.electacta.2010.11.101.

[63]. Shao, M. (2011) 'Palladium-based electrocatalysts for hydrogen oxidation and oxygen reduction reactions', *Journal of Power Sources*. Elsevier, 196(5), pp. 2433–2444. doi: 10.1016/J.JPOWSOUR.2010.10.093.

[64]. *Palladium Chart - Last 5 year* (no date). Available at: https://www.kitco.com/charts/popup/pd1825nyb.html (Accessed: 8 April 2019).

[65]. Li, R. *et al.* (2011) 'Ultrasonic-assisted synthesis of Pd–Ni alloy catalysts supported on multi-walled carbon nanotubes for formic acid electrooxidation', *Electrochimica Acta*. Pergamon, 56(19), pp. 6860–6865. doi: 10.1016/J.ELECTACTA.2011.05.097.

[66]. Nguyen, S. T. *et al.* (2011) 'Tb promoted Pd/C catalysts for the electrooxidation of ethanol in alkaline media', *International Journal of Hydrogen Energy*. Pergamon, 36(16), pp. 9645–9652. doi: 10.1016/J.IJHYDENE.2011.05.049.

[67]. Grdeń, M. *et al.* (2008) 'Electrochemical behaviour of palladium electrode: Oxidation, electrodissolution and ionic adsorption', *Electrochimica Acta*. Pergamon, 53(26), pp. 7583–7598. doi: 10.1016/J.ELECTACTA.2008.05.046.

[68]. Bianchini, C. and Shen, P. K. (2009) 'Palladium-Based Electrocatalysts for Alcohol Oxidation in Half Cells and in Direct Alcohol Fuel Cells', *Chemical Reviews*. American

Chemical Society, 109(9), pp. 4183–4206. doi: 10.1021/cr9000995.

[69]. Wei, Y.-C., Liu, C.-W. and Wang, K.-W. (2011) 'Improvement of oxygen reduction reaction and methanol tolerance characteristics for PdCo electrocatalysts by Au alloying and CO treatment', *Chemical Communications*. The Royal Society of Chemistry, 47(43), p. 11927. doi: 10.1039/c1cc15110j.

[70]. Fashedemi, O. O., Julies, B. and Ozoemena, K. I. (2013) 'Synthesis of Pd-coated FeCo@Fe/C core–shell nanoparticles: microwave-induced "top-down" nanostructuring and decoration', *Chemical Communications*. The Royal Society of Chemistry, 49(20), p. 2034. doi: 10.1039/c3cc38672d.

[71]. Fashedemi, O. O. and Ozoemena, K. I. (2013) 'Enhanced methanol oxidation and oxygen reduction reactions on palladium-decorated FeCo@Fe/C core–shell nanocatalysts in alkaline medium', *Physical Chemistry Chemical Physics*. The Royal Society of Chemistry, 15(48), p. 20982. doi: 10.1039/c3cp52601a.

[72]. Calvo, S. R. and Balbuena, P. B. (2007) 'Theoretical analysis of reactivity on Pt(1 1 1) and Pt–Pd(1 1 1) alloys', *Surface Science*. North-Holland, 601(21), pp. 4786–4792. doi: 10.1016/J.SUSC.2007.07.024.

[73]. Sotelo, J. C. and Seminario, J. M. (2007) 'Biatomic substrates for bulk-molecule interfaces: The PtCo-oxygen interface', *The Journal of Chemical Physics*. American Institute of Physics, 127(24), p. 244706. doi: 10.1063/1.2799997.

[74]. Riccardo Ferrando, *,†, Julius Jellinek, ‡ and and Johnston§, R. L. (2008) 'Nanoalloys: From Theory to Applications of Alloy Clusters and Nanoparticles'. American Chemical Society . doi: 10.1021/CR040090G.

[75]. Wang, L.-L. and Johnson, D. D. (2009) 'Predicted Trends of Core−Shell Preferences

for 132 Late Transition-Metal Binary-Alloy Nanoparticles', *Journal of the American Chemical Society*. American Chemical Society, 131(39), pp. 14023–14029. doi: 10.1021/ja903247x.

[76]. Yamauchi, H. (1985) 'Surface segregation in jellium binary solid solutions', *Physical Review B*. American Physical Society, 31(12), pp. 7688–7694. doi: 10.1103/PhysRevB.31.7688.

[77]. Fashedemi, O. O. (2014) 'Comparative electrocatalytic oxidation of ethanol, ethylene glycol and glycerol in alkaline medium at Pd-decorated FeCo@Fe/C core-shell nanocatalysts', *Electrochimica Acta*. Pergamon, 128, pp. 279–286. doi: 10.1016/J.ELECTACTA.2013.10.194.

[78]. Fashedemi, O. O. *et al.* (2015) 'Electro-oxidation of ethylene glycol and glycerol at palladium-decorated FeCo@Fe core–shell nanocatalysts for alkaline direct alcohol fuel cells: functionalized MWCNT supports and impact on product selectivity', *Journal of Materials Chemistry A*. The Royal Society of Chemistry, 3(13), pp. 7145–7156. doi: 10.1039/C5TA00076A.

[79]. Slanac, D. A. *et al.* (2012) 'Atomic Ensemble and Electronic Effects in Ag-Rich AgPd Nanoalloy Catalysts for Oxygen Reduction in Alkaline Media', *Journal of the American Chemical Society*. American Chemical Society, 134(23), pp. 9812–9819. doi: 10.1021/ja303580b.

[80]. Li, G. *et al.* (2011) 'Preparation and characterization of PdxAgy/C electrocatalysts for ethanol electrooxidation reaction in alkaline media', *Electrochimica Acta*. Pergamon, 56(22), pp. 7703–7711. doi: 10.1016/J.ELECTACTA.2011.06.036.

[81]. Qi, Z. *et al.* (2011) 'Novel nanocrystalline PdNi alloy catalyst for methanol and

ethanol electro-oxidation in alkaline media', *Journal of Power Sources*. Elsevier B.V., 196(14), pp. 5823–5828. doi: 10.1016/j.jpowsour.2011.02.083.

[82]. Amin, R. S., Hameed, R. M. A. and El–Khatib, K. M. (2014) 'Microwave heated synthesis of carbon supported Pd, Ni and Pd–Ni nanoparticles for methanol oxidation in KOH solution', *Applied Catalysis B: Environmental*. Elsevier, 148–149, pp. 557–567. doi: 10.1016/J.APCATB.2013.11.020

[83]. Amin, R. S. *et al.* (2014) 'Electrocatalytic activity of nanostructured Ni and Pd–Ni on Vulcan XC-72R carbon black for methanol oxidation in alkaline medium', *International Journal of Hydrogen Energy*. Pergamon, 39(5), pp. 2026–2041. doi: 10.1016/J.IJHYDENE.2013.11.033.

[84]. Liu, Z., Zhang, X. and Hong, L. (2009) 'Physical and electrochemical characterizations of nanostructured Pd/C and PdNi/C catalysts for methanol oxidation', *Electrochemistry Communications*. Elsevier B.V., 11(4), pp. 925–928. doi: 10.1016/j.elecom.2009.02.030.

[85]. Calderón, J. C. *et al.* (2016) 'Palladium–nickel catalysts supported on different chemically-treated carbon blacks for methanol oxidation in alkaline media', *International Journal of Hydrogen Energy*. Pergamon, 41(43), pp. 19556–19569. doi: 10.1016/J.IJHYDENE.2016.07.121

[86]. Singh, R. N., Singh, A. and Anindita (2009) 'Electrocatalytic activity of binary and ternary composite films of Pd, MWCNT and Ni, Part II: Methanol electrooxidation in 1 M KOH', *International Journal of Hydrogen Energy*. Elsevier Ltd, 34(4), pp. 2052–2057. doi: 10.1016/j.ijhydene.2008.12.047.

[87]. Chong Luo, Hui Xie, Qin Wang, Geng Luo, and Chao Liu. (2015). A Review of the

Application and Performance of Carbon Nanotubes in Fuel Cells. *Journal of Nanomaterials* . Vol. Volume 2015. p1-10.

[88]. Sharma, S. and Pollet, B. G. (2012) 'Support materials for PEMFC and DMFC electrocatalysts—A review', *Journal of Power Sources*. Elsevier, 208, pp. 96–119. doi: 10.1016/J.JPOWSOUR.2012.02.011.

[89]. Zhang, Z. *et al.* (2009) 'Ordered High-Density Si

[100] Nanowire Arrays Epitaxially Grown by Bottom Imprint Method', *Advanced Materials*. John Wiley & Sons, Ltd, 21(27), pp. 2824–2828. doi: 10.1002/adma.200802156.

[90]. Song, C.-H. *et al.* (2019) 'Effect of Dispersion Solvents in Catalyst Inks on the Performance and Durability of Catalyst Layers in Proton Exchange Membrane Fuel Cells', *Energies*. Multidisciplinary Digital Publishing Institute, 12(3), p. 549. doi: 10.3390/en12030549.

[91]. Qiao, Y. and Li, C. M. (2011) 'Nanostructured catalysts in fuel cells', *J. Mater. Chem.* The Royal Society of Chemistry, 21(12), pp. 4027–4036. doi: 10.1039/C0JM02871A.

[92]. Dhanasekaran, P. *et al.* (2019) 'Enhancing stability and efficiency of oxygen reduction reaction in polymer electrolyte fuel cells with high surface area mesoporous carbon synthesized from spent mushroom compost', *Sustainable Energy & Fuels*. The Royal Society of Chemistry, 3(4), pp. 1012–1023. doi: 10.1039/C8SE00520F.

[93]. Calderón, J. C. *et al.* (2012) 'Pt–Ru catalysts supported on carbon xerogels for PEM fuel cells', *International Journal of Hydrogen Energy*. Pergamon, 37(8), pp. 7200–7211. doi: 10.1016/J.IJHYDENE.2011.12.029.

[94]. Qiu, Z. *et al.* (2014) 'Biotemplated synthesis of bark-structured TiC nanowires as Pt catalyst supports with enhanced electrocatalytic activity and durability for methanol oxidation', *J. Mater. Chem. A.* The Royal Society of Chemistry, 2(21), pp. 8003–8008. doi: 10.1039/C4TA00277F.

[95]. Springer, T. E., Wilson, M. S. and Gottesfeld, S. (1993) 'Modeling and Experimental Diagnostics in Polymer Electrolyte Fuel Cells', *Journal of The Electrochemical Society*. The Electrochemical Society, 140(12), p. 3513. doi: 10.1149/1.2221120.

[96]. Philippot, K. and Serp, P. (no date) *Concepts in Nanocatalysis*. Available at: https://nccr.iitm.ac.in/nanocatalysis.pdf (Accessed: 8 April 2019).

[97]. Yuan, X. *et al.* (2013) 'Use of polypyrrole in catalysts for low temperature fuel cells', *Energy & Environmental Science*. The Royal Society of Chemistry, 6(4), p. 1105. doi: 10.1039/c3ee23520c.

[98]. Nanowerk. (2019). Carbon nanotubes- what they are, how they are made, what they are used for? Available from: https://www.nanowerk.com/nanotechnology/introduction/introduction_to_nanotechnology_22.php. [Accessed: 10/4/2019]

[99]. Szabó, A. *et al.* (2010) 'Synthesis methods of carbon nanotubes and related materials', *Materials*, 3(5), pp. 3092–3140. doi: 10.3390/ma3053092.

[100]. *Single-Walled Carbon Nanotubes: Descriptions, Usage and Applications - Nanografi Nano Technology* (2019). Available at: https://nanografi.com/blog/singlewalled-carbon-nanotubes-descriptions-usage-and-applications/ (Accessed: 8 April 2019).

[101]. L. Gan, R.T Lv, H.D. Du, B.H. Li, F.Y Kang. (2009). High loading Pt-Ru nanocatalyst by pentagon defects introduced in bamboo- shaped carbon nanotubes support for high performance anode of DMFC. Electrochem. Commun, 11, 355.

[102]. L. Lui el at. (2002). Preparation and characterization of Platinum based electrocatalyst on multi walled carbon nanotubes for proton exchange membrane fuel cell. Langmuir 18, 4054.

[103]. Huang, M. *et al.* (2017) 'Networks of connected Pt nanoparticles supported on carbon nanotubes as superior catalysts for methanol electrooxidation', *Journal of Power Sources*, 342, pp. 273–278. doi: 10.1016/j.jpowsour.2016.12.054.

[104]. Ye, K.-H. *et al.* (2013) 'Stability analysis of oxide (CeO2, NiO, Co3O4 and Mn3O4) effect on Pd/C for methanol oxidation in alkaline medium', *Electrochimica Acta*, 90, pp. 108–111. doi: 10.1016/j.electacta.2012.12.012.

[105]. Xu, C. *et al.* (2008) 'Oxide (CeO2, NiO, Co3O4 and Mn3O4)-promoted Pd/C electrocatalysts for alcohol electrooxidation in alkaline media', *Electrochimica Acta*, 53(5), pp. 2610–2618. doi: 10.1016/j.electacta.2007.10.036.

[106]. Tseng, Y. J. and Scott, D. (2018) 'A simple, membrane-free, direct glycerol fuel cell utilizing a precious metal-free cathode and gold-plated anode surfaces', *Energies*, 11(9). doi: 10.3390/en11092259.

CHAPTER 3

EXPERIMENTAL METHODOLOGY

3.1 MATERIALS AND REAGENTS

Multi-walled carbon nanotubes MWCNTs (Carbon Nano-material Technology, South Korea), potassium hydroxide pellets KOH (Alfa Aesar), sodium hydroxide NaOH (Alfa Aesar), sulfuric acid H_2SO_4 (KIMIX),nitric acid HNO_3 (KIMIX), palladium (II) chloride $PdCl_2$ (Alfa Aesar), nickel chloride $NiCl_2$ (Alfa Aesar), tin (II) chloride dehydrate $SnCl_2{\cdot}2H_2O$ (Alfa Aesar), cobalt (II,III) oxide Co_3O_4 (ALDRICH), Cerium(IV) oxide CeO_2 (ALDRICH), ethylene glycol $C_2H_4O_2$ (KIMIX), glycerol$C_3H_8O_3$ (Merck), Nafion (Alfa Aesar), isopropanol C_3H_8O (Alfa Aesar) and Ultrapure water was prepared with Milli-Q system. All the reagents were of analytical grade and were used as received from the suppliers without further purification.

3.2 SYNTHESIS AND EXPERIMENTAL PROCEDURE

3.2.1 FUNCTIONALIZATION OF MWCNTS

1. The pristine MWCNTs were first COO- functionalized. Briefly, 5g of MWCNTs was added to (3:1 ratio) HNO_3/H_2SO_4 mixture, made up of 90 ml HNO_3 and 10 ml H_2SO_4, the mixture was refluxed for 6 hours at 160 ^oC.
2. The carbon nanotube sediments were separated from the reaction mixture, washed with ultrapure water. The synthesis solution pH was adjusted to ~7 by using 2M NaOH solution.

3. The purified, acid-functionalized MWCNT slurry was then oven-dried at 80^{o}C overnight to obtain the solid black product.

3.2.2 PREPARATION OF MWCNT-M (M=Pd, Ni, Sn)

The metal (Pd, Ni and Sn) nanoparticle catalysts were supported onto the walls of MWCNTs by adopting the modified polyol reduction method.

1. 72 mg of $PdCl_2$ was added to a solution of (1:1 ratio) ethylene glycol (EG) and ultrapure water. They were introduced into a 250 mL Erlenmeyer flask, stirred and sonicated for 1 hour.
2. Then 200mg of MWCNTs was then added to a solution of (1:1 ratio) ethylene glycol (EG) and ultrapure water and were introduced into a 250 mL Erlenmeyer flask. They were, stirred and sonicated for 15 minutes. Then the above solutions were combined and ultrasonicated for 1 hour. The synthesis solution pH was adjusted to ~12 by using 2M NaOH solution.
3. Then refluxed at 160 ^{o}C for 6 hours. The reflux solution was allowed to cool down before the reaction vessel can be removed while stirring at room temperature.
4. Within 120–170 ^{o}C range, EG is believed to generate the reducing species for the reduction of the metal ions to metallic particles at high temperatures, so it is possible that metal reduction process occurred within the 6 hours reaction time.
5. The resulting suspension was separated by filtration and the obtained residue washed with ultrapure water. The final solid product (abbreviated herein as Pd/MWCNT) was dried at 80^{o}C overnight in an oven.
6. The PdNi/MWCNT and PdSn/MWCNT were prepared using a similar procedure to the Pd/ MWCNT using $NiCl_2$ and $SnCl_2$ precursors, respectively. Prepared catalysts are: Pd/MWCNT, PdNi/MWCNT, PdSn/MWCNT, $PdNiCo_3O_4$/MWCNT,

$PdSnCo_3O_4$/MWCNT, $PdCo_3O_4$/MWCNT, $PdNiCeO_2$/MWCNT, PdSnCeO2/MWCNT and $PdCeO_2$/MWCNT.

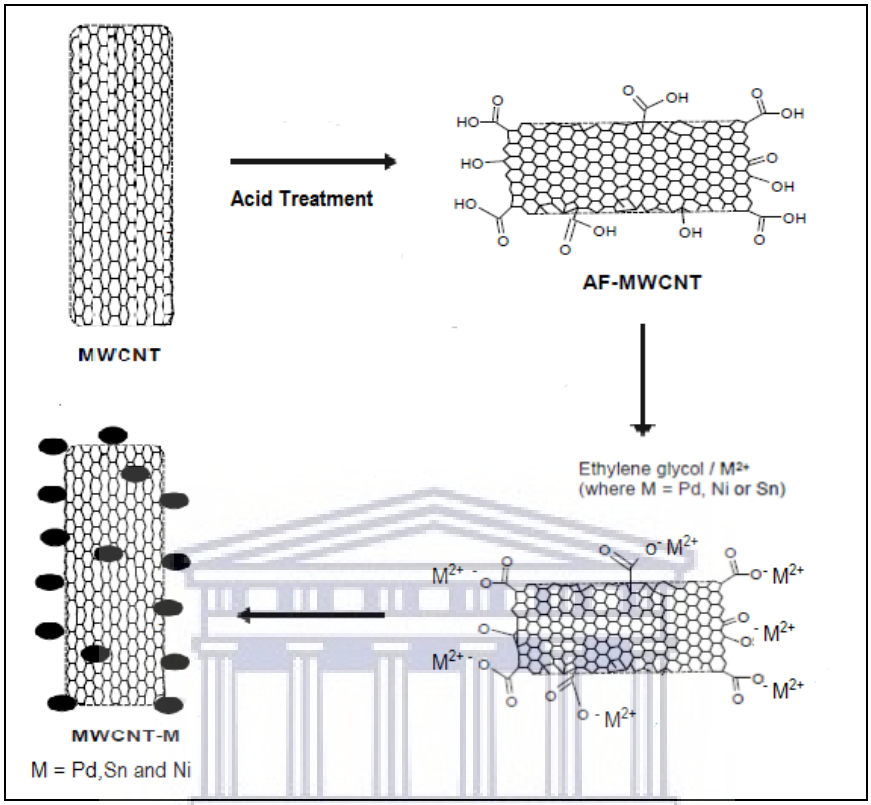

Figure 3. 1: Preparation MWCNT-M (M = Pd, Ni or Sn) nanocomposites using modified polyol method

3.2.3 INK PREPARATION

A stock solution of 20% isopropanol and 0.02% Nafion is prepared by mixing 79.6 ml of ultrapure water, 20ml of isopropanol and 0.4ml of 5 wt. % Nafion solution in 100ml volumetric flask.

1. 10mg of the catalyst is measured into a 10ml vial and 5ml of stock solution is added; mixed through and sonicated for 1 hour.

2. A 10 µl volume of the catalyst ink was then transferred via a syringe onto a freshly polished (mirror finish) Glassy Carbon (GC) electrode with a diameter of 3 mm (Single), Size: 25 x 25 mm.

3.3 CHARACTERIZATION TECHNIQUES

For structural identification of the catalyst- 2 instruments were used

- High-resolution transmission electron microscopy (HRTEM)
- X-ray diffraction microscopy (XRD)
- Small Area X-ray Scattering (SAXS)
- Fourier Transmission Infrared (FTIR) spectroscopy

For elemental analysis

- Energy dispersive spectroscopy (EDS)
- Inductively couple plasma (ICP)

For electrochemical characterization

- Cyclic voltammetry (CV)
- Linear sweep voltammetry (LSV)
- Electrochemical Impedance Spectroscopy (EIS)
- Chronoamperometry (CA)

3.3.1 PHYSICAL CHARACTERIZATION

3.3.1.1 TRANSMISSION ELECTRON MICROSCOPY (TEM)

Transmission electron microscopy is a microscopy technique where a beam of electrons produces a micrograph when transmitted through a specimen. The sample is regularly an ultrathin area below one hundred nm thick or a suspension on a grid. A micrograph is made from the association of the electrons with the sample as the beam is transmitted through the sample. The image is then amplified and centered onto an imaging device; a fluorescent screen, a layer of photographic film, or a sensor such as a charge-coupled device. A typical TEM consist of the following components: light source, condenser lens, specimen stage, objective lens and projector lens [1].

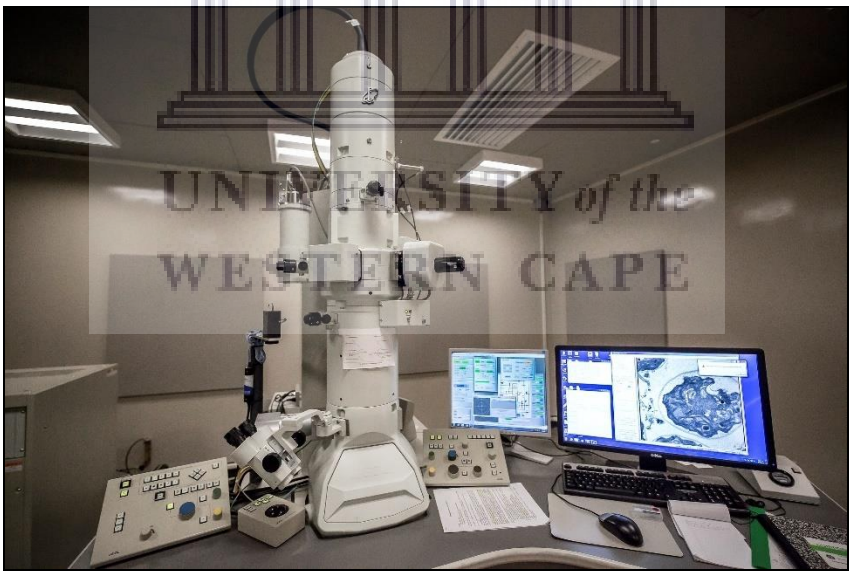

Figure 3. 2: Transmission Electron Microscopy (TEM) [2]

Transmission electron microscopes are ideal for imaging at higher resolution, owing from the littler de-Broglie wavelength of electrons. This empowers the instrument to detect fine detail-even as little as a single section of atoms [3]. Transmission electron microscopy is a crucial analysis strategy in the physical, chemical and natural sciences. TEMs are applied

in growth research and materials science in addition to research in virology, contamination, nanotechnology and semiconductor. At lower amplifications TEM micrograph contrast is because of differential absorption of electrons by the material due to contrasts in arrangement or thickness of the material. At higher amplifications, complex wave synergy tweaks the intensity of the picture, requiring experienced examination of the micrographs. Other interchangeable modes enable TEM to detect tweaks in chemical property, crystal arrangement, electronic structure and sample induced electron stage shift in addition to the standard absorption-based imaging [4]. The TEM used for analysis in this study is the TECNAI G2 F2O X-TWIN MAT 200 kV field emission, where nickel grid was used to coat the material for better conductivity with an average imaging resolution of 1.5 nm.

3.3.1.2 X-RAY DIFFRACTION (XRD)

X-ray diffraction (XRD) is a powerful non-destructive technique for characterizing crystalline material. It provides information on structures, phases, preferred crystal orientation, and other structural parameters such as, crystalline or grain size, crystallinity, and crystal defects. It is therefore, an indispensable tool for material characterization and thus, forms an integral part in a comprehensive characterization study of nanophase electro-catalyst. XRD in this study was utilized for the direct examination of crystalline structure, phase identification, particle size, and lattice parameter [5].

Working principle of XRD

In a typical XRD analysis, X-rays are generated in a cathode ray tube by heating the filament to produce electrons. The produced electrons are then accelerated toward the target material by applying voltage and bombarding the target material with electrons. When the electrons have enough energy to dislodge the inner shell electrons of the target

material, characteristic X-ray spectra are produced Copper is generally the most used target material for single-crystal diffraction, with a CuKα radiation of 1.5418Å.

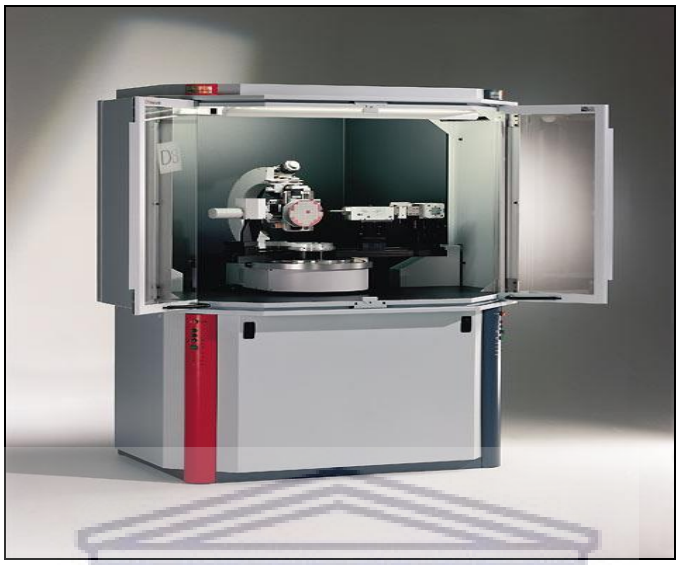

Figure 3. 3: X-ray Powder Diffraction (XRD) [6]

These X-rays are collimated and directed onto the sample. As the sample and detector are rotated, the intensity of the reflected X-rays is recorded. The interaction of the incident rays with the sample produces constructive interference and a peak in intensity occurs when the conditions satisfies Bragg's law (equation 3.1). A detector records and processes this X-ray signal and converts the signal to a count rate which is then output to a device such as computer or printer [6].

$$n\lambda = dsin\theta \tag{3.1}$$

By varying the angle θ, the Bragg's law conditions are satisfied by different d-spacing in polycrystalline materials. Plotting the angular positions and intensities of the resultant diffracted peaks of radiation produces a pattern, which is a representative of the sample where a mixture of different phases is present. The addition of an individual pattern then brings about a diffractogram. Now based on the principle of X-ray diffraction, a wealth of

structural, physical and chemical information about the material being investigated can therefore be acquired [7].

XRD can be used quantitatively for the determination of average particle size as mentioned above, using the Scherrera equation given below as:

$$D = \frac{0.9\lambda}{\beta cos\theta} \tag{3.2}$$

Where D is the particle size, 0.9 the shape factor, λ the wavelength of the X-ray, β is the peak width at half peak height (radians), and θ being the angle of reflection[8]. Crystalline size determination is performed by measuring the broadening of a particular peak in a diffraction pattern associated with a particular planar reflection from within the crystal unit cell. Particle size is inversely related to the half-width at half maximum of an individual peak. Typically the narrower and more intense the peak, the more crystalline the sample is. A broad peak is usually associated with small particle size and an amorphous material [9]. The X-ray diffraction used in this study is a BRUKER AXS DS Advance diffractometer with 2θ values ranging from 10-80 ^{o} , with a step size of 0.028 ^{o} operating at 45 kV and 40mA at Ithemba Labs Cape Town

3.3.1.3 SMALL AREA X-RAY SCATTERING (SAXS)

Small-angle X-ray scattering is a small-angle scattering technique with the aid of which nanoscale density differences in a pattern may be quantified. This implies it could determine nanoparticle size distributions, resolve the size and shape of (monodisperse) macromolecules, determine pore sizes, characteristic distances of partially ordered substances, and lots more. SAXS as a technique is used to offer information about the particle size distribution as well as the shape of the nanomaterials.

Figure 3. 4: Small Angel X-ray Scattering (SAXS) [10]

This is accomplished by analyzing the elastic scattering behavior of X-rays while traveling through the material, recording their scattering at small angles (generally 0.1 - 10°, for this reason it is called "Small-angle". It belongs to the family of small-angle scattering (SAS) techniques along with small-angle neutron scattering, and is commonly achieved by the usage of hard X-rays with a wavelength of 0.07 - 0.2 nm [11]. The SAXS instrument used in this study is SAXSpace Anton Paar 82024536 with a primux 3000 sealed Copper tube.

3.3.1.4 FOURIER TRANSFORM INFRARED SPECTROSCOPY (FTIR)

The discovery of infrared light may be dated back to the 19th century. Since then, scientists have established numerous methods to make use of infrared light. Infrared absorption spectroscopy is the approach which scientists use to determine the structure of molecules with the molecules' functional groups absorption of infrared radiation. Infrared spectrum is molecular vibrational spectrum [39]. When exposed to infrared radiation, sample molecules selectively absorb radiation of unique wavelengths which causes the change of dipole moment of sample molecules. Therefore, the vibrational energy levels of sample molecules switch from ground state to excited state. The frequency of the absorption peak is decided through the vibrational energy gap. The variety of absorption peaks is associated with the wide variety of vibrational freedom of the molecule. The intensity of absorption peaks is associated to the change of dipole moment and the possibility of the transition of energy levels. Consequently, through studying the infrared

spectrum, you could simply attain considerable information about the structure of a molecule. Most molecules are infrared active except for several mononuclear diatomic molecules such as O_2, N_2 and Cl_2 because of the zero dipole change within the vibration and rotation of these molecules. What makes infrared absorption spectroscopy even more useful is that it can successfully to investigate all gas, liquid and solid samples [40, 41].

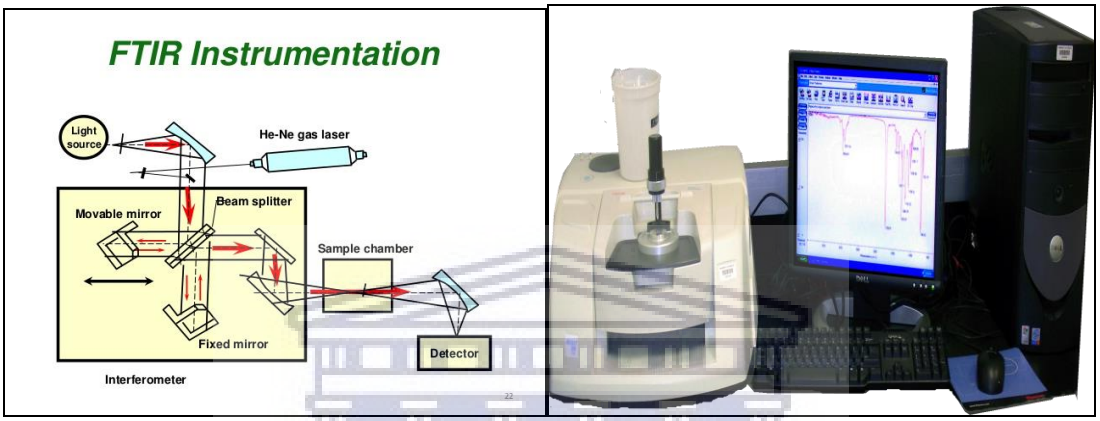

Figure 3. 5: Schematic 1) and 2) working station of FTIR spectroscopy [43, 44]

The range of Infrared region is 12800 ~ 10 $cm^{-1}$and may be divided into near-infrared area (12800 ~ 4000 cm^{-1}), mid-infrared location (4000 ~ 200 cm^{-1}) and a long way-infrared region (50 ~ a thousand cm^{-1}). The common place used region for infrared absorption spectroscopy is 4000 ~ 400 cm^{-1} because the absorption radiation of maximum natural compounds and inorganic ions is within this region [42].

3.3.2 ELEMENTAL ANALYSIS

3.3.2.1 ENERGY-DISPERSIVE X-RAY SPECTROSCOPY (EDX)

The Energy Dispersive X-ray (EDX) microanalysis is a technique of quantitative elemental analysis associated to electron microscopy based on the generation of characteristic X-rays that reveals the presence of elements present in the specimens [12]. When beam of electrons interact with a sample surface, variety of emissions including X-rays are produced. An energy-dispersive (EDS) detector is used to separate the characteristic x-rays of different elements into an energy spectrum, and EDS system software is used to analyze the energy spectrum in order to determine the abundance of specific elements [13].

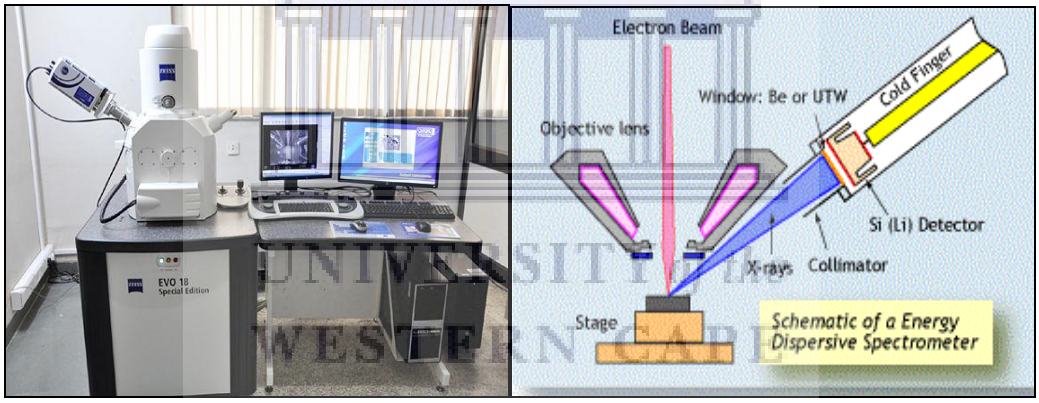

Figure 3. 6: 1) Energy-Dispersive X-ray spectroscopy (EDX) work stationand 2) Schematic of Energy Dispersive X-ray Spectrometer [14]

EDS can be used to find the chemical composition of materials down to a spot size of a few microns, and to create element composition maps over a much broader raster area. EDX systems include a sensitive x-ray detector, a liquid nitrogen Dewar for cooling, and software to collect and analyze energy spectra. The detector is mounted in the sample chamber of the main instrument at the end of a long arm, which is itself cooled by liquid

nitrogen. The most common detectors are made of Si (Li) crystals that operate at low voltages to improve sensitivity.

The detector contains a crystal that absorbs the energy of incoming x-rays by ionization, yielding free electrons in the crystal that become conductive and produce an electrical charge bias [15]. The x-ray absorption thus converts the energy of individual x-rays into electrical voltages of proportional size; the electrical pulses correspond to the characteristic x-rays of the element. A typical EDX spectrum is portrayed as a plot of x-ray counts vs. energy (in keV). Energy peaks correspond to the various elements in the sample. Generally they are narrow and readily resolved, but many elements yield multiple peaks. For example, iron commonly shows strong K-α and K-β peaks. Elements in low abundance will generate x-ray peaks that may not be resolvable from the background radiation [16]. The EDS instrument used in this study is an Oxford X-Max silicon drift EDS detector which produces high resolution EDS spectra with productive count rates at low beam currents.

3.3.2.2 INDUCTIVELY COUPLED PLASMA

The maximum generally used techniques for the determination of trace concentrations of elements in samples are based on atomic emission spectrometry (AES) and inductively coupled plasma is primarily based on AES. An-inductively coupled plasma can be generated by using directing the energy of a radio frequency generator into a suitable gas, typically ICP argon. Different plasma gases used are Helium and Nitrogen. It is crucial that the plasma gas is natural because contaminants within the gas would possibly quench the torch. Coupling is accomplished by generating a magnetic field by way of passing an excessive frequency electric current via a cooled induction coil. This inductor generates a rapidly oscillating magnetic field orientated within the vertical aircraft of the coil [17].

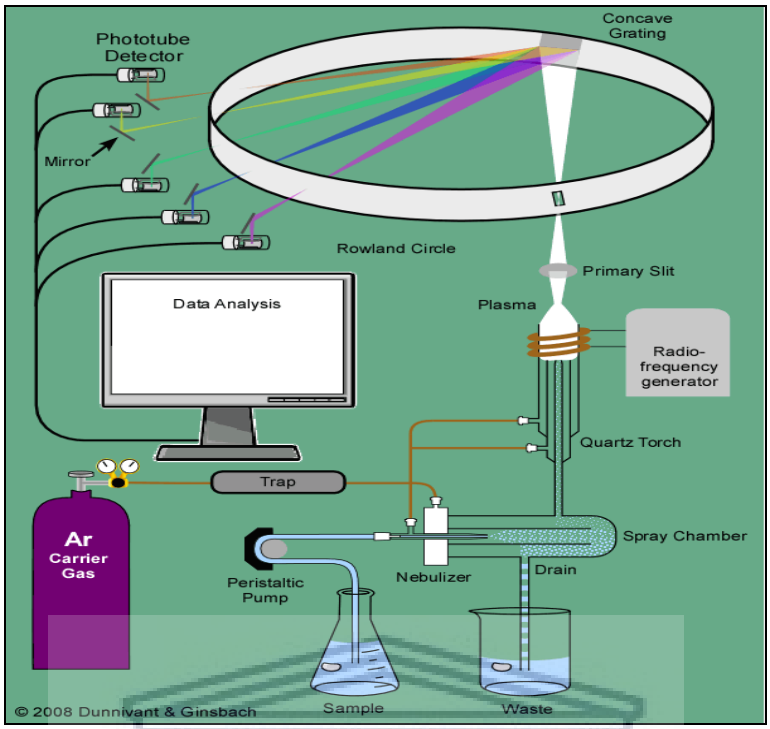

Figure 3. 7: Inductively Coupled Plasma with Atomic Emission Spectrometry (ICP-AES) [18]

Ionization of the flowing argon is initiated with the aid of a spark from a Tesla coil. The generated ions and their associated electrons from the Tesla coil then interact with the fluctuating magnetic field [19]. This generates enough strength to ionize more argon atoms by way of collision excitation. The electrons generated inside the magnetic field are accelerated perpendicularly to the torch. At excessive speeds, cations and electrons, called eddy current, will collide with argon atoms to produce further ionization which generate a notable temperature increase. Within 2 milli seconds, a regular state is created with a high electron density [20]. A plasma is created within the top of the torch. The temperature within the plasma ranges from 6,000-10,000 K. An extended, properly-defined tail emerges from the pinnacle of the high temperature plasma on the pinnacle of the torch. This torch is the spectroscopic source. It includes all the analyte atoms and ions that have been excited by the heat of the plasma. The fulfillment of ICP leans on its functionality to

analyze a big amount of samples in a quick period with excellent detection limits for most elements. ICPs used in the marketplace today are frequently connected to extraordinary detection systems, consisting of ICP mass spectrometry and ICP atomic emission spectrometry [21]. The ICP instrument used in this study is Thermo-Fisher X-Series II quadrupole ICP-MS with a new wave UP213 solid-state laser ablation system. The spot size of the laser can be set to various diameters between 10 and 300 microns.

3.3.3 ELECTROCHEMICAL CHARACTERIZATION

Electrochemistry studies the relationship between electric and chemical occurrences [22]. It covers especially two areas: electrolysis-conversion of chemical compounds by using passage of an electric and electrochemical power sources- energy of chemical reactions transformed into electricity. Electrochemistry is one powerful technique to take a look at electron transfer properties. When electron transfer is between a substrate and a solution species, it is name heterogeneous procedure. Inversely, if electron transfer happens among two species, each of which might be in solution, the reaction called is homogeneous. Therefore, electrochemistry can in particular be described as the technological know-how of structures and techniques at and thru the interface between an electronic (electrode) and an ionic conductor (electrolyte) or between ionic conductors [23].

Figure 3. 8: An electrochemical working station [27]

Electrochemistry is an interdisciplinary science that is especially rooted in chemistry and physics; however, additionally related to engineering and biochemistry/biology. Because of its range, electrochemistry has discovered utility in numerous working fields consisting of: analytical electrochemistry; environmental electrochemistry [24]; electrochemistry of glasses [25]; ionic liquids electrochemistry; micro-electrochemistry, surface electrochemistry; technical electrochemistry with several subtopics inclusive of: Batteries and energy storage [26]; Corrosion and corrosion inhibition. The work described in this dissertation includes current measurements, voltammetry and a number of voltammetry techniques, namely, cyclic voltammetry (CV), linear sweep voltammetry (LSV), chronoamperometry (CA) and Electrochemical Impedance Spectroscopy (EIS).

3.3.3.1 CYCLIC VOLTAMMETRY (CV)

This is a commonly utilized kind of voltammetry in which measurement of the current response of an electrode to a linearly increasing and decreasing potential cycle is carried out [28]. Figure 3.8 presents the resulting scan of potential against time, scanning linearly the potential of a stationary operating electrode in an unstirred solution, using a triangular

potential waveform and the corresponding voltammogram. The experiment is typically commenced at a potential wherein no electrode process occurs (0.2 V inside the plot) and the potential is scanned with a fixed scan rate to the switching potential (0.7 V in the plot). When an electrochemically active compound is present within the solution phase, an anodic current peak at the potential Epa is detected with the peak current Ipa. when the potential is swept back at some point of the reverse scan a in addition current peak on the potential Epc may be located with a cathodic peak modern Ipc.

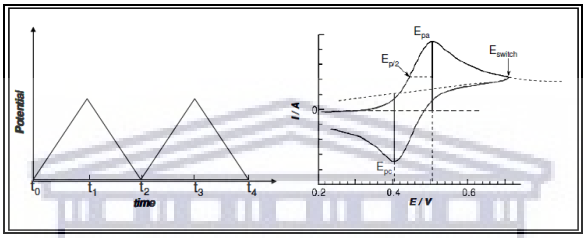

Figure 3. 9: The potential-time waveform and a typical cyclic voltammogram for a reversible redox process.

Cyclic voltammetry is an great approach to study the reactivity of new materials or compounds and can offer information about (i) the potential at which oxidation or reduction processes transpire, (ii) the oxidation state of the redox species, (iii) the number of electrons involved, (iv) the rate of electron transfer, (v) viable chemical processes corresponding with the electron transfer, and (vi) adsorption effects etc [29, 30, 31]. Electron transfer processes can be labelled reversible, irreversible or quasi-reversible, and are diagnosed by criteria that may be measured through cyclic voltammetry. The instrument used in study is an Autolab M204 with a potential range of +/- 10 V, compliance voltage +/- 20 V, maximum current +/- 400 mA, current ranges 100 mA to 10 nA, potential accuracy +/- 0.2 % , potential resolution 3 µV, current accuracy +/- 0.2 %, current resolution 0.0003 % (of current range), Input impedance > 100 GOhm and potentiostat bandwidth of 1 MHz.

3.3.3.2 LINEAR SWEEP VOLTAMMETRY

Linear sweep voltammetry (LSV) is a method wherein there is linear variant of the electrode potential with time with the scan rate (v), v = dE/dt and current versus potential is recorded. In LSV the required scan is primary half-cycle of a cyclic voltammogram which is conducted. Scanning begins at a potential wherein no electrochemical reaction takes place. Current may be discovered at the potential in which the charge transfer starts, which increases with the potential, nevertheless, after a maximum (peak current plateau) begins to decrease due to the depletion of the reacting species at the interface. Linear sweep voltammetry (LSV) differs from CV in that the applied potential is swept at a fixed sweep rate from an initial potential to a final potential and there is no back and forth [32]. The instrument used in study is an Autolab M204 with a potential range of +/- 10 V, compliance voltage +/- 20 V, maximum current +/- 400 mA, current ranges 100 mA to 10 nA, potential accuracy +/- 0.2 % , potential resolution 3 µV, current accuracy +/- 0.2 %, current resolution 0.0003 % (of current range), Input impedance > 100 GOhm and potentiostat bandwidth of 1 MHz.

3.3.3.3 ELECTROCHEMICAL IMPEDANCE SPECTROSCOPY (EIS)

Electrochemical impedance spectroscopy (EIS) is an effective method that may be utilized in-situ to signify the impedances in a fuel cell stack. AC impedance measurements may be helpful in identifying the kinetic, ohmic, electrolytic, and diffusion layer resistances, as well as the delivery limitations inside the machine. This technique makes use of a small sinusoidal perturbation potential at one or several frequencies, and the reaction is an alternating current (AC) sign of the identical frequency with a probable phase shift and amplitude trade. In a few dimension systems, the AC current is imposed on top of the DC

current generated by way of the fuel cell, and the voltage is recorded in place of the current. The recorded response is used to calculate the impedance using a mathematical method. Via repeating this at numerous frequencies, an electrochemical impedance spectrum is received. EIS is a noninvasive method that varies the current or voltage of the fuel cell by some percentage. The magnitude of the fluctuations is depending on the peak-peak current of the AC signal imposed and the impedance of the fuel cell at every frequency [33]. The AC-Impedance measurement is obtained with an electronic load, a function generator, and a computer. This is additionally the equal setup also can be used for obtaining a fuel cell polarization or IC curves. EIS is useful in characterizing rapid and gradual delivery phenomena as it tests each single and a big variety of frequencies. This check helps to signify mass transfer resistance, resistance to electron transfer at some stage in electrochemical reactions, and ionic resistance through the membrane. This data can then be used to evaluate the numerous impedances inside the gas cell [34].

The EIS technique is an extension of the high-frequency resistance (HFR) technique but differs in two approaches. The HFR method uses a single frequency and only examines the real components of the impedance. EIS measures an extensive variety of frequencies and monitors the resulting variations in value and segment of the cell voltage and current with a frequency response analyzer to determine the complex impedance (Z' and Z") of the fuel cell. Performing the test is simple except for selecting the characteristic generator frequency. Electrochemical impedance spectroscopy is the most widely utilized technique for distinguishing fuel cell losses [35].

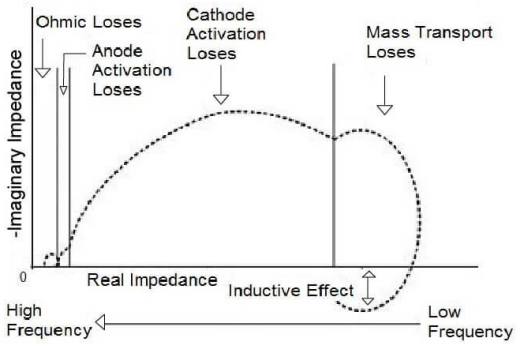

Figure 3. 10: Electrochemical Impedance Spectroscopy (EIS) [32]

Impedance is a measure of the ability of a circuit to resist the flow of electrical current. Impedance refers to the frequency dependent resistance to current flow of a circuit element (resistor, capacitor, inductor, etc.)Impedance assumes an AC current of a specific frequency in Hertz (cycles/s). The following equation describes impedance.

Impedance: $Z_\omega = E_\omega/I_\omega$(3.3)

Where E_ω = Frequency-dependent potential and I_ω= Frequency-dependent current. The information content of EIS is much higher than DC techniques or single frequency measurements and may be able to distinguish between two or more electrochemical reactions taking place, can identify diffusion-limited reactions, e.g., diffusion through a passive film, provides information on the capacitive behavior of the system. Test components within an assembled device using the device's own electrodes and can provide information about the electron transfer rate of reaction. Applications are study corrosion of metals, adsorption and desorption to electrode surface, the electrochemical synthesis of materials, the catalytic reaction kinetics, label free detection sensors and study the ions mobility in energy storage devices such as batteries and supercapacitors [36]. The instrument used in study is an Autolab M204 with a potential range of +/- 10 V, compliance voltage +/- 20 V, maximum current +/- 400 mA, current ranges 100 mA to 10

nA, potential accuracy +/- 0.2 % , potential resolution 3 µV, current accuracy +/- 0.2 %, current resolution 0.0003 % (of current range), Input impedance > 100 GOhm and potentiostat bandwidth of 1 MHz.

3.3.3.4 CHRONOAMPEROMETRY

In chronoamperometry the current is measured as a function of time after application of a potential step perturbation. When the potential of a working electrode is stepped from a rate at which no Faradaic reaction happens to a potential at which the surface concentration is effectively zero, is known as Chronoamperometry.

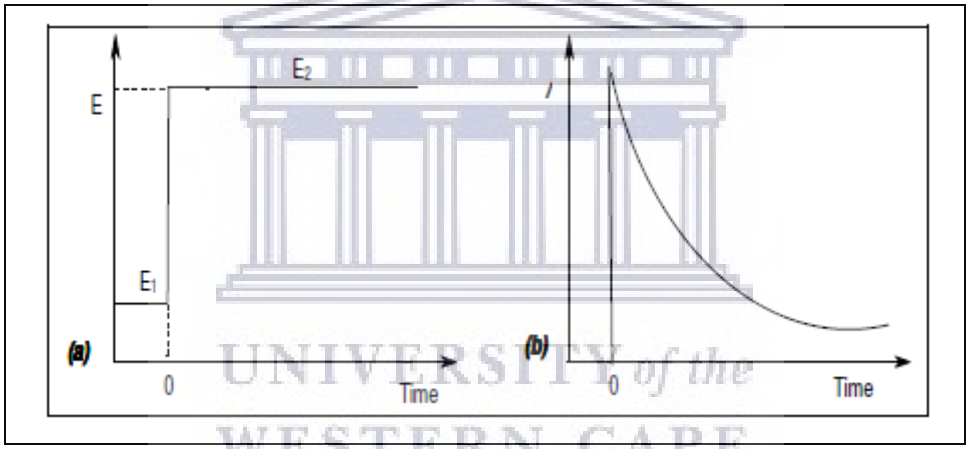

Figure 3. 11: Potential step chronoamperometry: (a) schematic application of potential step and (b) chronoamperometric response [32]

As an example, in figure 3.9a, if the potential is stepped from E1, where no current flows, i.e., in which the oxidation or reduction of the electrochemically active species does no longer take place, to E2 in which the current belongs to the electrode reaction. The electrode reaction is diffusion restricted. The generate current-time dependence is monitored. The current-time curve reflects the change in the concentration gradient in the place of the surface. This includes a sluggish expansion of the diffusion layer related to the depletion of the reactant as time progresses, consequently the current decays with time (at

a planar electrode) (Figure 3.9b). The current flows at any time after application of the potential step will obey the Cottrell equation.

$$i(t) = \frac{nFAcD^{\frac{1}{2}}}{\pi^{\frac{1}{2}} t^{\frac{1}{2}}} = kt^{-\frac{1}{2}} \quad (3.4)$$

Where *n*, F, A, c, D, and *t* are the number of electrons, Faraday constant, the surface area, the concentration, the diffusion coefficient, and time respectively. Chronoamperometry is often used for measuring the diffusion coefficient of electroactive species or the surface area of the working electrode. It can also be applied to the study of mechanisms of electrode processes [37, 38]. The instrument used in study is an Autolab M204 with a potential range of +/- 10 V, compliance voltage +/- 20 V, maximum current +/- 400 mA, current ranges 100 mA to 10 nA, potential accuracy +/- 0.2 % , potential resolution 3 µV, current accuracy +/- 0.2 %, current resolution 0.0003 % (of current range), Input impedance > 100 GOhm and potentiostat bandwidth of 1 MHz.

References

[1]. Kohl, H. and Reimer, L. (2008) *Transmission Electron Microscopy*. New York, NY: Springer New York (Springer Series in Optical Sciences). doi: 10.1007/978-0-387-40093-8.

[2]. John J. Bozzola, L. D. R. (2006) *Electron Microscopy: Principles and Techniques for Biologists - John J. Bozzola, Lonnie Dee Russell - Google Books*. Available at: https://books.google.co.za/books?hl=en&lr=&id=zMkBAPACbEkC&oi=fnd&pg=PR21&dq=J+Bozzola%3B+L+D+Russell.+Electron+microscopy:+principles+and+techniques+for+biologists.+Boston,+Jones+and+Bartlett,+2006.&ots=AcOZ_lkJN4&sig=N-LpWEHXKDZjxeITsLLyeqfhk0E#v=onepag (Accessed: 15 April 2019).

[3]. Brent Fultz, J. M. H. (2008) *Transmission Electron Microscopy and Diffractometry of Materials - Brent Fultz, James M. Howe - Google Books*. 4th edn. Available at: https://books.google.co.za/books?hl=en&lr=&id=tgOC3vlEY0sC&oi=fnd&pg=PR3&dq=B.+Fultz,+J.+Howe+Transmission+electron+microscopy+and+diffractometry+of+materials.+Berlin%3B+New+York:+Springer,+2008&ots=EyRO9y56np&sig=ibEZHCVDuDkLQfgpVMpzv-g9waY#v=onepage&q&f (Accessed: 15 April 2019).

[4]. Kang, F., Bonnamy, S. and Oberlin, A. (2016) 'Transmission Electron Microscopy', *Materials Science and Engineering of Carbon*. Butterworth-Heinemann, pp. 45–70. doi: 10.1016/B978-0-12-805256-3.00004-0.

[5]. Bunaciu, A. A., Udriştioiu, E. gabriela and Aboul-Enein, H. Y. (2015) 'X-Ray Diffraction: Instrumentation and Applications', *Critical Reviews in Analytical Chemistry*, 45(4), pp. 289–299. doi: 10.1080/10408347.2014.949616.

[6]. Barbara L Dutrow, C. M. C. (no date) *X-ray Powder Diffraction (XRD)*. Available at:

https://serc.carleton.edu/research_education/geochemsheets/techniques/XRD.html (Accessed: 12 April 2019).

[7]. Chatterjee, A. K. (2001) 'X-Ray Diffraction', *Handbook of Analytical Techniques in Concrete Science and Technology*. William Andrew Publishing, pp. 275–332. doi: 10.1016/B978-081551437-4.50011-4.

[8]. Epp, J. (2016) 'X-ray diffraction (XRD) techniques for materials characterization', *Materials Characterization Using Nondestructive Evaluation (NDE) Methods*. Woodhead Publishing, pp. 81–124. doi: 10.1016/B978-0-08-100040-3.00004-3.

[9]. Banerjee, D. (no date) *X-Ray Diffraction (XRD)*. Available at: https://www.iitk.ac.in/che/pdf/resources/XRD-reading-material.pdf (Accessed: 15 April 2019).

[10]. *Small Angle X-Ray Scattering - Point Source | Shared Materials Instrumentation Facility* (no date). Available at: http://smif.pratt.duke.edu/node/151 (Accessed: 17 April 2019).

[11]. Agbabiaka, A., Wiltfong, M. and Park, C. (2013) 'Small Angle X-Ray Scattering Technique for the Particle Size Distribution of Nonporous Nanoparticles', *Journal of Nanoparticles*, 2013, pp. 1–11. doi: 10.1155/2013/640436.

[12]. Scimeca, M. Bischetti, S. Lamsira, H. Bonfiglio, R. Bonanno, E. (2018) 'Energy Dispersive X-ray (EDX) microanalysis: A powerful tool in biomedical research and diagnosis.', *European journal of histochemistry : EJH*. PAGEPress, 62(1), p. 2841. doi: 10.4081/ejh.2018.2841.

[13]. Reed, S. J. B. (1995) 'Electron probe microanalysis', in *Microprobe Techniques in the Earth Sciences*. Boston, MA: Springer US, pp. 49–89. doi: 10.1007/978-1-4615-2053-

5_2.

[14]. *Energy Dispersive Spectroscopye* (no date). Available at: https://www.iitk.ac.in/dord/energy-dispersive-spectroscopye (Accessed: 12 April 2019).

[15]. *Energy dispersive X-ray spectroscopy (EDS) Wavelength dispersive X-ray spectroscopy (WDS)* (no date). Available at: https://fenix.tecnico.ulisboa.pt/downloadFile/282093452019577/11_TEM_Microscopy.pdf (Accessed: 15 April 2019).

[16]. Russ, J. C. (1984) *Fundamentals of Energy Dispersive X-Ray Analysis : Butterworths Monographs in Materials.* Elsevier Science. Available at: https://books.google.co.za/books?hl=en&lr=&id=Dg_-BAAAQBAJ&oi=fnd&pg=PP1&dq=Russ,+J.+C.+(1984)+Fundamentals+of+Energy+Dispersive+X-ray+Analysis,+Butterworths.+London.&ots=-hF-FJWN5j&sig=p71goGkHLoXXntmHfEmPuwZKo8k#v=onepage&q&f=false (Accessed: 15 April 2019).

[17]. *Inductively coupled plasma | HiQ* (no date). Available at: http://hiq.linde-gas.com/en/analytical_methods/inductively_coupled_plasma.html (Accessed: 15 April 2019)

[18]. Frank M. Dunnivant and Jake W. Gisnsbach. (2009). *Inductively Coupled Plasma - Atomic Emission Spectrometry*. Available from: http://people.whitman.edu/~dunnivfm/FAASICPMS_Ebook/CH3/index.html. [Accessed: 15/4/2019].

[19]. Boss, C. F. K. (1997) 'Concepts, Instrumentation and Techniques in Inductively Coupled Plasma Optical Emission Spectrometry', *Journal of Chemical Information and*

Modeling, 53, p. 160. doi: 10.1017/CBO9781107415324.004.

[20]. Ghosh, S. *et al.* (2016) 'Inductively coupled plasma - Optical emission spectroscopy : A review Inductively Coupled Plasma – Optical Emission Spectroscopy : A Review .', (September).

[21]. Jacobs, J. L. (no date) *Diagnostic studies of ion beam formation in inductively coupled plasma mass spectrometry with the collision reaction interface*. Available at: https://lib.dr.iastate.edu/etd/14814 (Accessed: 15 April 2019).

[22]. Bard, A., Methods, L. F.-E. and 2001, undefined (no date) 'Fundamentals and applications', *researchgate.net*. Available at: https://www.researchgate.net/profile/Leta_Menisa/post/Can_anyone_suggest_me_the_best_textbook_for_electrochemistry/attachment/5a962a9b4cde266d588e1d5d/AS:598859948494856@1519790746484/download/Electrochemical_methods_2ed_2001_-_Bard_Faulkner.pdf (Accessed: 15 April 2019).

[23]. Schmickler, W. (1996) 'Electronic Effects in the Electric Double Layer'. American Chemical Society . doi: 10.1021/CR940408C.

[24]. John O'M. Bockris, S. U. M. K. (2013) *Surface Electrochemistry: A Molecular Level Approach*. Available at: https://books.google.co.za/books?hl=en&lr=&id=iYjkBwAAQBAJ&oi=fnd&pg=PA3&dq=J.O'M+Bockris,+S.U.M+Khan,+Surface+Electrochemistry,+Plenum,+New+York,+(1993)&ots=QLxo6znSUa&sig=wZg-mS4UDFd5exZPVPgOubjTa_8#v=onepage&q=J.O'M Bockris%2C S.U.M (Accessed: 15 April 2019).

[25]. Bach, H., Baucke, F. and Krause, D. (2013) *Electrochemistry of glasses and glass melts, including glass electrodes*. Available at:

https://books.google.co.za/books?hl=en&lr=&id=HT7zCAAAQBAJ&oi=fnd&pg=PA5&dq=H+Bach,+F+Baucke,+D+Krause,+Electrochemistry+of+Glasses+and+Glass+Melts,+Including+Glass+Electrodes,+Schott+Series,+Springer,+Berlin+(2000)&ots=D9VLf6ngVu&sig=GahXYwkBNZA6iGGy3OqkDZYlx4M (Accessed: 15 April 2019).

[26]. Osaka, T. and Datta, M. (2000) *Energy storage systems in electronics*. Available at: https://content.taylorfrancis.com/books/download?dac=C2004-0-07709-0&isbn=9781482296891&format=googlePreviewPdf (Accessed: 15 April 2019).

[27]. *Metrohm Autolab Video Tutorials* (no date). Available at: https://www.metrohm.com/en-gb/support-and-service/autolab-video-tutorials/ (Accessed: 12 April 2019).

[28]. Nicholson, R. S. and Shain, I. (1964) 'Theory of Stationary Electrode Polarography. Single Scan and Cyclic Methods Applied to Reversible, Irreversible, and Kinetic Systems.', *Analytical Chemistry*. American Chemical Society, 36(4), pp. 706–723. doi: 10.1021/ac60210a007.

[29]. Elgrishi N, Rountree K, McCarthy B, Roantree S, Eisnharrt T, Dempsey J. (2017) '*A Practical Beginner's Guide to Cyclic Voltammetry*'J. Chem. Educ. 2018, 95, 197−206

[30]. Marken, F., Neudeck, A. and Bond, A. M. (2005) 'Cyclic Voltammetry', in *Electroanalytical Methods*. Berlin, Heidelberg: Springer Berlin Heidelberg, pp. 51–97. doi: 10.1007/978-3-662-04757-6_4.

[31]. Gosser D. K, (2006). 'Cyclic Voltammetry; Simulation and Analysis of Reaction Mechanisms, *Synthesis and Reactivity in Inorganic and Metal-Organic Chemistry*. Taylor & Francis Group , 24(7), pp. 1237–1238. doi: 10.1080/00945719408001398.

[32]. Mamuru S.A. (2011). 'SECTION A CHAPTER 2 Introduction' University of

Pretoria.

[33]. Spiegel, C. (2017) *Techniques for Measuring Fuel Cell Resistance*. Available at: https://www.fuelcellstore.com/blog-section/techniques-for-measuring-fuel-cell-resistance (Accessed: 17 April 2019).

[34]. Latorrata, S. Pesato, R. Stampino, P.G. Cristiani, C. Dotelli, G. (2018) 'Use of Electrochemical Impedance Spectroscopy for the Evaluation of Performance of PEM Fuel Cells Based on Carbon Cloth Gas Diffusion Electrodes', *Journal of Spectroscopy*. Hindawi, 2018, pp. 1–13. doi: 10.1155/2018/3254375.

[35]. Ciureanu M. and Roberge, R. (2001) 'Electrochemical Impedance Study of PEM Fuel Cells. Experimental Diagnostics and Modeling of Air Cathodes'. American Chemical Society . doi: 10.1021/JP003273P.

[36]. GAMRY (2010) 'Basics of Electrochemical Impedance Spectroscopy', *Application Note AC*, (1), pp. 1–17. doi: 10.1152/ajpregu.00432.2003.

[37]. Rieger, P. H. (1994) *Electrochemistry*. Dordrecht: Springer Netherlands. doi: 10.1007/978-94-011-0691-7.

[38]. BardA. J.(1994) 'Electroanalytical Chemistry', Marcel Dekker, New York pp.13

[39]. Subramanian, A. and Rodriguez-Saona, L. (2009) 'Fourier Transform Infrared (FTIR) Spectroscopy', *Infrared Spectroscopy for Food Quality Analysis and Control*, (July 2009), pp. 145–178. doi: 10.1016/B978-0-12-374136-3.00007-9.

[40]. Education, W. P.-J. of C. and 1986, undefined (no date) 'Fourier transform-infrared spectroscopy: Part l. Instrumentation', *ACS Publications*. Available at: https://pubs.acs.org/doi/pdf/10.1021/ed063pA5 (Accessed: 21 April 2019).

[41]. Saptari, V. (2004) *Fourier transform spectroscopy instrumentation engineering*. Available at: https://books.google.co.za/books?hl=en&lr=&id=G0JDJedNuOIC&oi=fnd&pg=PR11&dq=V.+Saptari,+Fourier-Transform+Spectroscopy+Instrumentation+Engineering,+SPIE+Publication,+Bellingham,+2003&ots=Gjbhs8kvzw&sig=jw6IySOiFb9oKBmy9yH0raOS3c0 (Accessed: 21 April 2019).

[42].Nicolet, T. and All, C. (2001) 'Thermogavimetric Analysis', 199(1), pp. 1–8.

[43]. *Infrared and FTIR spectroscopy Instrument* (no date). Available at: http://delloyd.50megs.com/MOBILE/infrared_spectroscopy.html (Accessed: 21 April 2019).

[44]. *Using FTIR Spectrometer* (no date). Available at: http://faculty.sdmiramar.edu/fgarces/LabMatters/Instruments/FTIR/FTIR_Operations/index.html (Accessed: 21 April 2019).

CHAPTER 4

RESULTS AND DISCUSSION I

This chapter will focus on analyzing the results obtained from various characterization techniques performed on the synthesized catalysts of Palladium on multi walled carbon nanotubes (Pd/MWCNT), Palladium nickel on multi walled carbon nanotubes (PdNi/MWCNT), Palladium tin on multi walled carbon nanotubes (PdSn/MWCNT) and Palladium on carbon (Pd/C) as the commercial catalyst. The various characterizations help determine the various properties exhibited by these synthesized nanoparticles.

4.1 FUNCTIONALIZATION OF MWCNTS

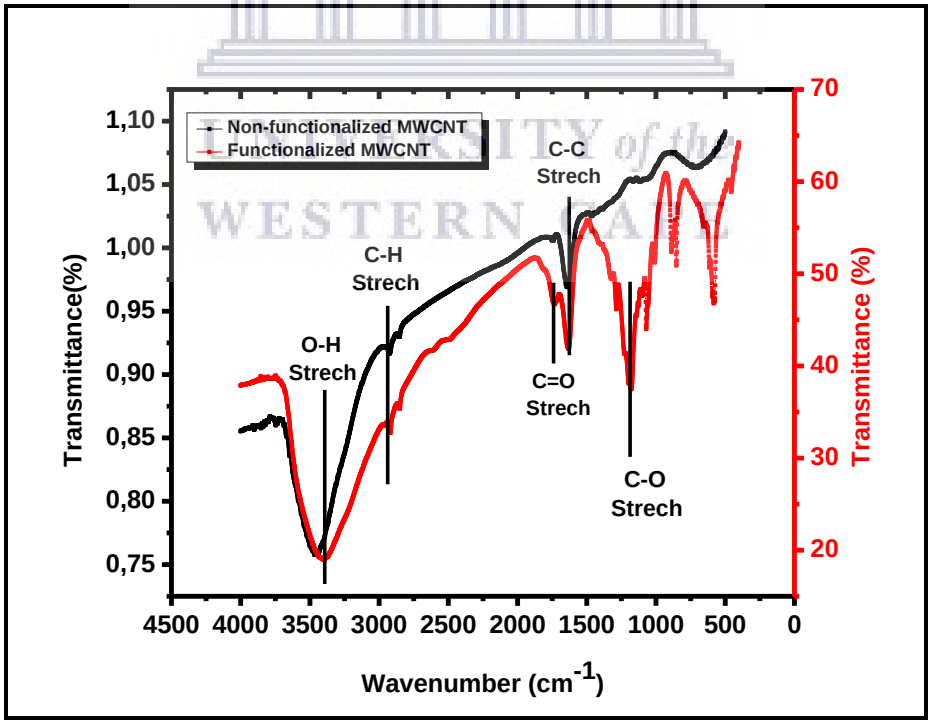

Figure 4. 1: FTIR of Functionalized MWCNTs with COOH

The functionalization of the MWCNTs nanoparticles was analyzed through Fourier transform infra-red spectroscopy **(**FTIR**)**. The vibration bands obtained from the spectra of the functionalized MWCNTs showed related vibrational bands characteristic of carboxylic groups on MWCNTs. FTIR spectra from the MWCNTs show a broad peak at ~ 3425 cm^{-1} in figure 4.1 above which can be assigned to the O–H stretch from carboxylic groups (O=C−OH and C−OH). The higher intensity of the peak at 3425 cm^{-1} indicated the high degree of covalent functionalization of MWCNTs by liquid phase oxidation using H_2SO_4/HNO_3 mixture. The peak at 2921 cm^{-1} can be associated with the C−H stretch from aromatic carbon nanotubes structure. The peak at 1736 cm^{-1}, associated with the stretch mode of carboxylic groups C=O as observed in the IR spectrum of the acid-treated MWCNTs indicating that carboxylic groups are formed due to the oxidation of some carbon atoms on the surface of the MWCNTs by nitric acid. The peak at 1640 cm^{-1} is related to the −C−C− stretch in a ring (aromatic) and the peak at 1185 cm^{-1} is associated with C−O stretch of carboxylic group. The overall peaks found in the spectrum are ν (O-H) (3750-3250 cm^{-1}), ν (C-H) (3000-2750 cm^{-1}), ν (C=O) (1760-1650 cm^{-1}), ν (C-C) (1600-1550 cm^{-1}) and ν (C-O) (1350-900 cm^{-1}). These vibrations are in good agreement with the spectrum of carboxylic groups on MWCNTs as reported by Atieh, M. A. *et al*. [1]

4.2 STRUCTURAL CHARACTERIZATION

Structural characterization of the synthesized catalysts was done using a variety of powerful techniques such as HR-TEM and SAXS.

4.2.1 INTERNAL STRUCTURE

The internal structure of the synthesized nanoparticles was evaluated by high resolution transmission electron microscope (HRTEM). The inner shape of the synthesized catalysts is unclear additionally the images show that catalysts they may be agglomerated with the exception of Pd/C and they have small particle size.

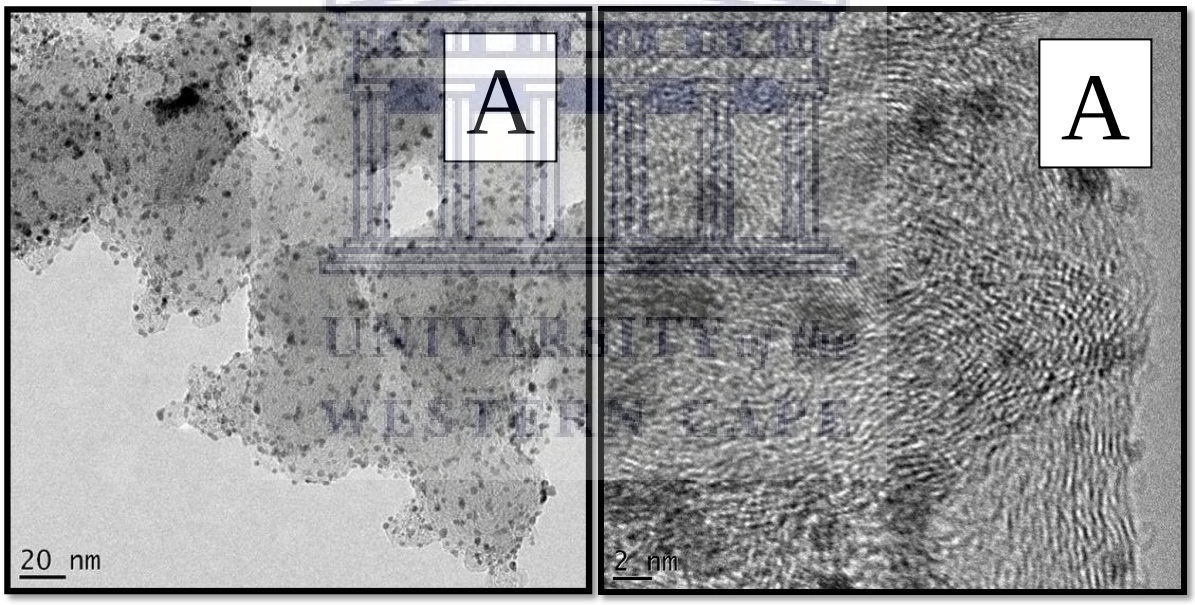

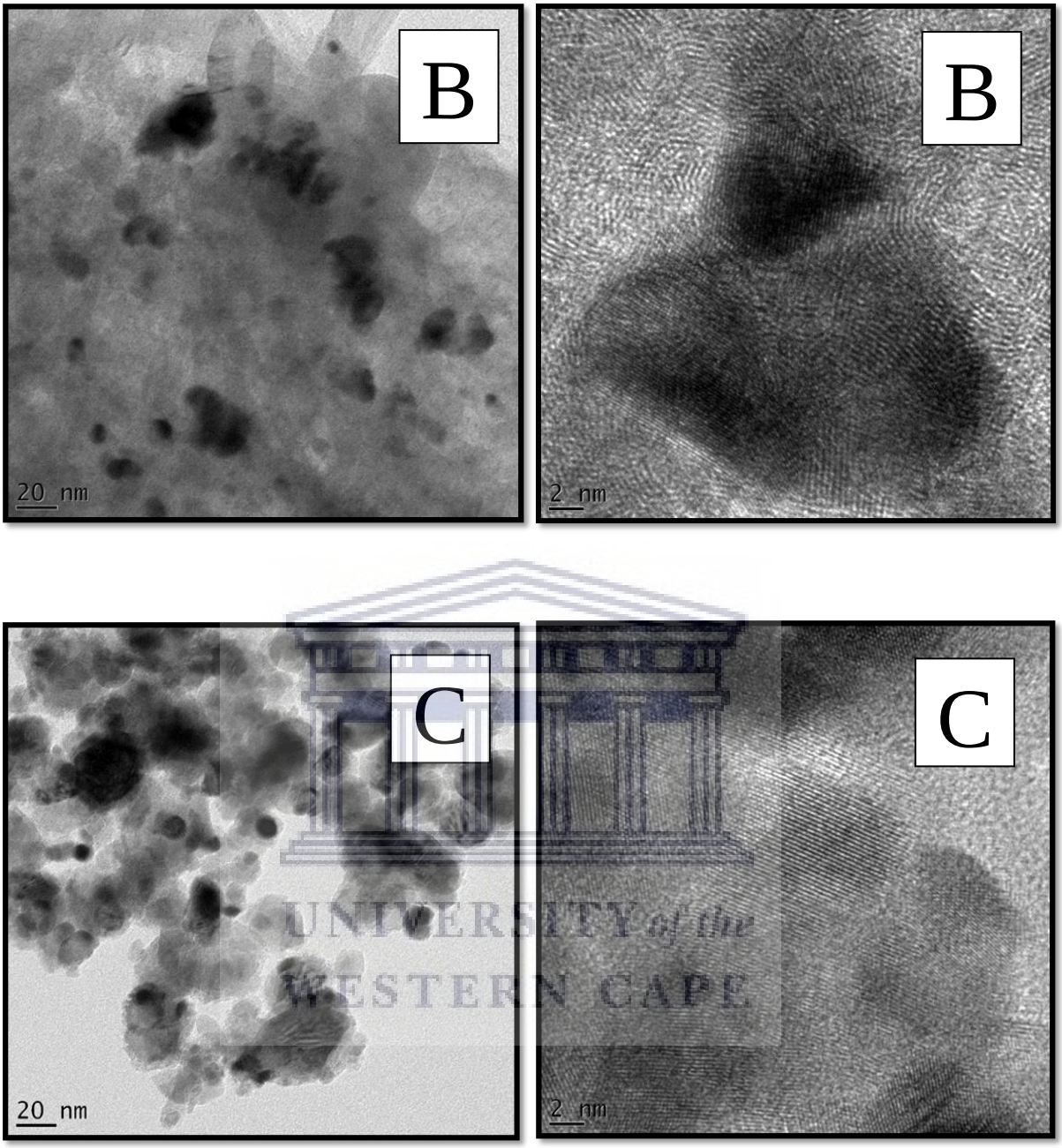

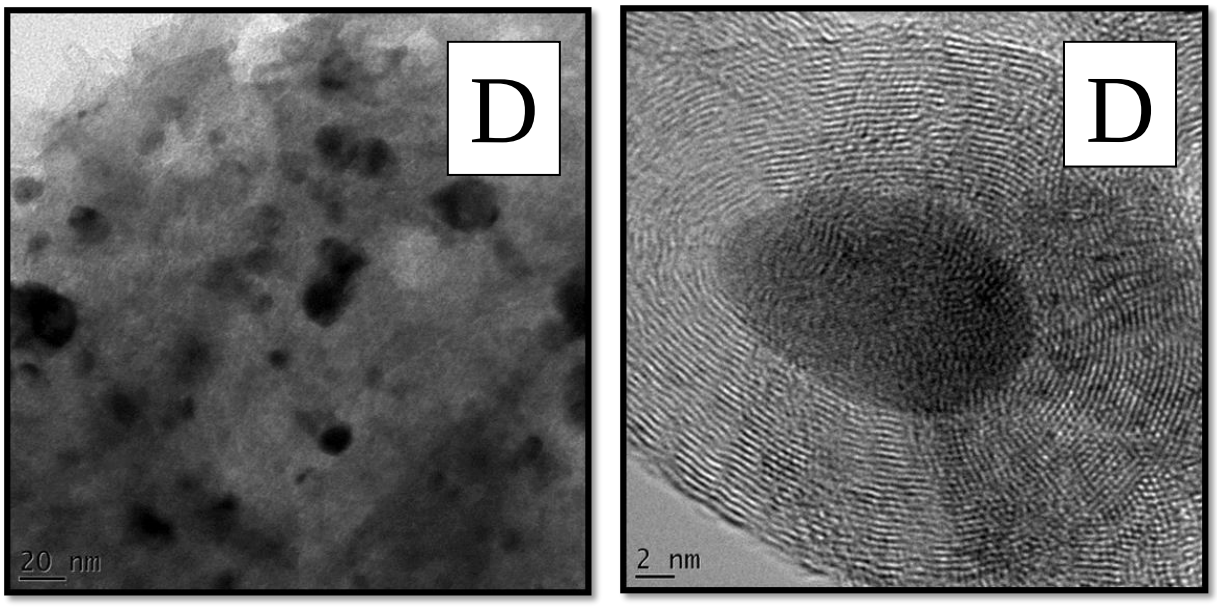

Figure 4. 2: HR-TEM images of the synthesized catalyst of (A) Pd/C (commercial), (B) Pd/MWCNT, (C) PdNi/MWCNT and (D) PdSn/MWCNT at low and high magnifications

Images B-D of figure 4.2 above compare the particle distribution of the catalysts Pd/MWCNT, PdNi/MWCNT and PdSn/MWCNT at low and high magnification. At low magnification the catalysts showed agglomeration on the MWCNT surface and at high magnification the d-spacing values of the four catalysts was calculated. Pd/C is 0.277 nm at 111 plane, Pd/MWCNT is 0.23 nm at 111 plane, PdNi/MWCNT is 0.186 nm at 220 plane and PdSn/MWCNT is 0.301 nm at 202 plane.

Small Angle X-ray Scattering (SAXS) is a technique that can be used to determine the internal structure of the synthesized catalysts. From the plot of the shape analysis it shows that the catalysts Pd/MWCNT, PdNi/MWCNT and PdSn/MWCNT were agglomerated as they have broad peaks. While Pd/C, Pd/MWCNT and PdNi/MWCNT had a core and a shell, with PdSn/MWCNT having a dumbbell shape. The shape obtained for the catalysts are illustrated in the table 4.1 below and plots can be seen in figure 4.3 below.

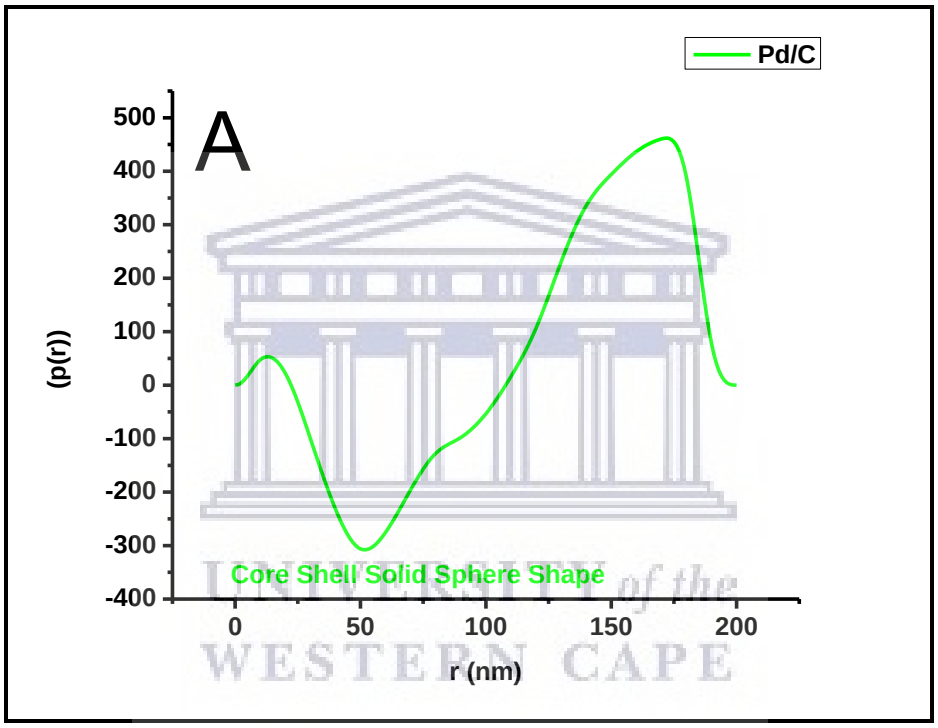

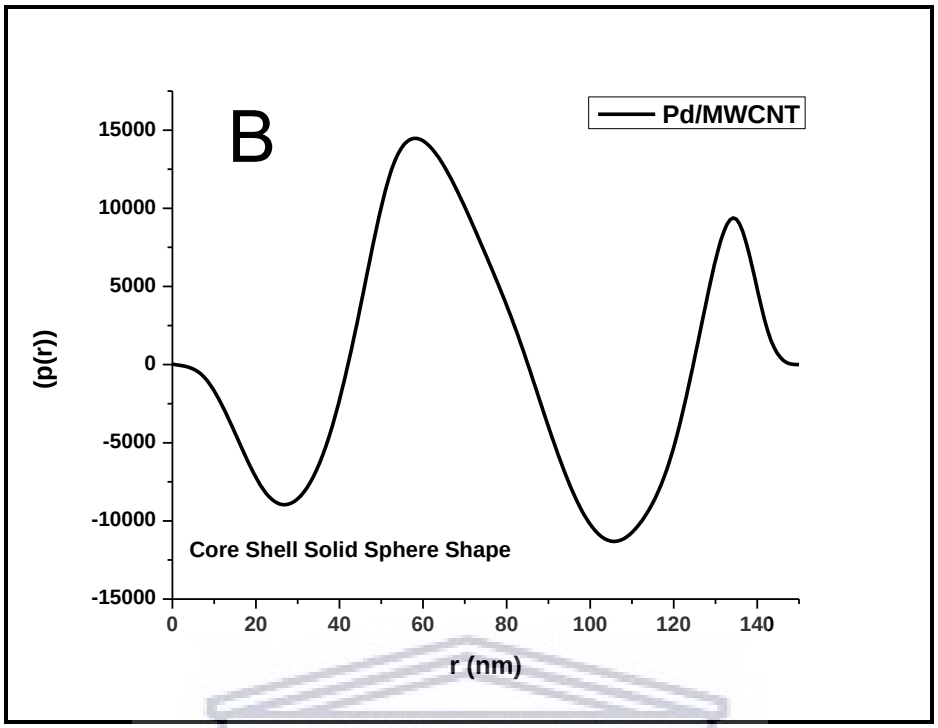

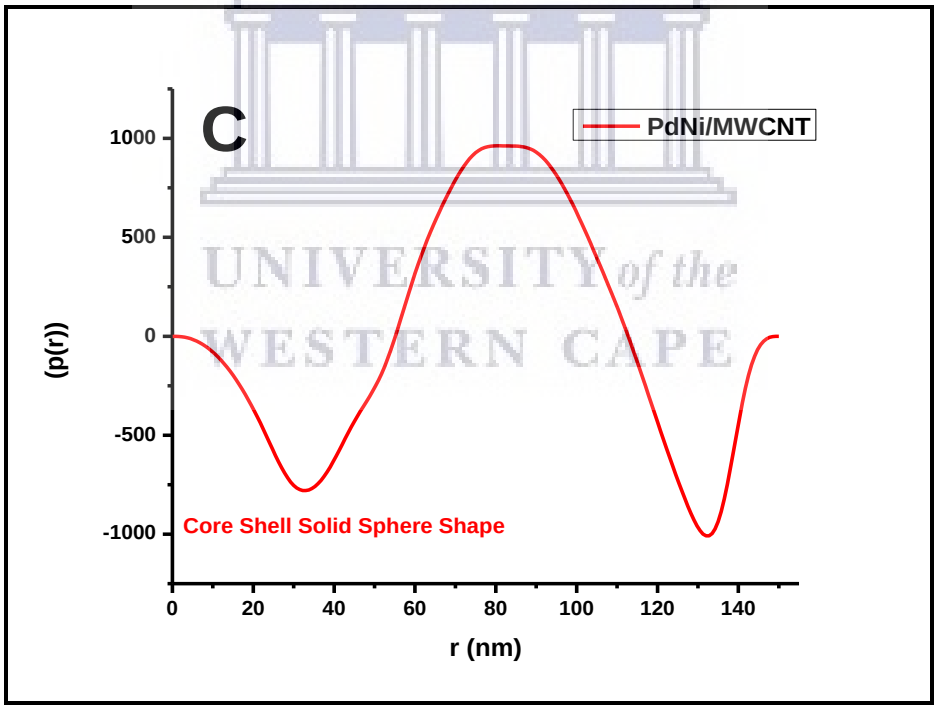

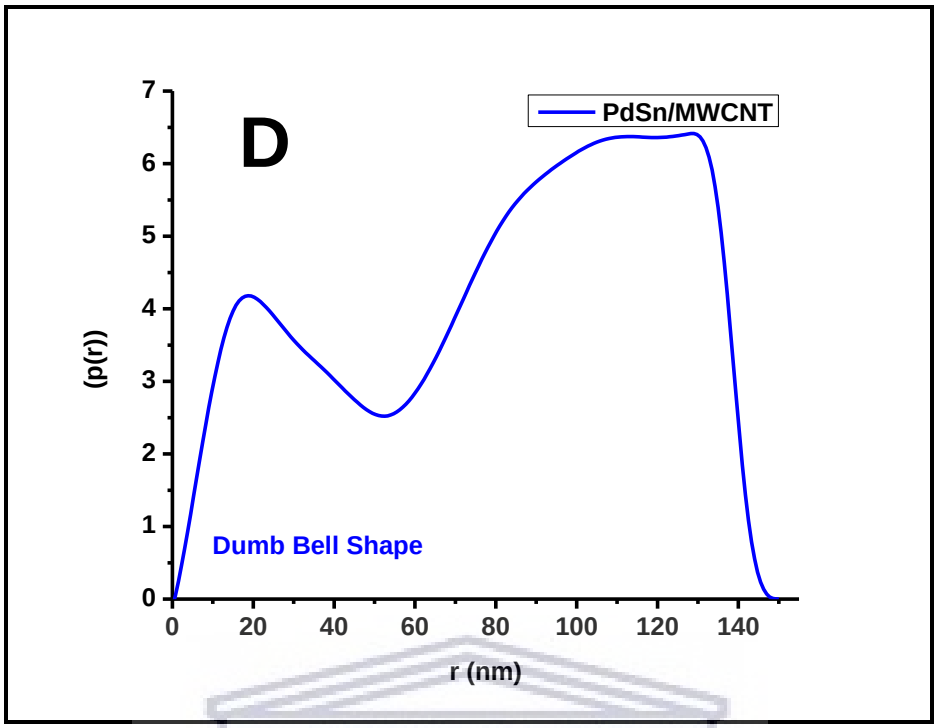

Figure 4. 3: SAXS plot of the shapes of the synthesized catalysts of (A) Pd/C (commercial), (B) Pd/MWCNT, (C) PdNi/MWCNT and (D) PdSn/MWCNT.

Table 4. 1: Shapes of obtained catalysts form SAXS

Samples	Shapes
Pd/C	Core Shell Solid Sphere
Pd/MWCNT	Core Shell Solid Sphere
PdNi/MWCNT	Core Shell Solid Sphere
PdSn/MWCNT	Dumb Bell

The broad shoulder in PdNi/MWCNT seen in the SAXS plot above indicate agglomeration of the catalysts as evident in HRTEM images in figures 4.2.

4.3 PHASE COMPOSITION (CRYSTALLINITY)

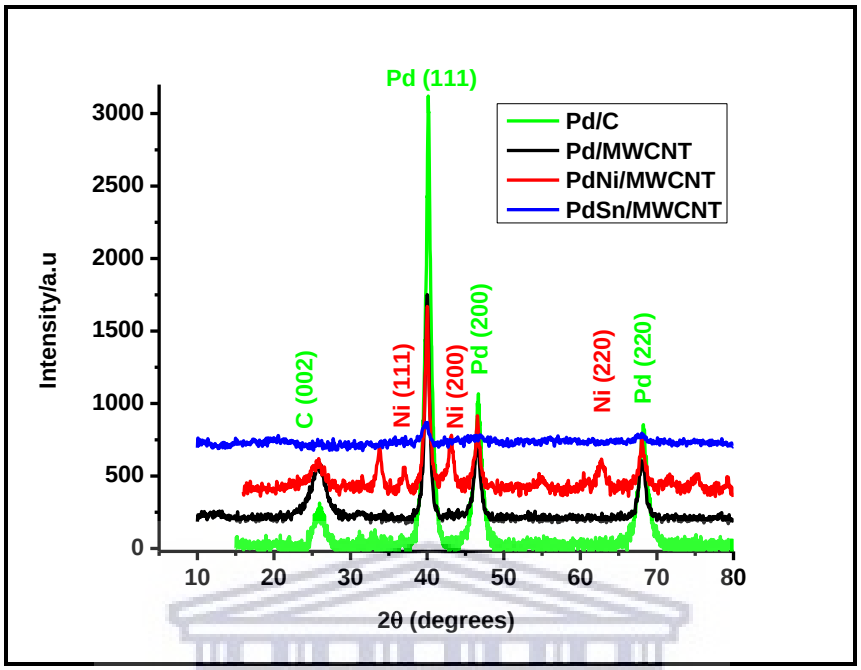

Figure 4. 4: XRD plot of the synthesized catalysts of Pd/C, Pd/MWCNT, PdNi/MWCNT and PdSn/MWCNT

The phase composition and crystalline structure of the synthesized nanoparticles were investigated through powder X-ray diffraction (XRD). The XRD patterns in figure 4.4 showed broad Bragg peaks indicative of small particle size. The catalysts of Pd/C (JCPDS 00-026-1076), Pd/MWCNT (JCPDS 00-046-1043) and PdNi/MWCNT (JCPDS 00-047-1049) showed a face-center cubic phase [6], while PdSn/MWCNT (JCPDS 00-082-0723) showed a tetragonal phase [2].

The peaks at 40.1 º , 46.7 º and 68.1 º can be assigned to (111), (200), and (220) for reflection of Pd/MWCNT with Pd/C having the same peaks. Meanwhile the peaks at 37.3 º , 43.3 º and 62.9 º are assigned to (111), (200) and (220) indexes of NiO in PdNi/MWCNT, then the peaks at 40.1 º , 46.7 º and 68.1 º can be assigned to (111), (200), and (220) indexes of Pd in PdNi/MWCNT (with an unlabeled peaks which cannot be indexed to any known phase that is due to PdO). Lastly the peaks at 39.1 º , 44.3 º ,

64.4 are assigned to (111), (200) and (220) indexes for Pd in PdSn/MWCNT, a slight shift is observed for the Pd peaks in PdSn/MWCNT as compared to Pd/MWCNT peaks. Peak shift indicates that there was alloying between Pd and Sn. The peaks at 47.8 º and 67.3 º can be assigned to (002), and (202) for reflection Sn in PdSn/MWCNT.

These peaks were also confirmed by the diffraction obtained from selected area electron diffraction (SAED) in figure 4.5 below. The crystallinity of the nanoparticles can also be seen from the spectrum which shows the nanoparticles to be polycrystalline. This is also an observable trend seen in SAED micrograph obtained from HR-TEM analysis. The images obtained shows that PdNi/MWCNT was more crystalline than Pd/MWCNT, PdSn/MWCNT and Pd/C in that order.

The planes found in XRD plot above was also observed in the SAED image obtained, which confirms the phase composition of the synthesized catalysts. The images obtained from SAED analysis, shows that PdNi/MWCNT was more crystalline than Pd/MWCNT and PdSn/MWCNT in that order.

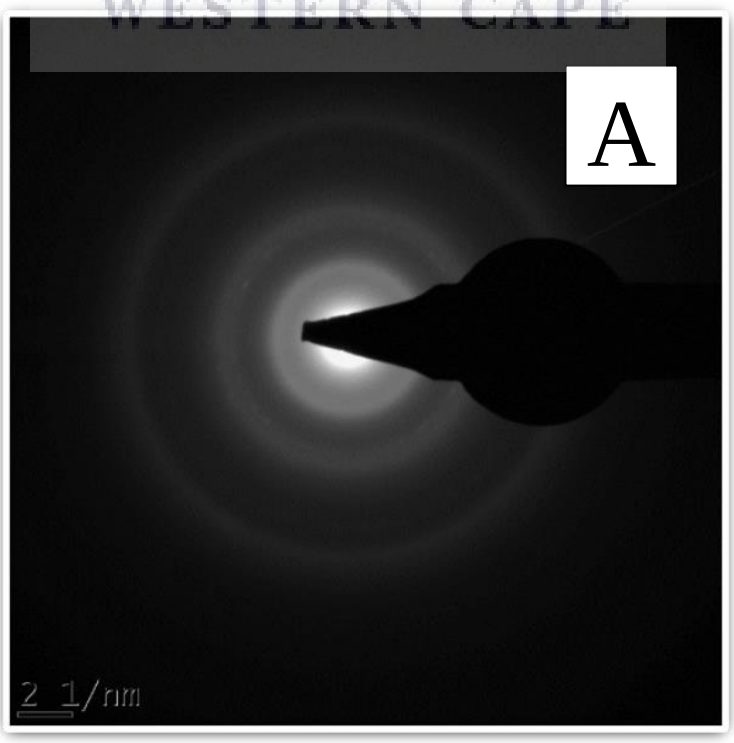

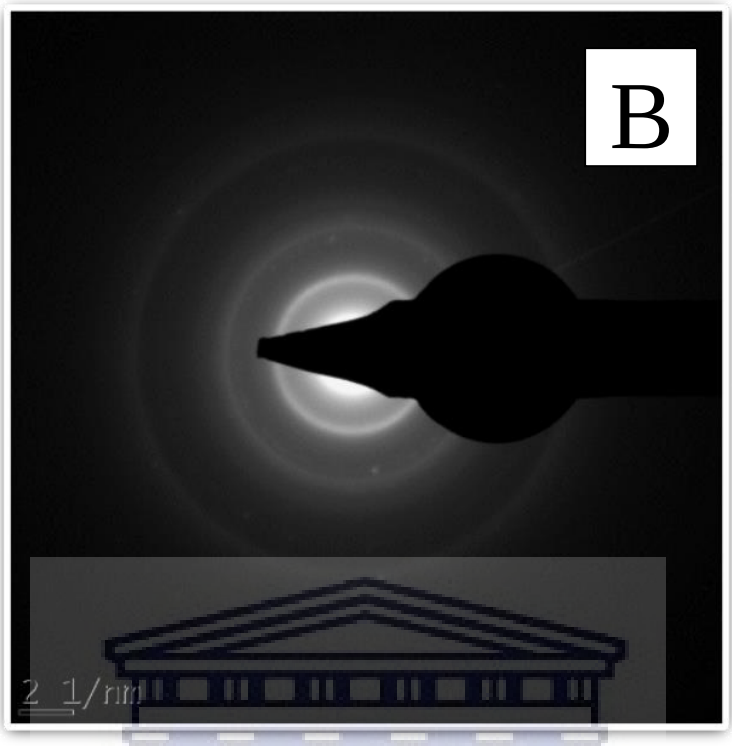

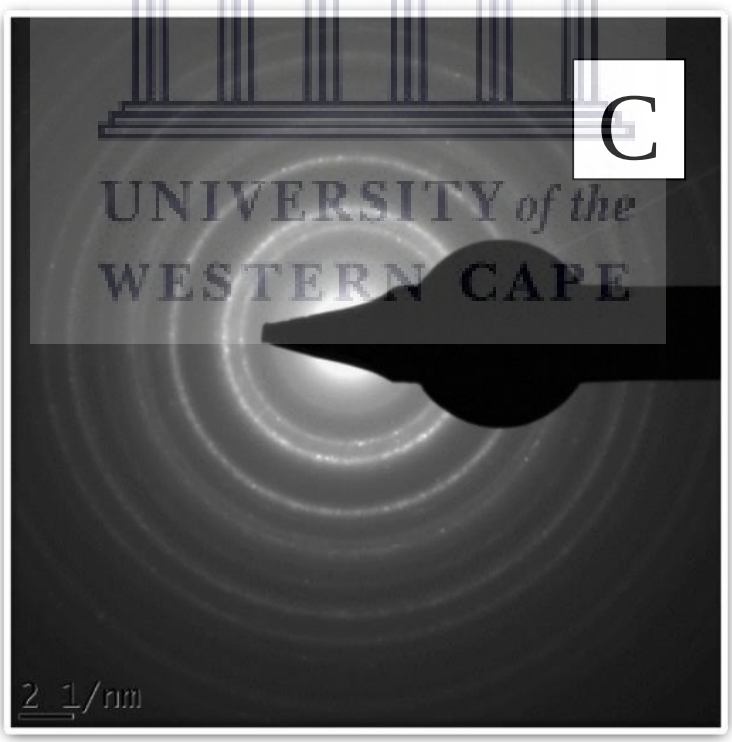

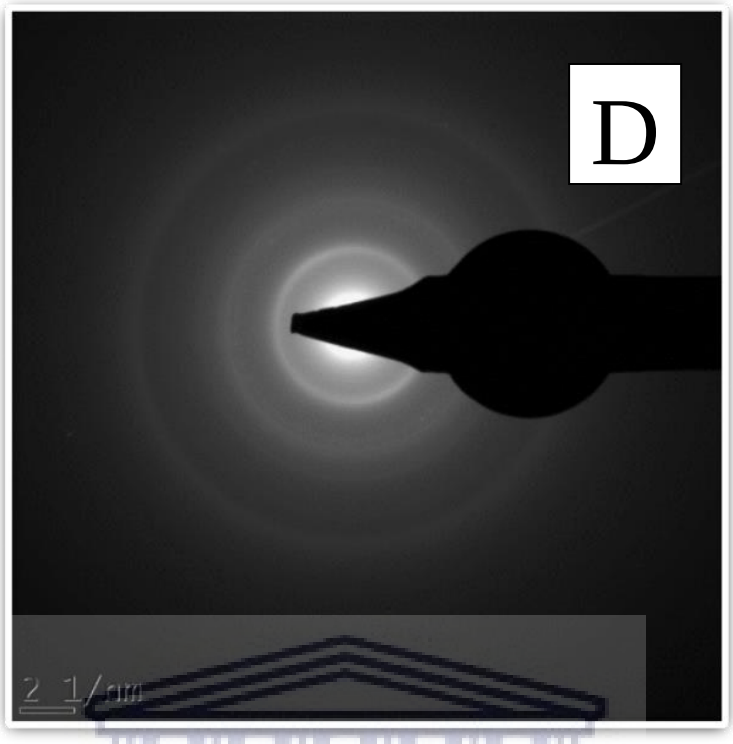

Figure 4. 5: SAED images of the synthesized catalysts of (A) Pd/MWCNT, (B) Pd/MWCNT (C) PdNi/MWCNT and (D) PdSn/MWCNT

The lattice fringe images obtained for the synthesized nanoparticles further confirms that the nanoparticles were crystalline and the d-spacing value of the lattice fringes was evaluated and assigned with the corresponding plane (miller index) as can be seen in figure 4.2 above confirming the hkl miller index (planes) found in XRD.

4.4 ELEMENTAL COMPOSITION

The elemental composition of the synthesized catalysts was evaluated using Energy Dispersive X-ray spectroscopy (EDX) and Inductively Couple Plasma (ICP). EDX was used to confirm the elements in the synthesized catalysts as shown in figure 4.6 and table 4.3 respectively. The instruments used are EDS analyzer coupled into the High-Resolution Transmission Electron Microscope used for HR-TEM analysis and ICP analyzer used techniques for the determination of trace concentrations of elements in samples.

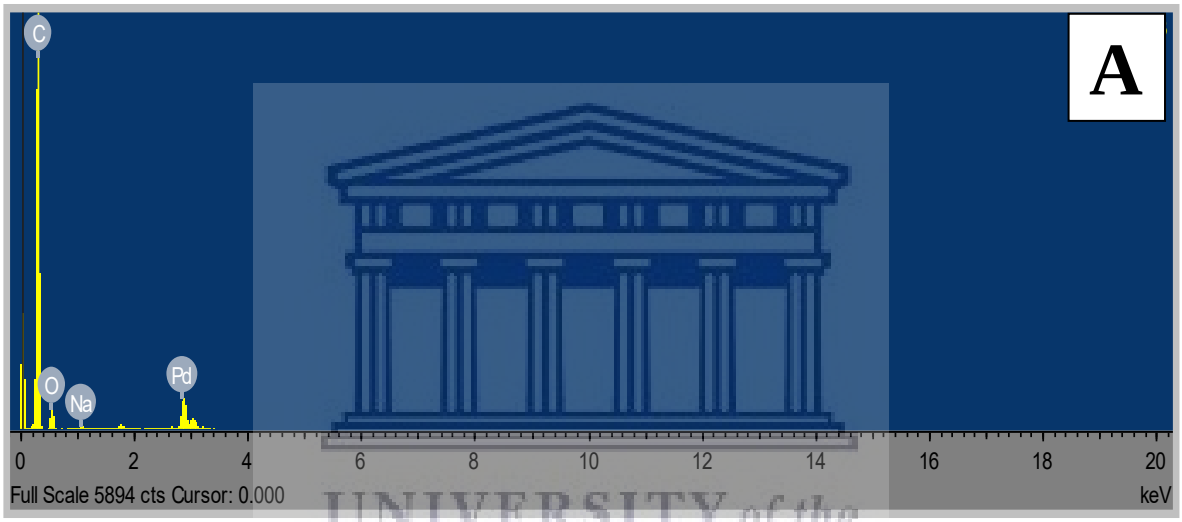

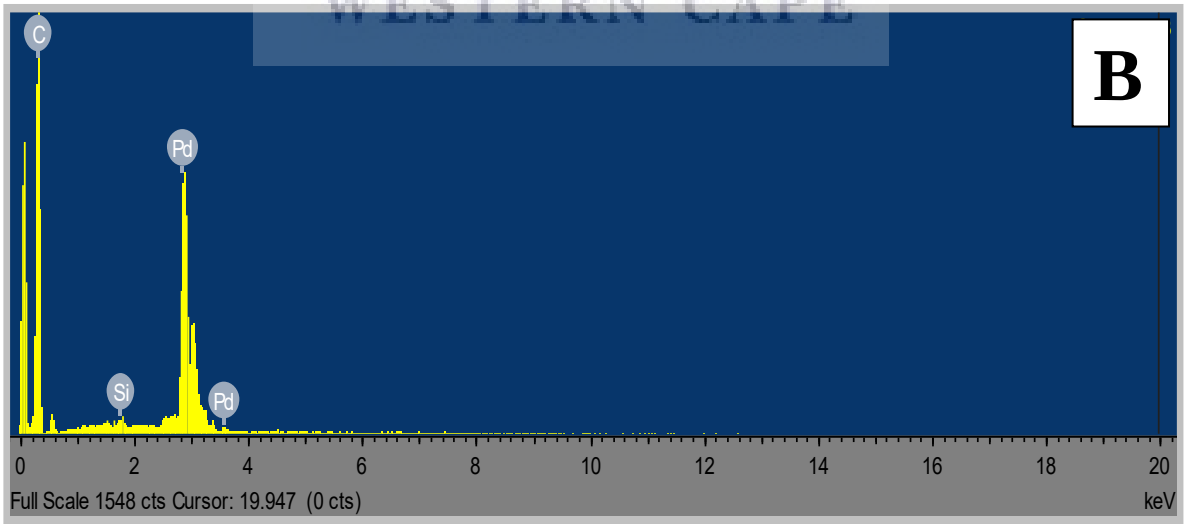

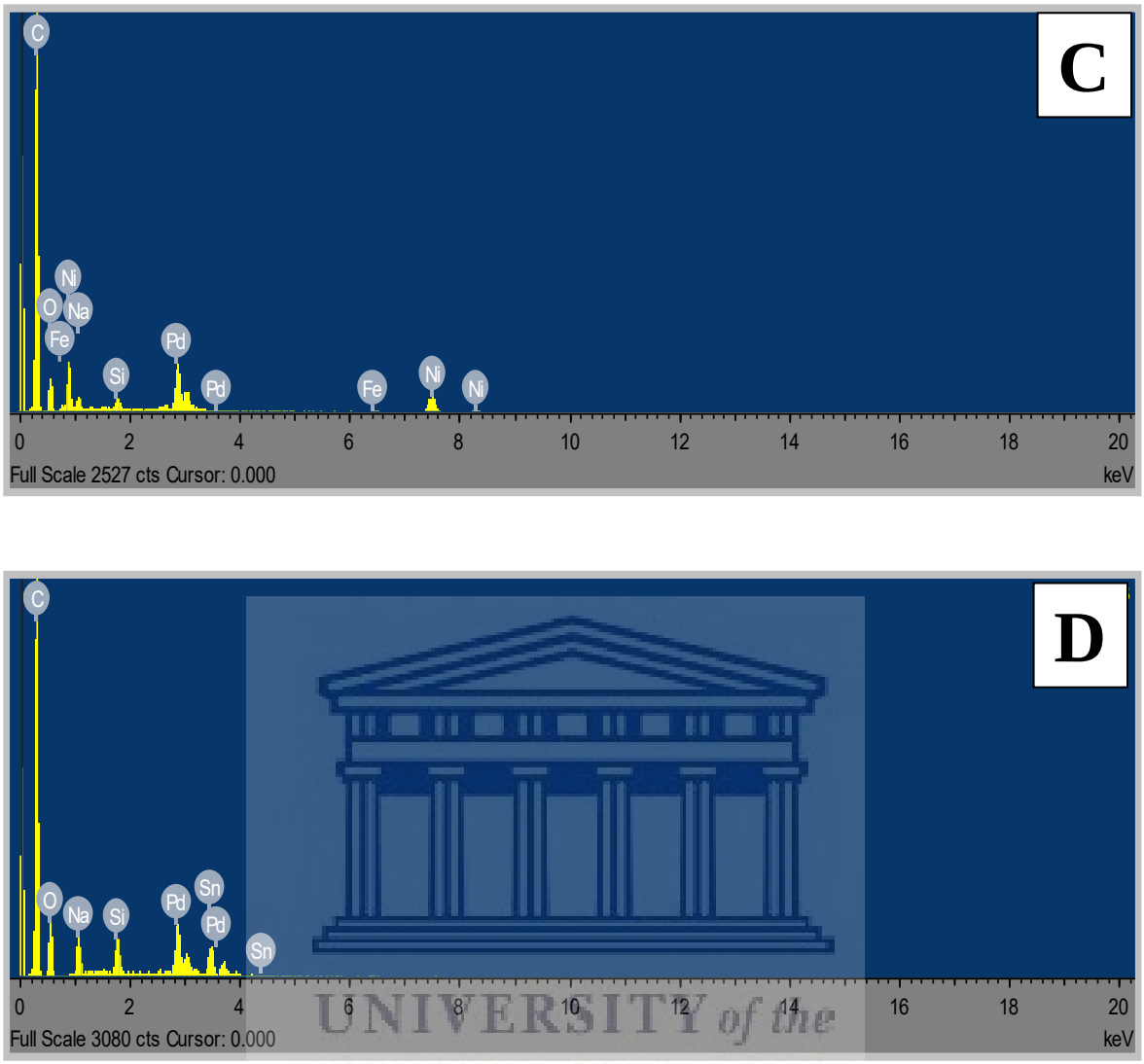

Figure 4. 6 : EDS plots of the synthesized catalysts of (A) Pd/MWCNT, (B) Pd/MWCNT (C) PdNi/MWCNT and (D) PdSn/MWCNT

The EDS of the catalysts showed all the elements expected for the nanoparticles. Pd/MWCNT spectra shows the presence of palladium and carbon. PdNi/MWCNT spectra shows the presence of palladium, nickel and carbon. PdSn/MWCNT spectra also showed the presence of palladium, tin and carbon.

Table 4. 2: ICP data of the catalysts

	Pd	Ni	Sn
Pd/C	190.07 mg/L	X	X
Pd/MWCNT	63.2 mg/L	X	X
PdNi/MWCNT	63.7 mg/L	72.5 mg/L	X
PdSn/MWCNT	70.8 mg/L	X	97.8 mg/L

Pd/C showed the most presence of palladium with a value of 190.07 mg/L. The palladium values for Pd/MWCNT and PdNi/MWCNT catalysts are relative the same at 63.2 mg/L and 63.7 mg/L respectively, while for PdSn/MWCNT its 70.8 mg/L. The nickel and tin values are 72.5 mg/L and 97.8 mg/L respectively.

4.5 SIZE DISTRIBUTION

The size distribution of the synthesized catalysts was studied and evaluated. The particle size was evaluated using SAXS and HR-TEM, while the crystal size was evaluated from XRD data of the synthesized catalysts. The summary of the size distribution for the synthesized nanoparticles is given by the SAXS plot of the size distribution and HR-TEM average particle.

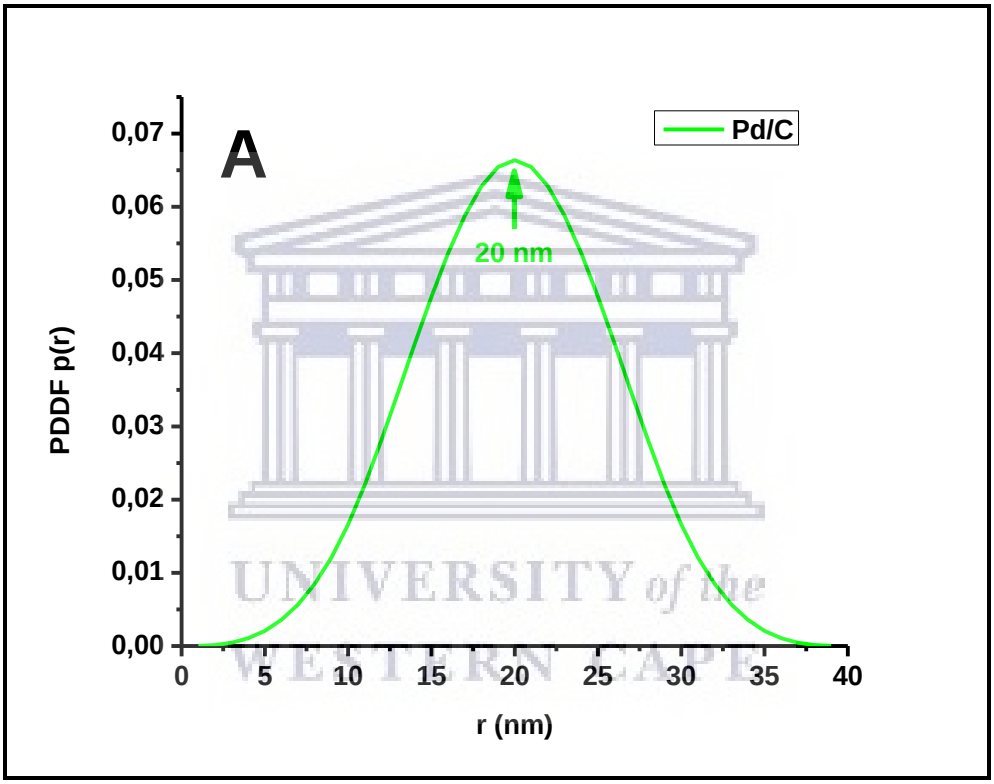

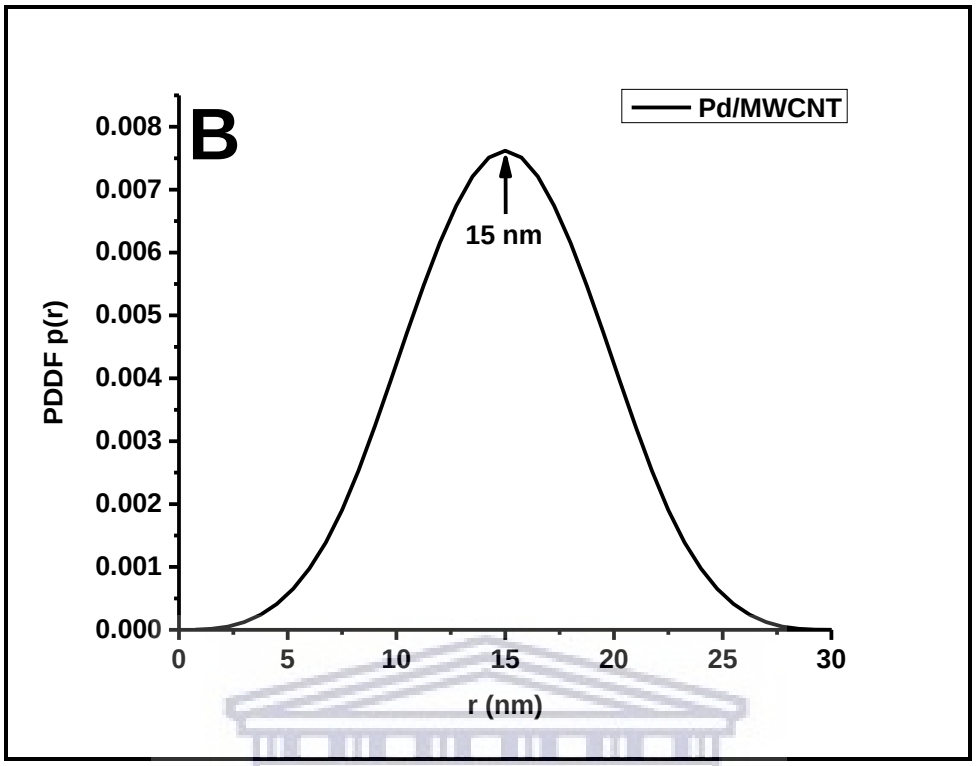

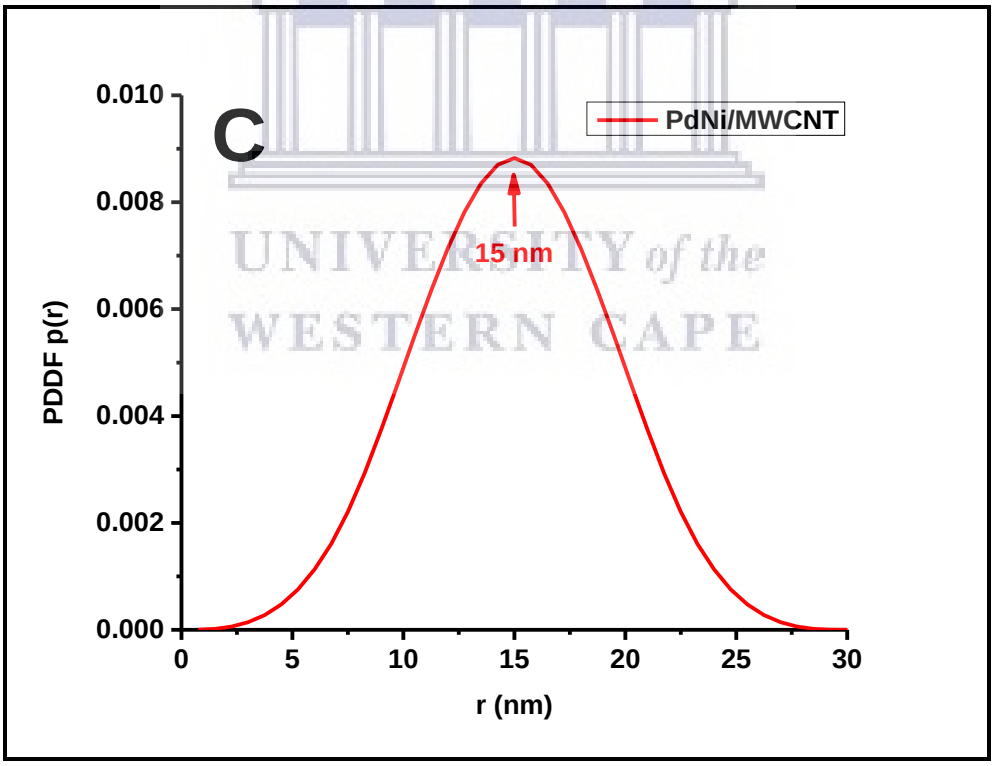

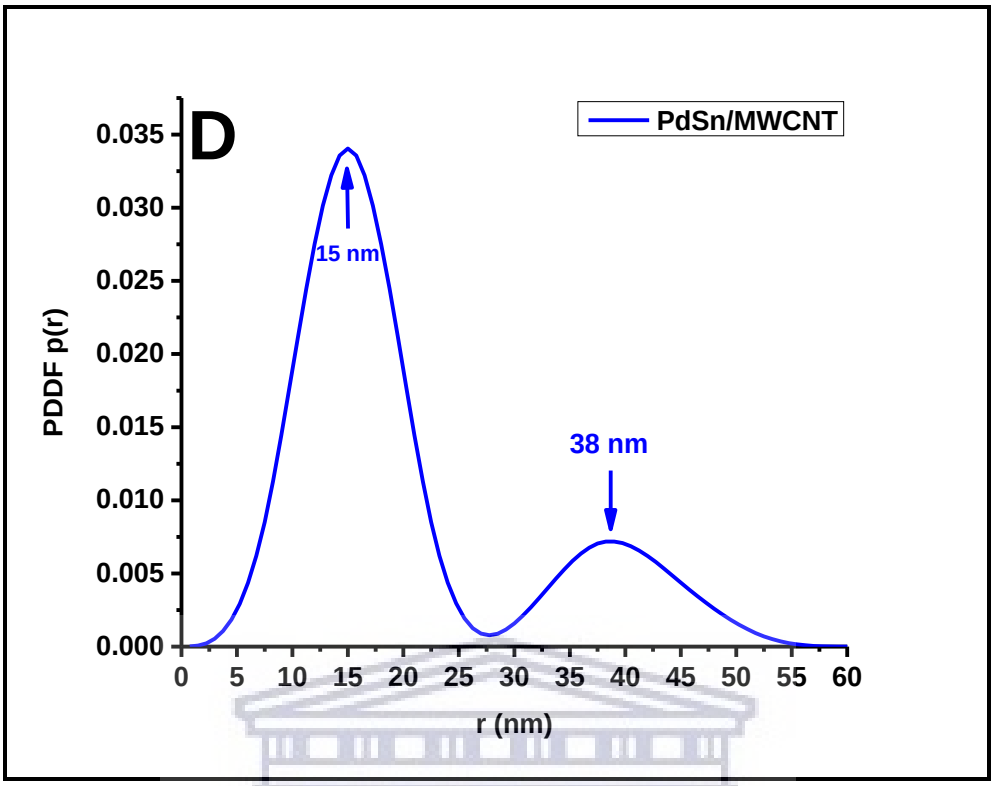

Figure 4. 7: SAXS plot of size distribution of the synthesized catalysts of (A) Pd/C, (B) Pd/MWCNT, (C) PdNi/MWCNT and (D) PdSn/MWCNT.

The particle size distribution obtained from SAXS plot shows that Pd/C has a mean particle size of 20 nm while Pd/MWCNT and PdNi/MWCNT has a mean particle size of 15 nm shown in figures 4.7. PdSn/MWCNT also has a mean particle size of 15 with a big particle size of 38 nm which is attributed to the agglomeration which can be seen in the SAXS shape plot and HR-TEM images form earlier in figure 4.2.

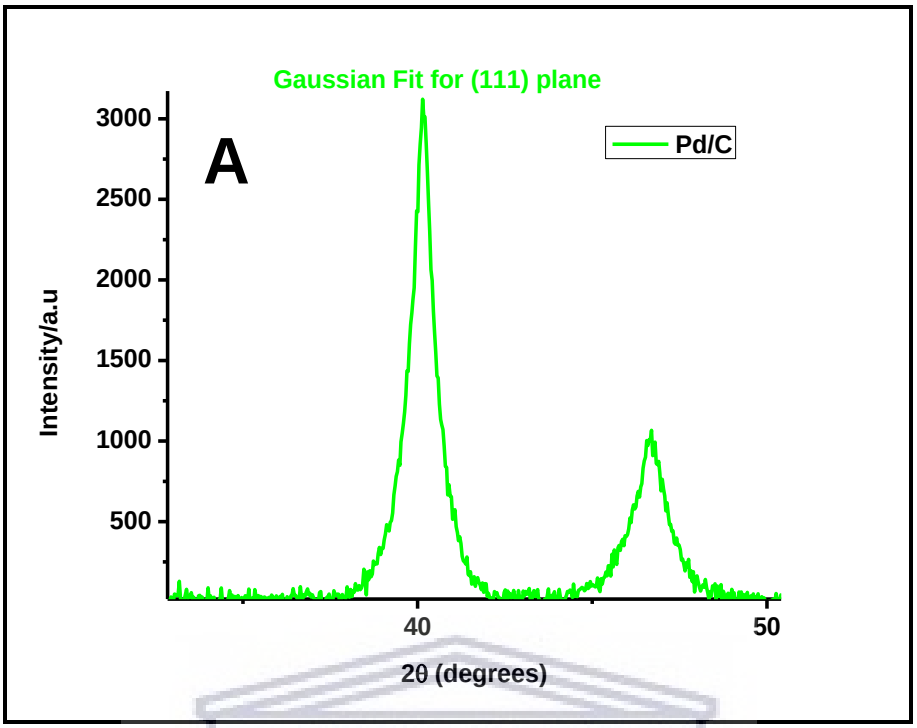

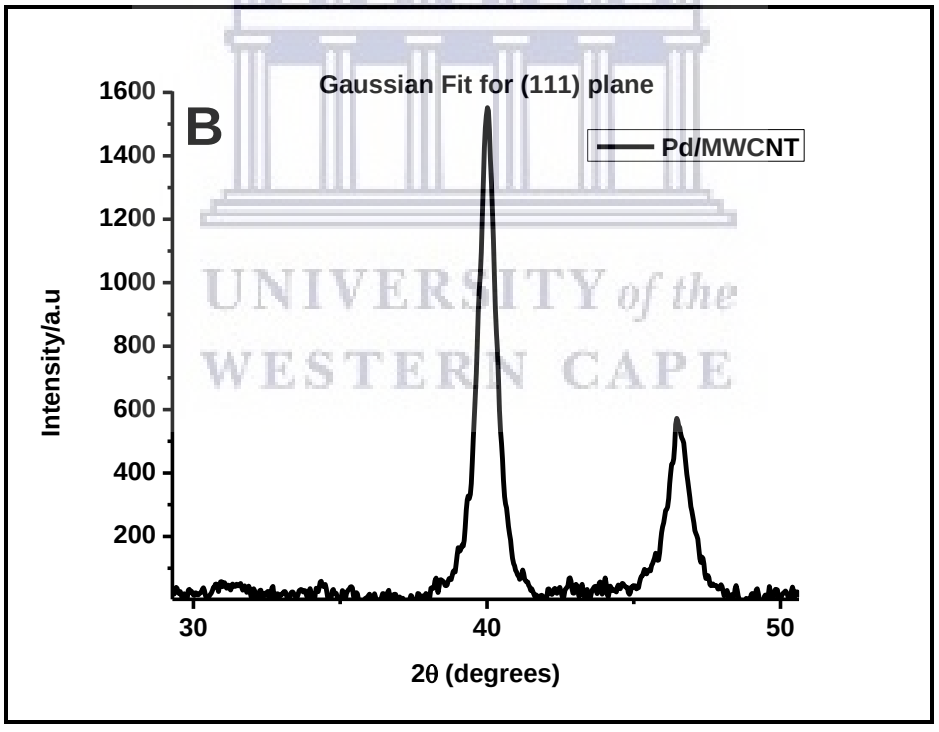

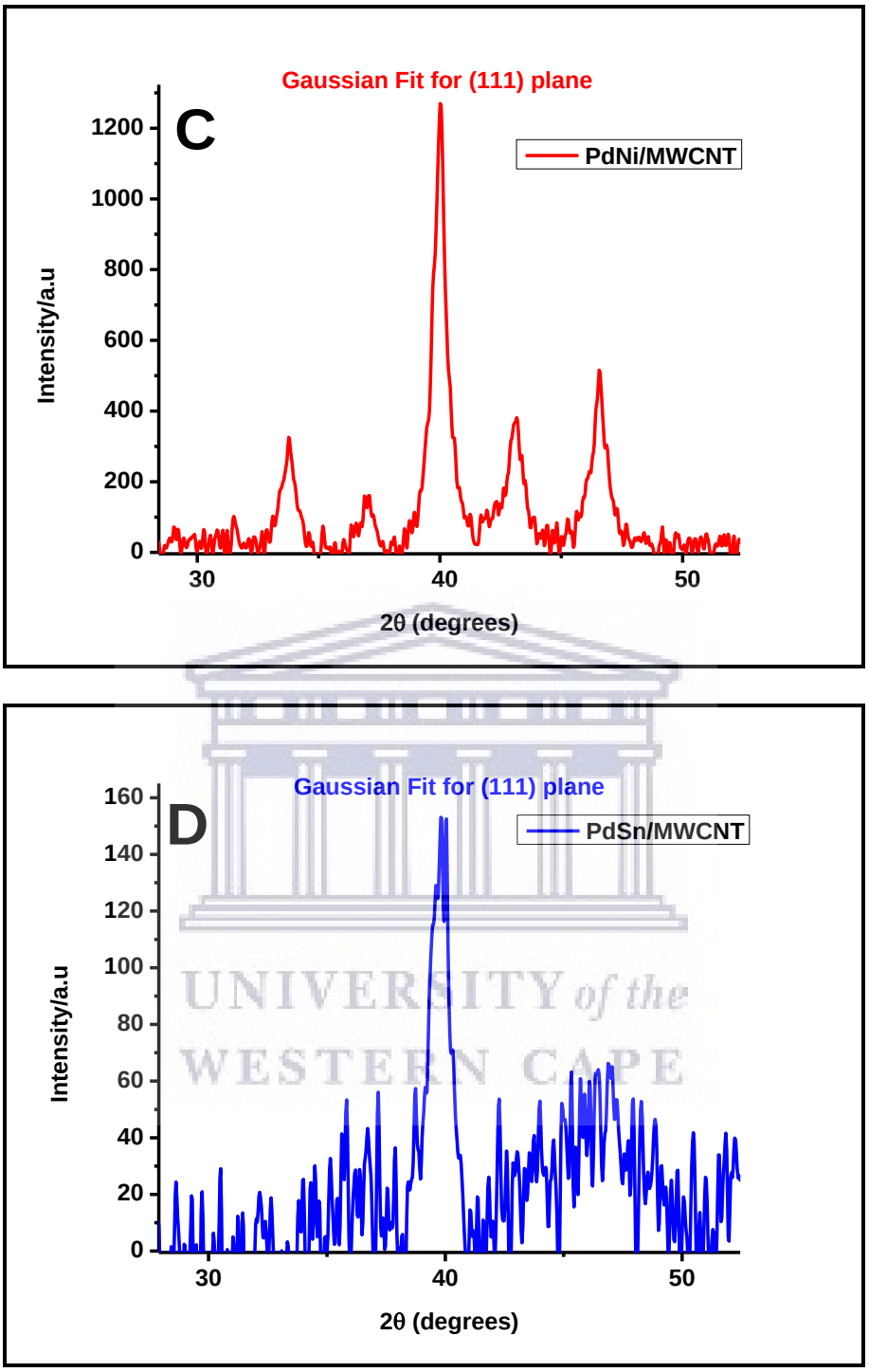

Figure 4. 8: XRD plot of Gaussian Fit for (111) plane for crystal size calculation of the catalysts of (A) Pd/C, (B) Pd/MWCNT, (C) PdNi/MWCNT and (D) PdSn/MWCNT.

The Debye-Scherrer equation was used to calculate the crystal size and the equation is given as:

$$d = \frac{k\lambda}{B2\theta Cos\theta} \quad (4.1)$$

Where $B_{2\Theta}$ is full width at half maximum, *k* is Scherrer constant which can take values from 0.9 to 1, for this calculation I chose to use 0.9, λ is the wavelength of the x-ray which has a value of 1.540598 in Angstroms, and θ is the angle. Plus, the FWHM value is converted to radians. The plane calculated was the (111) which had the most intense peak. Table 4.4 below gives the various data points acquired to make the calculations.

Table 4. 3: XRD data of Gaussian Fit for (111) plane for crystal size calculation.

	2Θ	Θ	FWHM	FWHM (radians)	Crystallite Size (nm)
Pd/C	40.14327	20.07163	1.00427	0.01752	8.4
Pd/MWCNT	40.00846	20.00423	0.76689	0.01338	11.0
PdNi/MWCNT	39.99229	19.99615	0.74359	0.01297	11.4
PdSn/MWCNT	39.84054	19.92027	0.89039	0.01554	9.5

From the table above, the crystal size for Pd/C is 8.4 nm, Pd/MWCNT is 11.0 nm, PdNi/MWCNT is 11.4 nm and PdSn/MWCNT is 9.5 nm. These values are in close proximate with the values obtained from SAXS plot of the particle size distribution of the synthesized nanoparticles which had value for Pd/MWCNT, PdNi/MWCNT and PdSn/MWCNT as 15 nm.

HR-TEM images were also used to calculate particle size of the catalysts as can be seen below in the histogram plots. The particle size obtained for the catalysts is summarized in plots below.

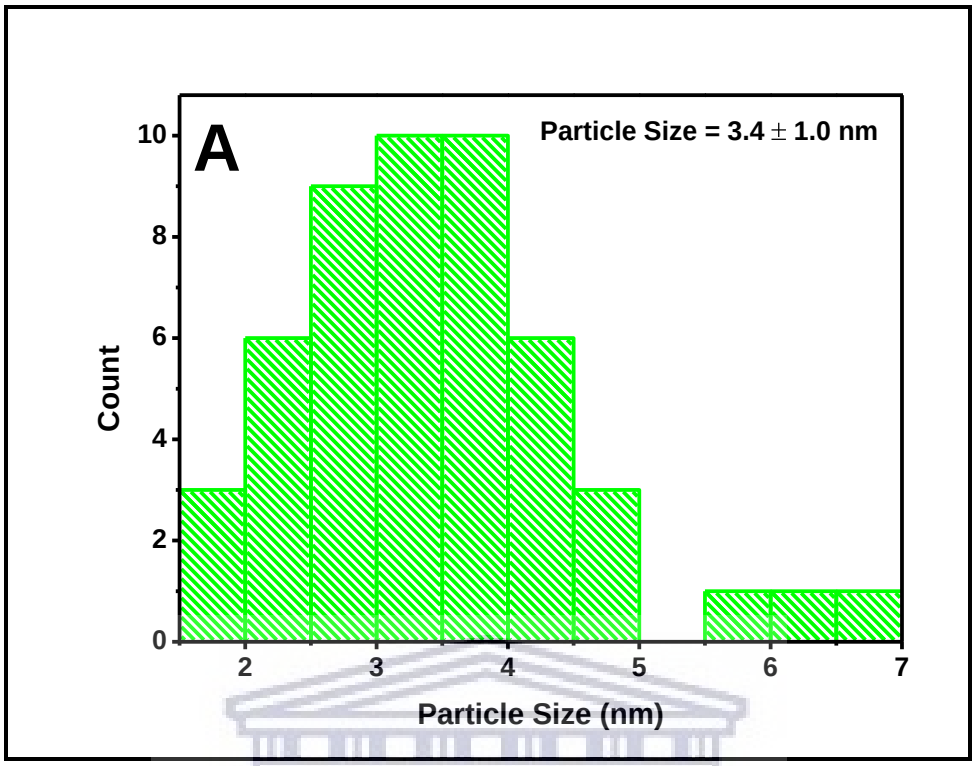

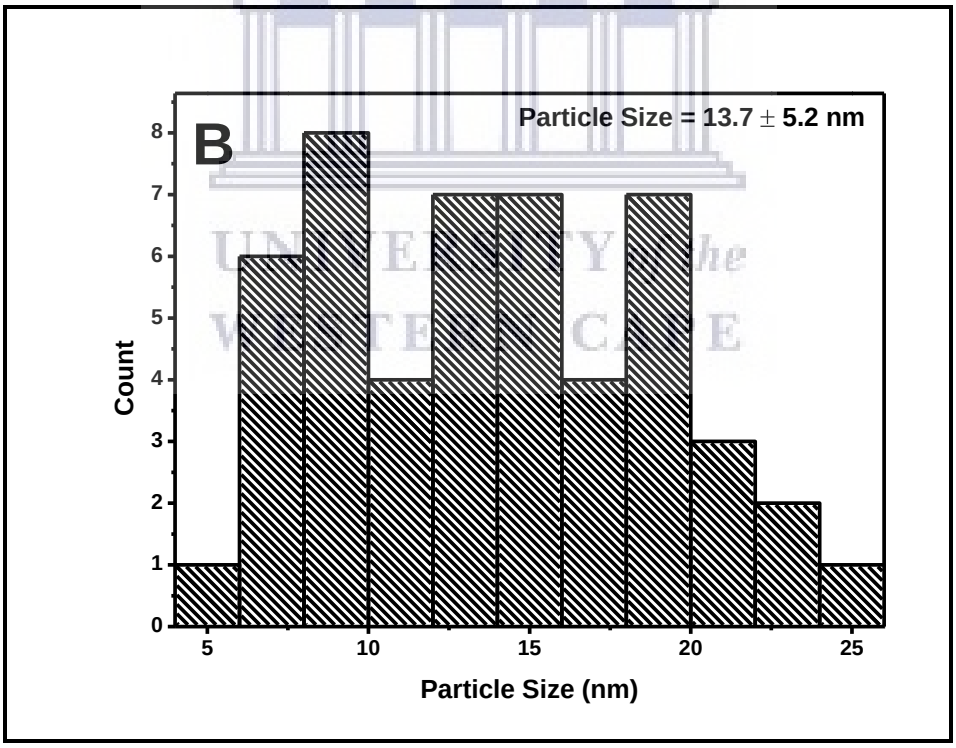

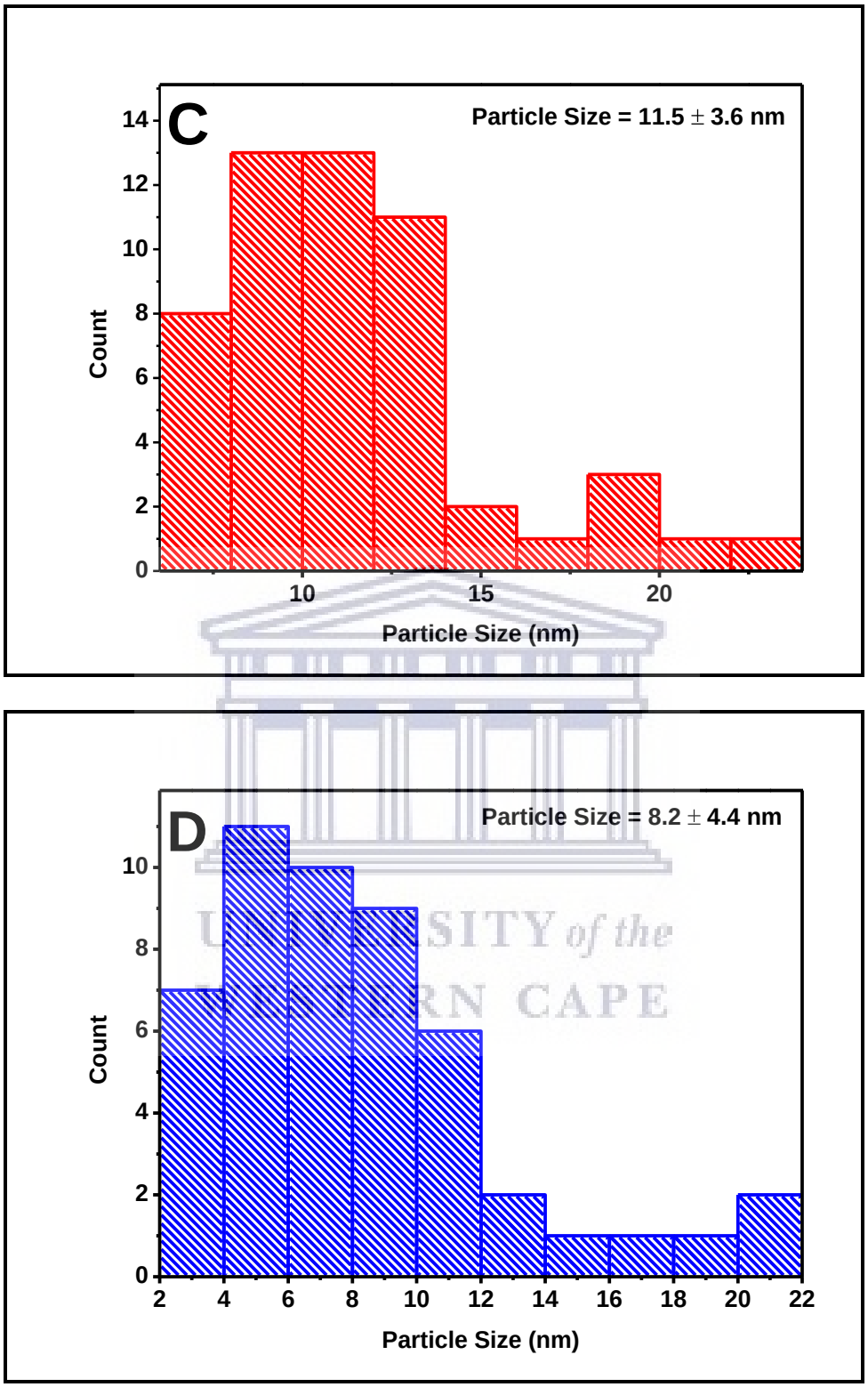

Figure 4. 9: Mean particle size plots from HR-TEM images of the synthesized catalysts of (A) Pd/C, (B) Pd/MWCNT, (C) PdNi/MWCNT and (D) PdSn/MWCNT

From the plots above, the particle size for Pd/C is 3.4 nm with a standard deviation of ± 1.0 nm [3], Pd/MWCNT is 13.7 nm with a standard deviation of ± 5.2 nm, PdNi/MWCNT is 11.5 nm with a standard deviation of ± 3.6 nm and PdSn/MWCNT is 8.2 nm with a standard deviation of ± 4.4 nm. These values above are summarized in the table below with values obtained from XRD and SAXS.

Table 4. 4: SAXS, XRD and HR-TEM particle size summary data

	SAXS (nm)	XRD (nm)	HR-TEM (nm)
Pd/C	20	8.4	3.4
Pd/MWNCT	15	11.0	13.7
PdNi/MWCNT	15	11.4	11.5
PdSn/MWCNT	15	9.5	8.2

4.6 ELECTROCHEMISTRY OF THE NANOPARTICLES

The electrochemical properties of the synthesized nanoparticles were investigated by the following electrochemical techniques:

• Cyclic Voltammetry (CV)

• Linear Sweep Voltammetry (LSV)

• Electrochemical Impedance spectroscopy (EIS)

• Chonoamperometry (CA)

The electroactivity of the synthesized catalysts was investigated through cyclic voltammetry using 1M KOH as electrolyte and 1M Glycerol as the alcohol. The potential window used for the investigation is -1.2 V to +0.8 V. The synthesized catalysts that were investigated were Pd/C (commercial), Pd/MWCNT, PdNi/MWCNT and PdSn/MWCNT. A three-electrode system comprising of working electrode, counter electrode and reference electrode was used. The working electrode used was glassy-carbon electrode while the counter electrode was platinum electrode and the reference electrode used was Ag/AgCl saturated in KCl.

4.6.1 CYCLIC VOLTAMMETRY AND LINEAR SWEEP VOLTAMMETRY

4.6.1.1 INVESTIGATION OF THE ECSA

A large electro-chemical surface area indicates a better electrode, as more catalyst sites are available for electro-chemical reactions. It is reported that the performance degradation of DGFC is largely owed to the electrochemical active surface area loss of the electrodes. The decrease in the electrochemical active surface area mainly results from the growth of palladium alloy nanoparticles size, the dissolution of palladium and/or other palladium

alloy nanoparticles from the carbon support material. This results in poor durability of the fuel cell catalyst and, accordingly, the fuel cell system.

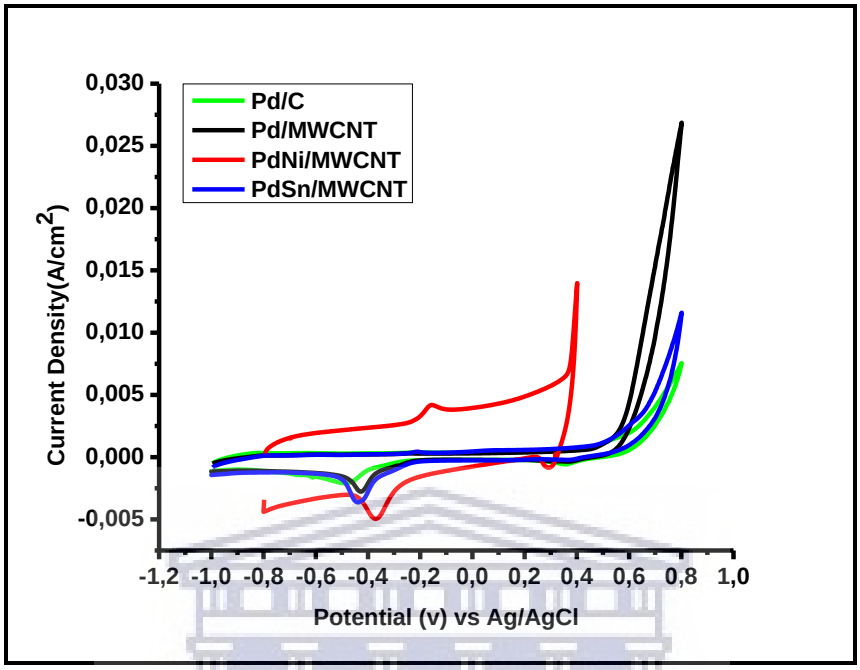

Figure 4. 10: Presents cyclic voltammograms of the synthesized electrocatalyst supported on MWCNTs compared to Pd/C commercial electrocatalyst in 1M KOH @ 30mV/s.

Figure. 4.10 compares the electrochemical responses of Pd/C (commercial), Pd/MWCNT, PdNi/MWCNT and PdSn/MWCNT in 1.0 M KOH without the presence of glycerol, measured in the potential range between -1.2 and 0.8 vs Ag/AgCl. The typical voltammetric curve of Pd in alkaline media was observed the electrochemical active surface area (ECSA) of Pd/C (commercial), Pd/MWCNT, PdNi/MWCNT and PdSn/MWCNT catalysts was then calculated. As this analysis is conducted under alkaline environment it can be found that the onset of the oxide formation and the peak potential of the oxide reduction for PdSn/MWCNT shifted to more negative potentials which exhibit the chemisorption of OH on the Pd at a negative potential.

The Electrochemical Active Surface Area (ECSA) was calculated from the density of charge associated to the reduction of a full monolayer of Pd oxides [4]. This area was then

converted into the effective active surface area by using the factor 420μC.cm^{-2} for the monolayer of Pd Oxides. The results were collected and presented in Table 4.6 below. All ECSA calculations for this study were done following equation 4.6 given below:

$$ECSA = \frac{QH-adsorption\ (c)}{420\ \mu C.cm^{-2}.(L_{Pd}).(Ag)} \quad (4.6)$$

Q_H = is the charge area from $Pd_{(reduction)}$ peak; 420μC.cm^{-2} is the charge of full coverage for clean polycrystalline Pd and is used as the conversion factor; L_{Pd} is the working electrode Pd loading (μg.cm^{-2}); and Ag is the geometric surface area of the glassy carbon electrode (i.e. 0.196 cm^{-2}). The values for ECSA are reported in m^2.g^{-1}.

Table 4. 5: XRD, HR-TEM and SAXS particle size summary data with ECSA

Catalysts	Particle Size (nm)			ECSA (m^2.g^{-1})
	XRD	HR-TEM	SAXS	
Pd/C	8.4	3.4	20	0.72
Pd/MWCNT	11.0	13.7	15.0	0.75
PdNi/MWCNT	11.4	11.5	15.0	4.8
PdSn/MWCNT	9.5	8.2	15.0	0.85

The table above displays the obtained data of ECSA for the synthesized catalysts, with PdNi/MWCNT having the larges ECSA followed by PdSn/MWCNT, Pd/MWCNT and Pd/C respectively. This is attributed to the smaller metal particles for PdNi/MWCNT and PdSn/MWCNT with a better distribution in comparison to Pd/MWCNT that is agglomerated due to growth of palladium alloy nanoparticles size as seen is TEM images in figures 4.2.

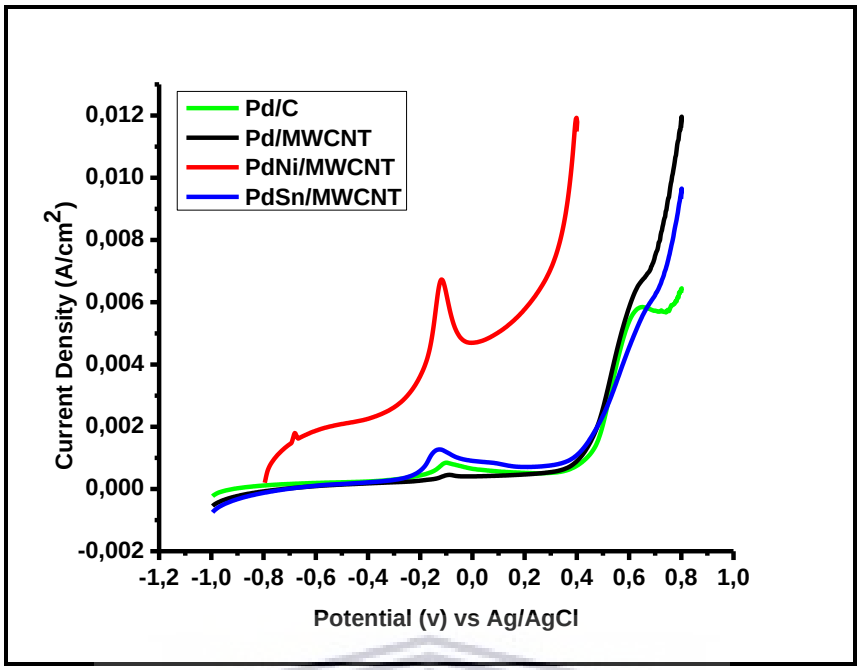

Figure 4. 11: Linear Sweep Voltammetry of the synthesized electrocatalyst supported on MWCNTs compared to Pd/C commercial electrocatalyst in 1M KOH + 1M Glycerol @ 30mV/s.

Figures 4.11 shows the LSV scans for Pd/C (commercial), Pd/MWCNT, PdNi/MWCNT and PdSn/MWCNT catalyst for glycerol oxidation in 1.0 M KOH solution containing 1.0 M glycerol in the potential range -1.2V to 0.8V. In these LSV scans, a peak is an indication of surface interaction or reaction between some species and catalyst. In the positive-going (forward scan), is attributed to the electrooxidation of glycerol on the catalysts. Between the four synthesized catalysts, the bimetallic catalyst which is PdNi/MWCNT shows the best performance towards glycerol oxidation in alkaline media followed by PdSn/MWCNT, Pd/C and Pd/MWCNT current density. The peak current density (If) for PdNi/MWCNT is 6.657 mA/cm^{-2} which is highest compared to PdSn/MWCNT 1.277 mA/cm^{-2}, Pd/C 0.8426 mA/cm^{-2} and Pd/MWCNT 0.4498 mA/cm^{-2} respectively [5]. The results in forward scan shows that the addition of a secondary metals (Ni and Sn) in Pd to form bimetallic catalyst can significantly improve the catalytic activity

of Pd for glycerol oxidation in alkaline media. This indicates, the significant enhancement oxidation kinetic activity for glycerol by addition of a secondary metal. However, Pd/C and Pd/MWCNT show high tolerance towards glycerol oxidation.

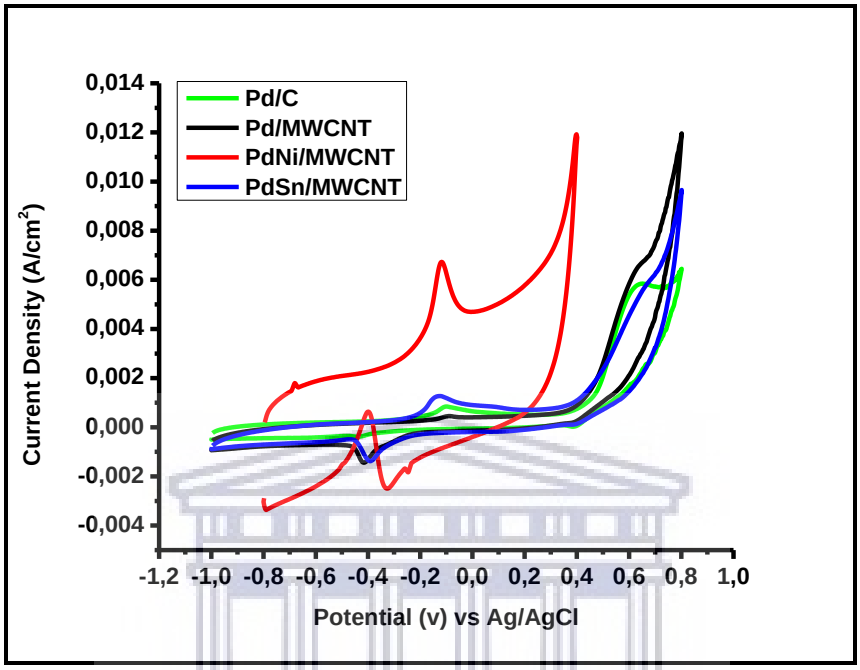

Figure 4. 12: Cyclic Voltammetry of the synthesized electrocatalyst supported on MWCNTs compared to Pd/C commercial electrocatalyst in 1M KOH + 1M Glycerol @ 30mV/s.

Glycerol is a complex molecule, due to this the oxidation of glycerol in alkaline medium can form numbers of possible oxide/hydrous or oxide/hydroxyl surface molecules. This is having been described in reduction wave [6]. Based on the previous study the major electrooxidation of glycerol by using Pd catalyst in alkaline media can be described as equation 4.2 – 4.5 follow [7];

$$Pd + OH^- \leftrightarrow Pd - [OH]_{ads} + e^- \quad (4.2)$$

$$Pd + C_2H_3OH{-}CH_2OH + 3OH^- \leftrightarrow Pd - [C_2H_3(OH)_2{-}CO]_{ads} + 3H_2O + 3e^- \quad (4.3)$$

$$Pd{-}[OH]_{ads} + Pd - [C_2H_3(OH)_2 - CO]_{ads} \rightarrow C_2H_3(OH)_2 - COOH + 2Pd \quad (4.4)$$

$$C_2H_3(OH)_2 - COOH + OH^- \rightarrow C_2H_3(OH)_2 - COO^- + H_2O \quad (4.5)$$

Figure 4.12 above explains the peaks which are the indication of surface interaction or reaction between some species and catalyst. In the positive-going (forward scan), is attributed to the electrooxidation of glycerol on the catalysts. Meanwhile, during the reverse scan there is a secondary oxidation peak which associated with incomplete oxidation of carbonaceous residues from the glycerol in forward scan. The actual performance glycerol oxidation in alkaline media has been summarized on Table 4.7 below.

Table 4. 6: Electrocatalytic properties of Pd/MWCNT, PdNi/MWCNT and PdSn/MWCNT catalysts for glycerol oxidation

	$E_{f(oxidation)}$ (mV vs Ag/AgCl)	$I_{f(oxidation)}$ (mA/cm^{-2})	$E_{r(reduction)}$ (mV vs Ag/AgCl)	$I_{r(reduction)}$ (mA/cm^{-2})	$\frac{I_f}{I_r}$
Pd/C	-101.4	0.8426	-440.1	-0.3959	2.13
Pd/MWCNT	-91.75	0.4498	-414.0	-1.446	0.31
PdNi/MWCNT	-119.7	6.657	-397.9	0.6102	10.91
PdSn/MWCNT	-127.1	1.277	-389.5	-1.379	0.92

The data in table 4.7 shows with the addition of Ni making the adsorption of oxygen species such as OH occurs at much lower potential than on monometallic Pd and Ni surface to oxidize CO or adsorbed CO-like carbonaceous species on Pd sites. The addition of Ni as second metal in PdNi/MWCNT also contribute to sufficient oxygen containing species such as OH to remove the adsorbed carbonaceous species and in other way it will beneficial in oxidation of glycerol. Meanwhile the catalyst poisoning against the carbonaceous species can be traced from the forward scan to backward (I_f/I_r) scan peak current density ratio as shown in Table 4.7. The ratio of PdNi/MWCNT catalyst show higher value compare to Pd/C, PdSn/MWCNT and Pd/MWCNT. Therefore

PdNi/MWCNT show better oxidation of glycerol to carbon dioxide during anodic scan and less accumulation of carbonaceous species on the catalyst surface compare to Pd/C, PdSn/MWCNT and Pd/MWCNT [5].

4.6.2 ELECTROCHEMICAL IMPEDANCE SPECTROSCOPY (EIS)

EIS was used to investigate the overall kinetics of glycerol oxidation at different potentials. The technique enabled to dissect the various impedance parameters for the charge transfer reaction occurring across the electrode solution interface. Nyquist plots for glycerol oxidation for 1.0 M glycerol in 1.0M KOH solution at 25 ^{o}C are shown in Figure 4.13. The effective charge transfer resistance (*R*ct) was used to analyze the electrode kinetics of the reaction process.

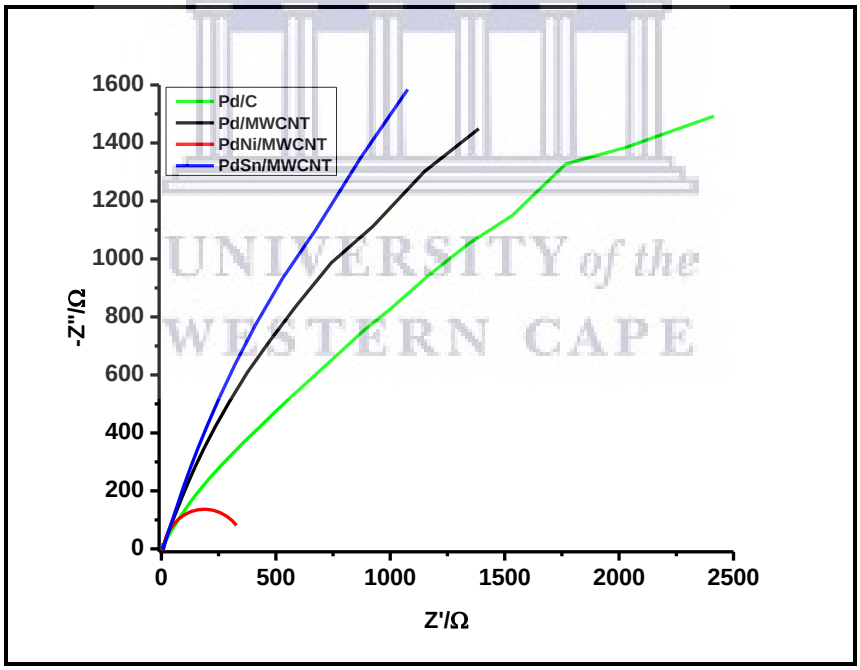

Figure 4. 13: EIS of the synthesized electrocatalyst Pd/MWCNT, PdNi/MWCNT and PdSn/MWCNT compared to Pd/C commercial in 1M KOH + 1M Glycerol @ 30mV.

Shown in Figure 4.13, is the Nyquist plot is characterized by a capacitive feature for Pd/C, Pd/MWCNT and PdSn/MWCNT, as expected for hydrogen adsorption/desorption and double layer charging/ discharging phenomena. However, for PdNi/MWCNT there is a

changeover from capacitive behavior to resistive behavior, as shown in Figure 4.13. At this potential, the Nyquist plot resembles a semicircle, which can be assigned to kinetically controlled reaction. The small arc in the high frequency region may be associated with the chemisorption and dehydrogenation of the glycerol molecule at the initial stage of the oxidation process. A charge transfer resistance (*R*ct) for the kinetically controlled reactions may be represented by the diameter of the semicircle in the medium frequency and is related to the charge transfer reaction kinetics according to

$$R_{ct} = \frac{RT}{nF\, i_o} \tag{4.7}$$

$$i_o = nFAk_o C_o^{(1-\alpha)} C_R^{\alpha} \tag{4.8}$$

where *R*: molar gas constant (J.mol^{-1} k^{-1}); *T*: temperature (K); *n*: number of electrons transferred; *F*: Faraday constant (C); i_o: exchange current (A); *A*: reaction area (cm^2); k_0: standard heterogeneous rate constant (cm.sec^{-1}); C_o, C_R: bulk concentration of oxidant and reductant species (mol.L^{-1}); α: transfer coefficient.

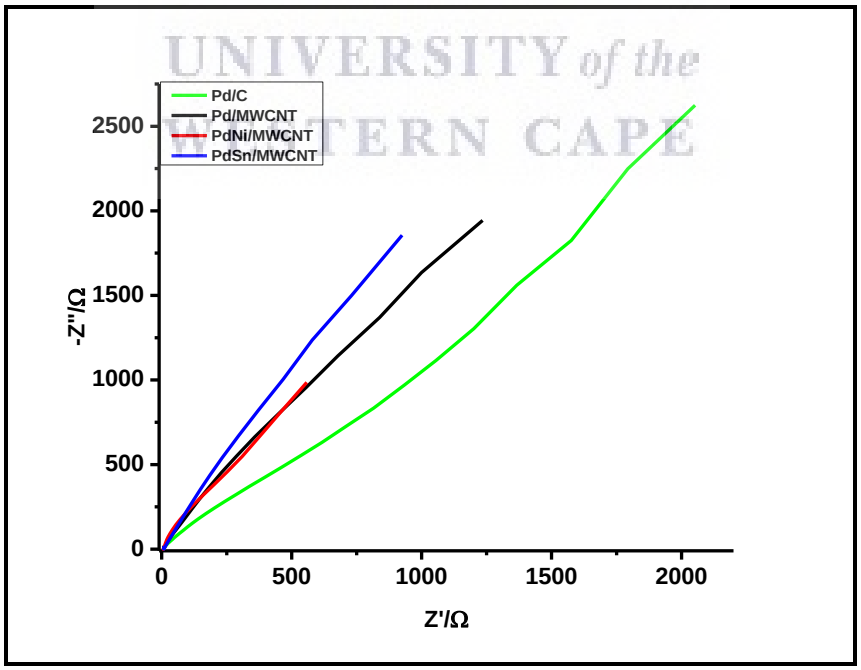

Figure 4. 14: EIS of the synthesized electrocatalyst Pd/MWCNT, PdNi/MWCNT and PdSn/MWCNT compared to Pd/C commercial in 1M KOH + 1M Glycerol @ 10mV.

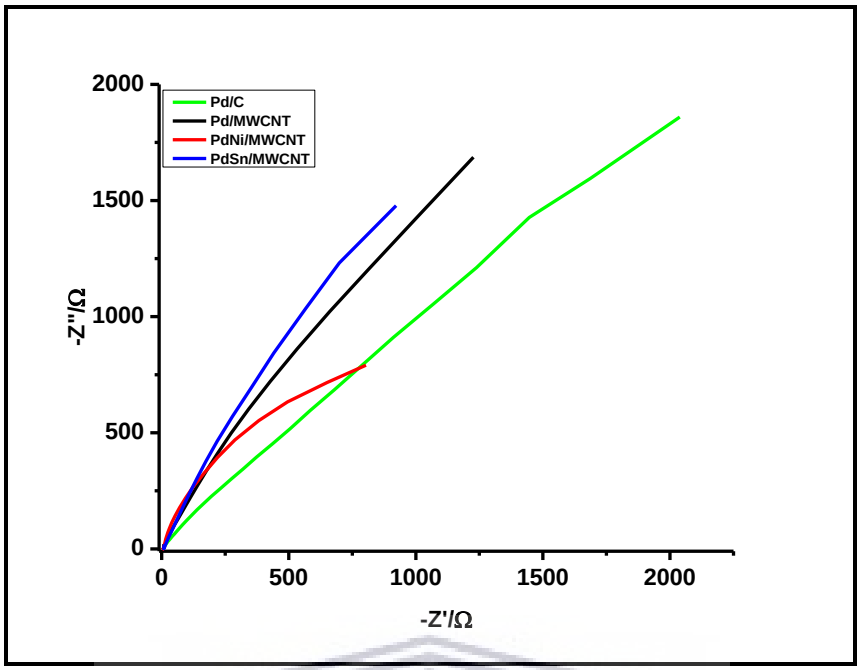

Figure 4. 15: EIS of the synthesized electrocatalyst Pd/MWCNT, PdNi/MWCNT and PdSn/MWCNT compared to Pd/C commercial in 1M KOH + 1M Glycerol @ -10mV.

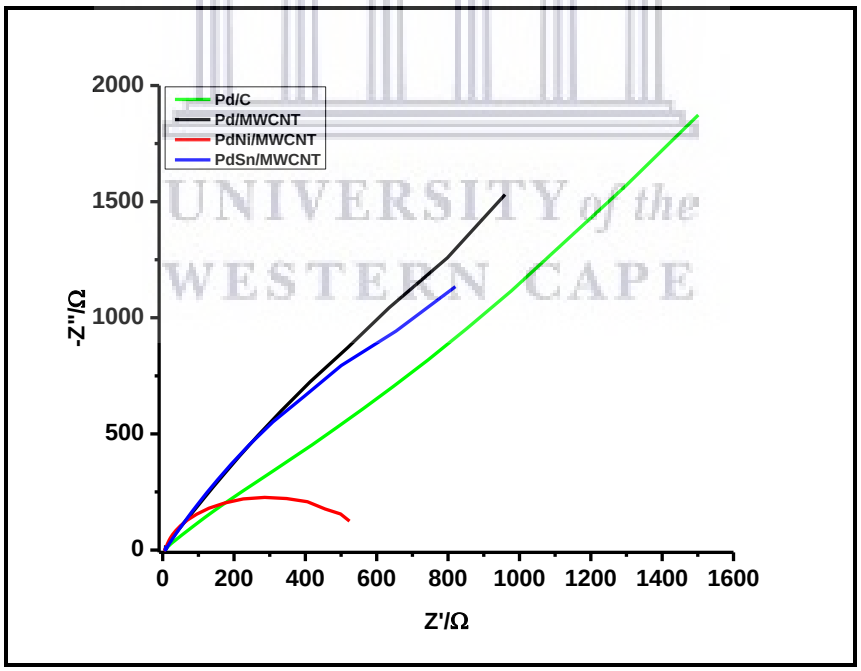

Figure 4. 16: EIS of the synthesized electrocatalyst Pd/MWCNT, PdNi/MWCNT and PdSn/MWCNT compared to Pd/C commercial in 1M KOH + 1M Glycerol @ -30mV.

Figure 4.14 and figure 4.15 all of the catalyst display a similar trend of capacitive behavior with Pd/C being having high kinetic followed by PdNi/MWCNT, Pd/MWCNT and

PdSn/MWCNT respectively. In figure 4.16, PdNi/MWCNT resembles a semicircle, which can be assigned to kinetically controlled reaction and displays a resistive behavior, while Pd/C, PdSn/MWCNT and PdNi/MWCNT capacitive behavior.

4.6.3 CHRONOAMPEROMETRY

Chronoamperometric study has been employed for 3600s, where the considerable stability and tolerance to poisoning by intermediates species can be tested. Figure 4.17 below shows the chronoamperometry obtained at room temperature in solutions of 1.0 M KOH and 1.0 M glycerol for 3600s. For all four catalysts, we can observe a decay of current value in the time interval measured for the studied electrocatalysts. However, after the initial drops the performance become stable for all the catalyst tested. From Figure 4.17 shows that the PdNi/MWCNT demonstrates better stability compared to PdSn/MWCNT, Pd/MWCNT and Pd/C respectively, indicating that the present of Ni could improve the stability of the catalyst by give a balance adsorption between OH species from Ni and species from glycerol adsorption on Pd [5].

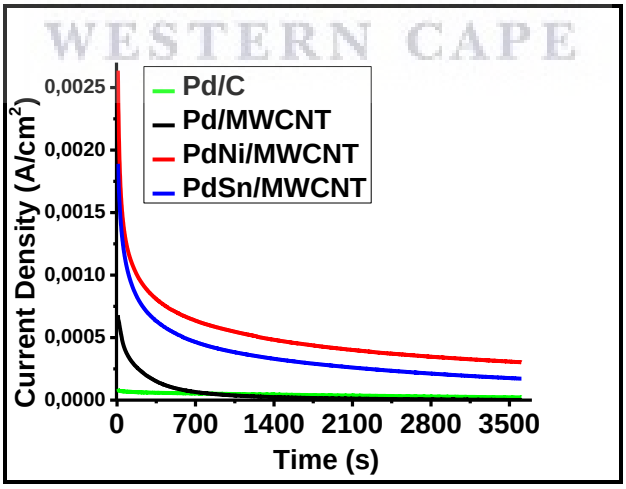

Figure 4. 17: Chronoamperometry of the synthesized electrocatalyst Pd/MWCNT, PdNi/MWCNT and PdSn/MWCNT compared to Pd/C commercial in 1.0 M KOH + 1.0 M Glycerol @ -20mV

CHAPTER 5

RESULTS AND DISCUSSION II

This chapter will focus on analyzing the results obtained from various characterization techniques performed on the synthesized catalysts Palladium nickel and cobalt oxide on multi walled carbon nanotubes ($PdNiCo_3O_4$/MWCNT), Palladium tin and cobalt oxide on multi walled carbon nanotubes ($PdSnCo_3O_4$/MWCNT), Palladium nickel and cerium oxide on multi walled carbon nanotubes ($PdNiCeO_2$/MWCNT) and Palladium tin and cerium oxide on multi walled carbon nanotubes ($PdSnCeO_2$/MWCNT). The various characterizations help determine the various properties exhibited by these synthesized nanoparticles.

5.1 INTERNAL STRUCTURE

The internal structure of the synthesized nanoparticles was evaluated by high resolution transmission electron microscope (HR-TEM). As seen below from figure 5.1 the images obtained from HR-TEM shows a great deal of the internal structure of the synthesized catalysts as the multi walled carbon nanotubes can be seen under the catalysts composite. However the catalysts composite does not show any internal structure. The inner shape of the synthesized catalysts is unclear additionally the images show that catalysts may be agglomerated and they have small particle size. Although as said above the internal shape of the catalysts cannot be fully analyzed by the use of HR-TEM because of unclear internal structures the catalysts.

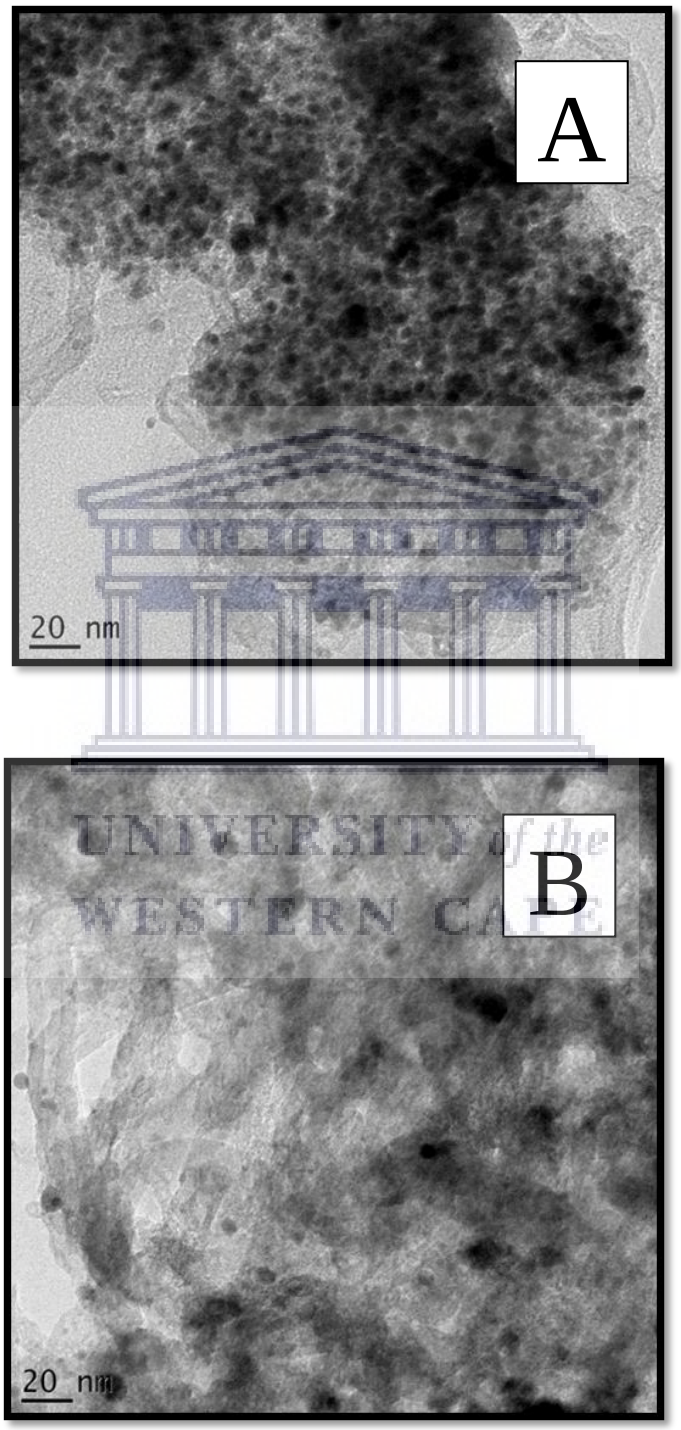

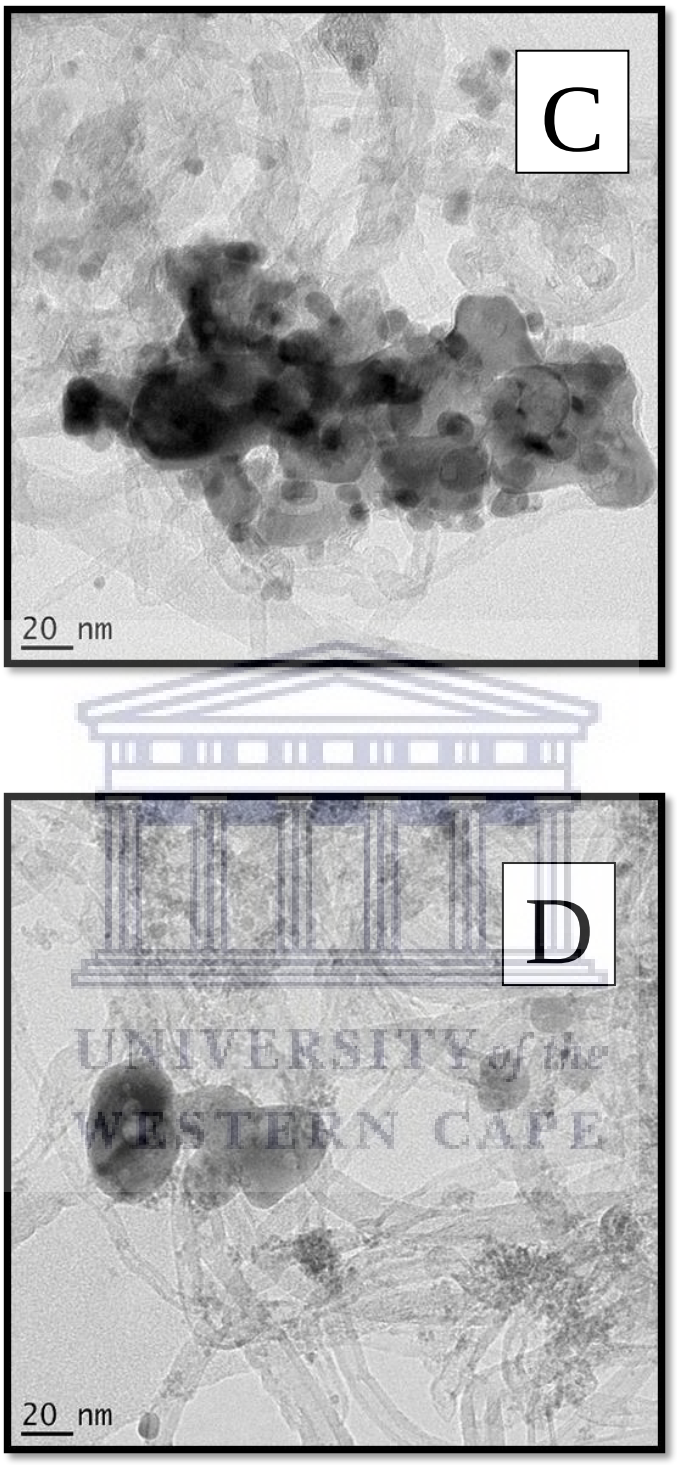

Figure 5. 1: HR-TEM images of the synthesized catalyst of (A) $PdNiCo_3O_4$/MWCNT, (B) $PdSnCo_3O_4$/MWCNT, (C) $PdNiCeO_2$/MWCNT and (D) $PdSnCeO_2$/MWCNT

Small Angle X-ray Scattering (SAXS) is a technique that can be used to determine the internal structure of the synthesized catalysts. The SAXS analysis was performed using SAXS Space by Anton Paar. From the plot of the shape analysis it shows that all the catalysts were agglomerated and that $PdNiCo_3O_4$/MWCNT and $PdSnCeO_2$/MWCNT had a core shell solid sphere, while $PdSnCo_3O_4$/MWCNT and $PdNiCeO_2$/MWCNT had a core shell hollow sphere. The shell could be attributed to the secondary catalyst (Nickel or Sn), the core would then be the primary catalysts palladium. The shape obtained for the catalysts are illustrated in the table 5.1 below and plots can be seen in figure 5.2 below.

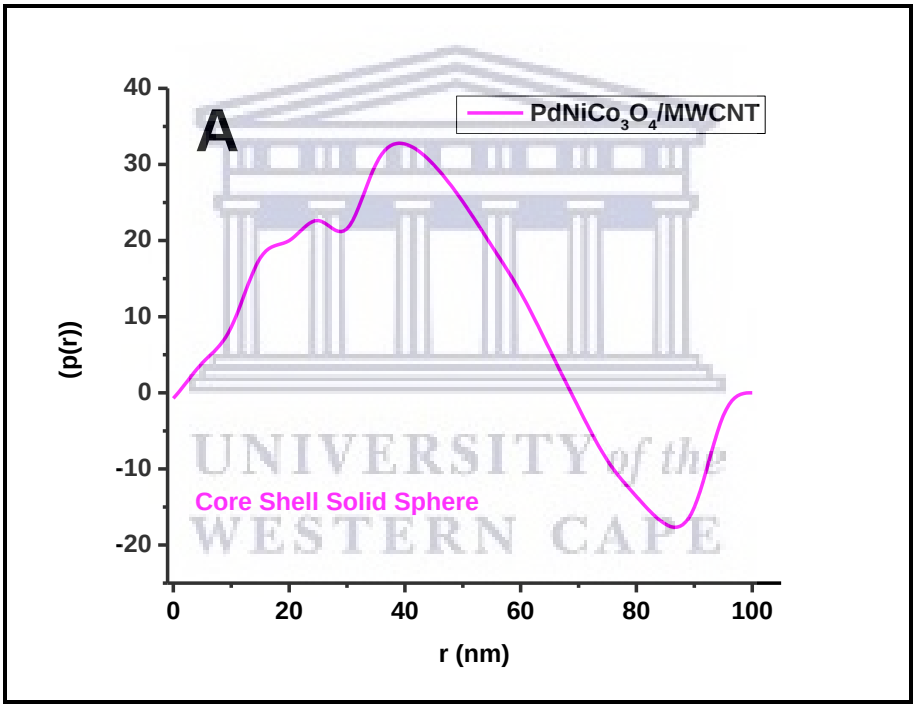

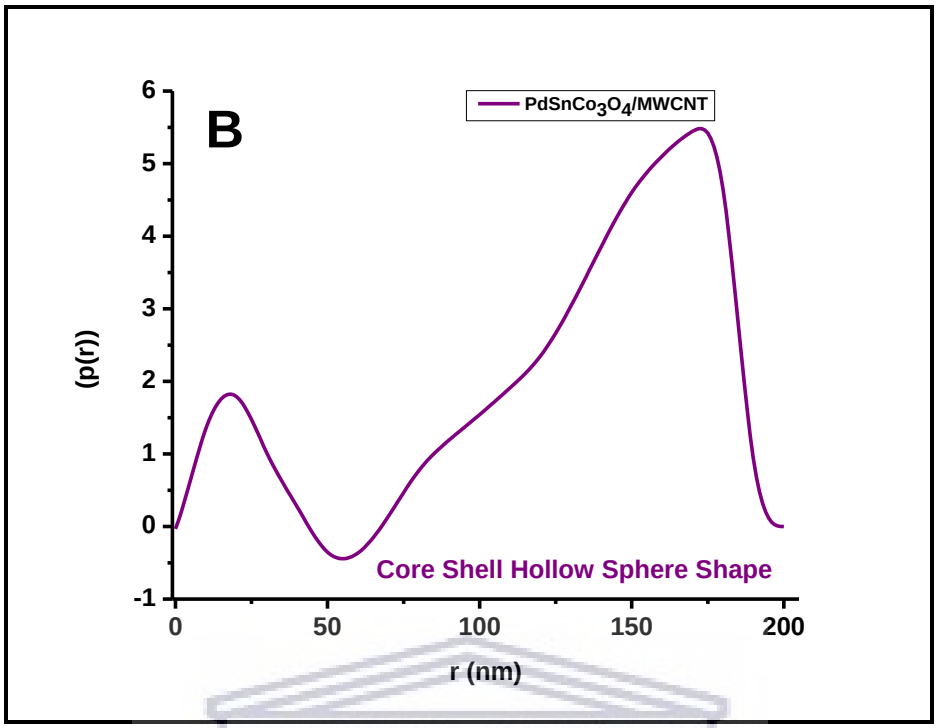

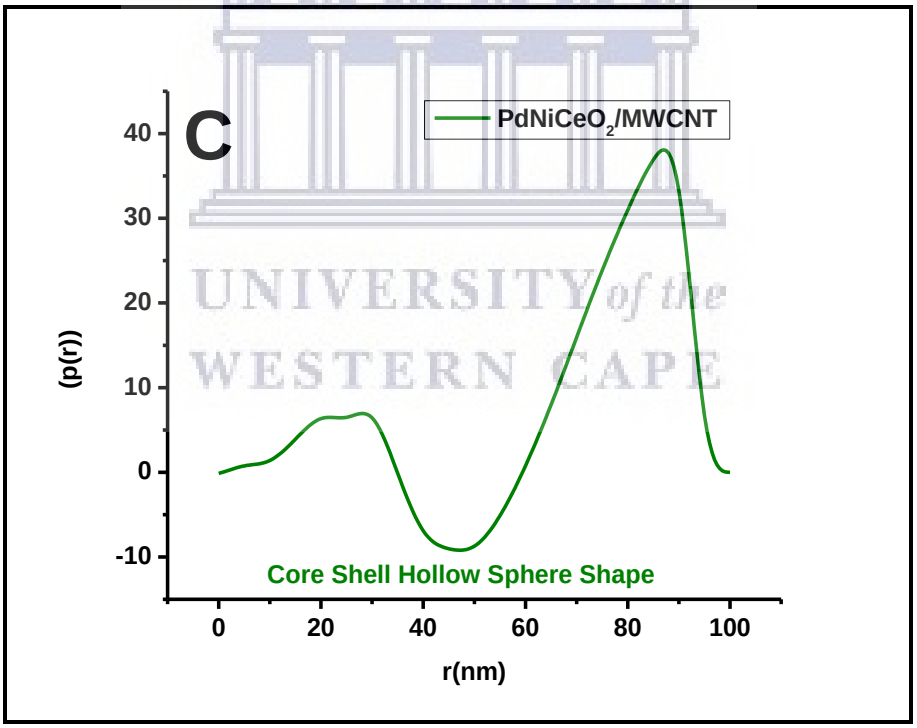

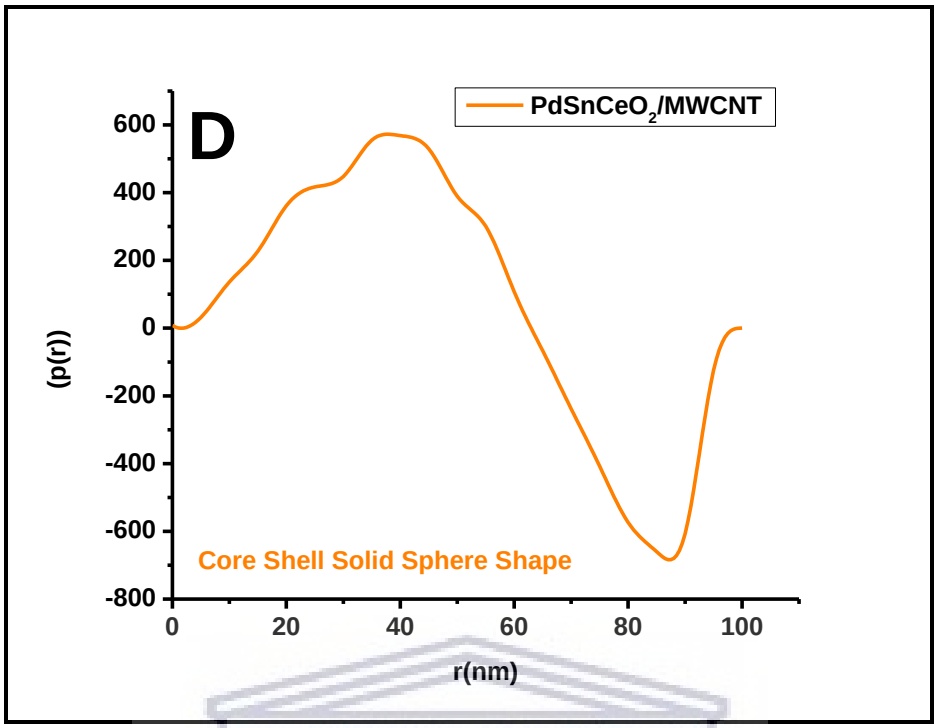

Figure 5. 2: SAXS plot of the shapes of the synthesized catalysts of (A) $PdNiCo_3O_4$/MWCNT, (B) $PdSnCo_3O_4$/MWCNT, (C) $PdNiCeO_2$/MWCNT and (D) $PdSnCeO_2$/MWCNT.

Table 5. 1: Shapes of obtained catalysts form SAXS

Samples	Shapes
$PdNiCo_3O_4$/MWCNT	Core Shell Solid Sphere
$PdSnCo_3O_4$/MWCNT	Core Shell Hollow Sphere
$PdNiCeO_2$/MWCNT	Core Shell Hollow Sphere
$PdSnCeO_2$/MWCNT	Core Shell Solid Sphere

The broad shoulders seen in the SAXS plots above indicate agglomeration of the catalysts as evident in HR-TEM images in figures 5.1.

5.2 PHASE COMPOSITION (CRYSTALLINITY)

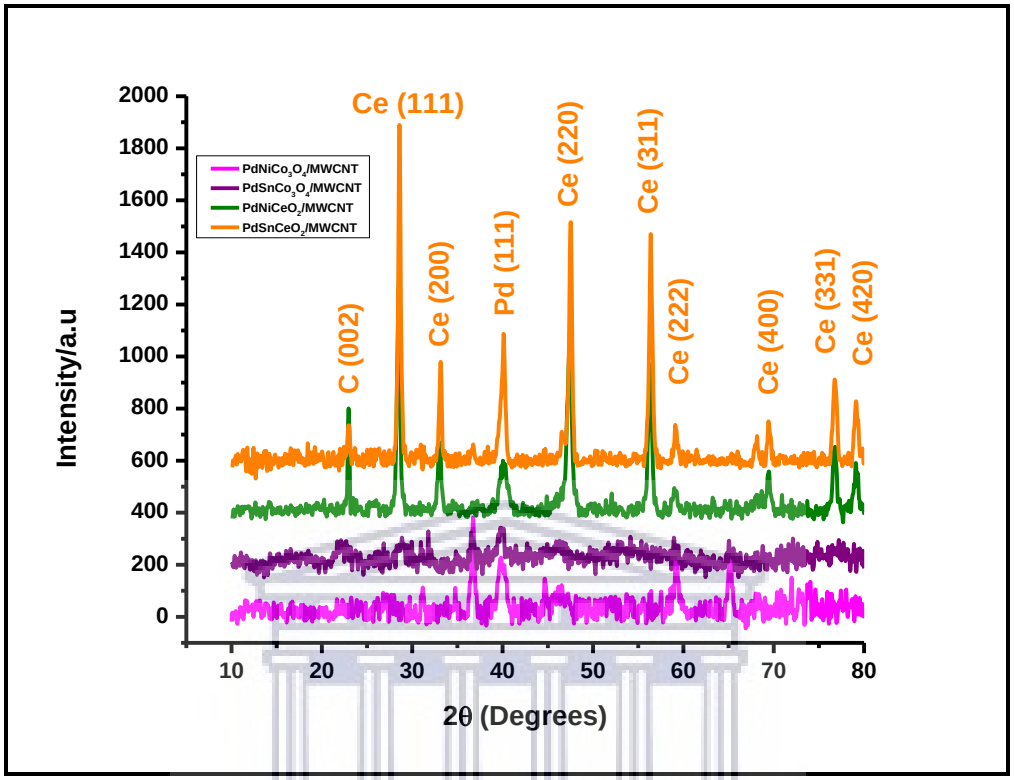

Figure 5. 3: XRD plot of the synthesized catalysts of $PdNiCo_3O_4$/MWCNT, $PdSnCo_3O_4$/MWCNT, $PdNiCeO_2$/MWCNT and $PdSnCeO_2$/MWCNT.

The phase composition and crystalline structure of the synthesized nanoparticles were investigated through powder X-ray diffraction (XRD). The catalysts of $PdNiCo_3O_4$/MWCNT (JCPDS 00-043-1003), $PdSnCo_3O_4$/MWCNT (JCPDS 00-043-1003), $PdNiCeO_2$/MWCNT (JCPDS 00-034-0394) and $PdSnCeO_2$/MWCNT (JCPDS 00-034-0394) all showed a face-center cubic phase and are represented by figure 5.3 above.

The peaks at 40.1 ° and 46.7 ° can be assigned to (111) and (200) for reflection of Pd in $PdNiCo_3O_4$/MWCNT. Meanwhile the peaks at 36.85 ° , 59.17 ° and 65.21 ° are assigned to (311), (511) and (440) indexes of Co_3O_4 in $PdNiCo_3O_4$/MWCNT, then $PdSnCo_3O_4$/MWCNT has similar peaks to $PdNiCo_3O_4$/MWCNT peaks with less intensity.

For $PdSnCo_3O_4$/MWCNT the peaks are 40.1 º and 46.7 º which are assigned to (111) and (200) for reflection of Pd in $PdSnCo_3O_4$/MWCNT, then peaks at 36.85 º , 59.17 º and 65.21 º are assigned to (311), (511) and (440) indexes of Co_3O_4.

$PdNiCeO_2$/MWCNT and $PdSnCeO_2$/MWCNT have similar peaks with the Pd peak at 40.1 º with the index (111) for both of the catalyst and the following peaks arise from CeO_2 which are 28.55 º , 33.08 º , 47.48 º , 56.09 º , 59.09 º , 69.04 º , 76.70 º and 79.07 º and are assigned to these miller indexes (111), (200), (220), (311), (222), (400), (331) and (420) respectively.

These peaks were also confirmed by the diffraction obtained from selected area electron diffraction (SAED) in figure 5.4 below. The crystallinity of the nanoparticles can also be seen from the spectrum which shows the nanoparticles to be polycrystalline. This is also an observable trend seen in SAED micrograph obtained from HR-TEM analysis. The trend for the crystallinity of the nanoparticles was $PdNiCo_3O_4$/MWCNT > $PdSnCeO_2$/MWCNT > $PdSnCo_3O_4$/MWCNT > $PdNiCeO_2$/MWCNT meaning that $PdNiCo_3O_4$/MWCNT had the highest degree of crystallinity.

Selected Area Electron Diffraction (SAED) was obtained from HR-TEM which revealed and confirmed that the synthesized catalysts were crystalline. The planes found in XRD plot above was also observed in the SAED image obtained, which confirms the phase composition of the synthesized catalysts and the hkl miller index (planes) found in XRD.

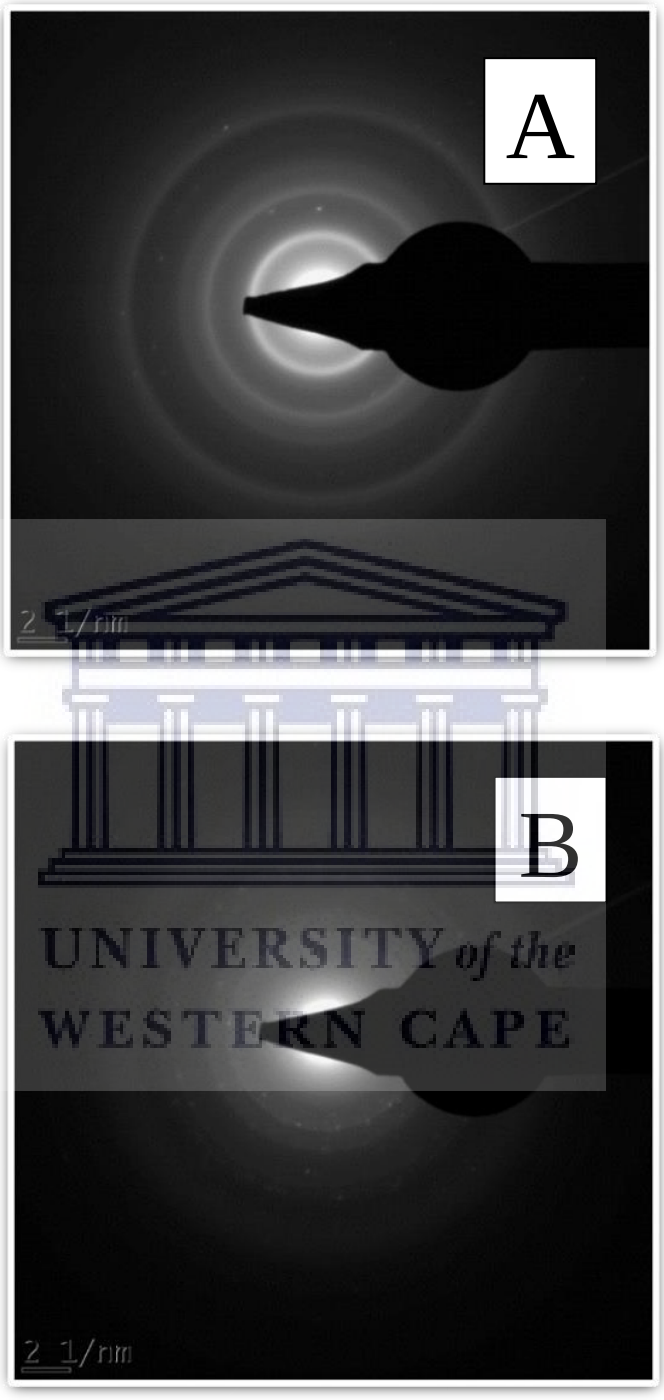

Figure 5. 4: SAED images of the synthesized catalysts of (A) $PdNiCo_3O_4$/MWCNT, (B) $PdSnCo_3O_4$/MWCNT, (C) $PdNiCeO_2$/MWCNT and (D) $PdSnCeO_2$/MWCNT

The lattice fringe images obtained for the synthesized nanoparticles further confirms that the nanoparticles were crystalline and the d-spacing value of the lattice fringes was evaluated and assigned with the corresponding plane (miller index) as can be seen in figure 5.5 below

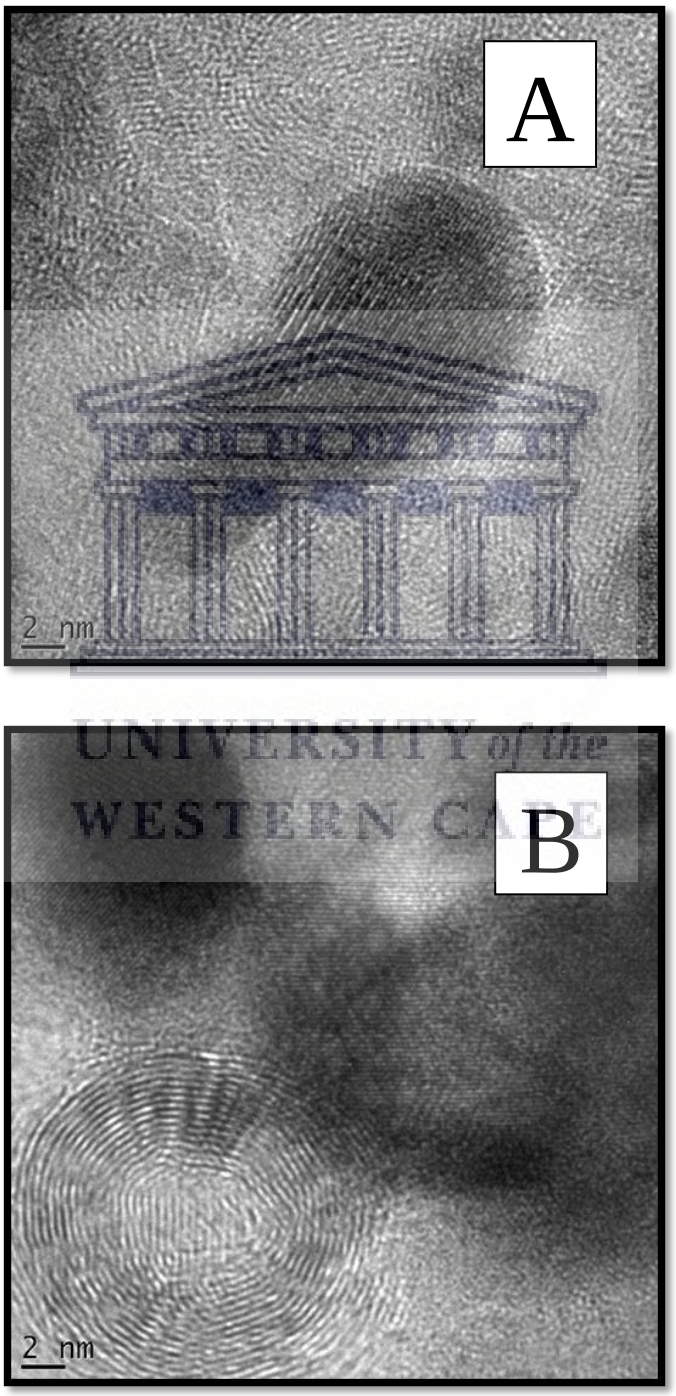

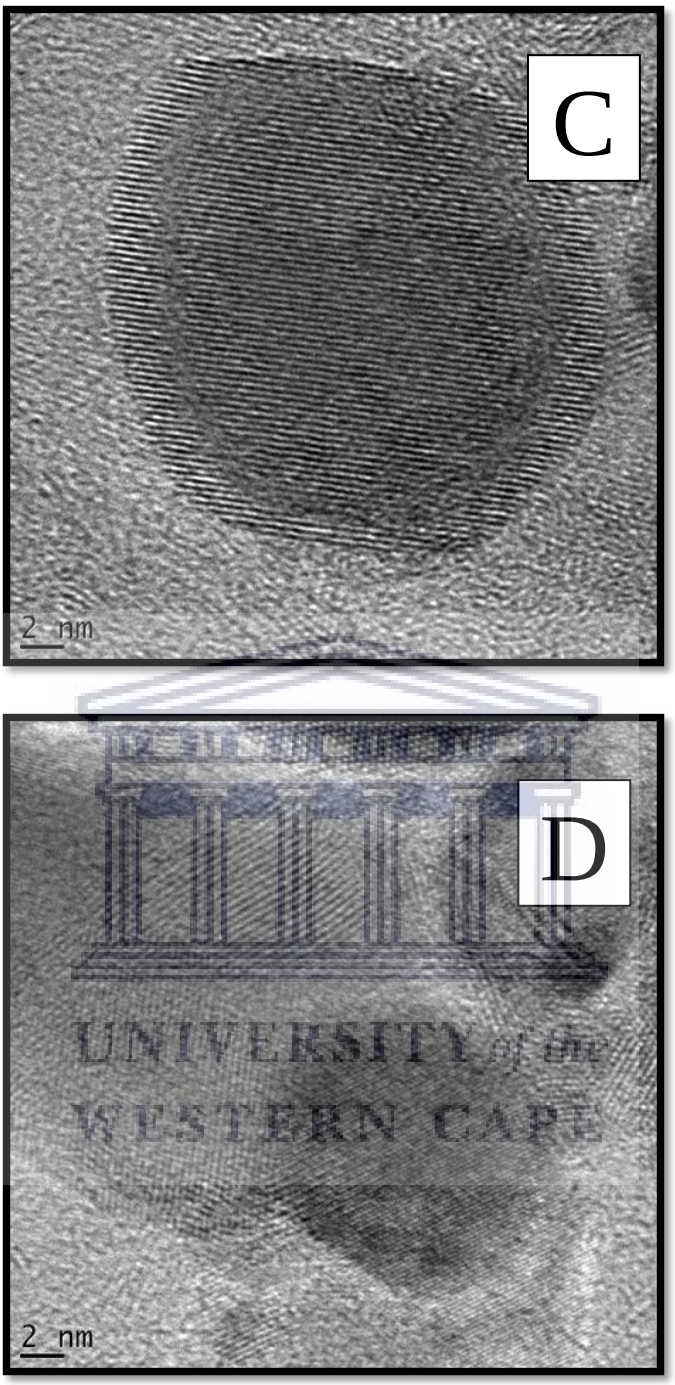

Figure 5. 5: HR-TEM image showing the lattice fringe and d-spacing value of the lattice fringe indicating the plane with the d-space value for the synthesized nanoparticles of (A) $PdNiCo_3O_4$/MWCNT, (B) $PdSnCo_3O_4$/MWCNT, (C) $PdNiCeO_2$/MWCNT and (D) $PdSnCeO_2$/MWCNT

The calculated d-spacing value for the four samples are $PdNiCo_3O_4$/MWCNT is 0.195 nm at 331 plane, $PdSnCo_3O_4$/MWCNT is 0.284 nm at 220 plane, $PdNiCeO_2$/MWCNT is 0.304 nm at 111 plane and $PdSnCeO_2$/MWCNT is 0.275 nm at 200 plane.

5.3 ELEMENTAL COMPOSITION

The elemental composition of the synthesized catalysts was evaluated using Energy Dispersive X-ray spectroscopy (EDX) and Inductive Couple Plasma (ICP) as shown in figure 5.2 and table 5.3 respectively. The instruments used are EDS analyzer coupled into the High-Resolution Transmission Electron Microscope used for HR-TEM analysis and ICP analyzer used techniques for the determination of trace concentrations of elements in samples.

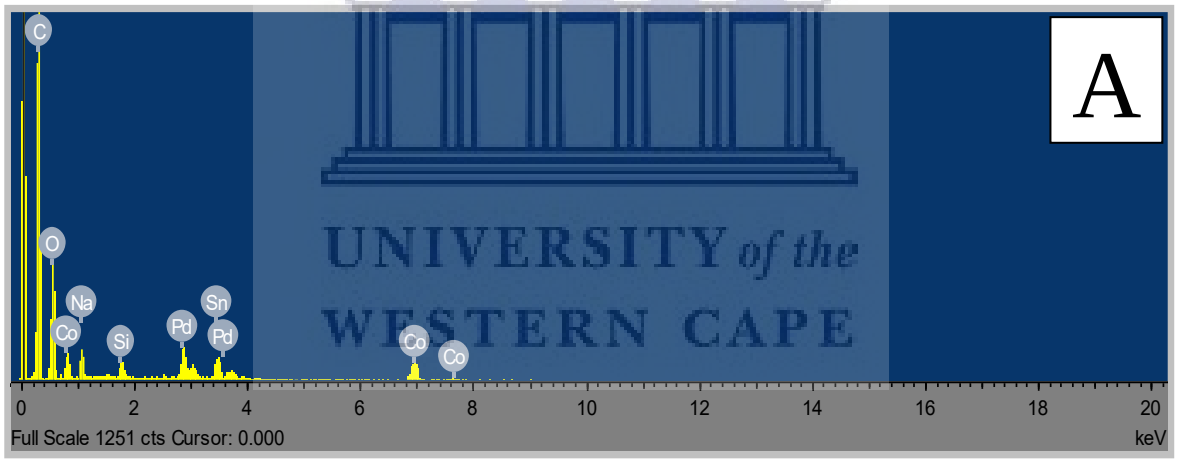

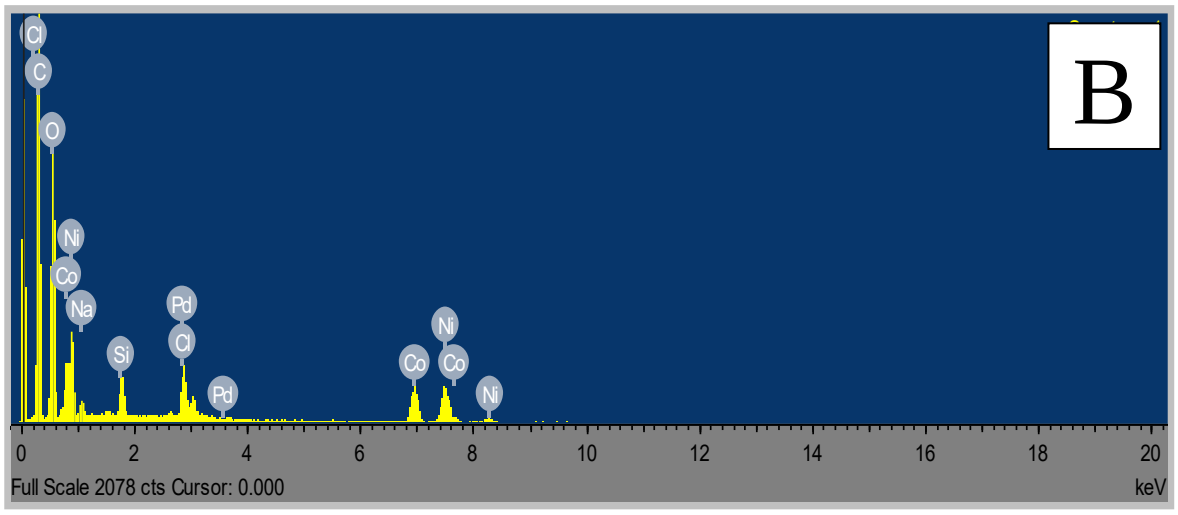

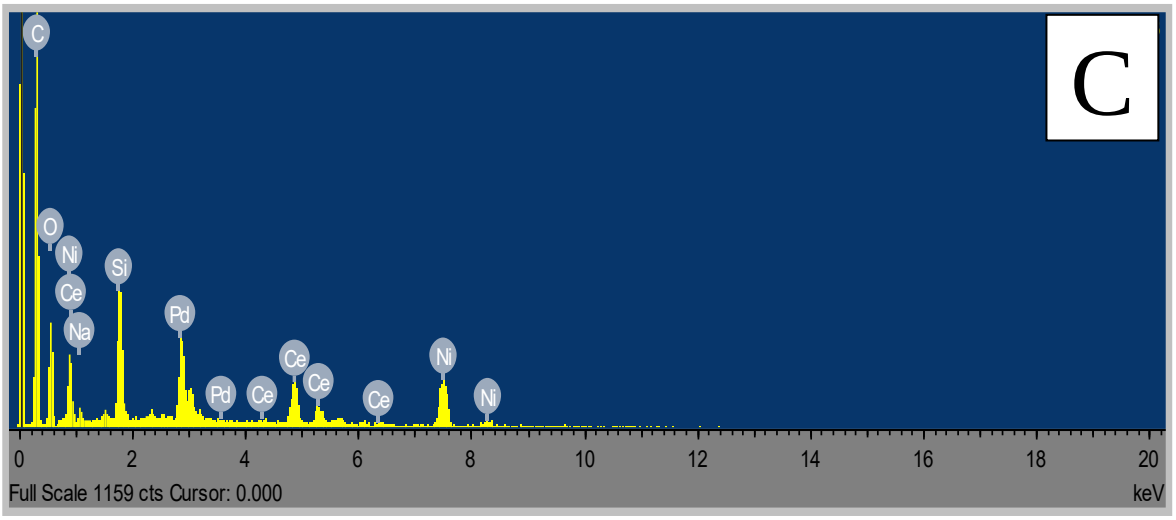

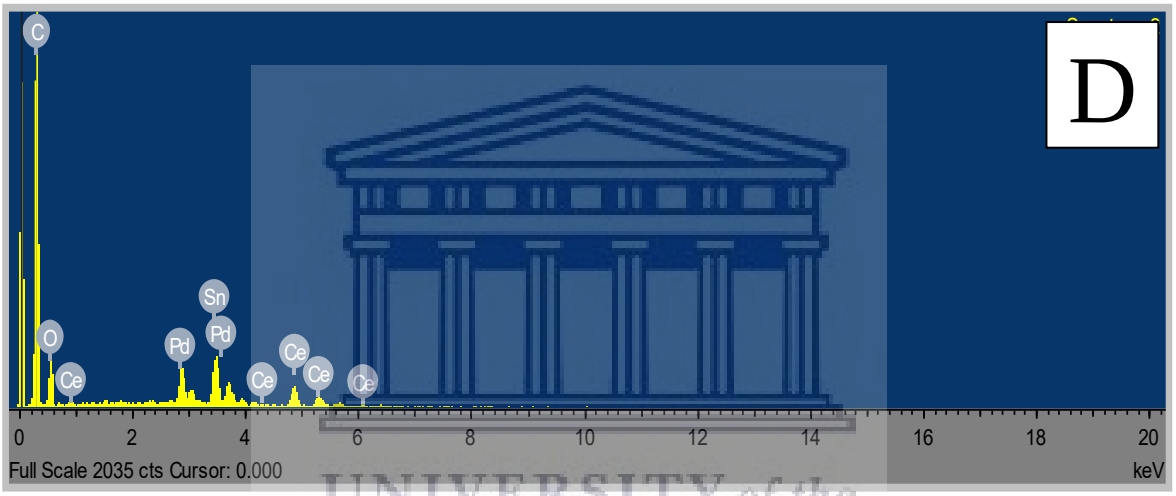

The EDS of the catalysts showed all the elements expected for the nanoparticles. $PdNiCo_3O_4$/MWCNT shows the presence of palladium, nickel, cobalt, oxygen and multi walled carbon nanotubes. $PdSnCo_3O_4$/MWCNT shows the presence of palladium, tin, cobalt, oxygen and multi walled carbon nanotubes. $PdNiCeO_2$/MWCNT shows the presence of palladium, nickel, cerium, oxygen and multi walled carbon nanotubes. $PdSnCeO_2$/MWCNT shows the presence of palladium, tin, cerium, oxygen and multi walled carbon nanotubes.

Table 5. 2: ICP data of the catalysts of $PdNiCo_3O_4$/MWCNT, $PdSnCo_3O_4$/MWCNT, $PdNiCeO_2$/MWCNT and $PdSnCeO_2$/MWCNT

	Pd	Ni	Sn	Co	Ce
$PdNiCo_3O_4$/MWCNT	73.84 mg/L	127.31 mg/L	X	101.93 mg/L	X
$PdSnCo_3O_4$/MWCNT	63.20 mg/L	X	141.17 mg/L	102.89 mg/L	X
$PdNiCeO_2$/MWCNT	41.99 mg/L	42.65 mg/L	X	X	452.87mg/L
$PdSnCeO_2$/MWCNT	39.12 mg/L	X	65.35mg/L	X	432.62 mg/L

5.4 SIZE DISTRIBUTION

The size distribution of the synthesized catalysts was studied and evaluated. The particle size was evaluated using SAXS and HR-TEM, while the crystal size was evaluated from XRD data of the synthesized catalysts. The summary of the size distribution for the synthesized nanoparticles is given by the SAXS plot of the size distribution and HR-TEM average particle.

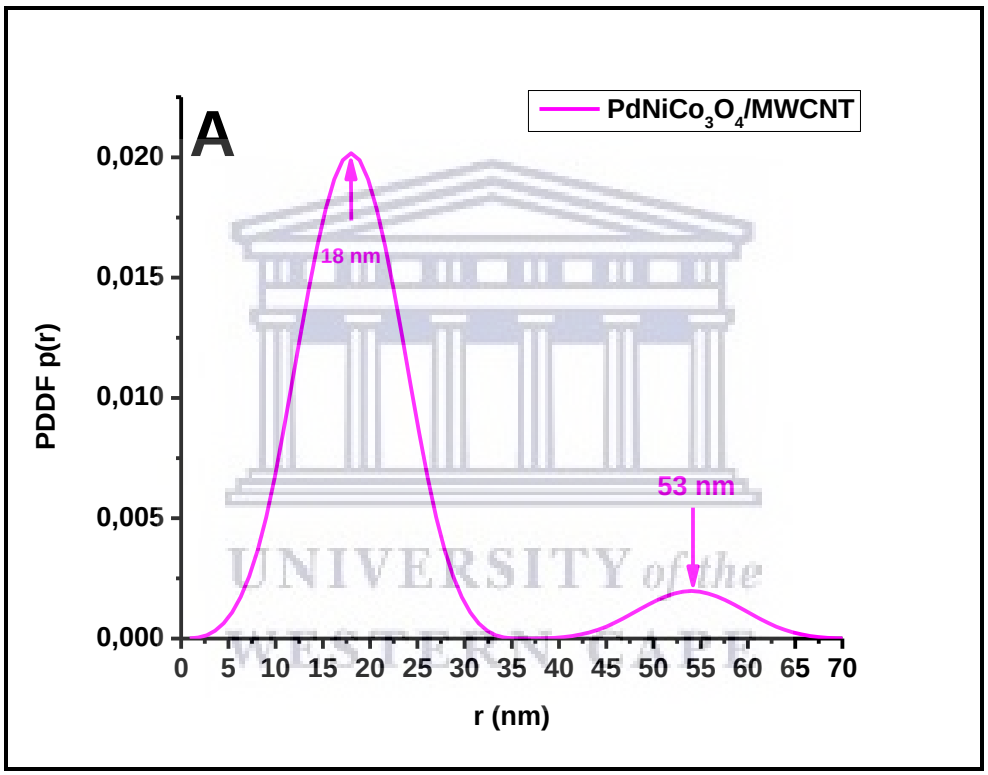

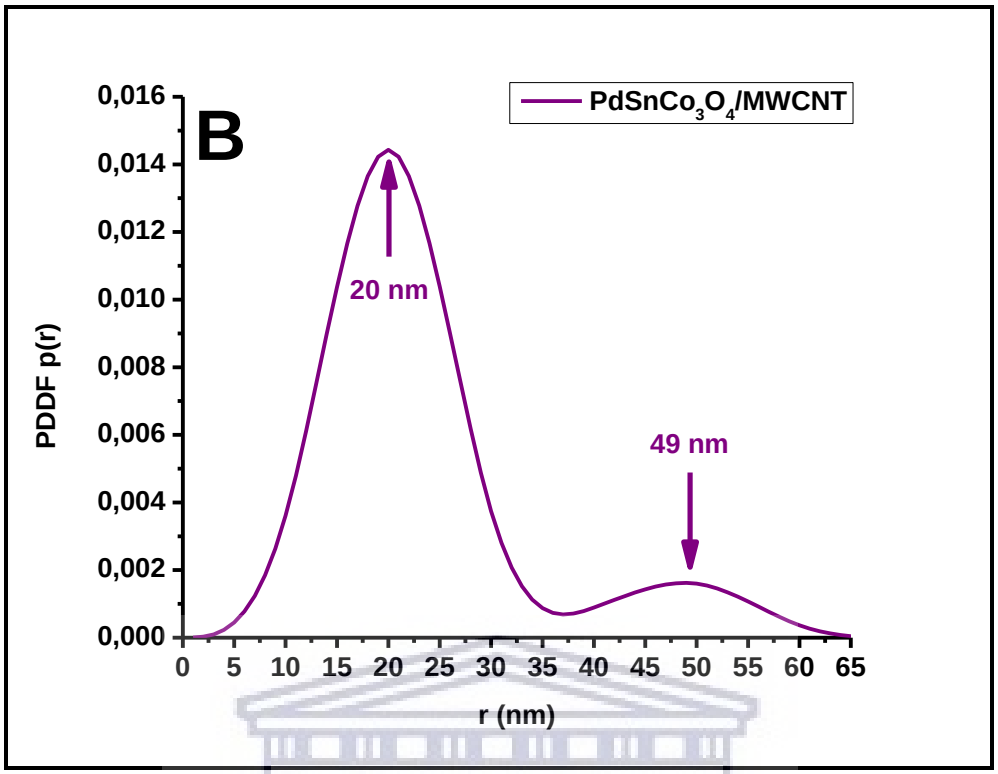

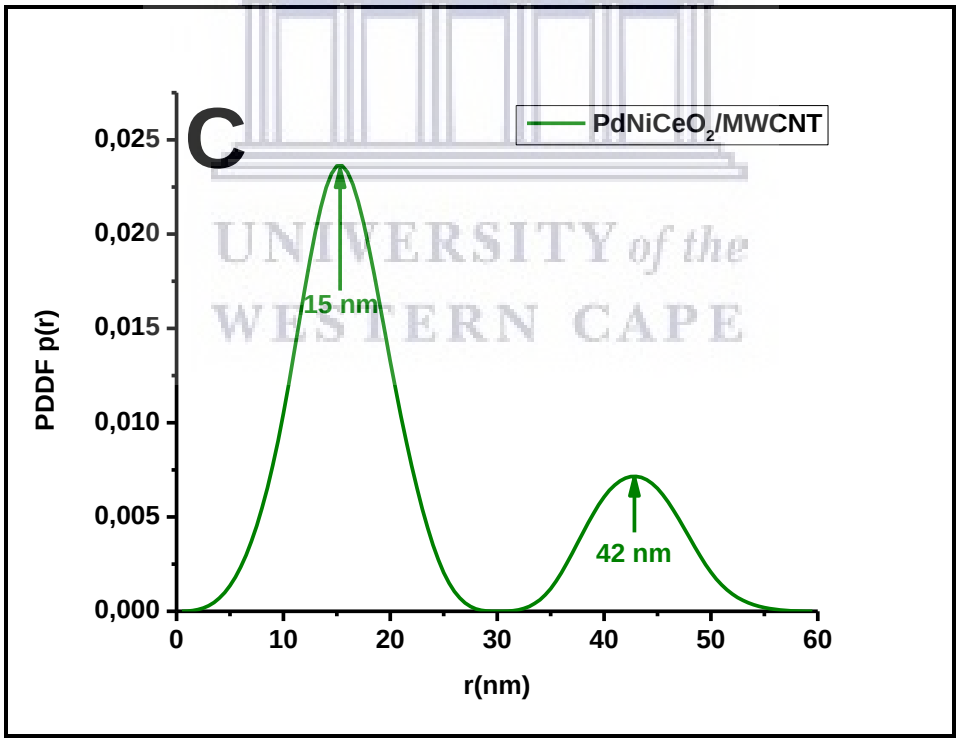

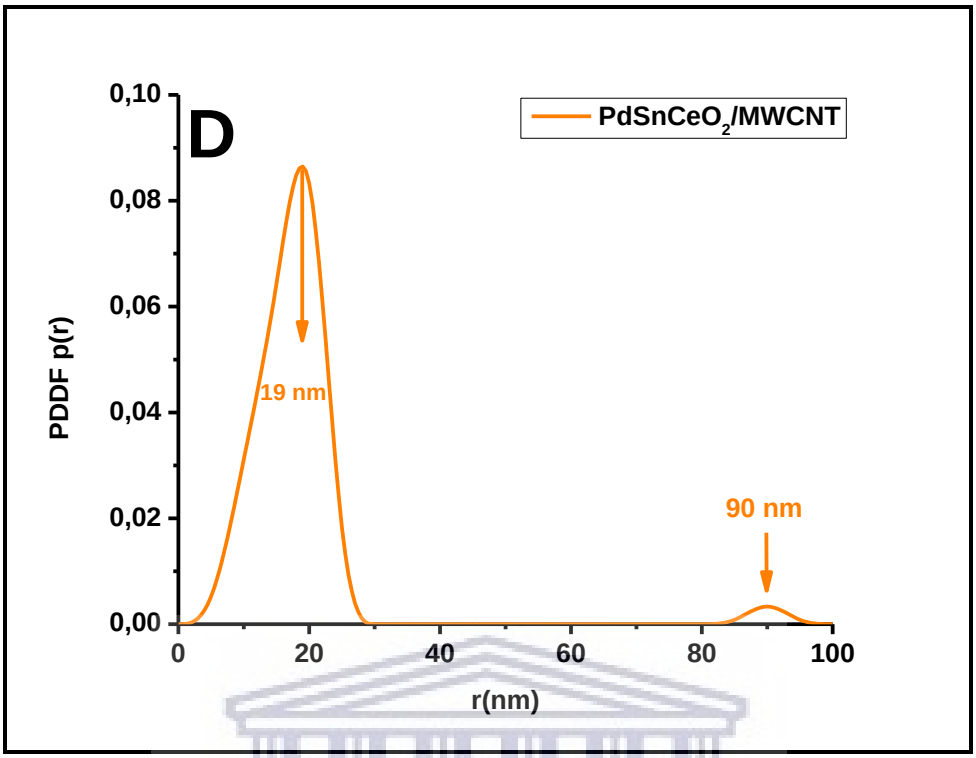

Figure 5. 6: SAXS plot of size distribution of the synthesized catalysts of (A) $PdNiCo_3O_4$/MWCNT, (B) $PdSnCo_3O_4$/MWCNT, (C) $PdNiCeO_2$/MWCNT and (D) $PdSnCeO_2$/MWCNT

The particle size distribution obtained from SAXS plot above in figure 5.6 shows that $PdNiCo_3O_4$/MWCNT has a mean particle size of 15 nm with a big particle size of 53 nm which is attributed to the agglomeration. $PdSnCo_3O_4$/MWCNT has a mean particle size of 20 nm with a big particle size of 49 nm which is attributed to the agglomeration. $PdNiCeO_2$/MWCNT has a mean particle size of 15 nm with a big particle size of 42 nm which is attributed to the agglomeration. Then $PdSnCeO_2$/MWCNT has a mean particle size of 19 nm with a big particle size of 90 nm which is attributed to the agglomeration. TEM images form earlier in figure 5.2 confirm the agglomeration of the catalysts.

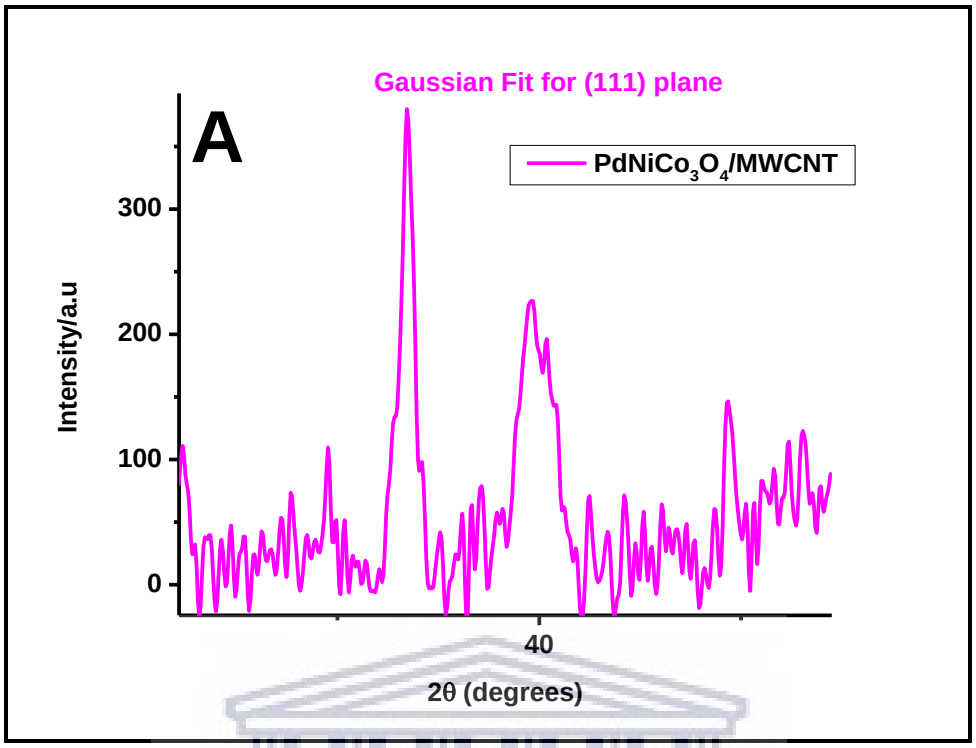

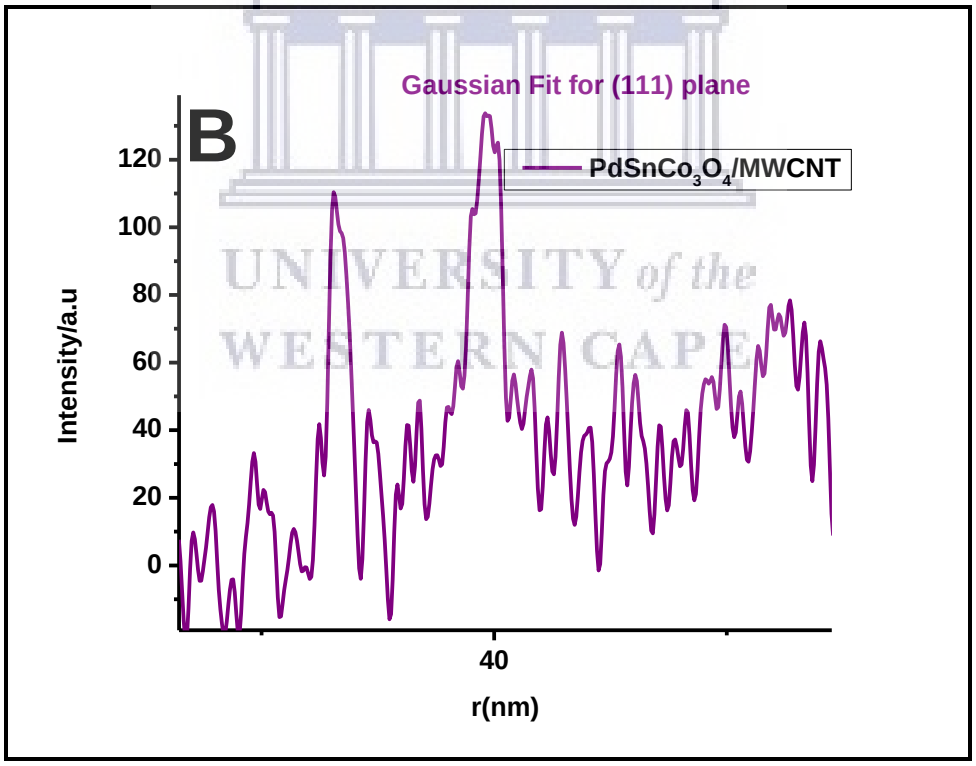

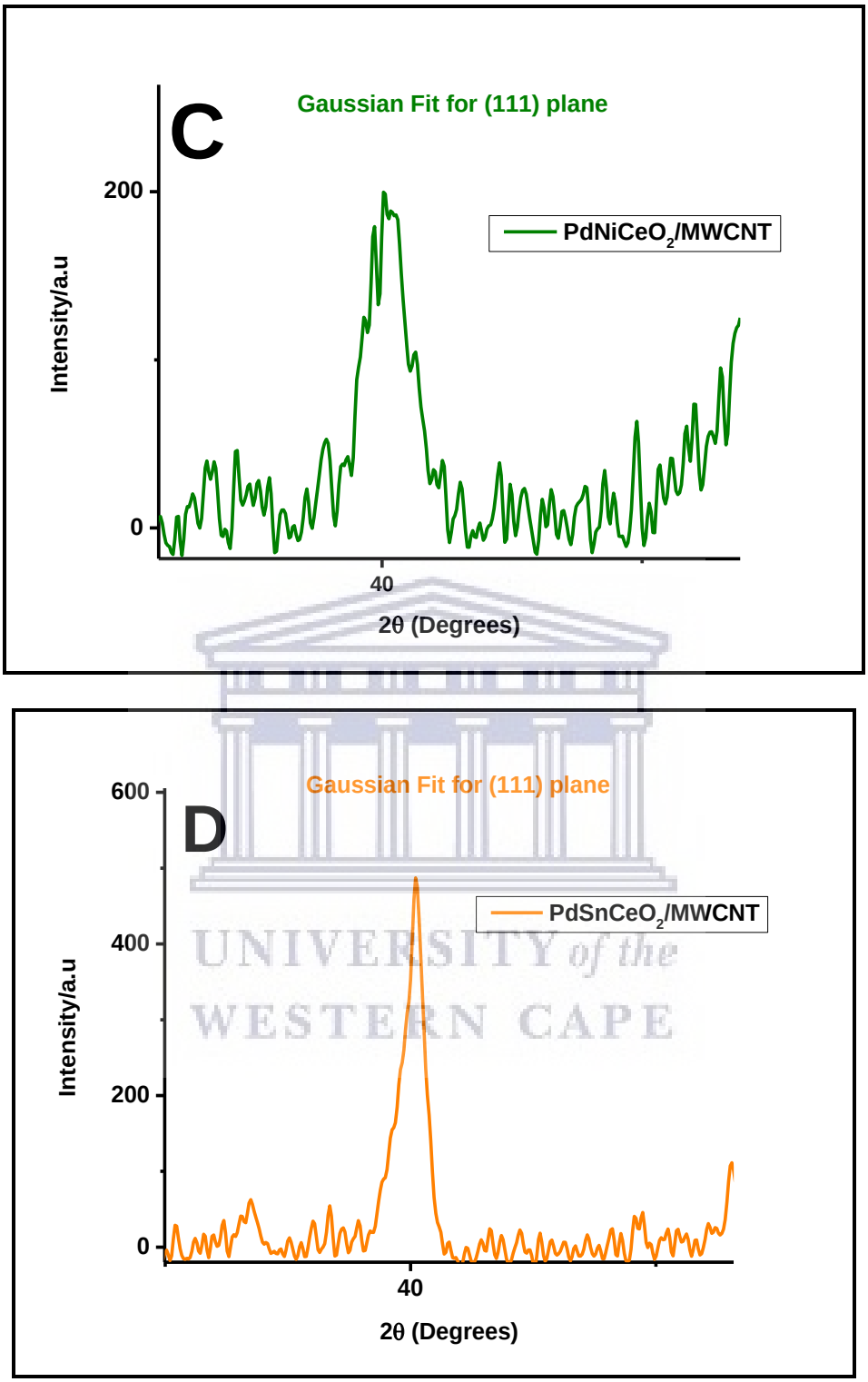

Figure 5. 7: XRD plot of Gaussian Fit for (111) plane for crystal size calculation of the catalysts of (A) $PdNiCo_3O_4$/MWCNT, (B) $PdSnCo_3O_4$/MWCNT, (C) $PdNiCeO_2$/MWCNT and (D) $PdSnCeO_2$/MWCNT

The Debye-Scherrer equation was used to calculate the crystal size and the equation is given as:

$$d = \frac{k\lambda}{B2\theta Cos\theta} \quad (4.1)$$

Where $B_{2\Theta}$ is full width at half maximum, *k* is Scherrer constant which can take values from 0.9 to 1, for this calculation I chose to use 0.9, λ is the wavelength of the x-ray which has a value of 1.540598 in Angstroms, and θ is the angle. Plus, the FWHM value is converted to radians. The plane calculated was the (111) which had the most intense peak.

Table 5. 3: XRD data of Gaussian Fit for (111) plane for crystal size calculation.

	2Θ	Θ	FWHM	FWHM (radians)	Crystallite Size (nm)
$PdNiCo_3O_4$/MWCNT	39.9077	19.95385	0.87152	0.01521	9.7
$PdSnCo_3O_4$/MWCNT	39.8299	19.91495	0.82745	0.01444	10
$PdNiCeO_2$/MWCNT	39.9957	19.99785	0.99927	0.01744	8.5
$PdSnCeO_2$/MWCNT	40.1445	20.07225	0.60133	0.01049	14

From table 5.4 above, the crystal size for $PdNiCo_3O_4$/MWCNT is 9.7 nm, $PdSnCo_3O_4$/MWCNT is 10 nm, $PdNiCeO_2$/MWCNT is 8.5 nm and $PdSnCeO_2$/MWCNT is 14 nm.

HR-TEM images were also used to calculate particle size of the catalysts as can be seen below in the histogram plots. The particle size obtained for the catalysts is summarized in plots below.

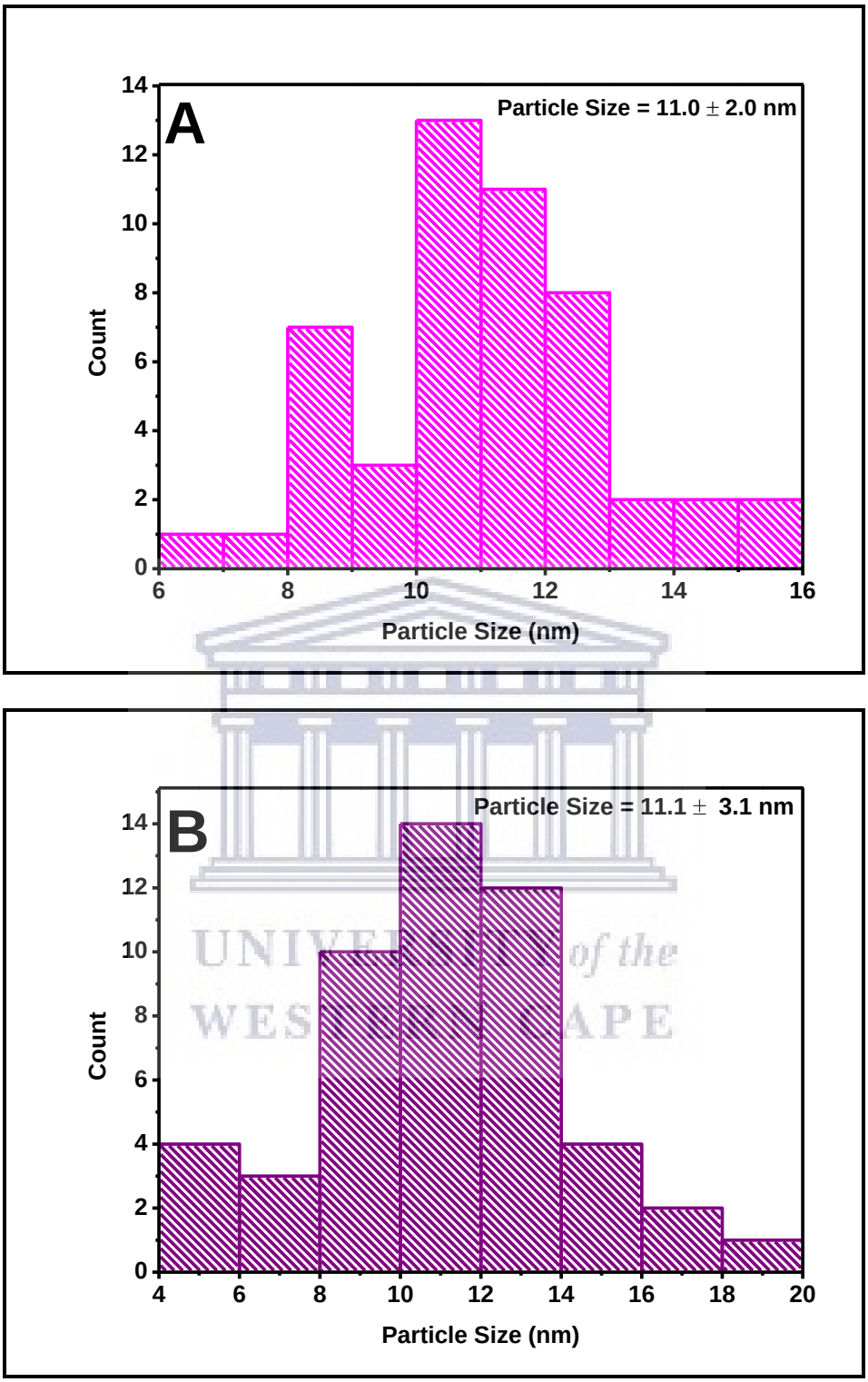

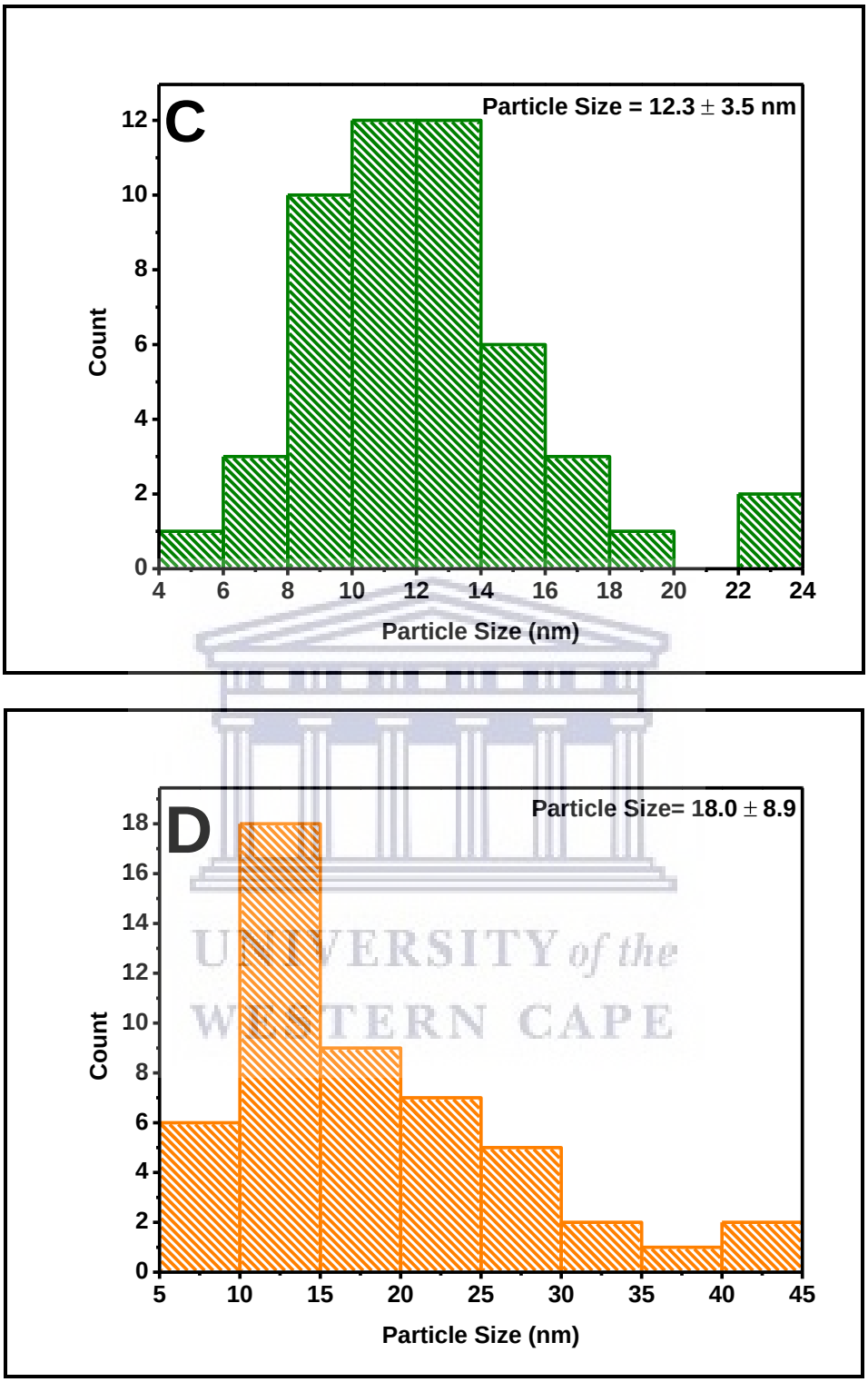

Figure 5. 8: Mean particle size plots from HR-TEM images of the synthesized catalysts of (A) $PdNiCo_3O_4$/MWCNT, (B) $PdSnCo_3O_4$/MWCNT, (C) $PdNiCeO_2$/MWCNT and (D) $PdSnCeO_2$/MWCNT

From the plots above, the particle size for $PdNiCo_3O_4$/MWCNT is 11 nm with a standard deviation of ± 2.0 nm, $PdSnCo_3O_4$/MWCNT is 11.1 nm with a standard deviation of ± 3.1 nm, $PdNiCeO_2$/MWCNT is 12.3 nm with a standard deviation of ± 3.5 nm and $PdSnCeO_2$/MWCNT is 18.0 nm with a standard deviation of ± 8.9 nm. These values above are summarized in the table below with values obtained from XRD and SAXS

Table 5. 4: SAXS, XRD and HR-TEM particle size summary data

Catalysts	SAXS (nm)	XRD (nm)	HR-TEM (nm)
$PdNiCo_3O_4$/MWCNT	18	9.7	11
$PdSnCo_3O_4$/MWCNT	20	10	11.1
$PdNiCeO_2$/MWCNT	15	8.5	12.3
$PdSnCeO_2$/MWCNT	19	14	18

5.5 ELECTROCHEMISTRY OF THE NANOPARTICLES

The electrochemical properties of the synthesized nanoparticles were investigated by the following electrochemical techniques:

• Cyclic Voltammetry (CV)

• Linear Sweep Voltammetry (LSV)

• Electrochemical Impedance spectroscopy (EIS)

• Chonoamperometry

The electroactivity of the synthesized catalysts was investigated through cyclic voltammetry using 1M KOH as electrolyte and 1M Glycerol as the alcohol. The potential window used for the investigation is -1.2 V to +0.8 V. The synthesized catalysts that were investigated were $PdNiCo_3O_4$/MWCNT, $PdSnCo_3O_4$/MWCNT, $PdNiCeO_2$/MWCNT and $PdSnCeO_2$/MWCNT. A three-electrode system comprising of working electrode, counter electrode and reference electrode was used. The working electrode used was glassy-carbon electrode while the counter electrode was platinum electrode and the reference electrode used was Ag/AgCl saturated in KCl.

5.6.1 CYCLIC VOLTAMMETRY AND LINEAR SWEEP VOLTAMMETRY

5.6.1.1 INVESTIGATION OF THE ECSA

A large electro-chemical surface area indicates a better electrode, as more catalyst sites are available for electro-chemical reactions. It is reported that the performance degradation of DGFC is largely owed to the electrochemical active surface area loss of the electrodes. The decrease in the electrochemical active surface area mainly results from the growth of palladium alloy nanoparticles size, the dissolution of palladium and/or other palladium

alloy nanoparticles from the carbon support material. This results in poor durability of the fuel cell catalyst and, accordingly, the fuel cell system.

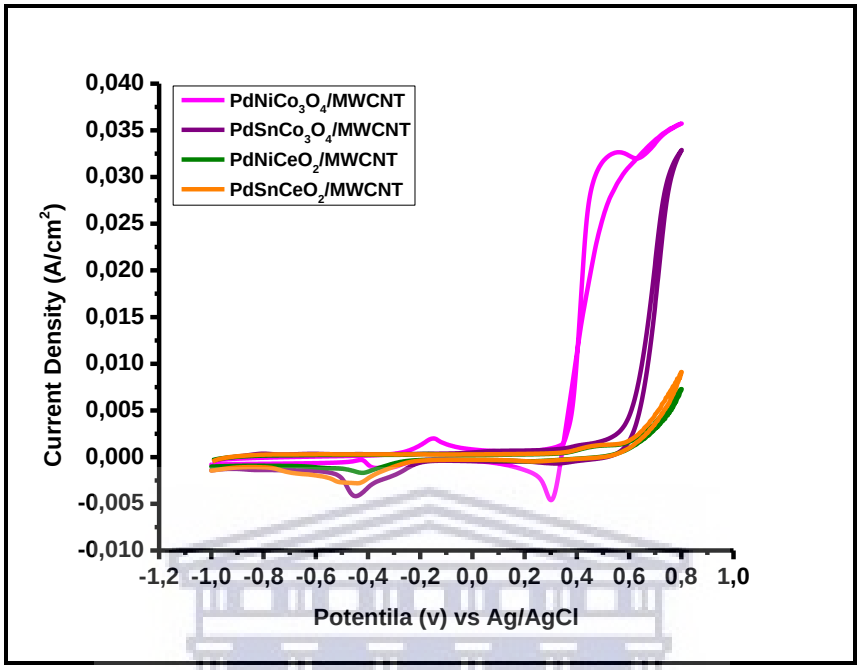

Figure 5. 9: Presents cyclic voltammograms of the synthesized electrocatalyst $PdNiCo_3O_4$/MWCNT, $PdSnCo_3O_4$/MWCNT, $PdNiCeO_2$/MWCNT and $PdSnCeO_2$/MWCNT supported on MWCNTs in 1M KOH @ 30mV/s.

Figure 5.9 compares the electrochemical responses of $PdNiCo_3O_4$/MWCNT, $PdSnCo_3O_4$/MWCNT, $PdNiCeO_2$/MWCNT and $PdSnCeO_2$/MWCNT in 1.0 M KOH without the presence of glycerol, measured in the potential range between -1.2 and 0.8 vs Ag/AgCl. The typical voltammetry curve of Pd in alkaline media was observed, which showed both the oxidation and reduction processes of molecular species. The electrochemical active surface area (ECSA) of $PdNiCo_3O_4$/MWCNT, $PdSnCo_3O_4$/MWCNT, $PdNiCeO_2$/MWCNT and $PdSnCeO_2$/MWCNT catalyst was then calculated. The scan in the negative direction for $PdNiCo_3O_4$/MWCNT showed a peak at 0.28 V vs. Ag/AgCl, following the reduction of NiOOH, without loss of electrochemical activity since NiOOH is a reversible oxide [7]. As this analysis is conducted under alkaline

environment it can be found that the onset of the oxide formation and the peak potential of the oxide reduction for $PdSnCo_3O_4$/MWCNT, $PdNiCeO_2$/MWCNT and $PdSnCeO_2$/MWCNT shifted to more negative potentials which exhibit the chemisorption of OH on the Pd at a negative potential.

The Electrochemical Active Surface Area (ECSA) was calculated from the density of charge associated to the reduction of a full monolayer of Pd oxides [4]. This area was then converted into the effective active surface area by using the factor 420μC.cm^{-2} for the monolayer of Pd Oxides. The results were collected and presented in Table 4.6 below. All EASA calculations for this study were done following equation 4.6 given below:

$$EASA = \frac{QH - adsorption\ (c)}{420\ \mu C.cm^{-2}.(L_{Pd}).(Ag)} \quad (4.6)$$

Q_H = is the charge area from $Pd_{(reduction)}$ peak; 420μC.cm^{-2} is the charge of full coverage for clean polycrystalline Pd and is used as the conversion factor; L_{Pd} is the working electrode Pd loading (μg.cm^{-2}); and Ag is the geometric surface area of the glassy carbon electrode (i.e. 0.196 cm^{-2}). The values for ECSA are reported in m^2.g^{-1}.

Table 5. 5: XRD, HR-TEM and SAXS particle size summary data with ECSA

Catalysts	Particle Size (nm)			ECSA (m^2.g^{-1})
	XRD	HR-TEM	SAXS	
$PdNiCo_3O_4$/MWCNT	9.7	11	18	0.74
$PdSnCo_3O_4$/MWCNT	10	11.1	20	1.3
$PdNiCeO_2$/MWCNT	8.5	12.3	15	5.02
$PdSnCeO_2$/MWCNT	14	18	19	1.14

The table above displays the obtained data of ECSA for the synthesized catalysts, with $PdNiCeO_2$/MWCNT having the larges ECSA followed by $PdSnCo_3O_4$/MWCNT, $PdSnCeO_2$/MWCNT and $PdNiCo_3O_4$/MWCNT respectively. This is attributed to the smaller particles for $PdNiCeO_2$/MWCNT and $PdSnCo_3O_4$/MWCNT with a better particle distribution in comparison to $PdSnCeO_2$/MWCNT and $PdNiCo_3O_4$/MWCNT that are agglomerated due to growth of palladium alloy nanoparticles size as seen is HR-TEM images and SAXS plot in figures 5.1 and 5.6 respectively.

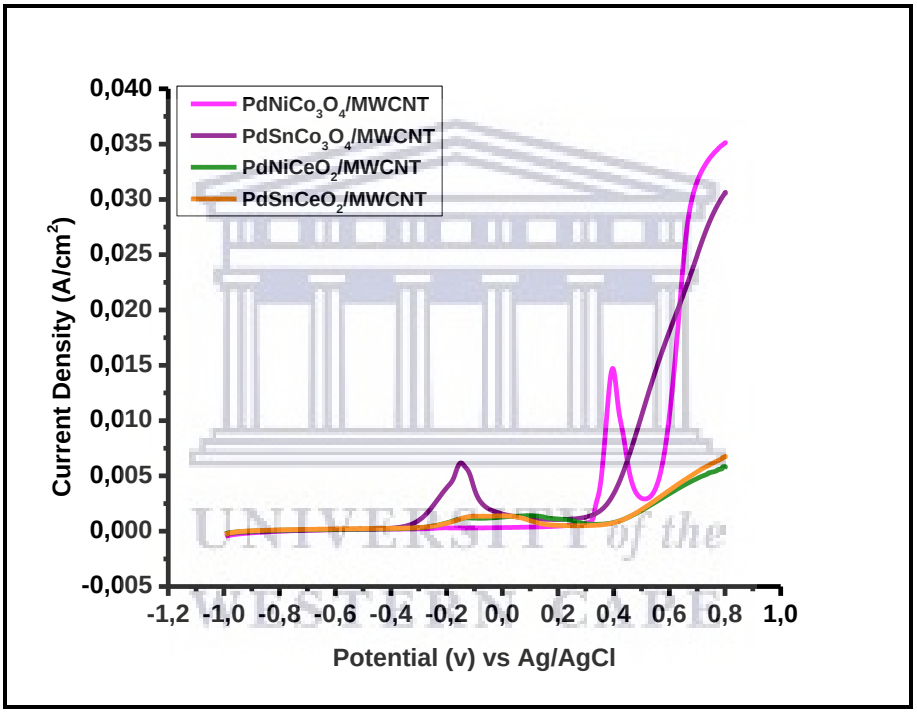

Figure 5. 10: Linear Sweep Voltammetry of the synthesized electrocatalyst $PdNiCo_3O_4$/MWCNT, $PdSnCo_3O_4$/MWCNT, $PdNiCeO_2$/MWCNT and $PdSnCeO_2$/MWCNT supported on MWCNTs in 1M KOH + 1M Glycerol @ 30mV/s.

Figures 5.10 shows the LSV scans for catalyst for $PdNiCo_3O_4$/MWCNT, $PdSnCo_3O_4$/MWCNT, $PdNiCeO_2$/MWCNT and $PdSnCeO_2$/MWCNT glycerol oxidation in 1.0 M KOH solution containing 1.0 M glycerol in the potential range -1.2V to 0.8V. In these LSV scans, a peak is an indication of surface interaction or reaction between some species and catalyst. In the positive-going (forward scan), is attributed to the

electrooxidation of glycerol on the catalysts. Between four synthesized catalysts, the catalyst which shows the best performance towards glycerol oxidation in alkaline media is $PdNiCo_3O_4$/MWCNT followed by $PdNiCeO_2$/MWCNT, $PdSnCo_3O_4$/MWCNT and $PdSnCeO_2$/MWCNT current density respectively. The peak current density (If) for $PdNiCo_3O_4$/MWCNT is 14.46 mA/cm^{-2} which is highest compare to $PdNiCeO_2$/MWCNT 6.137 mA/cm^{-2}, $PdSnCo_3O_4$/MWCNT is 1.412 mA/cm^{-2} and $PdSnCeO_2$/MWCNT is 1.358 mA/cm^{-2} respectively. The results in forward scan shows that the addition of a secondary metals (Ni) in Pd to form catalysts with an oxide can significantly improve the catalytic activity of Pd for glycerol oxidation in alkaline media. This indicates, the significant enhancement oxidation kinetic activity for glycerol by addition of a secondary metal. However, addition of the oxides (Co_3O_4 and CeO_2) help with improving the stability and durability of the catalyst.

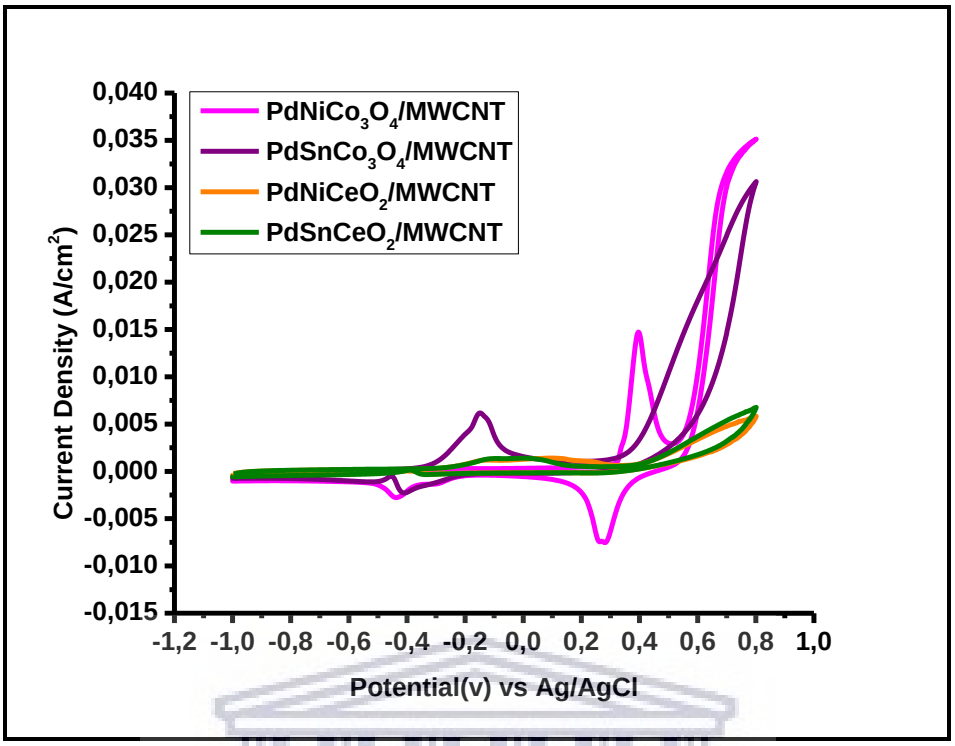

Figure 5. 11: Cyclic Voltammetry of the synthesized electrocatalyst $PdNiCo_3O_4$/MWCNT, $PdSnCo_3O_4$/MWCNT, $PdNiCeO_2$/MWCNT and $PdSnCeO_2$/MWCNT supported on MWCNTs in 1M KOH + 1M Glycerol @ 30mV/s.

Figure 5.11 above explains the peaks which are the indication of surface interaction or reaction between some species and catalyst. In the positive-going (forward scan), is attributed to the electrooxidation of glycerol on the catalysts. Meanwhile, during the reverse scan there is a secondary oxidation peak which associated with incomplete oxidation of carbonaceous residues from the glycerol in forward scan.

Glycerol is a complex molecule, due to this the oxidation of glycerol in alkaline medium can form numbers of possible oxide/hydrous or oxide/hydroxyl surface molecules. This is having been described in reduction wave [6]. Based on the previous study the major electrooxidation of glycerol by using Pd catalyst in alkaline media can be described as equation 4.2 – 4.5 follow [7];

$$Pd + OH^- \leftrightarrow Pd - [OH]_{ads} + e^- \quad (4.2)$$

$$Pd + C_2H_3OH{-}CH_2OH + 3OH^- \leftrightarrow Pd - [C_2H_3(OH)_2{-}CO]_{ads} + 3H_2O + 3e^- \quad (4.3)$$

$$Pd{-}[OH]_{ads} + Pd - [C_2H_3(OH)_2 - CO]_{ads} \rightarrow C_2H_3(OH)_2 - COOH + 2Pd \quad (4.4)$$

$$C_2H_3(OH)_2 - COOH + OH^- \rightarrow C_2H_3(OH)_2 - COO^- + H_2O \quad (4.5)$$

The actual performance glycerol oxidation in alkaline media has been summarized on Table 5.7 below.

Table 5. 6: Electrocatalytic properties of $PdNiCo_3O_4$/MWCNT, $PdSnCo_3O_4$/MWCNT, $PdNiCeO_2$/MWCNT and $PdSnCeO_2$/MWCNT catalysts for glycerol oxidation

	$E_{f(oxidation)}$ (mV vs Ag/AgCl)	$I_{f(oxidation)}$ (mA/cm^{-2})	$E_{r(reduction)}$ (mV vs Ag/AgCl)	$I_{r(reduction)}$ (mA/cm^{-2})	$\frac{I_f}{I_r}$
$PdNiCo_3O_4$/MWCNT	391.9	14.46	-438.5	-2.766	5.23
$PdSnCo_3O_4$/MWCNT	-145.7	6.137	-407.9	-2.289	2.68
$PdNiCeO_2$/MWCNT	98.4	1.412	-361.6	-0.0625	22.59
$PdSnCeO_2$/MWCNT	-68.6	1.358	-387.7	-0.1384	9.81

The data in table 5.7 the catalyst poisoning against the carbonaceous species can be traced from the forward scan to backward (I_f/I_r) scan peak current density ratio as shown in Table 5.7. The ratio of $PdNiCeO_2$/MWCNT catalyst show higher value compared to $PdSnCeO_2$/MWCNT, $PdNiCo_3O_4$/MWCNT and $PdSnCo_3O_4$/MWCNT respectively. The CeO_2 oxide promotes the adsorption of oxygen species such as OH on bimetallic PdNi and PdSn surface to oxidize CO or adsorbed CO-like carbonaceous species on Pd sites. Plus the fewer amount of oxygen on the oxides helps reduce amount of CO carbonaceous

species produced. Therefore $PdNiCeO_2$/MWCNT show better oxidation of glycerol to carbon dioxide during anodic scan and less accumulation of carbonaceous species on the catalyst surface compare to $PdSnCeO_2$/MWCNT, $PdNiCo_3O_4$/MWCNT and $PdSnCo_3O_4$/MWCNT respectively.

5.6.2 ELECTROCHEMICAL IMPEDANCE SPECTROSCOPY (EIS)

EIS was used to investigate the overall kinetics of glycerol oxidation at different potentials. The technique enabled to dissect the various impedance parameters for the charge transfer reaction occurring across the electrode solution interface. Nyquist plots for glycerol oxidation for 1.0 M glycerol in 1.0M KOH solution at 25 ^oC are shown in Figure 5.12. The effective charge transfer resistance (*R*ct) was used to analyze the electrode kinetics of the reaction process.

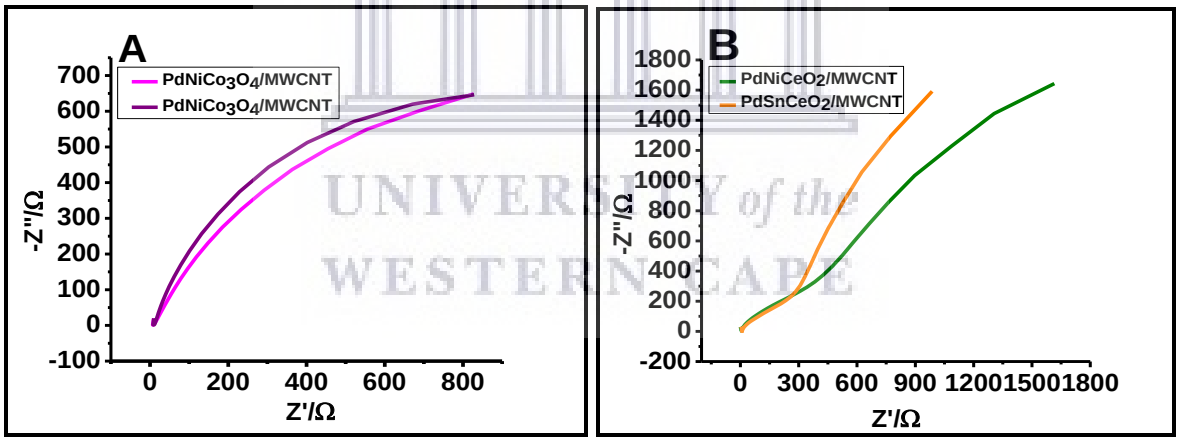

Figure 5. 12: EIS of the synthesized electrocatalyst (A) $PdNiCo_3O_4$/MWCNT, $PdSnCo_3O_4$/MWCNT, (B) $PdNiCeO_2$/MWCNT and $PdSnCeO_2$/MWCNT in 1M KOH + 1M Glycerol @ 30mV.

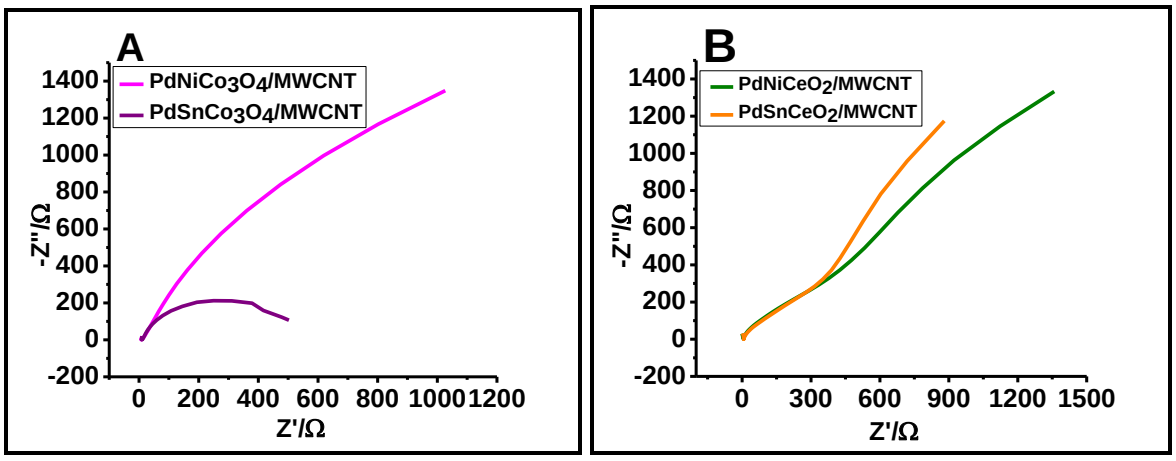

Figure 5. 13: EIS of the synthesized electrocatalyst (A) $PdNiCo_3O_4$/MWCNT, $PdSnCo_3O_4$/MWCNT, (B) $PdNiCeO_2$/MWCNT and $PdSnCeO_2$/MWCNT in 1M KOH + 1M Glycerol @ -30mV.

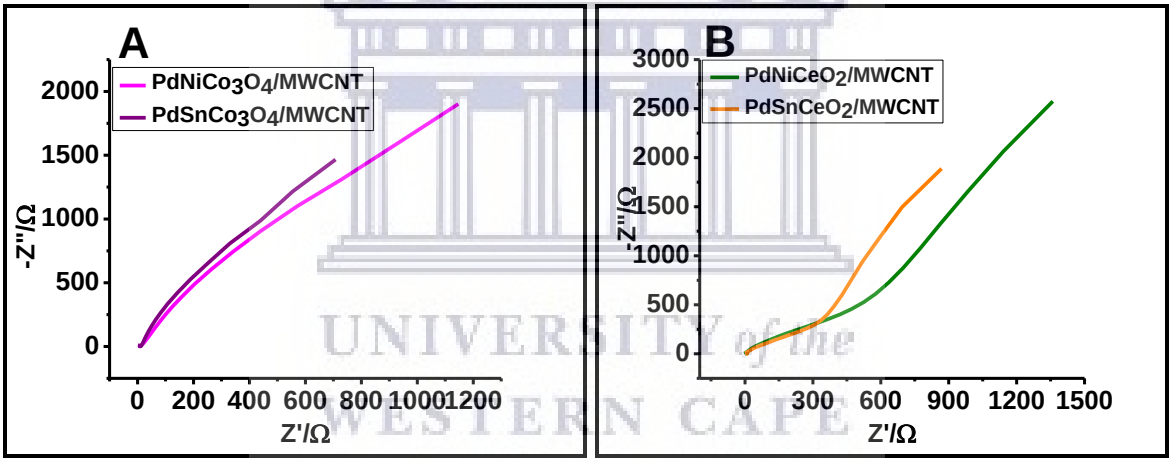

Figure 5. 14: EIS of the synthesized electrocatalyst (A) $PdNiCo_3O_4$/MWCNT, $PdSnCo_3O_4$/MWCNT, (B) $PdNiCeO_2$/MWCNT and $PdSnCeO_2$/MWCNT in 1M KOH + 1M Glycerol @ 10mV.

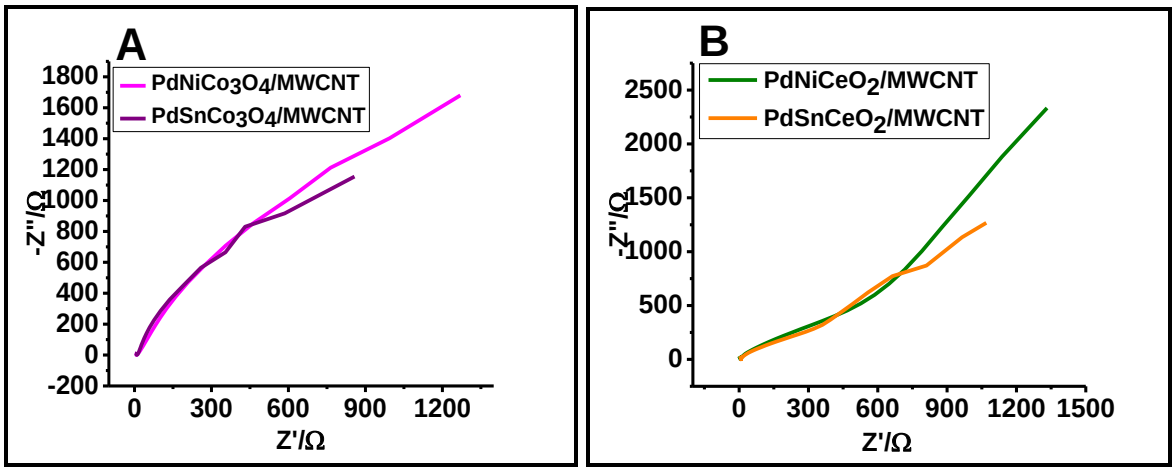

Figure 5. 15: EIS of the synthesized electrocatalyst (A) $PdNiCo_3O_4$/MWCNT, $PdSnCo_3O_4$/MWCNT, (B) $PdNiCeO_2$/MWCNT and $PdSnCeO_2$/MWCNT in 1M KOH + 1M Glycerol @ -10mV.

On graph A of Figures 5.12, 5.13, 5.14, and 5.14 at -30mv and -10mv catalyst $PdSnCo_3O_4$/MWCNT shows better performance with a semi-circle capacitive behavior at -30mv. At 30mv and 10mv $PdNiCo_3O_4$/MWCNT shows better performance. On graph B of Figures 5.12, 5.13, 5.14, and 5.14 the $PdNiCeO_2$/MWCNT and $PdSnCeO_2$/MWCNT catalyst display an ionic resistance that may be due to the a less homogenous catalyst layer on the ink prepared for electrode coating [8].

5.6.3 CHRONOAMPEROMETRY

Chronoamperometric study has been employed for 3600s, where the considerable stability and tolerance to poisoning by intermediates species can be tested. Figure 4.16 below shows the chronoamperometry obtained at room temperature in solutions of 1.0 M KOH and 1.0 M glycerol for 3600s. For all four catalysts, we can observe a decay of current value in the time interval measured for the studied electrocatalysts. However, after the initial drops the performance become stable for all the catalyst tested. From Figure 4.16 shows that the $PdNiCeO_2$/MWCNT demonstrates better stability compared to $PdSnCo_3O_4$/MWCNT, $PdSnCeO_2$/MWCNT and $PdNiCo_3O_4$/MWCNT respectively, indicating that the presence of CeO_2 improves the stability of the catalyst by give a balance adsorption between OH species from Ni and species from glycerol adsorption on Pd, better than the Co_3O_4.

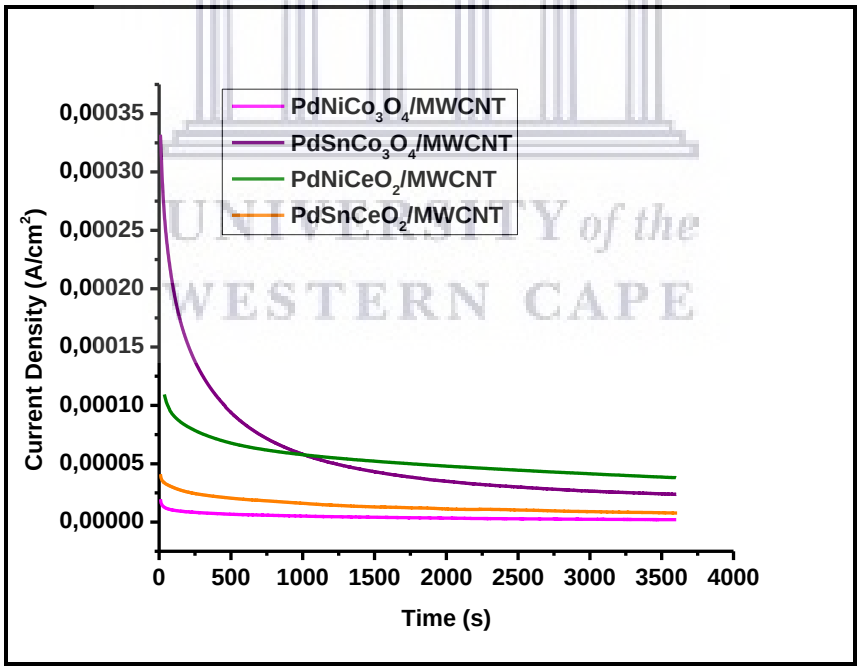

Figure 5. 16: Chronoamperometry of the synthesized electrocatalyst $PdNiCo_3O_4$/MWCNT, $PdSnCo_3O_4$/MWCNT, $PdNiCeO_2$/MWCNT and $PdSnCeO_2$/MWCNT in 1.0 M KOH + 1.0 M Glycerol @ -20mV

CHAPTER 6

RESULTS AND DISCUSSION III

This chapter will focus on analyzing the results obtained from various characterization techniques performed on the synthesized catalysts Palladium cobalt oxide on multi walled carbon nanotubes ($PdCo_3O_4$/MWCNT) and Palladium cerium oxide on multi walled carbon nanotubes ($PdCeO_2$/MWCNT). The various characterizations help determine the various properties exhibited by these synthesized nanoparticles.

6.1 INTERNAL STRUCTURE

The internal structure of the synthesized nanoparticles was evaluated by high resolution transmission electron microscope (HR-TEM). As seen below from figure 6.1 the images obtained from HR-TEM shows a great deal of the internal structure of the synthesized catalysts as the multi walled carbon nanotubes can be seen under the catalysts composite. The inner shape of the synthesized catalysts is unclear additionally the images show that catalysts they may be agglomerated and they have small particle size. Although as said above the internal shape of the catalysts cannot be fully analyzed by the use of HR-TEM because of unclear internal structures the catalysts.

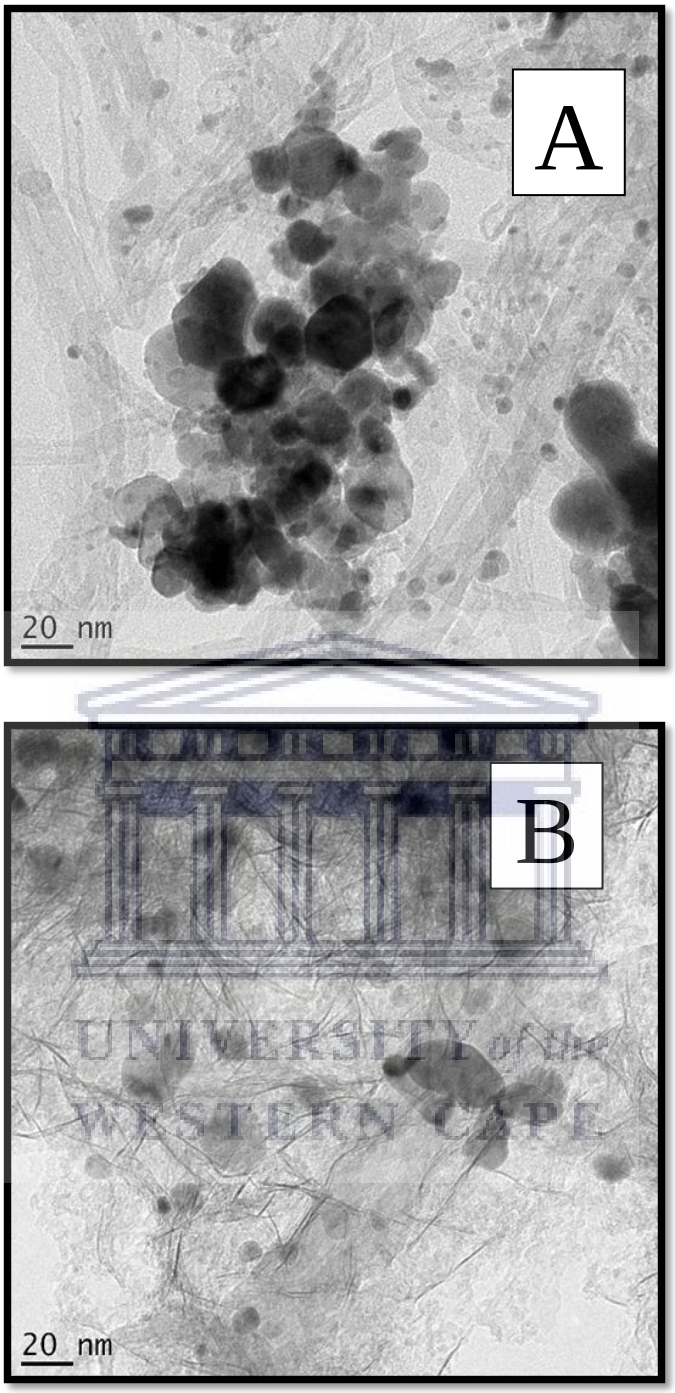

Figure 6. 1: HR-TEM images of the synthesized catalyst of (A) $PdCo_3O_4$/MWCNT and (B) $PdCeO_2$/MWCNT.

Small Angle X-ray Scattering (SAXS) is a technique that can be used to determine the internal structure of the synthesized catalysts. The SAXS analysis was performed using SAXS Space by Anton Paar. From the plot of the shape analysis it shows that all the catalysts were agglomerated and that $PdCo_3O_4$/MWCNT and $PdCeO_2$/MWCNT had a core shell solid sphere.

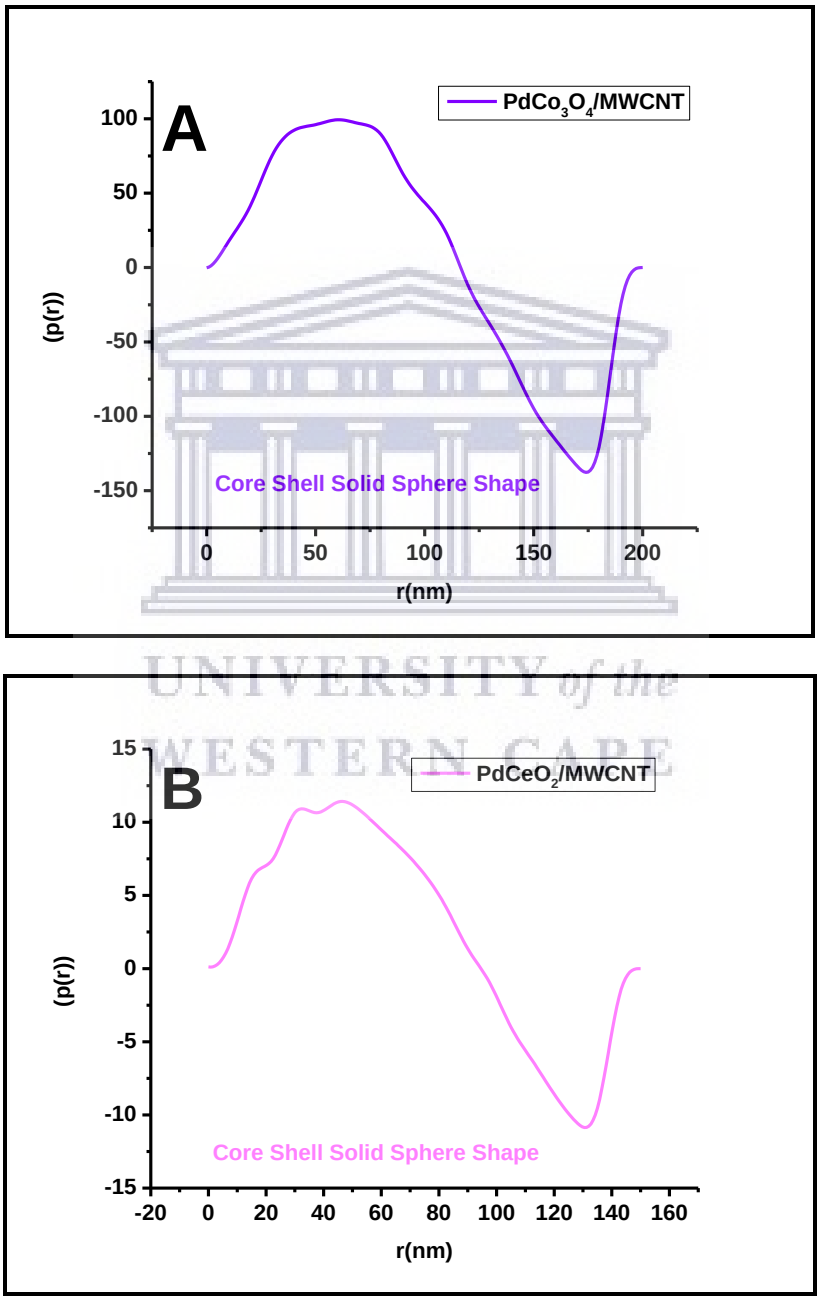

Figure 6. 2: SAXS plot of the shapes of the synthesized catalysts of (A) $PdCo_3O_4$/MWCNT and (B) $PdSnCeO_2$/MWCNT.

Table 6. 1: Shapes of obtained catalysts form SAXS

Sample	Shape
$PdCo_3O_4$/MWCNT	Core Shell Solid Sphere
$PdCeO_2$/MWCNT	Core Shell Solid Sphere

The broad shoulders seen in the SAXS plots above indicate agglomeration of the catalysts as evident in HR-TEM images in figures 6.1.

6.2 PHASE COMPOSITION (CRYSTALLINITY)

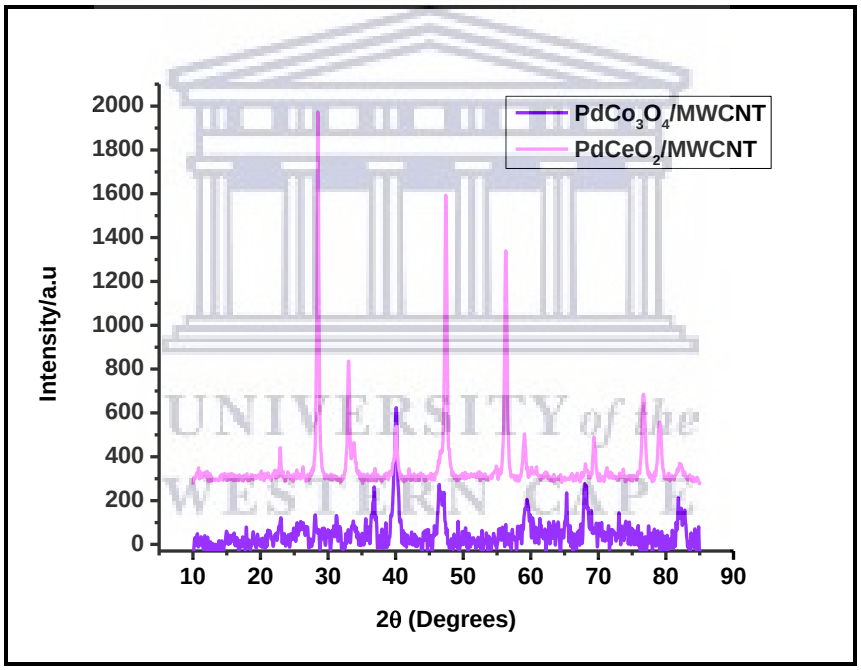

Figure 6. 3: XRD plot of the synthesized catalysts of $PdCo_3O_4$/MWCNT and $PdCeO_2$/MWCNT

The phase composition and crystalline structure of the synthesized nanoparticles were investigated through powder X-ray diffraction (XRD). The catalysts of $PdCo_3O_4$/MWCNT (JCPDS 00-042-1467) and $PdCeO_2$/MWCNT (JCPDS 00-034-0394) both showed a face-center cubic phase.

The peaks at 40.1 º , 46.7 º and 68.63 ° can be assigned to (111), (200) and (531) for reflection of Pd in $PdCo_3O_4$/MWCNT. Meanwhile the peaks at 31.27 º , 36.85 º , 44.99 º , 59.35 º and 65.23 º are assigned to (311), (220), (400), (511) and (440) indexes of Co_3O_4 in $PdCo_3O_4$/MWCNT. For $PdCeO_2$/MWCNT the peaks are 40.1 º and 46.7 º which are assigned to (111) and (200) for reflection of Pd in $PdCeO_2$/MWCNT, then peaks at 28.55 º , 33.08 º , 47.48 º , 56.09 º , 59.09 º , 69.04 º , 76.70 º and 79.07 º and are assigned to these miller indexes (111), (200), (220), (311), (222), (400), (331) and (420) respectively [6].

These peaks were also confirmed by the diffraction obtained from selected area electron diffraction (SAED) in figure 6.4 below. The crystallinity of the nanoparticles can also be seen from the spectrum which shows the nanoparticles to be polycrystalline. This is also an observable trend seen in SAED micrograph obtained from HR-TEM analysis. The trend for the crystallinity of the nanoparticles was $PdCo_3O_4$/MWCNT > $PdCeO_2$/MWCNT meaning that $PdCo_3O_4$/MWCNT had the highest degree of crystallinity.

Selected Area Electron Diffraction (SAED) was obtained from HR-TEM which revealed and confirmed that the synthesized catalysts were crystalline. The planes found in XRD plot above was also observed in the SAED image obtained, which confirms the phase composition of the synthesized catalysts.

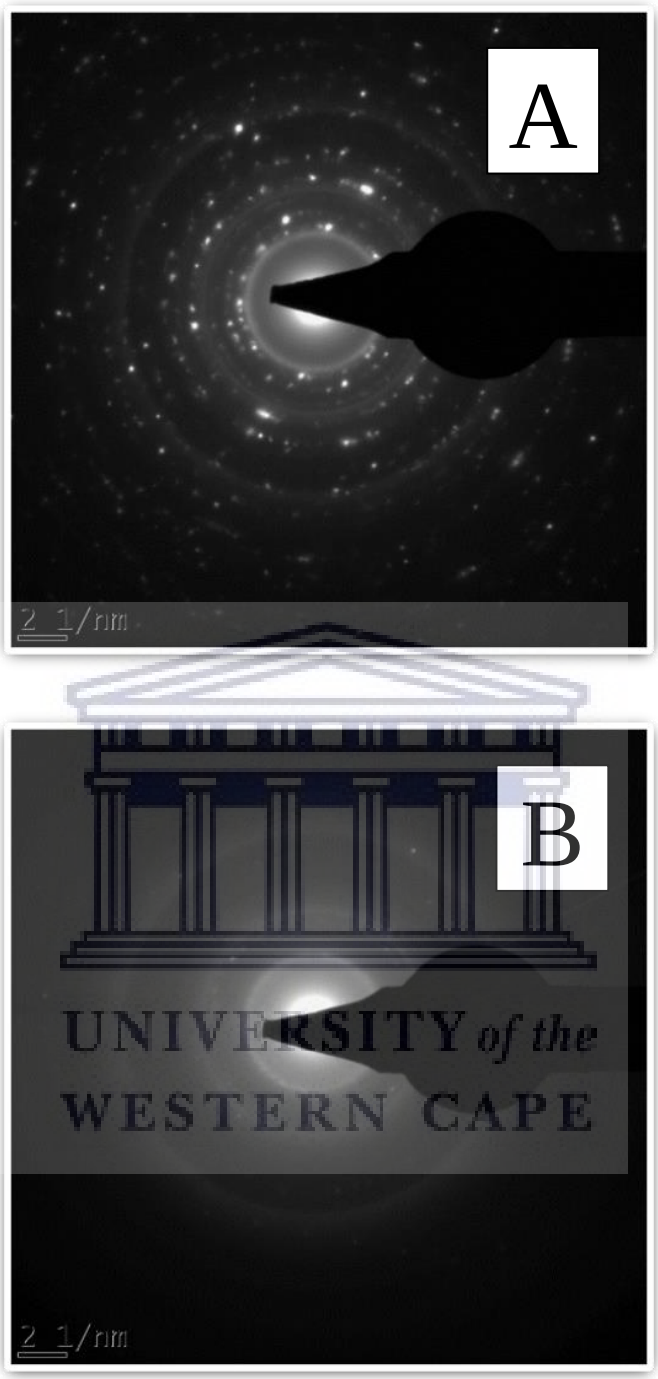

Figure 6. 4: SAED images of the synthesized catalysts of (A) $PdNiCo_3O_4$/MWCNT and (B) $PdSnCo_3O_4$/MWCNT

The lattice fringe images obtained for the synthesized nanoparticles further confirms that the nanoparticles were crystalline and the d-spacing value of the lattice fringes was

evaluated and assigned with the corresponding plane (miller index) as can be seen in figure 6.5 below.

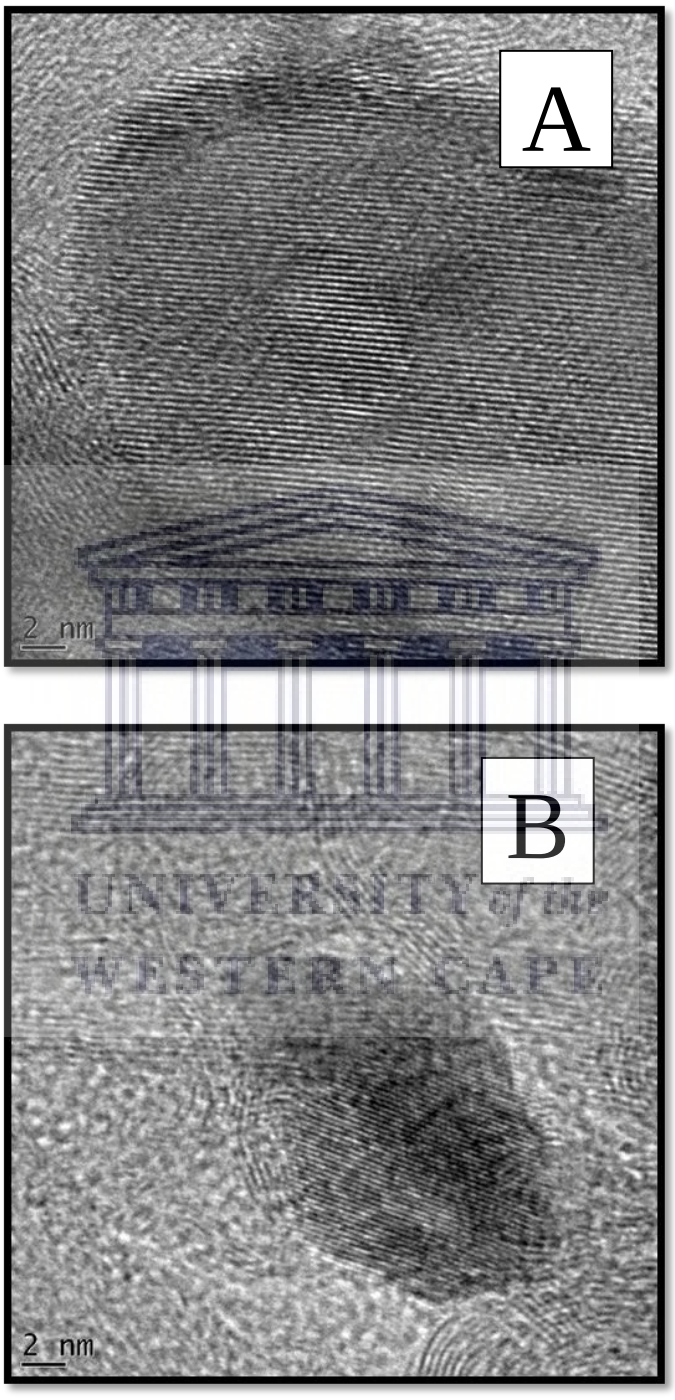

Figure 6. 5: HR-TEM image showing the lattice fringe and d-spacing value of the lattice fringe indicating the plane with the d-space value for the synthesized nanoparticles of (A) $PdCo_3O_4$/MWCNT and (B) $PdSnCo_3O_4$/MWCNT

The calculated d-spacing value for the four samples are $PdCo_3O_4$/MWCNT is 0.366 nm at 111 plane and for $PdCeO_2$/MWCNT is 0.278 nm at 200 plane.

6.3 ELEMENTAL COMPOSITION

The elemental composition of the synthesized catalysts was evaluated using Energy Dispersive X-ray spectroscopy (EDX) and Inductive Couple Plasma (ICP) as shown in Figure 6.2 and table 6.3 respectively. The instruments used are EDS analyzer coupled into the High-Resolution Transmission Electron Microscope used for HR-TEM analysis and ICP analyzer used techniques for the determination of trace concentrations of elements in samples.

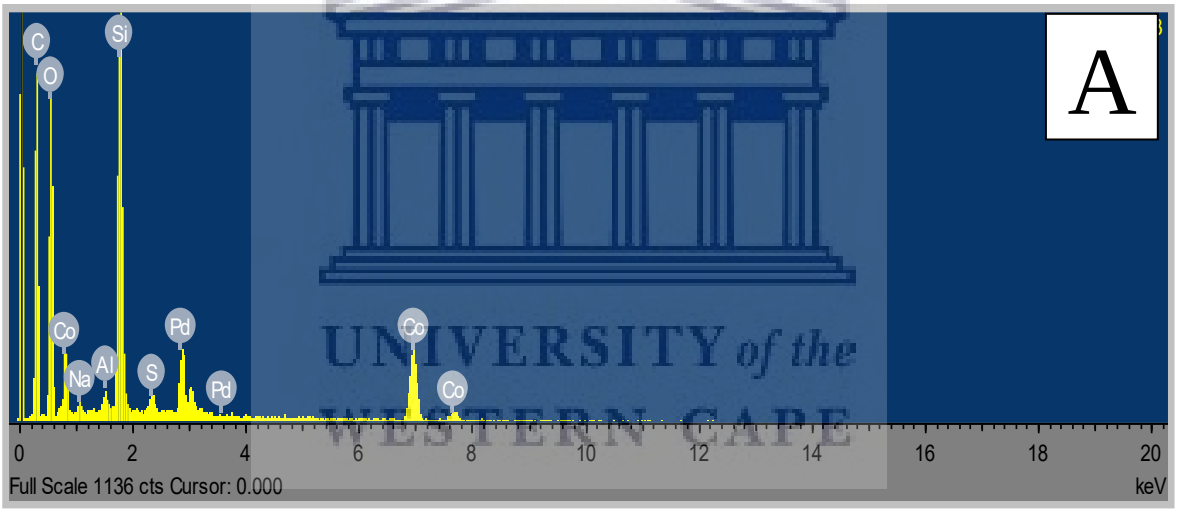

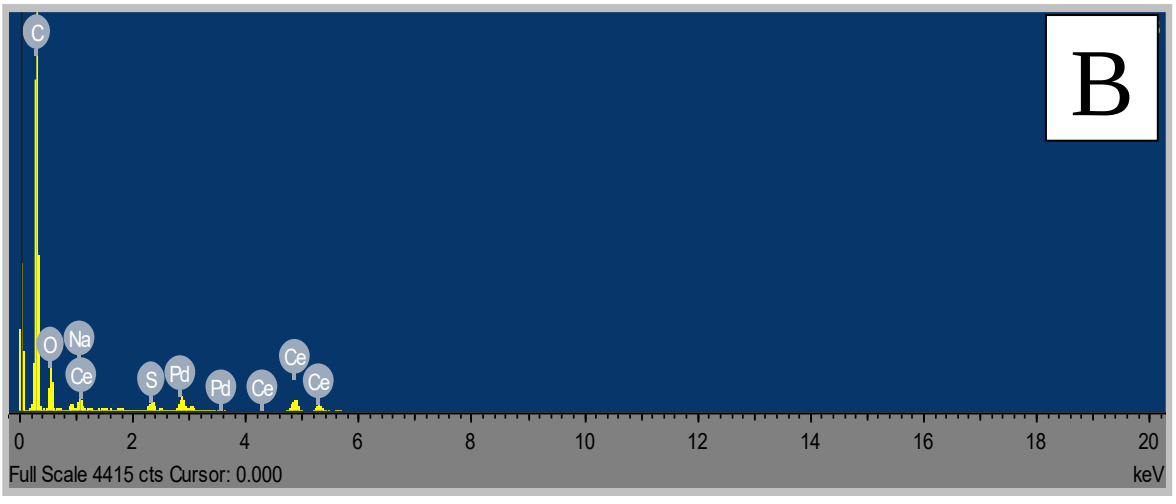

The EDS of the catalysts showed all the elements expected for the nanoparticles. $PdCo_3O_4$/MWCNT spectra shows the presence of palladium, cobalt, oxygen and carbon. $PdCeO_2$/MWCNT spectra shows the presence of palladium, cerium, oxygen and carbon. The percent amount of the elemental compositions are in the table above.

Table 6. 2: ICP data of the catalysts

	Pd	Co	Ce
$PdCo_3O_4$/MWCNT	26.94 mg/L	61.06 mg/L	X
$PdCeO_2$/MWCNT	50.19 mg/L	X	907.39 mg/L

Pd/C showed the most presence of palladium with a value of 190.07 mg/L. The palladium values for Pd/MWCNT and PdNi/MWCNT catalysts are relative the same at 63.2 mg/L and 63.7 mg/L respectively, while for PdSn/MWCNT its 70.8 mg/L. The nickel and tin values are 72.5 mg/L and 97.8 mg/L respectively.

6.4 SIZE DISTRIBUTION

The size distribution of the synthesized catalysts was studied and evaluated. The particle size was evaluated using SAXS and HR-TEM, while the crystal size was evaluated from XRD data of the synthesized catalysts. The summary of the size distribution for the synthesized nanoparticles is given by the SAXS plot of the size distribution and HR-TEM average particle.

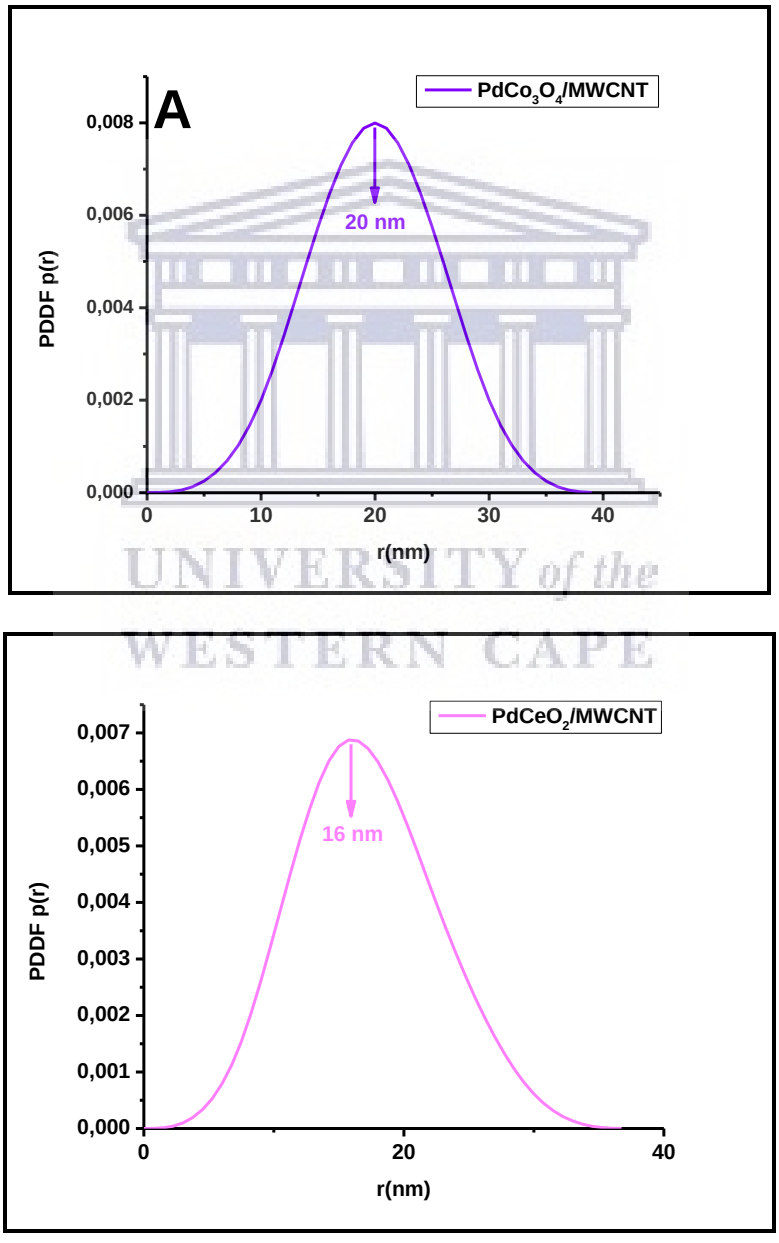

Figure 6. 6: SAXS plot of size distribution of the synthesized catalysts of (A) $PdCo_3O_4$/MWCNT and (B) $PdCeO_2$/MWCNT.

The particle size distribution obtained from SAXS plot above in figure 6.6 shows that $PdCo_3O_4$/MWCNT has a mean particle size of 20 nm and for $PdCeO_2$/MWCNT has a mean particle size of 16 nm.

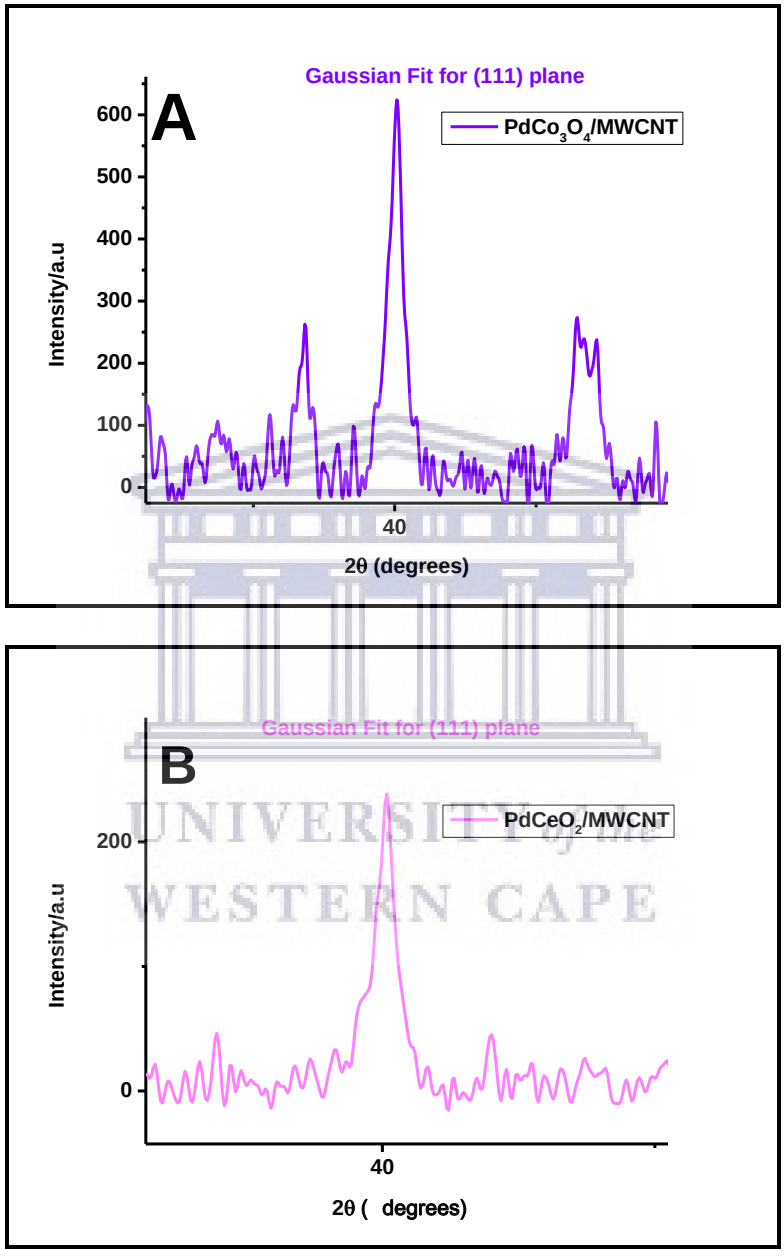

Figure 6. 7: XRD plot of Gaussian Fit for (111) plane for crystal size calculation of the catalysts of (A) $PdCo_3O_4$/MWCNT and (B) $PdCeO_2$/MWCNT.

The Debye-Scherrer equation was used to calculate the crystal size and the equation is given as:

$$d = \frac{k\lambda}{B2\theta Cos\theta} \quad (4.1)$$

Where $B_{2\Theta}$ is full width at half maximum, *k* is Scherrer constant which can take values from 0.9 to 1, for this calculation I chose to use 0.9, λ is the wavelength of the x-ray which has a value of 1.540598 in Angstroms, and θ is the angle. Plus, the FWHM value is converted to radians. The plane calculated was the (111) which had the most intense peak. Table 6.4 below gives the various data points acquired to make the calculations.

Table 6. 3: XRD data of Gaussian Fit for (111) plane for crystal size calculation.

	2Θ	Θ	FWHM	FWHM (radians)	Crystallite Size (nm)
$PdCo_3O_4$/MWCNT	40.036	20.0183	0.68037	0.0118746	12
$PdCeO_2$/MWCNT	40.047	20.0235	0.55684	0.0097186	15

From table 6.4 above, the crystal size for $PdCo_3O_4$/MWCNT is 12 nm and $PdCeO_2$/MWCNT is 15 nm. HR-TEM images were also used to calculate particle size of the catalysts as can be seen below in the histogram plots. The crystal size obtained for the catalysts is summarized in plots below.

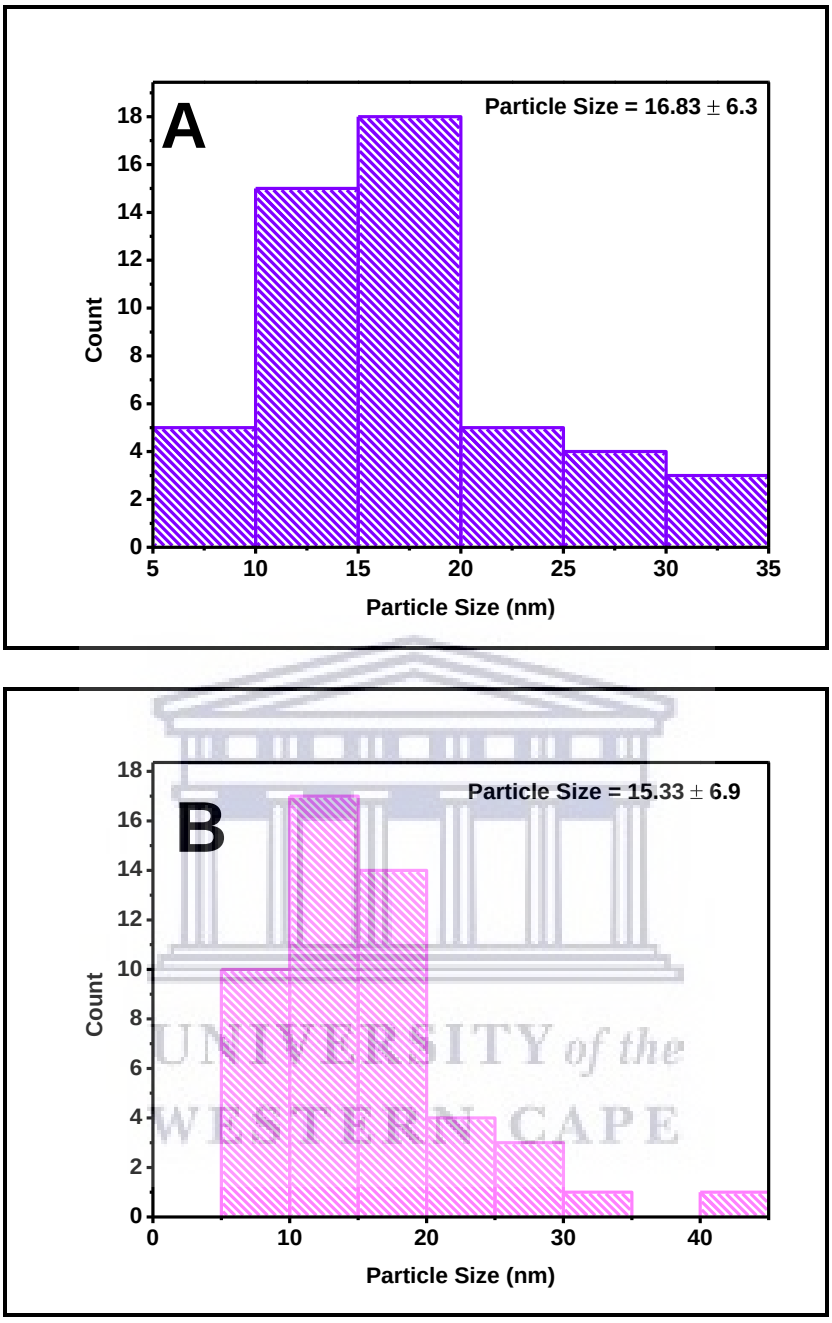

Figure 6. 8: Mean particle size plots from HR-TEM images of the synthesized catalysts of (A) $PdCo_3O_4$/MWCNT and (B) $PdCeO_2$/MWCNT

From the plots above, the particle size for $PdCo_3O_4$/MWCNT is 16.83 nm with a standard deviation of ± 6.3 nm and $PdCeO_2$/MWCNT is 15.33 nm with a standard deviation of ± 6.9 nm. These values above are summarized in the table below with values obtained from XRD and SAXS

Table 6. 4: SAXS, XRD and HR-TEM particle size summary data

Catalysts	SAXS (nm)	XRD (nm)	HR-TEM (nm)
$PdCo_3O_4$/MWCNT	20	12	16.83
$PdCeO_2$/MWCNT	16	15	15.33

6.5 ELECTROCHEMISTRY OF THE NANOPARTICLES

The electrochemical properties of the synthesized nanoparticles were investigated by the following electrochemical techniques:

• Cyclic Voltammetry (CV)

• Linear Sweep Voltammetry (LSV)

• Electrochemical Impedance spectroscopy (EIS)

• Chonoamperometry (CA)

The electroactivity of the synthesized catalysts was investigated through cyclic voltammetry using 1M KOH as electrolyte and 1M Glycerol as the alcohol. The potential window used for the investigation is -1.2 V to +0.8 V. The synthesized catalysts that were investigated were $PdCo_3O_4$/MWCNT and $PdCeO_2$/MWCNT. A three-electrode system comprising of working electrode, counter electrode and reference electrode was used. The working electrode used was glassy-carbon electrode while the counter electrode was platinum electrode and the reference electrode was Ag/AgCl saturated in KCl.

6.6.1 CYCLIC VOLTAMMETRY AND LINEAR SWEEP VOLTAMMETRY

6.6.1.1 INVESTIGATION OF THE ECSA

A large electro-chemical surface area indicates a better electrode, as more catalyst sites are available for electro-chemical reactions. It is reported that the performance degradation of DGFC is largely owed to the electrochemical active surface area loss of the electrodes. The decrease in the electrochemical active surface area mainly results from the growth of palladium alloy nanoparticles size, the dissolution of palladium and/or other palladium alloy nanoparticles from the carbon support material. This results in poor durability of the fuel cell catalyst and, accordingly, the fuel cell system.

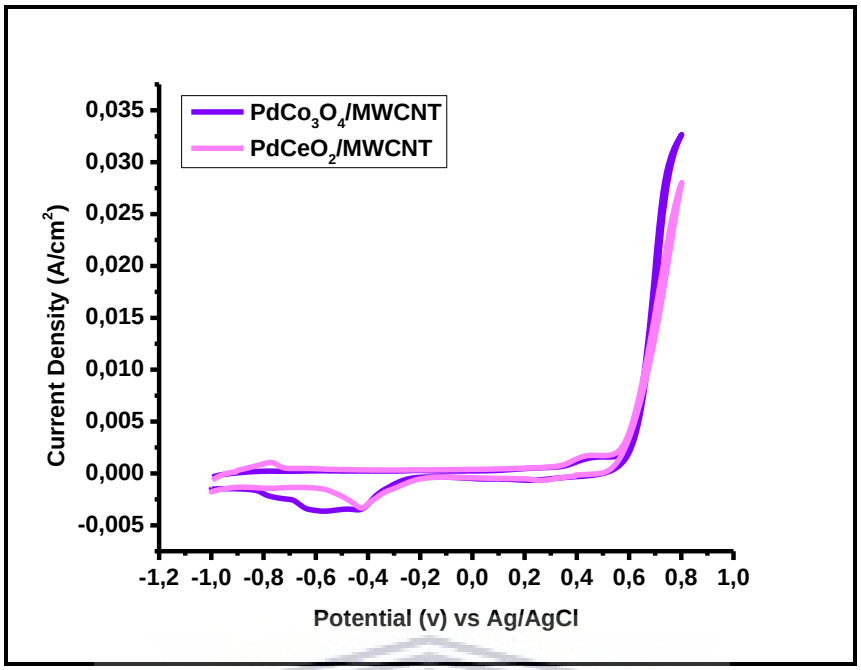

Figure 6. 9: Presents cyclic voltammograms of the synthesized electrocatalyst $PdCo_3O_4$/MWCNT and $PdCeO_2$/MWCNT supported on MWCNTs in 1M KOH @ 30mV/s.

Figure 6.9 compares the electrochemical responses of $PdCo_3O_4$/MWCNT and $PdCeO_2$/MWCNT in 1.0 M KOH without the presence of glycerol, measured in the potential range between -1.2 and 0.8 vs Ag/AgCl. The typical voltammetric curve of Pd in alkaline media was observed the electrochemical active surface area (ECSA) of $PdCo_3O_4$/MWCNT and $PdCeO_2$/MWCNT catalyst was then calculated.

As this analysis is conducted under alkaline environment it can be found that the onset of the oxide formation and the peak potential of the oxide reduction for $PdCo_3O_4$/MWCNT shifted to more negative potentials which exhibit the chemisorption of OH on the Pd at a negative potential.

The Electrochemical Active Surface Area (ECSA) was calculated from the density of charge associated to the reduction of a full monolayer of Pd oxides [4]. This area was then converted into the effective active surface area by using the factor 420μC.cm^{-2} for the

monolayer of Pd Oxides. The results were collected and presented in Table 6.5 below. All ECSA calculations for this study were done following equation 4.6 given below:

$$EASA = \frac{QH - adsorption\ (c)}{420\ \mu C.cm^{-2}.(L_{pd}).(Ag)} \quad (4.6)$$

Q_H = 420μC.cm^{-2} is the charge of full coverage for clean polycrystalline Pd and is used as the conversion factor; L_{Pd} is the working electrode Pd loading (μg.cm^{-2}); and Ag is the geometric surface area of the glassy carbon electrode (i.e. 0.196 cm^{-2}). The values for ECSA are reported in m^2.g^{-1}.

Table 6. 5: XRD, HR-TEM and SAXS particle size summary data with ECSA

Catalysts	Particle Size (nm)			ECSA (m^2.g^{-1})
	XRD	HR-TEM	SAXS	
$PdCo_3O_4$/MWCNT	12	16.83	20	1.89
$PdCeO_2$/MWCNT	15	15.33	16	0.99

The table above displays the obtained data of ECSA for the synthesized catalysts, with $PdCo_3O_4$/MWCNT having the larges ECSA followed by $PdCeO_2$/MWCNT respectively. This is attributed to the smaller particles for $PdCo_3O_4$/MWCNT with a better particle distribution in comparison to $PdCeO_2$/MWCNT. $PdCeO_2$/MWCNT is agglomerated due to growth of palladium alloy nanoparticles size as seen is HR-TEM images and SAXS plot in figures 6.1 and 6.6 respectively.

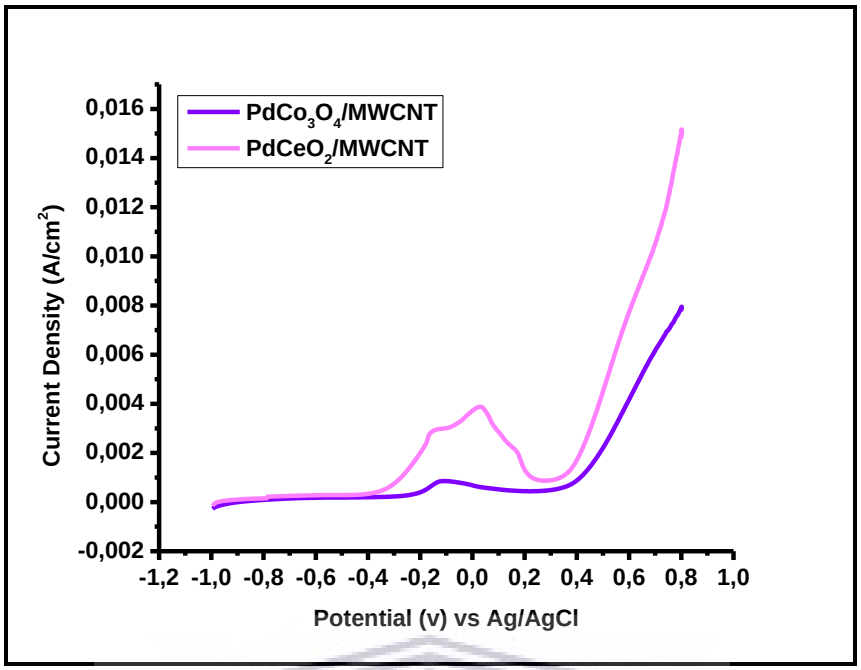

Figure 6. 10: Linear Sweep Voltammetry of the synthesized electrocatalyst $PdCo_3O_4$/MWCNT and $PdCeO_2$/MWCNT supported on MWCNTs in 1M KOH + 1M Glycerol @ 30mV/s.

Figures 6.10 shows the LSV scans for $PdCo_3O_4$/MWCNT and $PdCeO_2$/MWCNT catalyst for glycerol oxidation in 1.0 M KOH solution containing 1.0 M glycerol in the potential range -1.2V to 0.8V. In these LSV scans, a peak is an indication of surface interaction or reaction between some species and catalyst. In the positive-going (forward scan), is attributed to the electrooxidation of glycerol on the catalysts. Between two synthesized catalysts, the $PdCeO_2$/MWCNT catalyst shows the best performance towards glycerol oxidation in alkaline media followed by $PdCo_3O_4$/MWCNT current density. The peak current density (If) for $PdCeO_2$/MWCNT is 3.899 mA/cm^{-2} which is highest compared to $PdCo_3O_4$/MWCNT 0.8295 mA/cm^{-2}.

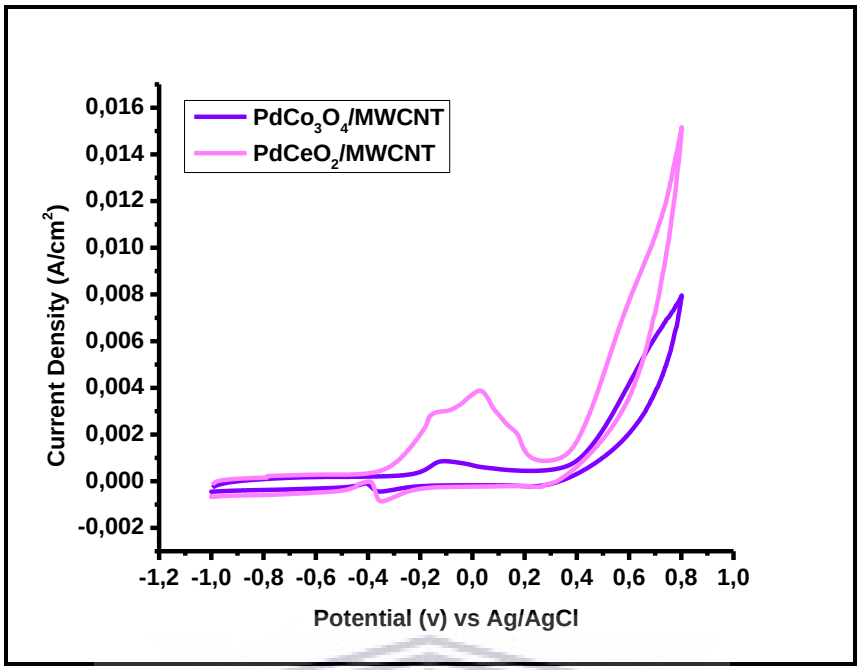

Figure 6. 11: Cyclic Voltammetry of the synthesized electrocatalyst $PdCo_3O_4$/MWCNT and $PdCeO_2$/MWCNT supported on MWCNTs in 1M KOH + 1M Glycerol @ 30mV/s.

Figure 6.11 above explains the peaks which are the indication of surface interaction or reaction between some species and catalyst. In the positive-going (forward scan), is attributed to the electrooxidation of glycerol on the catalysts Meanwhile, during the reverse scan there is a secondary oxidation peak which associated with incomplete oxidation of carbonaceous residues from the glycerol in forward scan.

Glycerol is a complex molecule, due to this the oxidation of glycerol in alkaline medium can form numbers of possible oxide/hydrous or oxide/hydroxyl surface molecules. This is having been described in reduction wave [6]. Based on the previous study the major electrooxidation of glycerol by using Pd catalyst in alkaline media can be described as equation 4.2 – 4.5 follow [7];

$$Pd + OH^- \leftrightarrow Pd - [OH]_{ads} + e^- \quad (4.2)$$

$$Pd + C_2H_3OH{-}CH_2OH + 3OH^- \leftrightarrow Pd - [C_2H_3(OH)_2{-}CO]_{ads} + 3H_2O + 3e^- \quad (4.3)$$

$$Pd{-}[OH]_{ads} + Pd - [C_2H_3(OH)_2 - CO]_{ads} \rightarrow C_2H_3(OH)_2 - COOH + 2Pd \quad (4.4)$$

$C_2H_3(OH)_2 - COOH + OH^- \rightarrow C_2H_3(OH)_2 - COO^- + H_2O$ (4.5)

The actual performance glycerol oxidation in alkaline media has been summarized on Table 6.7 below.

Table 6. 6: Electrocatalytic properties of $PdCo_3O_4$/MWCNT and $PdCeO_2$/MWCNT catalysts for glycerol oxidation.

	$E_{f(oxidation)}$ (mV vs Ag/AgCl)	$I_{f(oxidation)}$ (mA/cm^{-2})	$E_{r(reduction)}$ (mV vs Ag/AgCl)	$I_{r(reduction)}$ (mA/cm^{-2})	$\frac{I_f}{I_r}$
$PdCo_3O_4$/MWCNT	-108.5	-0.8295	-359.73	-0.4046	2.05
$PdCeO_2$/MWCNT	28.33	3.899	-349.78	-0.8606	4.53

The data in table 6.7 the catalyst poisoning against the carbonaceous species can be traced from the forward scan to backward (I_f/I_r) scan peak current density ratio as shown in Table 6.7. The ratio of $PdCeO_2$/MWCNT catalyst show higher value compare to $PdCo_3O_4$/MWCNT. Therefore $PdCeO_2$/MWCNT show better oxidation of glycerol to carbon dioxide during anodic scan and less accumulation of carbonaceous species on the catalyst surface compare to $PdCo_3O_4$/MWCNT [6].

6.6.2 ELECTROCHEMICAL IMPEDANCE SPECTROSCOPY (EIS)

EIS was used to investigate the overall kinetics of glycerol oxidation at different potentials. The technique enabled to dissect the various impedance parameters for the charge transfer reaction occurring across the electrode solution interface. Nyquist plots for glycerol oxidation for 1.0 M glycerol in 1.0M KOH solution at 25 ^{o}C are shown in Figure 4.12. The effective charge transfer resistance (*R*ct) was used to analyze the electrode kinetics of the reaction process.

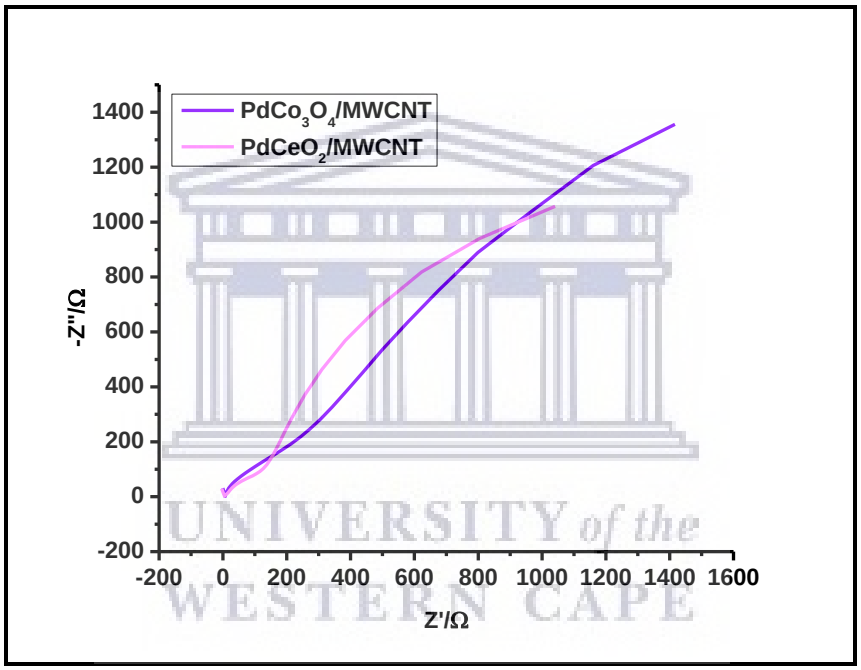

Figure 6. 12: EIS of the synthesized electrocatalyst $PdCo_3O_4$/MWCNT and $PdCeO_2$/MWCNT in 1M KOH + 1M Glycerol @ 30mV.

Shown in Figure 6.12, is the Nyquist plot is characterized by a capacitive feature for Pd/C, Pd/MWCNT and PdSn/MWCNT, as expected for hydrogen adsorption/desorption and double layer charging/ discharging phenomena. However, for PdNi/MWCNT there is a changeover from capacitive behavior to resistive behavior, as shown in Figure 4.13. At this potentials, the Nyquist plot resembles a semicircle, which can be assigned to kinetically

controlled reaction. The small arc in the high frequency region may be associated with the chemisorption and dehydrogenation of the glycerol molecule at the initial stage of the oxidation process. A charge transfer resistance (*R*ct) for the kinetically controlled reactions may be represented by the diameter of the semicircle in the medium frequency and is related to the charge transfer reaction kinetics according to

$$R_{ct} = \frac{RT}{nF\, i_o} \tag{4.7}$$

$$i_o = nFAk_o C_o^{(1-\alpha)} C_R^{\alpha} \tag{4.8}$$

where *R*: molar gas constant (J.mol^{-1} k^{-1}); *T*: temperature (K); *n*: number of electrons transferred; *F*: Faraday constant (C); i_o: exchange current (A); *A*: reaction area (cm^2); k_0: standard heterogeneous rate constant (cm.sec^{-1}); C_o, C_R: bulk concentration of oxidant and reductant species (mol.L^{-1}); α: transfer coefficient.

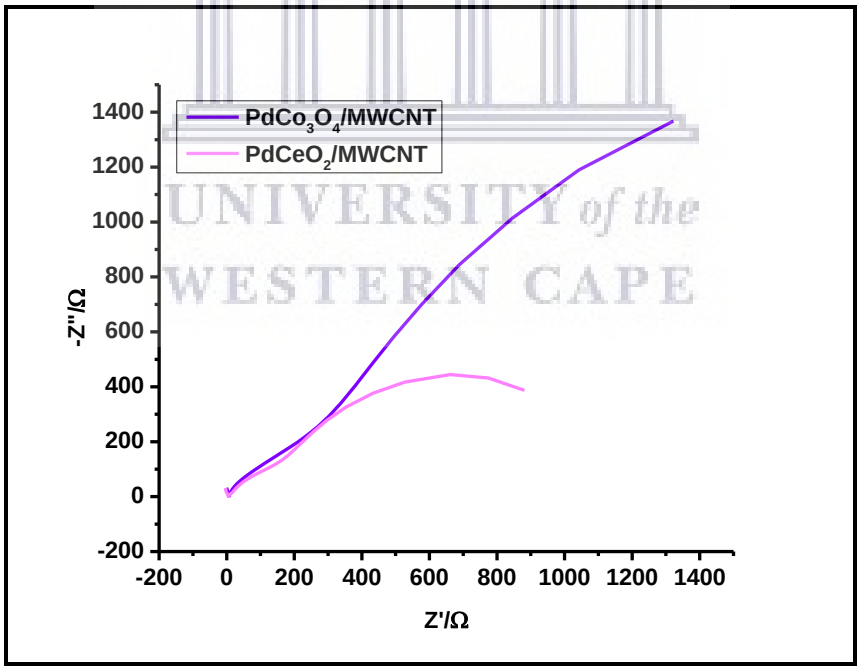

Figure 6. 13: EIS of the synthesized electrocatalyst $PdCo_3O_4$/MWCNT and $PdCeO_2$/MWCNT in 1M KOH + 1M Glycerol @ -30mV.

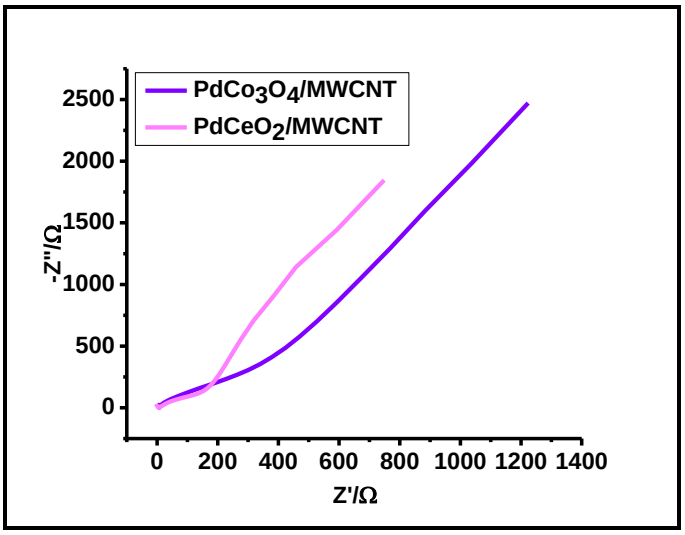

Figure 6. 14: EIS of the synthesized electrocatalyst $PdCo_3O_4$/MWCNT and $PdCeO_2$/MWCNT in 1M KOH + 1M Glycerol @ 10mV.

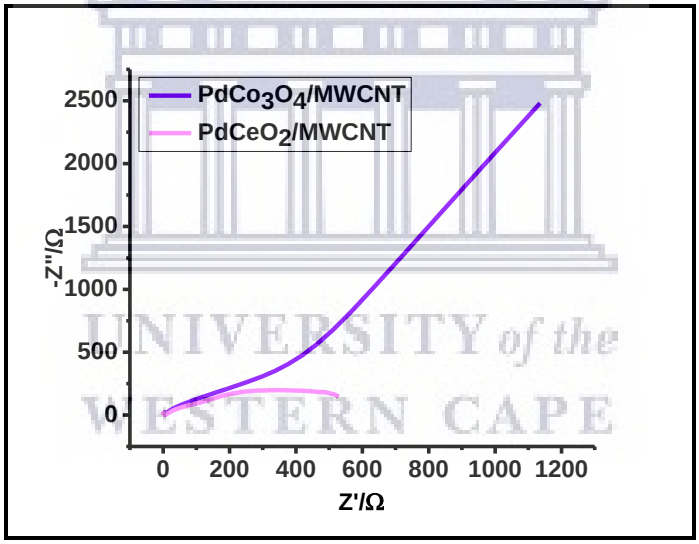

Figure 6. 15: EIS of the synthesized electrocatalyst $PdCo_3O_4$/MWCNT and $PdCeO_2$/MWCNT in 1M KOH + 1M Glycerol @ -10mV.

$PdCo_3O_4$/MWCNT on has an ionic resistance on all the different voltages, with $PdCeO_2$/MWCNT behaving the same at 30mv and 10mv. While $PdCo_3O_4$/MWCNT performing better than $PdCeO_2$/MWCNT at 30mv and 10mv. $PdCeO_2$/MWCNT performs better than $PdCo_3O_4$/MWCNT at -30mv and -10mv displaying a semicircle for its resistive behavior

6.6.3 CHRONOAMPEROMETRY

Chronoamperometric study has been employed for 3600s, where the considerable stability and tolerance to poisoning by intermediates species can be tested. Figure 6.16 below shows the chronoamperometry obtained at room temperature in solutions of 1.0 M KOH and 1.0 M glycerol for 3600s. For the two catalysts, we can observe a decay of current value in the time interval measured for the studied electrocatalysts. However, after the initial drops the performance become stable for all the catalyst tested. From Figure 6.16 shows that the $PdCeO_2$/MWCNT demonstrates better stability compared to $PdCo_3O_4$/MWCNT, indicating that the presence of CeO_2 improves the stability of the catalyst by give a balance adsorption between OH species from CeO_2 and species from glycerol adsorption on Pd, better than the Co_3O_4. While the solubility of the $PdCo_3O_4$/MWCNT metal oxides in alkaline solution have decrease the catalysts stability [9].

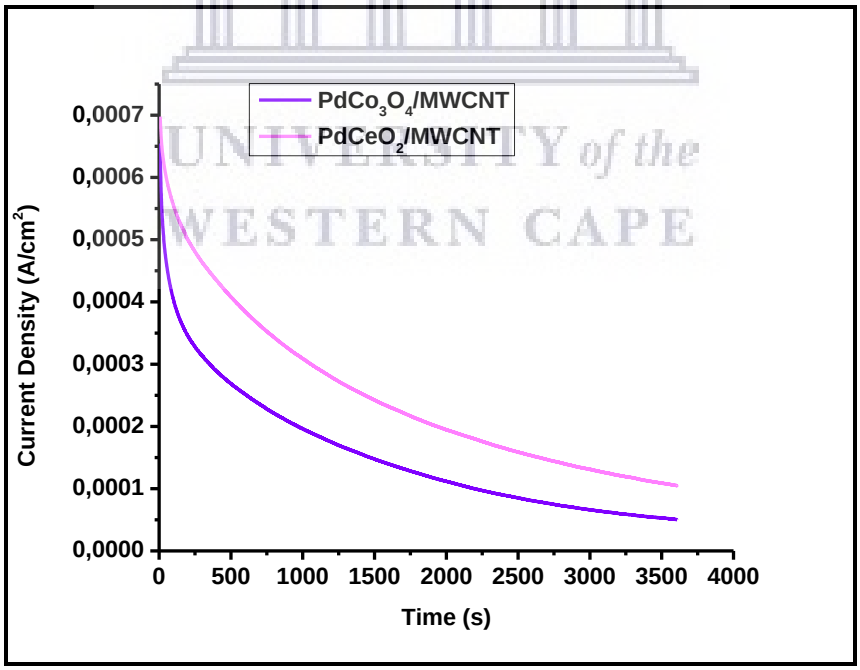

Figure 6. 16: Chronoamperometry of the synthesized electrocatalyst $PdCo_3O_4$/MWCNT and $PdCeO_2$/MWCNT in 1.0 M KOH + 1.0 M Glycerol @ -20mV

References

[1]. Atieh, M. A. *et al.* (2010) 'Effect of carboxylic functional group functionalized on carbon nanotubes surface on the removal of lead from water.', *Bioinorganic chemistry and applications*. doi: 10.1155/2010/603978.

[2]. Fontes, E. H. *et al.* (2019) 'Structural analysis of PdRh/C and PdSn/C and its use as electrocatalysts for ethanol oxidation in alkaline medium', *International Journal of Hydrogen Energy*. Elsevier Ltd, 44(2), pp. 937–951. doi: 10.1016/j.ijhydene.2018.11.049.

[3]. Frota, E., Purgatto, Â. and Linares, J. J. (2014) 'Pt/C, Au/C and Pd/C catalysts for alkaline-based direct glycerol fuel cells', *Chemical Engineering Transactions*, 41(Special Issue), pp. 253–258. doi: 10.3303/CET1441043.

[4]. Lukaszewski, M., Soszko, M. and Czerwiński, A. (2016) 'Electrochemical methods of real surface area determination of noble metal electrodes - an overview', *International Journal of Electrochemical Science*, 11(6), pp. 4442–4469. doi: 10.20964/2016.06.71.

[5]. Yi, Q. *et al.* (2015) 'High Performance Pd, PdNi, PdSn and PdSnNi Nanocatalysts Supported on Carbon Nanotubes for Electrooxidation of C2-C4 Alcohols', *Electroanalysis*, 27(2), pp. 388–397. doi: 10.1002/elan.201400423.

[6]. Gliserol, P. E. *et al.* (2017) 'PRELIMINARY STUDY ON Pd-BASED BINARY CATALYSTS SUPPORTED WITH CARBON NANOFIBER FOR THE ELECTROOXIDATION OF (Kajian Awal ke atas Mangkin Berasaskan Pd Disokong dengan Gentian Nano Karbon untuk', 21(3), pp. 700–708.

[7]. Zhang, Z. *et al.* (2011) 'Pd-Ni electrocatalysts for efficient ethanol oxidation reaction in alkaline electrolyte', *International Journal of Hydrogen Energy*. Elsevier Ltd, 36(20),

pp. 12686–12697. doi: 10.1016/j.ijhydene.2011.06.141.

[8]. Yuan, X.-Z. *et al.* (2010) 'EIS Diagnosis for PEM Fuel Cell Performance', in *Electrochemical Impedance Spectroscopy in PEM Fuel Cells*. Springer London, pp. 193–262. doi: 10.1007/978-1-84882-846-9_5.

[9]. Bianchini, C. and Shen, P. K. (2009) 'Palladium-Based Electrocatalysts for Alcohol Oxidation in Half Cells and in Direct Alcohol Fuel Cells', *Chemical Reviews*. American Chemical Society, 109(9), pp. 4183–4206. doi: 10.1021/cr9000995.

CHAPTER 7

CONCLUSION AND RECOMMEDATIONS

7.1 CONCLUSION

Catalyst materials which are able to harness the energy from chemical reaction in fuel cells are researched to effectively improve energy production in the world. Fuel cells are able to convert chemical energy into electrical energy. Progress has been made in this regard as the development of different catalyst have been fabricated that are able to harness this chemical energy into electrical. Direct Alcohol Fuel Cells has been an example of the remarkable breakthrough in relation to fuel cell, but due to the high cost involved in its production process, attention has been shifted towards finding catalyst and fuels which are cheaper to produce, non-toxic and are made of readily available materials that are earth abundant. Palladium catalyst which are alloyed to secondary transitional metals with or without an oxide, coupled to it applied in alkaline solution have attracted so much attention over the years due to its ability to produce the same efficiency compared to the most used more expensive platinum catalyst and the alloys can altered and improved. The purpose of this work was to incorporate nickel, tin, cobalt oxide and cerium oxide, into the palladium catalyst supported on MWCNT to improve its catalytic activity towards the oxidation of glycerol. Pd/MWCNT, PdNi/MWCNT, PdSn/MWCNT, $PdNiCo_3O_4$/MWCNT,

$PdSnCo_3O_4$/MWCNT, $PdCo_3O_4$/MWCNT, $PdNiCeO_2$/MWCNT, $PdSnCeO_2$/MWCNT and $PdCeO_2$/MWCNT were synthesized through the modified polyol method using ethylene glycol (EG) as solvent and reducing agent. The synthesized nanoparticles were then analyzed to determine their properties.

Firstly, MWCNT were first COOH functionalized with (3:1 ratio) HNO_3/H_2SO_4 mixture, and the functionalized MWCNT nanoparticles were investigated through FTIR and the spectrum obtained reveals the presence of some functional group such as O-H stretching, C=O stretching, C-C stretching, C-O stretching and C-H stretching. All these bands were attributed to the solvent used during synthesis. The MWCNT were successfully functionalized. Secondly, Pd-based catalysts supported on MWCNT were prepared through polyol method according to literature. In this work, ethylene glycol was used for the synthesis which allowed controlling the particle size and to minimize particle agglomeration and also act as a reducing agent for Pd^{2+} to Pd, PdNi/MWCNT, PdSn/MWCNT, $PdNiCo_3O_4$/MWCNT, $PdSnCo_3O_4$/MWCNT, $PdCo_3O_4$/MWCNT, $PdNiCeO_2$/MWCNT, $PdSnCeO_2$/MWCNT and $PdCeO_2$/MWCNT were successfully synthesized.

The electrochemical active surface area (ECSA) of the synthesized catalysts was obtained from cyclic voltammetry plot. The calculated ECSA were 0.72 m^2/g for commercial Pd/C, 0.75 m^2/g for Pd/MWCNT, 4.8 m^2/g for PdNi/MWCNT, 0.85 m^2/g for PdSn/MWCNT,

0.74 m^2/g for $PdNiCo_3O_4$/MWCNT, 1.3 m^2/g for $PdSnCo_3O_4$/MWCNT, 5.02 m^2/g for $PdNiCeO_2$/MWCNT, 1.14 m^2/g for $PdSnCeO_2$/MWCNT, for 0.99 m^2/g $PdCeO_2$/MWCNT and 1.89 m^2/g for $PdCo_3O_4$/MWCNT. The ECSA obtained for the alloyed palladium catalysts shows a successfully outcome of the introduction of the secondary metal and oxide into the palladium. The morphology of the synthesized catalysts from HR-TEM gave the expected dot-like appearance mostly reported for palladium catalysts, with the structure of the MWCNT support showing a rod-like appearance. The HR-TEM micrographs as well as the SAXS plot of shape revealed that the nanoparticles were polydispersed due to slight agglomeration of catalyst particles. The particle size of the nanoparticles was obtained through SAXS plot of size distribution which confirm that the synthesized particle was of small size radius in nanoscale. The particle size obtained were 20 nm for Pd/C, 15 nm for Pd/MWCNT, 15 nm for PdNi/MWCNT, 15 nm for PdSn/MWCNT, 18 nm for $PdNiCo_3O_4$/MWCNT, 20 nm for $PdSnCo_3O_4$/MWCNT, 20 nm for $PdCo_3O_4$/MWCNT, 15 nm for $PdNiCeO_2$/MWCNT, 19 nm for $PdSnCeO_2$/MWCNT and 16 nm for $PdCeO_2$/MWCNT. The crystallite size of the nanoparticles was obtained using Debye-Scherrer equation from XRD data of the nanoparticles and were 8.4 nm for Pd/C, 11 nm for Pd/MWCNT, 11.4 nm for PdNi/MWCNT, 9.5 nm for PdSn/MWCNT, 9.7 nm for $PdNiCo_3O_4$/MWCNT, 10 nm for $PdSnCo_3O_4$/MWCNT, 12 nm for $PdCo_3O_4$/MWCNT, 8.5 nm for $PdNiCeO_2$/MWCNT, 14 nm for $PdSnCeO_2$/MWCNT and 15 nm for $PdCeO_2$/MWCNT. The HR-TEM micro graphs were used to obtain the particle size of the

synthesized catalysts, the obtained particle sizes were 3.4 nm for Pd/C, 13.7 nm for Pd/MWCNT, 11.5 nm for PdNi/MWCNT, 8.2 nm for PdSn/MWCNT, 11 nm for $PdNiCo_3O_4$/MWCNT, 11.1 nm for $PdSnCo_3O_4$/MWCNT, 16.83 nm for $PdCo_3O_4$/MWCNT, 12.3 nm for $PdNiCeO_2$/MWCNT, 18 nm for $PdSnCeO_2$/MWCNT and 15.33 nm for $PdCeO_2$/MWCNT. The crystallinity of the nanoparticles was examined through XRD and SAED. The plot of the XRD data revealed the presence of the palladium phase (fcc for Pd) in all the synthesized catalysts. The peaks obtained in the XRD were further confirmed by the SAED micrograph.

The electroactivity of the catalysts was evaluated through CV, EIS and CA. The CV results of Pd/C and Pd/MWCNT were compared to the bimetallic catalysts PdNi/MWCNT and PdSn/MWCNT. PdNi/MWCNT showed highest peak current density in glycerol oxidation with 6.657 mA/cm^2 followed by 1.277 mA/cm^2 for PdSn/MWCNT, 0.842 mA/cm^2 for Pd/C and 0.449 mA/cm^2 for Pd/MWCNT respectively. PdSn/MWCNT had the highest ECSA and was expected to have the highest oxidation peak, however it had poor particles distribution on the surface of the MWCNT which resulted into agglomeration and can be seen on the SAXS plot. The addition of the secondary metal to palladium did improve the glycerol oxidation current density. The catalyst poisoning by the carbonaceous species is traced from the forward scan to backward (I_f/I_r) scan peak current density ratio, with PdNi/MWCNT having the highest ratio at 10.91 meaning low catalyst poisoning followed

by 2.13 for Pd/C, 0.92 for PdSn/MWCNT and 0.31 for Pd/MWCNT. This trend is confirmed by EIS with PdNi/MWCNT being the best overall performing catalyst followed by Pd/C, Pd/MWCNT and PdSn/MWCNT. However Pd/MWCNT is perfoming better than PdSn/MWCNT while PdSn/MWCNT has a higher (I_f/I_r) ratio, this is due to the agglomeration of which affects it kinetically PdSn/MWCNT. Plus Pd/C, Pd/MWCNT and PdSn/MWCNT display a capacitive feature expected for hydrogen adsorption/desorption and double layer charging/ discharging phenomena. PdNi/MWCNT there is a changeover from capacitive behavior to resistive behavior as indicated by a semicircle, which can be assigned to kinetically controlled reaction. The stability of the catalysts was evaluated through Chronoamperometry. The addition of the secondary metal to palladium did improve the catalyst stability with PdNi/MWCNT having the best catalyst stability, followed by PdSn/MWCNT, Pd/C and Pd/MWCNT respectively. Ni has similar electronic properties to Pd compared to Sn, as it is a group above Pd in the periodic table this contributes to Pd catalyst stability and electroactivity.

The electroactivity results of $PdNiCo_3O_4$/MWCNT, $PdSnCo_3O_4$/MWCNT, $PdNiCeO_2$/MWCNT and $PdSnCeO_2$/MWCNT were compared. The peak current density (If) for $PdNiCo_3O_4$/MWCNT is 14.46 mA/cm^{-2} which is highest compare to $PdNiCeO_2$/MWCNT 6.137 mA/cm^{-2}, $PdSnCo_3O_4$/MWCNT is 1.412 mA/cm^{-2} and $PdSnCeO_2$/MWCNT is 1.358 mA/cm^{-2} respectively. The forward scan results show that

the addition of a secondary metal Ni in Pd to form catalysts with an oxide can significantly improve the catalytic activity of Pd for glycerol oxidation in alkaline media. The catalyst poisoning against the carbonaceous species is traced from the forward scan to backward (I_f/I_r) scan peak current density ratio. The ratio for $PdNiCeO_2$/MWCNT was 22.59 and showed a higher value compared to 9.81 for $PdSnCeO_2$/MWCNT, 5.23 for $PdNiCo_3O_4$/MWCNT and 2.68 for $PdSnCo_3O_4$/MWCNT respectively. The CeO_2 oxide promotes the adsorption of oxygen species such as OH on bimetallic PdNi and PdSn surface to oxidize CO or adsorbed CO-like carbonaceous species on Pd sites. Plus the fewer amount of oxygen on the oxides helps reduce amount of CO carbonaceous species produced. Therefore $PdNiCeO_2$/MWCNT showed better oxidation of glycerol to carbon dioxide during anodic scan and less accumulation of carbonaceous species on the catalyst surface compared to $PdSnCeO_2$/MWCNT, $PdNiCo_3O_4$/MWCNT and $PdSnCo_3O_4$/MWCNT. EIS results of $PdNiCeO_2$/MWCNT and $PdSnCeO_2$/MWCNT catalyst display an ionic resistance that may be due to a less homogenous catalyst layer on the ink prepared for electrode coating and the addition of CeO_2 oxide may have contributed to the behavior. $PdSnCo_3O_4$/MWCNT shows better performance with a semi-circle capacitive behavior at -30mv only and mostly displaying a capacitive behavior with $PdNiCo_3O_4$/MWCNT. The stability of $PdNiCeO_2$/MWCNT was better than that of $PdSnCeO_2$/MWCNT. $PdSnCo_3O_4$/MWCNT was most stable compared to $PdNiCo_3O_4$/MWCNT. The overall stability trend from the best stable catalyst to the least

stable catalyst is as follows $PdNiCeO_2$/MWCNT, $PdSnCo_3O_4$/MWCNT, $PdSnCeO_2$/MWCNT and $PdNiCo_3O_4$/MWCNT. On the CeO_2 oxide the PdNi alloy has better stability compared to PdSn alloy and on the Co_3O_4 oxide, PdSn alloy has better stability than PdNi alloy.

$PdCeO_2$/MWCNT showed highest (I_f) peak current density in glycerol oxidation of 3.899 mA/cm^2 followed by 0.8295 mA/cm^2 for $PdCo_3O_4$/MWCNT. The catalyst poisoning against the carbonaceous species is traced (I_f/I_r) current density ratio. The ratio for $PdCeO_2$/MWCNT was 4.53 and showed a higher value compared to 2.05 for $PdCo_3O_4$/MWCNT. The CeO_2 oxide promotes the adsorption of oxygen species such as OH on Pd surface to oxidize CO or adsorbed CO-like carbonaceous species on Pd sites. In EIS at -30mv and -10mv $PdCeO_2$/MWCNT shows better performance with a semi-circle capacitive behavior to compared to $PdCo_3O_4$/MWCNT that displayed an ionic resistance. At 30mv and 10mv $PdCo_3O_4$/MWCNT display better ionic resistance compared to $PdCeO_2$/MWCNT catalyst. The overall best catalysts performance for the binary catalysts is PdNi/MWCNT, for the oxides is $PdCeO_2$/MWCNT and for the ternary catalysts is $PdNiCeO_2$/MWCNT

7.2 RECOMMENDATIONS

This study therefore recommends that the PdNi catalysts supported on multi-walled carbon nanotubes should be used as glycerol oxidation tolerant catalyst as they show both activity and durability over the PdSn catalysts supported on multi-walled carbon nanotubes. Therefore, in terms of reducing the metal loading nickel and cerium oxide are the recommended material of choice as this study discovered that the Pd binds well to the nickel and cerium oxide during synthesis. Further studies are also recommended on the role of supporting materials as these materials have great influence on the cost, activity and durability of the fuel cell catalyst and, accordingly, the fuel cell system.